Hadron production and polarisation of gluons in the nucleon in the μ–N interactions in the COMPASS experiment at CERN

Grzegorz Brona

Ph.D. thesis
performed under supervision of Professor Barbara Badełek

Faculty of Physics, University of Warsaw

Warsaw, 2007

For Alicja Kownacka and Roman Kownacki, my Grandparents

Dla Alicji i Romana Kownackich, moich Babci i Dziadka

Abstract

This thesis presents a determination of the gluon polarisation $\Delta G/G$ in the nucleon. The result was obtained studying the Photon–Gluon Fusion process with the open charm mesons production. The data come from the COMPASS experiment at CERN using a polarised ^{6}LiD target and a 160 GeV polarised muon beam. The analysis is based on the data taken in 2002–2004. The result is $\mathbf{\Delta G/G = -0.62 \pm 0.44}$(stat.) $\pm\, \mathbf{0.18}$(syst.) at the QCD scale μ^2 =13 GeV^2 and the average x_g equal to 0.15 with RMS of 0.08. This result translates into $\Delta G(x_g = 0.15, \mu^2 = 13\mathrm{GeV}^2) = -8.0 \pm 6.3$ for the GRV98 gluon distribution. The presented value is the first experimental determination of the gluon polarisation done with the open charm mesons method and also a primary objective of COMPASS. It is in agreement with other lepton scattering results, obtained with the high-$\mathrm{p_T}$ method (COMPASS, SMC and HERMES) and with results from proton-proton interactions (STAR and PHENIX). All of the measurements point towards a small gluon polarisation in the nucleon. As the analysis requires charm particles reconstruction, a special attention was given to the studies of the hadron mass spectroscopy with the COMPASS spectrometer. These studies are also summarised in the thesis.

Contents

Introduction

"...It is a mysterious beast, and yet its practical effect prevails over the whole of science. The existence of spin, and the statistics associated with it, is the most subtle and ingenious design of Nature – without it the whole Universe would collapse..." **Tomonaga**

In the early 1925 Pauli proposed the idea that electrons are described with an extra "classically undescribable two-valuedness" quantum number. The concept was motivated by an observation of the atomic energy levels impossible to be explained by the naïve quantum theory existing at the time. With an additional quantum number, Pauli was able to formulate the famous exclusion principle, according to which two electrons cannot be in the same quantum state. Later that year Uhlenbeck and Goudsmit suggested that this quantum number is related to the electron intrinsic angular momentum, called spin. Soon it was realised that the Stern and Gerlach experiment, conducted as early as 1921 but misinterpreted then, had provided with an evidence of the subsistence of intrinsic angular momentum of electron and proved it is quantized. The idea of electron being spin $\frac{1}{2}$ particle and having two possible projections of spin at a given axis: $s_z = +\frac{1}{2}$ and $s_z = -\frac{1}{2}$ was accepted[1]. The proton spin determination was performed by the end of the twenties. Later also the neutron spin was measured. They are the same as that of electron.

The structure of nucleon can be probed scattering a beam of high energy leptons on a nuclear target. Such measurements performed at SLAC in the late sixties provided evidence for a quark substructure of the nucleon. The image developed since then perceives nucleons as composed of two kinds of objects – quarks and gluons. Quarks are spin $\frac{1}{2}$ particles and apart from the fractional electric charge, carry also colour charge. There exist six kinds of quarks, called flavours: up (u), down (d), strange (s), charm (c), bottom (b) and top (t); but only three of them (u,d,s) share masses smaller than the nucleon mass and thus can contribute significantly to its internal structure. The quarks can interact with each other through exchange of gluons being also endowed with the colour charge. Gluons are spin 1 particles and are electrically neutral. Both, quarks and gluons, can contribute to the total spin of the nucleon. The analysis presented in this thesis aims at the direct measurement of the gluons contribution.

If $\Delta\Sigma$ denotes the number of quarks with spins parallel to the nucleon spin minus the number of quarks with anti-parallel spins, the quark spin contribution is equal to $\frac{1}{2}\Delta\Sigma$. Similarly, the contribution from the gluons is equal to the number of gluons with spins parallel minus the number of gluons with spins anti-parallel to the nucleon spin and is denoted by ΔG. Contributions from the angular momenta of quarks and gluons

---

[1] Throughout this thesis $\hbar = c = 1$ is assumed.

are called J. Thus the nucleon spin (s_z) can be written as:

$$\frac{1}{2} = \frac{1}{2}\Delta\Sigma + \Delta G + J \tag{1}$$

The $\Delta\Sigma$ can be further decomposed into the contributions from quarks and anti-quarks of different flavours:

$$\Delta\Sigma = \Delta u + \Delta d + \Delta s + \Delta\overline{u} + \Delta\overline{d} + \Delta\overline{s} \tag{2}$$

With the three independent quantities, $\Delta\Sigma$, ΔG and J, various scenarios fulfilling the sum rule (1) are possible. The simplest scenario based on the non-relativistic QPM assumes that two valence quarks have their spins parallel to the spin of the nucleon and one has its spin anti-parallel. This corresponds to the $\Delta\Sigma$=1, ΔG=J=0. Including relativistic effects results in $\Delta\Sigma \approx$0.6 [1].

The first experiment to measure the polarisation effects in the inelastic lepton-nucleon scattering, E80 [2], was conducted in the mid-seventies at SLAC in USA. In the eighties the kinematical range for the measurements was considerably extended by the European Muon Collaboration (EMC) [3] at CERN due to the much higher beam energy. The result for $\Delta\Sigma$ was 0.12±0.09±0.14; considerably smaller than 0.6. The EMC result triggered a number of experiments in Europe – SMC at CERN [4], HERMES at DESY [5], and in USA – E142, E143 and E155 at SLAC [6–8]. They all confirmed the EMC observation. Presently COMPASS at CERN [9] aims at a direct measurement of the ΔG. Two different approaches based on tagging the Photon–Gluon Fusion (PGF) process are used here. The tagging is via the detection of the open charm mesons or the high–$\mathrm{p_T}$ hadron pairs. This thesis is dedicated to the first method. That approach has never been used for polarisation effects studies before. The other method, employed also previously by SMC and HERMES experiments, depends strongly on Monte Carlo simulations.

Studies of the open charm mesons require very efficient hadron identification and reconstruction. Therefore this thesis consists of two parts: the first one dedicated to the hadron spectroscopy and the second – focused directly on the ΔG measurement. The structure is the following. Chapter 1 describes the theoretical motivation and methods used for the determination of the gluon polarisation in the nucleon. In the second chapter the COMPASS spectrometer and the software tools used for the events reconstruction and analysis are presented. The chapter is concluded with a section dedicated to a new detector that was constructed in Warsaw. Chapter 3 describes the studies of the reconstruction of neutral hadrons decaying into charged particles in the detector and outlines the search for rare hadronic states. The next chapter presents cuts leading to the most efficient selection of the open charm mesons while chapter 5 introduces mathematical techniques aiming at the estimation of ΔG. Chapter 6 presents the final result on the gluon polarisation determined in the open charm production channel. Chapter 7 deals with a detailed discussion of systematic effects. A summary of the analysis and an outlook on the future improvements of the gluon polarisation measurement are presented in chapter 8.

A measurement of the gluon polarisation with the open charm method is the main goal of COMPASS. The author has performed one of the two parallel analyses of the data which included: selection of the open charm events, optimisation of the cuts, simulations of the analysing power and studies of the systematic error. The author was also involved in the studies of the low momenta tracks poorly reconstructed in the spectrometer and in the tests that led to the optimisation of the features of a new detector added to the COMPASS experimental setup in 2006. The part dedicated to the hadron spectroscopy is the author's own contribution as well.

Results described in this thesis were presented by the author at the following conferences:

- Cracow Epiphany Conference on Hadron Spectroscopy, Cracow, 2005 [10];
- Cascade Physics - A New Window on Baryon Spectroscopy, Jefferson Laboratory, USA, 2005;
- SPIN-PRAHA-2006, Prague, 2006 [11];
- 42nd Rencontre de Moriond, QCD and High Energy Hadronic Interactions, La Thuile, 2007 [12].

A part of the thesis dedicated to the hadron spectroscopy is described in [13]. A paper with results on the gluon polarisation studied with the open charm mesons will soon be submitted for publication in the Physical Review Letters.

Chapter 1

Theoretical and Experimental Introduction to the ΔG Measurement

In this chapter a short introduction to the polarised lepton-nucleon inelastic scattering is presented. A discussion of the spin independent and spin dependent structure of the nucleon is included. It is focused on the measurements of the gluon polarisation inside the nucleon. The chapter is composed of three parts: dedicated to relevant theoretical ideas, to the experimental methods, and presenting a short overview of the present and past experiments measuring the polarised gluon distribution.

1.1 Inelastic Scattering

Knowledge of the internal structure of the nucleon is obtained mainly from the inelastic scattering measurements. Here we call inelastic scattering a process of high energy lepton scattering on constituents of a nucleon. The scattering is via a virtual boson exchange and leads to a destruction of the initial nucleon. In what follows the scattering is considered for the fixed target experiments as all the information on the polarised nucleon structure obtained up to now comes practically from such measurements.

The scattering measurements can be restricted only to two independent variables, that is to the energy of the scattered lepton (E') and its deflection angle (θ) with respect to the direction of flight of the incoming lepton. Such measurements are called inclusive. Often also specific interaction products are measured. Such analyses are referred to as semi-inclusive or exclusive (when the whole final state is reconstructed). The analysis presented in this thesis is based on the reconstruction of the open charm mesons. Therefore it is of the semi-inclusive kind.

In the case of COMPASS the interacting lepton is a muon and the mediating boson (muon-nucleon centre-of-mass energy about 17 GeV) is a photon. Since the electromagnetic constant α is small it is well justified to assume that during the interaction only one photon is exchanged[1].

The inelastic scattering interaction diagram is presented in Fig. 1.1. If the laboratory system coordinates are fixed with the Z axis pointing in the direction of the incoming

---

[1] This assumption is valid for the targets composed of light elements ($Z \ll 1/\alpha$), *e.g.* for the COMPASS target.

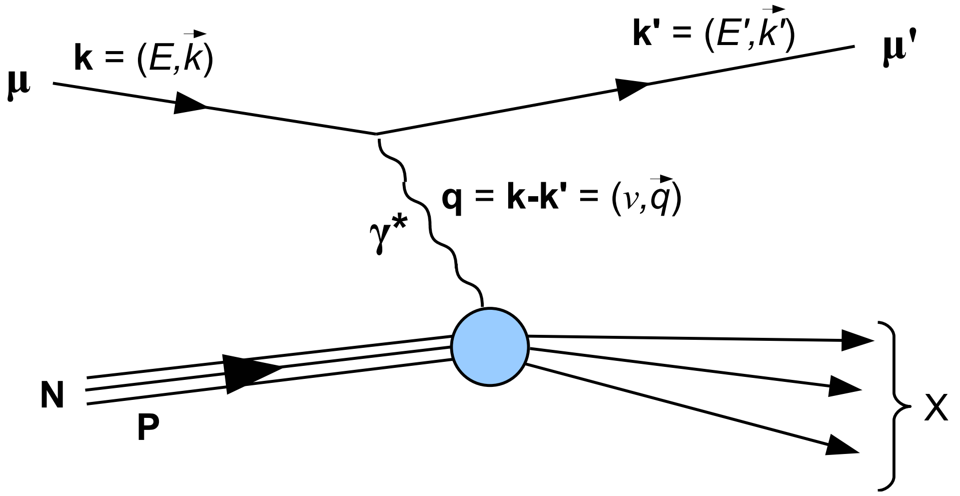

Figure 1.1: Diagram of the inclusive inelastic μN scattering in the one photon exchange approximation.

muon its momentum four-vector is defined as:

$$\mathbf{k} = (E, \overrightarrow{k}) \overset{LAB}{=} (E, 0, 0, |\overrightarrow{k}|) \tag{1.1}$$

Here E and $\overrightarrow{k}$ are energy and momentum vector of the incoming muon. The momentum four-vector of the target nucleon, at rest in the LAB system, is given by:

$$\mathbf{P} \overset{LAB}{=} (M, 0, 0, 0) \tag{1.2}$$

where M is the nucleon mass. The $\mathbf{q}$ is a four-momentum transfer from the lepton to the hadronic system:

$$\mathbf{q} = \mathbf{k} - \mathbf{k}' \tag{1.3}$$

We choose the following Lorentz invariants to describe the interaction: Q^2, x and y. They are defined as:

$$Q^2 = -\mathbf{q}^2 = -(\mathbf{k} - \mathbf{k}')^2 \overset{LAB}{=} -2(m_\mu^2 - EE' + |\overrightarrow{k}||\overrightarrow{k'}|\cos\theta) \tag{1.4}$$

$$y = \frac{\mathbf{P} \cdot \mathbf{q}}{\mathbf{P} \cdot \mathbf{k}} \overset{LAB}{=} \frac{\nu}{E} \tag{1.5}$$

$$x = \frac{Q^2}{2\mathbf{P} \cdot \mathbf{q}} \overset{LAB}{=} \frac{Q^2}{2M\nu} \tag{1.6}$$

where $\nu = E - E'$ and m_μ is the muon mass. The Q^2 variable is a photon virtuality and the Bjorken scaling variable x can be treated as a measure of the elasticity of the process, in the Quark Parton Model in the Breit frame[2] it is interpreted as a fraction of the nucleon momentum carried by the struck quark [14]. The y is the fraction of the incoming lepton energy carried by the photon. At a given interaction energy only two of the above variables are independent.

The analysis presented in this thesis is based on the COMPASS ability to measure

---

[2] Breit frame is defined with: $\overrightarrow{q} + 2x\overrightarrow{P} = 0$. The Z-axis coincides with the nucleon-photon axis.

at least a part of the final hadronic system. For a description of such a semi-inclusive process another Lorentz invariant variable, called z, is defined:

$$z = \frac{\mathbf{P} \cdot \mathbf{P_h}}{\mathbf{P} \cdot \mathbf{q}} \tag{1.7}$$

where $\mathbf{P_h}$ is a momentum four-vector of a hadron that is measured in the final hadronic state. In the laboratory system z can be rewritten as:

$$z \overset{LAB}{=} \frac{E_h}{\nu} \tag{1.8}$$

It describes a fraction of the energy of the interacting photon carried by a given hadron.

1.2 The Cross-Section

The differential cross-section for the inclusive scattering is given by the following formula [15]:

$$\frac{\mathrm{d}^2\sigma}{\mathrm{d}\Omega \mathrm{d}E'} = \frac{e^4}{16\pi^2 Q^4} \frac{E'}{ME} L_{\mu\nu} W^{\mu\nu} \tag{1.9}$$

where $L_{\mu\nu}$ is a leptonic tensor corresponding to a virtual photon emission from the lepton line, and $W^{\mu\nu}$ is a hadronic tensor which represents the virtual photon-hadron interaction. The former is well described by the **Q**uantum **E**lectro**D**ynamics (QED) while the latter cannot be calculated directly (*e.g.* in QCD) since it depends also on the non-perturbative dynamics. For inclusive scattering involving the projectile and the target polarisations, the tensors depend on the momenta and spins four-vectors of particles taking part in the interaction: $L_{\mu\nu}(\mathbf{s}, \mathbf{k}, \mathbf{k}')$, $W^{\mu\nu}(\mathbf{S}, \mathbf{P}, \mathbf{q})$. For simplicity we will discuss the formalism for spin $\frac{1}{2}$ target first, and then the considerations will be broaden to cover also spin 1 case.

Both tensors, $L_{\mu\nu}$ and $W_{\mu\nu}$, can be split into two parts – symmetric and an anti-symmetric with respect to the interchange of $\mu\nu$ indices. Only the anti-symmetric parts depend on the polarisation:

$$L_{\mu\nu}(\mathbf{s}, \mathbf{k}, \mathbf{k}') = L^S_{\mu\nu}(\mathbf{k}, \mathbf{k}') + iL^A_{\mu\nu}(\mathbf{s}, \mathbf{k}, \mathbf{k}') \tag{1.10}$$

$$W^{\mu\nu}(\mathbf{S}, \mathbf{P}, \mathbf{q}) = W^{\mu\nu}_S(\mathbf{P}, \mathbf{q}) + iW^{\mu\nu}_A(\mathbf{S}, \mathbf{P}, \mathbf{q}) \tag{1.11}$$

The $L^S_{\mu\nu}$ and $L^A_{\mu\nu}$ can be calculated in the QED:

$$L^S_{\mu\nu}(\mathbf{k}, \mathbf{k}') = 2(k'_\mu k_\nu + k'_\nu k_\mu + (m^2 - \mathbf{k}' \cdot \mathbf{k}) g_{\mu\nu}) \tag{1.12}$$

$$L^A_{\mu\nu}(\mathbf{s}, \mathbf{k}, \mathbf{k}') = -2m\epsilon_{\mu\nu\rho\sigma} q^\rho s^\sigma \tag{1.13}$$

where $\epsilon_{\mu\nu\rho\sigma}$ is the fully anti-symmetric Levi-Civita tensor defined by ϵ_{1234}=1 and $g_{\mu\nu}$ is the diagonal metric tensor.

The $W^{\mu\nu}_S$ and $W^{\mu\nu}_A$ can be parameterised in the following way (cf. [16]):

$$W^{\mu\nu}_S(\mathbf{P}, \mathbf{q}) = -g^{\mu\nu} F_1 + \frac{F_2}{\mathbf{P} \cdot \mathbf{q}} P^\mu P^\nu \tag{1.14}$$

$$W_A^{\mu\nu}(\mathbf{S},\mathbf{P},\mathbf{q}) = g_1\frac{M}{\mathbf{P}\cdot\mathbf{q}}\epsilon^{\mu\nu\lambda\delta}q_\lambda S_\delta + g_2\frac{M}{(\mathbf{P}\cdot\mathbf{q})^2}\epsilon^{\mu\nu\lambda\delta}q_\lambda(\mathbf{P}\cdot\mathbf{q}S_\delta - \mathbf{S}\cdot\mathbf{q}p_\delta) \tag{1.15}$$

where F_1, F_2, g_1, g_2 are functions of x and Q^2 and contain information on the internal structure of the target nucleon. They are called structure functions and have to be measured in experiments. After the contraction of the $L_{\mu\nu}W^{\mu\nu}$ tensors the formula (1.9) for the cross-section can be decomposed into a sum of two terms, the first one proportional to $L^S_{\mu\nu}W^{\mu\nu}_S$ and the other proportional to $L^A_{\mu\nu}W^{\mu\nu}_A$. The differential cross-section can be rewritten as:

$$\frac{\mathrm{d}^3\sigma}{\mathrm{d}x\mathrm{d}Q^2\mathrm{d}\vartheta} = \frac{\mathrm{d}^3\overline{\sigma}}{\mathrm{d}x\mathrm{d}Q^2\mathrm{d}\vartheta} - \frac{1}{2}h\frac{\mathrm{d}^3\Delta\sigma}{\mathrm{d}x\mathrm{d}Q^2\mathrm{d}\vartheta} \tag{1.16}$$

where the first part is independent of the spin orientations of the interacting particles while the second part depends on the relative spin orientation of the target and of the projectile. The angle ϑ is an angle between the projections of $\vec{k'}$ and $\vec{S}$ onto the XY plane, transverse to the direction of the incoming lepton, Fig. 1.2. The h is the lepton's helicity. The second term in this equation can be further decomposed into two parts:

$$\frac{\mathrm{d}^3\Delta\sigma}{\mathrm{d}x\mathrm{d}Q^2\mathrm{d}\vartheta} = \cos\alpha\frac{\mathrm{d}^3\Delta\sigma_\parallel}{\mathrm{d}x\mathrm{d}Q^2\mathrm{d}\vartheta} + \sin\alpha\frac{\mathrm{d}^3\Delta\sigma_T}{\mathrm{d}x\mathrm{d}Q^2\mathrm{d}\vartheta} \tag{1.17}$$

where α is an angle between $\vec{S}$ and $\vec{k}$. Here the first term describes the case when the spin of the interacting lepton is parallel to the spin of the target particle while the other corresponds to the projectile spin oriented transversely with respect to the spin of the nucleon. For a discussion of the presented decomposition and relations between the cross-section and the structure functions see *e.g.* [17].

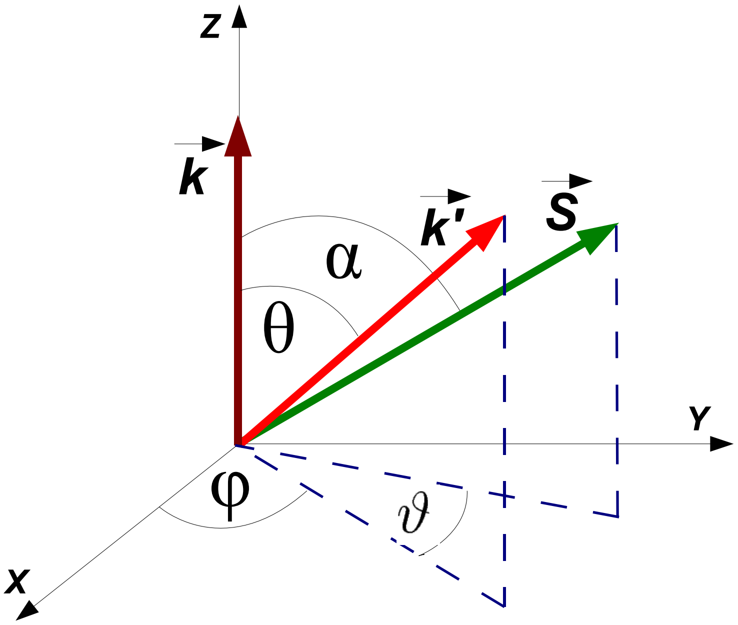

Figure 1.2: Definition of the angles used for the description of polarised scattering.

1.3 The Nucleon Structure Functions

The four structure functions: F_1, F_2, g_1 and g_2, that parameterise the structure of the nucleon cannot be derived from theory. They have to be measured in experiments.

1.3.1 Structure Functions in the Quark Parton Model

The Quark Parton Model describes the internal nucleon structure in terms of the non-interacting, pointlike and massless particles called partons. It is defined in the nucleon's infinite momentum frame. In this frame partons do not carry transverse momenta. The photon probing the nucleon structure is thus interacting with a given parton which during the interaction does not feel the existence of other surrounding partons. The interaction can occur only if a parton carries an electric charge. The charged partons are identified with quarks.

In the QPM the structure functions depend only on x, a fraction of a nucleon momentum carried by a struck quark. The structure functions can be related to the functions that define quark distributions in the nucleon, $q_f^+(x)$ and $q_f^-(x)$, where f denotes the quark flavour while "+" and "−" refer to the quark spin orientation, parallel and anti-parallel to the spin of the nucleon respectively. The distribution functions are the probability densities of finding a quark of a given flavour, spin orientation and momentum fraction x in the nucleon. The F_1 structure function in the QPM can be expressed as:

$$F_1(x) = \frac{1}{2}\sum_f e_f^2(q_f^+(x) + q_f^-(x)) = \frac{1}{2}\sum_f e_f^2 q_f(x) \tag{1.18}$$

where e_f is an electric charge, in units of the elementary charge, carried by a quark of a flavour f. The summation is over all flavours. The F_2 in the QPM can be obtained from F_1 function using the Callan-Gross relation [18]:

$$F_2(x) = 2xF_1(x) = x\sum_f e_f^2(q_f^+(x) + q_f^-(x)) \tag{1.19}$$

The experiments performed in the sixties at SLAC confirmed an approximate dependence of F_1 and F_2 on x only. A discovery of this effect, called the Bjorken scaling, was a stunning success of the QPM. The next experiments have shown that the scaling is not complete and a weak F_1 and F_2 dependence on Q^2, of the order of 10%, appears. It will be a subject of the next section. The F_2 structure function for the proton was thoroughly measured in various experiments, Fig. 1.3.

The g_1 structure function in the QPM has a form similar to that of F_1. It is a square of electric charge weighted difference of distributions of quarks with spin parallel and anti-parallel to the spin of the nucleon:

$$g_1(x) = \frac{1}{2}\sum_f e_f^2\Big[q_f^+(x) - q_f^-(x)\Big] = \frac{1}{2}\sum_f e_f^2\Delta q_f(x) \tag{1.20}$$

where $\Delta q_f(x) = q_f^+(x) - q_f^-(x)$. The measured values of g_1 for proton are presented in Fig. 1.4. In the QPM the g_2 structure function is equal to 0 at all x.

For the spin 1 target the hadronic tensor is parameterised by eight structure functions. Apart from the spin-independent F_{1-2} and the spin-dependent g_{1-2} structure functions, four additional structure functions b_{1-4} are needed (cf. [27]). All these functions depend on x and Q^2. The b_{1-4} are predicted to be small and can be neglected at the precision at which the target is probed in COMPASS [28, 29]. Neglecting those functions makes the formalism introduced for spin $\frac{1}{2}$ hold also for the spin 1 target.

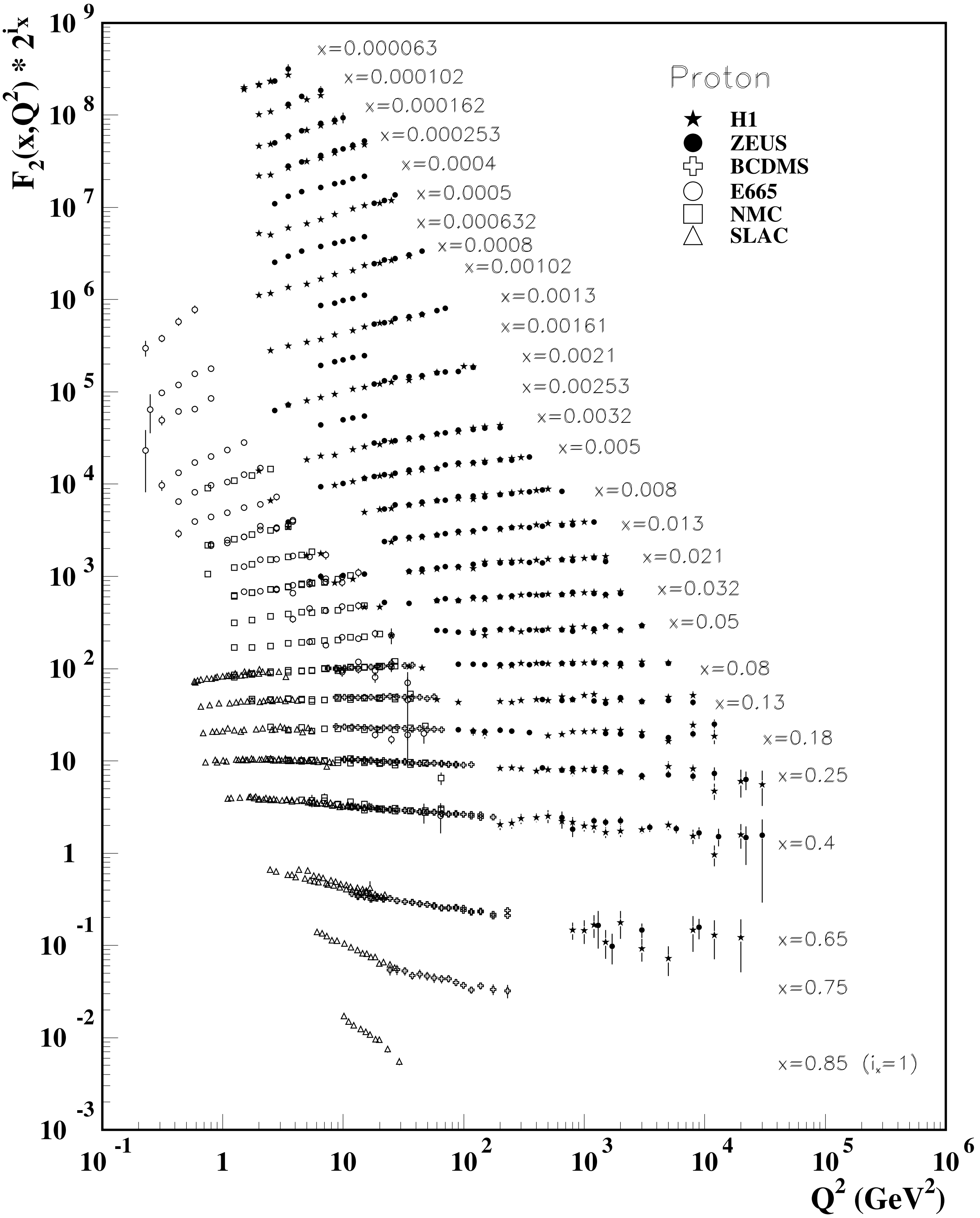

Figure 1.3: The proton F_2^p structure function measured in the scattering of positrons on protons at ZEUS [19] and H1 [20] at the HERA collider, and in the scattering of electrons and muons on fixed proton targets at BCDMS [21], E665 [22], NMC [23] and SLAC [24]. Errors are statistical and systematic uncertainties added in quadratures. For the purpose of clarity the F_2^p was multiplied by 2^{i_x}, where i_x is the x–bin number (for $x = 0.85$ the $i_x = 1$, for $x = 0.000063$ the $i_x = 28$). Plot taken from [25].

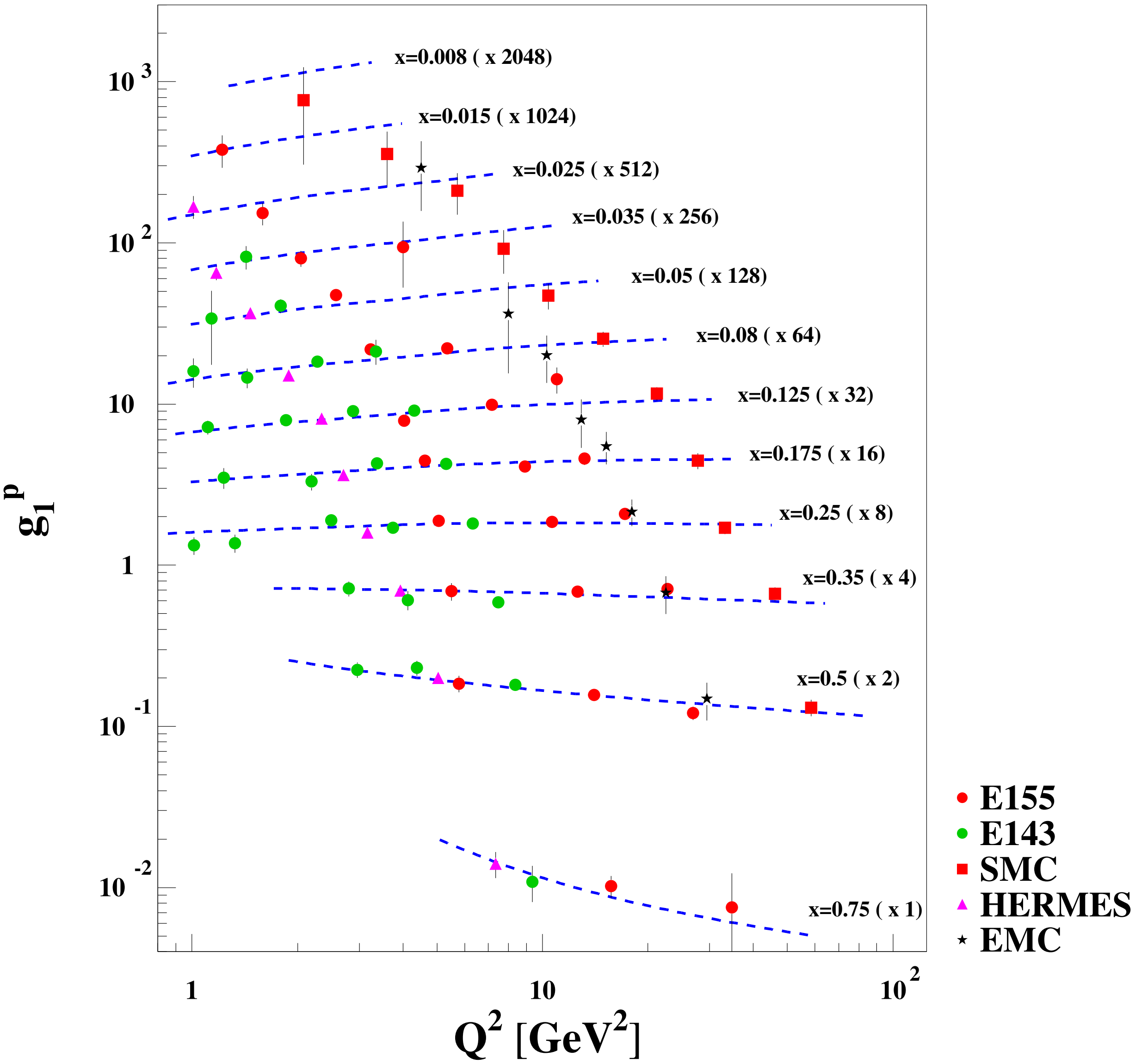

Figure 1.4: The proton spin dependent structure function, g_1^p, measured in the scattering of charged leptons on fixed proton targets. The dashed lines are from a functional fit to the world g_1^p data. The points and lines were scaled by the factors in parentheses. Plot taken from [26].

1.3.2 QCD Improved Parton Model

The QCD model of strong interactions enriched the simple picture of the nucleon with gluons. Gluons are massless bosons responsible for the mediation of the strong forces between partons. Unpolarised inclusive inelastic lepton-nucleon scattering have shown that quarks carry only about a half of the total nucleon momentum. The rest of it is attributed to gluons. The gluons are thus as important as quarks when the internal structure of the nucleon is considered.

The presence of the strong interactions between partons introduces the Q^2 dependence to the structure functions. A quark can emit a gluon, a gluon can split into a $q\overline{q}$ pair. A quark from that pair can subsequently emit another gluon and so on. Increasing the Q^2

of the interaction, increases the resolution of the nucleon probing. Therefore at higher Q^2 a parton reveals its QCD structure of a compound of quarks and gluons. The photons of higher Q^2 can resolve the gluon emissions from the quarks and thus the observed quarks momenta are reduced (cf. Fig. 1.5). Therefore a probability of finding a quark of small x increases with increasing Q^2, while a probability of finding a quark with large x decreases at the same time. The effect of the Q^2 dependence of the structure functions is called a violation of the Bjorken scaling and is well documented in experiments (cf. Fig. 1.3). Distributions of quarks q_f are thus functions of two independent variables $q_f = q_f(x, Q^2)$. Distribution of gluons also depends on x and Q^2: $G = G(x, Q^2)$. For fixed x the dependence of quark and gluon distribution functions on Q^2 is given by the **D**okshitzer–**G**ribov–**L**ipatov–**A**ltarelli–**P**arisi (DGLAP) equations [30–32]:

$$\frac{dq_f(x,Q^2)}{d\ln Q^2} = \frac{\alpha_S(Q^2)}{2\pi}\int_x^1 \frac{dx'}{x'}\left[q_f(x',Q^2)P_{qq}\left(\frac{x}{x'}\right) + G(x',Q^2)P_{qG}\left(\frac{x}{x'}\right)\right] \tag{1.21}$$

$$\frac{dG(x,Q^2)}{d\ln Q^2} = \frac{\alpha_S(Q^2)}{2\pi}\int_x^1 \frac{dx'}{x'}\left[\sum_f q_f(x',Q^2)P_{Gq}\left(\frac{x}{x'}\right) + G(x',Q^2)P_{GG}\left(\frac{x}{x'}\right)\right] \tag{1.22}$$

where α_S is a running coupling constant of strong interactions and P_{ij} are the splitting functions describing the probability of a parton j having a momentum fraction x' to become a parton i with a momentum fraction x (cf. Fig. 1.6).

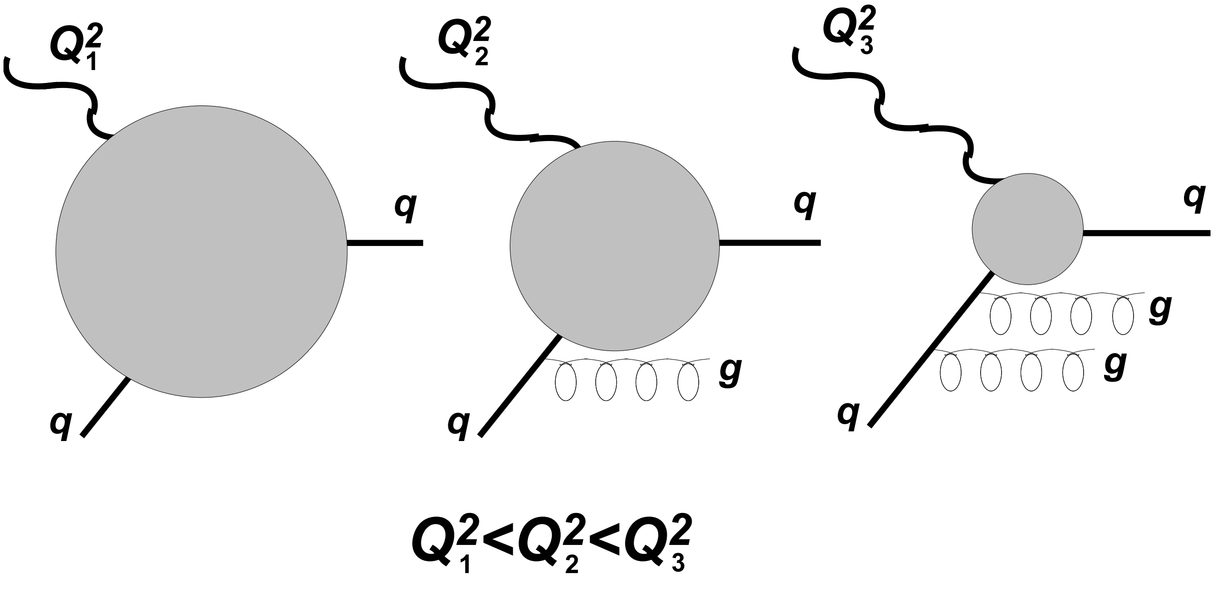

Figure 1.5: Probing quark distributions with photons of different Q^2 resolves the gluons emissions and results in decreasing the quark momenta.

The DGLAP equations describe the evolution of partons densities in Q^2 at a fixed x. They are the deferential equations and require a knowledge of the distributions at certain Q_0^2 at $0 \leq x \leq 1$ which has to be obtained from measurements and extrapolated to the unmeasured region of small and large x.

As the measurements are more scarce for the polarised case, in this case only the fol-

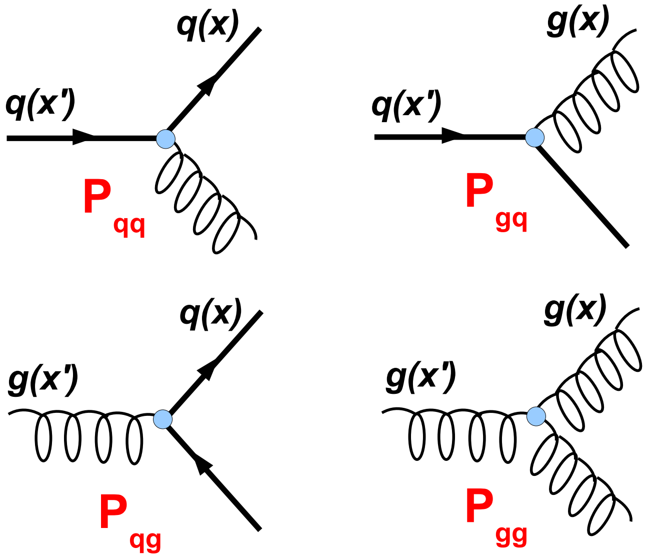

Figure 1.6: Splittings described by DGLAP equation. Upper: quark splitting; bottom: gluon splitting.

lowing DGLAP equations are used to describe the Q^2 evolution [33]:

$$\frac{d}{d\ln Q^2}\Delta q^{NS}(x,Q^2) = \frac{\alpha_S(Q^2)}{2\pi}\Delta P^{NS}_{qq} \otimes \Delta q^{NS}(x,Q^2) \tag{1.23}$$

$$\frac{d}{d\ln Q^2}\begin{pmatrix} \Delta\Sigma(x,Q^2) \\ \Delta G(x,Q^2) \end{pmatrix} = \frac{\alpha_S(Q^2)}{2\pi}\begin{pmatrix} \Delta P^S_{qq} & 2n_f \Delta P^S_{qg} \\ \Delta P^S_{gq} & \Delta P^S_{gg} \end{pmatrix} \otimes \begin{pmatrix} \Delta\Sigma(x,Q^2) \\ \Delta G(x,Q^2) \end{pmatrix} \tag{1.24}$$

A convolution of functions is given by:

$$(A \otimes B)(x) = \int_x^1 \frac{dx}{x'} A\Big(\frac{x}{x'}\Big) B(x) \tag{1.25}$$

The Δq^{NS} and $\Delta\Sigma$ are the flavour non-singlet and flavour singlet distributions defined as:

$$\Delta q^{NS}(x,Q^2) = \sum_f \left(\frac{e_f^2}{\frac{1}{n_f}\sum_f e_f^2} - 1 \right) \Delta q_f(x,Q^2) \tag{1.26}$$

$$\Delta\Sigma(x,Q^2) = \sum_f \Delta q_f(x,Q^2) \tag{1.27}$$

and $\Delta G(x,Q^2)$ is a distribution of gluon polarisation. The integral of $\Delta G(x,Q^2)$ over x at a fixed Q^2 gives a contribution of gluon polarisation to the nucleon spin at that Q^2.

The flavour non-singlet distribution evolves independently of the gluon distribution, while the evolution of the flavour singlet and of the gluon distribution depend on both these distributions at a given Q_0^2 scale. The ΔP_{ij} are defined through the splitting functions for the unpolarised case: $\Delta P_{ij} = P_{i+j+} - P_{i-j+}$, where "+" and "–" correspond to the helicities of the j-th and i-th parton.

With the introduction of the DGLAP evolution equations the simple formula for g_1, (Eq. (1.20)), becomes:

$$\begin{aligned} g_1(x,Q^2) = \left[\frac{1}{2n_f}\sum_f e_f^2\right] \cdot \Big[\; & C_q^{NS}(x,Q^2) \otimes \Delta q^{NS}(x,Q^2) \; + \\ & C_q{}^S(x,Q^2) \otimes \Delta\Sigma(x,Q^2) \; + \\ & C_g(x,Q^2) \otimes \Delta G(x,Q^2) \; \Big] \end{aligned} \tag{1.28}$$

The C_g, C_q^{NS} and C_q^S are the coefficient functions. Their dependence on Q^2 is through $\alpha_S(Q^2)$: $C_i(x,Q^2) = C_i(x,\alpha_S(Q^2))$. It implies that the C_i functions can be expanded in the powers of α_S. This treatment is restricted to the perturbative regime, that is for high Q^2, where the expansion takes form:

$$C_i(x,\alpha_S(Q^2)) = C_i^0(x) + \frac{\alpha_S(Q^2)}{2\pi}C_i^1(x) + \mathcal{O}(\alpha_S^2(Q^2)) \tag{1.29}$$

The splitting functions can also be expanded in the power series of α_S:

$$\Delta P(x,\alpha_S(Q^2)) = \Delta P^0(x) + \frac{\alpha_S(Q^2)}{2\pi}\Delta P^1(x) + \mathcal{O}(\alpha_S^2(Q^2)) \tag{1.30}$$

First elements in both expansions do not depend on Q^2. They are called the Leading Order (LO) elements. The splitting functions as well as coefficient functions are known to the Next-to-Leading Order (NLO) accuracy [34,35]. Recently also the first results on the Next-to-Next-to-Leading Order (NNLO) were obtained [36].

1.4 The First Moment of the g_1 Distribution

We will come back now to the QPM, where dependence on Q^2 is not present. In this model the g_1 function is given by the formula (1.20). Its first moment is equal to:

$$\begin{aligned} \Gamma_1 &= \int_0^1 g_1(x)dx = \int_0^1 \frac{1}{2}\sum_f e_f^2\Big[q_f^+(x) - q_f^-(x)\Big]dx = \frac{1}{2}\sum_f e_f^2 \int_0^1 \Big[q_f^+(x) - q_f^-(x)\Big]dx = \\ &= \frac{1}{2}\sum_f e_f^2 \Delta q_f \end{aligned} \tag{1.31}$$

Here $\Delta q_f = \int_0^1 (q_f^+(x) - q_f^-(x))dx$. In the proton case the first moment is given by:

$$\Gamma_1^p = \frac{1}{2}\left(\frac{4}{9}\Delta q_u + \frac{1}{9}\Delta q_d + \frac{1}{9}\Delta q_s\right) \tag{1.32}$$

The Γ_1^n for the neutron can be obtained from Γ_1^p by assuming the isospin symmetry, *i.e.* exchanging: $\Delta q_u \leftrightarrow \Delta q_d$.

The Δq_f defined as above, are related to the weak axial-vector couplings a_0, a_3 and a_8:

$$a_0 = (\Delta q_u + \Delta q_d + \Delta q_s) \tag{1.33}$$

$$a_3 = (\Delta q_u - \Delta q_d) \tag{1.34}$$

$$a_8 = (\Delta q_u + \Delta q_d - 2\Delta q_s) \tag{1.35}$$

The couplings are calculated from the hadron matrix elements of the $SU(3)$ flavour octet axial-vector currents $J_{5\mu}^j$ $(j = 1,...,8)$ and of the flavour singlet axial current $J_{5\mu}^0$ defined as [37]:

$$J_{5\mu}^j = \overline{\Psi}\gamma_\mu\gamma_5\frac{\lambda_j}{2}\Psi \tag{1.36}$$

$$J^0_{5\mu} = \overline{\Psi}\gamma_\mu\gamma_5\Psi \tag{1.37}$$

where Ψ is a flavour vector:

$$\begin{pmatrix} \Psi_u \\ \Psi_d \\ \Psi_s \end{pmatrix} \tag{1.38}$$

and λ_j are the Gell-Mann matrices. The matrix elements are given by:

$$Ma_jS_\mu = \left\langle P,S|J^j_{5\mu}|P,S\right\rangle \tag{1.39}$$

$$2Ma_0S_\mu = \left\langle P,S|J^0_{5\mu}|P,S\right\rangle \tag{1.40}$$

In this equation P is the nucleon momentum four-vector and S is its spin.

For the neutron the equations similar to (1.33–1.35), but with Δq_u and Δq_d interchanged are valid. The Γ^p_1 and Γ^n_1 take form:

$$\Gamma^p_1 = \frac{1}{9}a_0 + \frac{1}{12}(a_3 + \frac{1}{3}a_8) \tag{1.41}$$

$$\Gamma^n_1 = \frac{1}{9}a_0 + \frac{1}{12}(-a_3 + \frac{1}{3}a_8) \tag{1.42}$$

The a_3 and a_8 are related to parameters which describe beta decays of neutrons and hyperons. The value of the a_3 is expressed as the ratio of the axial vector and vector coupling constants:

$$a_3 = \left|\frac{g_A}{g_V}\right| \tag{1.43}$$

Values of the a_3 and a_8 have been measured directly in many experiments with high accuracy: $a_3 = 1.2695 \pm 0.0029$ and $a_8 = 0.579 \pm 0.025$ [25]. Therefore, from the knowledge of Γ^p_1 or Γ^n_1 and using Eq. (1.41) or (1.42), one find a_0. Here a_0 is equal to $\Delta\Sigma$, Eq. (1.33). Another conclusion is the Bjorken sum rule [38]:

$$\Gamma^p_1 - \Gamma^n_1 = \frac{1}{6}a_3 = \frac{1}{6}\left|\frac{g_A}{g_V}\right| \tag{1.44}$$

This sum rule establishes a link between the beta decays, the right hand side of the equation, with the integrated structure functions of both, the neutron and the proton, the left hand side of the equation.

In the QCD improved parton model the first moment of g_1 has a form:

$$\Gamma_1(Q^2) = \left[\frac{1}{2n_f}\sum_f e_f^2\right]\cdot\left[C^{NS}_q(Q^2)\Delta q^{NS}(Q^2) + C_q{}^S(Q^2)\Delta\Sigma(Q^2) + C_g(Q^2)\Delta G(Q^2)\right] \tag{1.45}$$

Each of the three components of the above formula has two separate parts – the hard and the soft. The former parts encompass coefficient functions $C_i(Q^2)$ while the latter the polarised quarks and gluons distributions. The soft parts cannot be calculated directly from QCD and have to be determined by experiments. Separation between the soft and the hard parts is not strict, and different factorisation and renormalisation schemes can be introduced. The schemes vary by the contributions which are absorbed into hard and soft parts. Two common choices are the Modified **M**inimal **S**ubtraction ($\overline{\text{MS}}$) [39] and the **A**dler-**B**ardeen (AB) [40] schemes.

The coefficient functions C_i can be expanded in power series of α_S. In this expansion in the LO approximation the ΔG does not enter the g_1 nor Γ_1 irrespectively of the applied QCD scheme. In the NLO the expansion terms differ in $\overline{\text{MS}}$ and AB. In the former scheme the ΔG does not enter NLO term either, while this term in the latter scheme does depend on ΔG. As a consequence $\Delta\Sigma$ becomes scheme dependent:

$$\Delta\Sigma(Q^2)_{\overline{MS}} = \Delta\Sigma_{AB} - n_f \frac{\alpha_S(Q^2)}{2\pi} \Delta G(Q^2) \tag{1.46}$$

while in both schemes ΔG is defined in the same way:

$$\Delta G(Q^2)_{\overline{MS}} = \Delta G(Q^2)_{AB} \tag{1.47}$$

The a_0 now becomes:

$$a_0(Q^2) = \Delta\Sigma(Q^2)_{\overline{MS}} = \Delta\Sigma_{AB} - n_f \frac{\alpha_S(Q^2)}{2\pi} \Delta G(Q^2) \tag{1.48}$$

The gluon contribution to the $a_0(Q^2)$ is called the Adler–Bell–Jackiw anomaly [41, 42]. In both schemes a_0 is a function of Q^2: through $\Delta\Sigma(Q^2)$ in $\overline{\text{MS}}$ or through $\Delta G(Q^2)$ in AB. As a consequence also the Bjorken sum rule has to be modified. With $C_q^{NS}(Q^2)$ calculated in the $\overline{\text{MS}}$ scheme it takes a form:

$$\Gamma_1^p(Q^2) - \Gamma_1^n(Q^2) = \frac{1}{6}\left|\frac{g_A}{g_V}\right| C_q^{NS}(Q^2) \tag{1.49}$$

and the first moments of g_1 for the proton and the neutron are given with:

$$\Gamma_1^p(Q^2) = \frac{1}{9} a_0(Q^2) C_q^S(Q^2) + \frac{1}{12}(a_3 + \frac{1}{3}a_8) C_q^{NS}(Q^2) \tag{1.50}$$

$$\Gamma_1^n(Q^2) = \frac{1}{9} a_0(Q^2) C_q^S(Q^2) + \frac{1}{12}(-a_3 + \frac{1}{3}a_8) C_q^{NS}(Q^2) \tag{1.51}$$

They differ from Eq. (1.41) and (1.42) by the coefficient functions, C_q, and the explicit Q^2 dependence of the a_0. A measurement of the first moment of g_1 at a given Q^2 allows to extract a_0 at the same Q^2 which is immediately translated to $\Delta\Sigma(Q^2)_{\overline{MS}}$, Eq. (1.48). The knowledge of $\Delta G(Q^2)$ allows the calculation of $\Delta\Sigma_{AB}$.

1.5 Cross-Section Asymmetries

The spin effects are studied in the experiments measuring the cross-sections for interactions occurring with a given relative spin orientation of the projectile and of the target. These cross-sections change with a change of the spin orientation.

1.5.1 The Lepton-Nucleon and the Virtual Photon-Nucleon Asymmetries

The main observables in the spin dependent inelastic lepton-nucleon scattering are the cross-section asymmetries for different relative polarisations. In COMPASS the polarisation of the lepton beam is fixed while the direction of the deuteron target polarisation can be changed. To probe different aspects of the nucleon structure the polarisation of the target can be set to parallel (anti-parallel) or transverse to the beam direction. As a consequence the longitudinal and the transverse cross-section asymmetries for the lepton-deuteron interactions are measured:

$$A_{\parallel} = \frac{\sigma^{\overset{\leftarrow}{\Rightarrow}} - \sigma^{\overset{\leftarrow}{\Leftarrow}}}{\sigma^{\overset{\leftarrow}{\Rightarrow}} + \sigma^{\overset{\leftarrow}{\Leftarrow}}} \tag{1.52}$$

$$A_{\perp} = \frac{\sigma^{\leftarrow\Downarrow} - \sigma^{\leftarrow\Uparrow}}{\sigma^{\leftarrow\Downarrow} + \sigma^{\leftarrow\Uparrow}} \tag{1.53}$$

where $\leftarrow$ and $\Leftarrow$ represent polarisations directions of the muon beam and of the deuteron target, respectively. The longitudinal and transverse virtual photon-deuteron asymmetries, A_1 and A_2, are defined via the asymmetry of absorption cross-sections of transversely polarised photon as:

$$A_1 = \frac{\sigma_0^T - \sigma_2^T}{2\sigma^T} \tag{1.54}$$

$$A_2 = \frac{\sigma_0^{TL} + \sigma_1^{TL}}{2\sigma^T} \tag{1.55}$$

where σ_J^T is the virtual photon-deuteron absorption cross-section for a total spin projection J in the photon direction, σ_J^{TL} results from the interference between transverse and longitudinal amplitudes for $J = 0, 1$, and σ^T is the total transverse photoabsorption cross-section. The experimental asymmetries $A_{\parallel}$ and $A_{\perp}$ are related with A_1 and A_2 through equations:

$$A_{\parallel} = D(A_1 + \eta A_2) \tag{1.56}$$

$$A_{\perp} = d(A_2 - \xi A_1) \tag{1.57}$$

where D, d, η and ξ are kinematical factors depending on Q^2 and y, see *e.g.* [43]. The virtual photon-deuteron asymmetries can be translated into g_1 and g_2 according to[3]:

$$A_1 = \frac{g_1 - \gamma^2 g_2}{F_1} \qquad\qquad A_2 = \gamma\frac{g_1 + g_2}{F_1} \tag{1.58}$$

where $\gamma = \sqrt{Q^2}/\nu$. Bringing together equations (1.56–1.57), (1.58) and eliminating A_1 and $A_{\perp}$ the formulas for g_1 and g_2 give:

$$g_1 = \frac{F_1}{1+\gamma^2}\left[\frac{A_{\parallel}}{D} + (\gamma - \eta)A_2\right] \tag{1.59}$$

$$g_2 = \frac{F_1}{1+\gamma^2}\left[-\frac{A_{\parallel}}{D} + (\frac{1}{\gamma} + \eta)A_2\right] \tag{1.60}$$

The structure functions g_1 and g_2 can be obtained from these equations provided all the kinematical factors are known and $A_{\parallel}$, A_2, F_1 were measured.

1.5.2 Approximate Formula for g_1

The A_2 asymmetry was measured for the proton as well as for the deuteron in an x range between 0.003 and 0.8 cf. [44]. The measurements have shown that the A_2 is small. Moreover the factors γ^2 and η in the COMPASS kinematics also are small: below

---

[3] Note that here when talking about lepton-deuteron scattering the structure functions are defined for the deuteron. They are denoted usually with d index: g_1^d, g_2^d, F_1^d. Here the index was omitted for simplicity.

10^{-3} and 10^{-2} respectively. Therefore the terms γA_2 and ηA_2 can be neglected. Then the expression (1.59) becomes:

$$g_1 \approx \frac{F_1}{1+\gamma^2}\frac{A_\parallel}{D} \approx F_1 \frac{A_\parallel}{D} \tag{1.61}$$

Under the same approximations Eq. (1.56) and (1.58) lead to:

$$A_\parallel \approx DA_1 \qquad\qquad g_1 \approx A_1 F_1 \tag{1.62}$$

The first formula gives a simple interpretation of the D factor. It describes the polarisation transfer from the polarised lepton to the virtual photon and is thus called a depolarisation factor. It is defined as:

$$D = \frac{y\Big[(1+\gamma^2 y/2)(2-y) - 2y^2 m_\mu^2/Q^2\Big]}{y^2(1-2m_\mu^2/Q^2)(1+\gamma^2) + 2(1+R)(1-y-\gamma^2 y^2/4)} \tag{1.63}$$

where R is the ratio of longitudinal (σ^L) and transverse photoabsorption cross-sections, $R = \sigma^L/\sigma^T$. For the analysis performed in LO QCD $R = 0$. Observe that $0 < D < 1$.

The results on A_1 measured for deuteron are presented in Fig. 1.7.

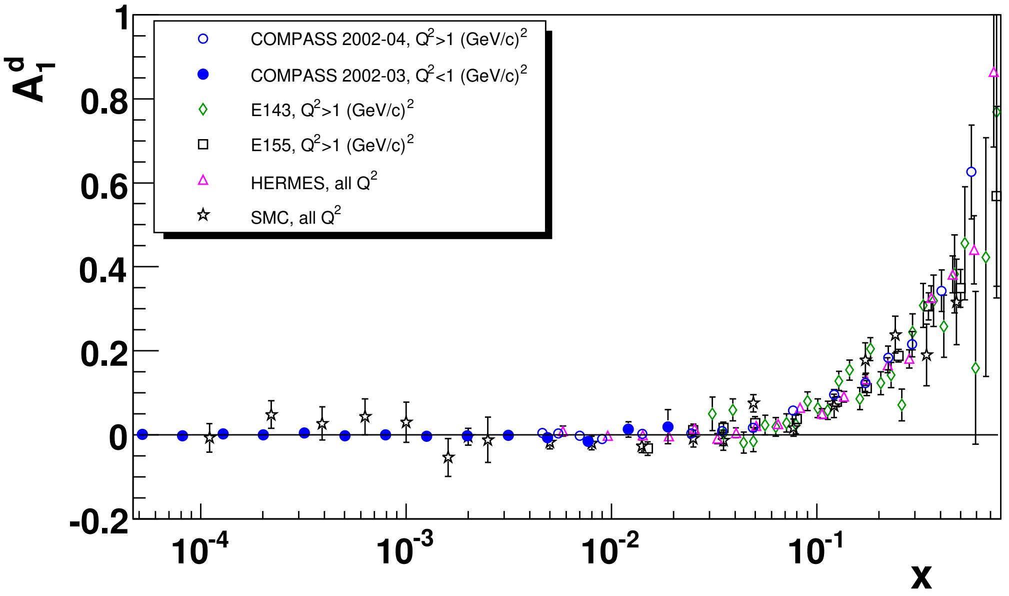

Figure 1.7: The asymmetry A_1 for a deuteron as a function of x at the measured values of Q^2 from COMPASS, SMC, HERMES, E143 and E155. For details see [43] from which the plot was taken.

1.6 Experimental Methods and Results on ΔG

Experiments with the inelastic polarised lepton scattering have been collecting data over the last 30 years. Spin studies of protons and neutrons were performed. As there are no purely neutron polarised targets, for the neutron studies deuterium or helium-3 was used. To measure the polarised effects on neutrons it is then necessary to subtract the effects coming from protons[4]. The compilation of data from neutrons and protons is required *e.g.* for tests of the Bjorken sum rule, cf. Eq. (1.49), and for the flavour dependent polarised partons distribution studies. Here we will present the polarised measurements from which conclusions on the ΔG can be drawn.

1.6.1 Results on the Quarks Polarisation

Experiments that measured the polarisation effects in inelastic lepton-nucleon scattering were conducted for the first time in mid-seventies at SLAC in USA. These pioneering experiments (E80 [2] and later E130 [45]) provided results on A_1 for the electron-proton scattering at $x \in (0.1, 0.7)$. In the eighties the kinematical range for the measurement of A_1 on proton was extended to $x = 0.01$ by the European Muon Collaboration (EMC) [3] at CERN.

The g_1 for proton measured by the EMC permitted to calculate Γ_1^p. In the unmeasured range of small and large x the g_1 was extrapolated. For small x phenomenological models were used. The uncertainty that was introduced due to the extrapolation was included into the systematic error. Then the a_0 was calculated taking known a_3 and a_8. Finally $\Delta\Sigma$ was derived with $\Delta\Sigma = a_0$. The obtained value was $\Delta\Sigma = 0.12 \pm 0.09 \pm 0.14$ [3], far from the naïve expectation of $\Delta\Sigma \approx 0.6$. The number of the EMC followers: SMC [4] and COMPASS [46] at CERN, HERMES [47,48] at DESY, E142 [6], E143 [7], E155 [8] at SLAC confirmed the EMC result. The recent analysis of the world data [46] gave $\Delta\Sigma$ at $Q^2 = 3$ GeV^2 equal to:

$$\Delta\Sigma(Q^2 = 3\ \mathrm{GeV}^2) = 0.30 \pm 0.01 \pm 0.03 \tag{1.64}$$

The result was obtained in the NLO with $\overline{\mathrm{MS}}$ scheme, that is $\Delta\Sigma(Q^2) = a_0(Q^2)$. The obtained value does not fulfil the sum rule (1). The missing fraction of the nucleon spin may be carried by gluons or it may arise from the orbital angular momenta of partons moving inside the nucleon.

The flavour dependent polarisation of the sea quarks can be measured studying semi-inclusive channels where a particle of a given type is detected. The results from these studies done at HERMES are presented in Tab. 1.1. In the SMC the flavour independent sea quarks polarisation analysis was performed. It gave $\Delta\overline{q} = 0.01 \pm 0.04 \pm 0.03$ [49], where $\Delta\overline{q} = \Delta\overline{u} = \Delta\overline{d} = \Delta\overline{s} = \Delta s$ was assumed. The SMC and HERMES analyses were performed at the LO QCD accuracy. Their results are compatible with the zero polarisation of the sea quarks. Two independent NLO analyses based on the world data gave results for the sea quarks polarisation slightly negative: $\Delta\overline{q} = -0.062 \pm 0.023$ [50] and $\Delta\overline{q} = -0.074 \pm 0.017$ [51]. The deviations from zero are at the level of 3–4 σ.

1.6.2 The ΔG from the QCD Evolution

Evolution of the $\Delta\Sigma(x, Q^2)$, $\Delta q^{NS}(x, Q^2)$ and $\Delta G(x, Q^2)$ in Q^2 at fixed x is described by the DGLAP equations (1.23–1.24). The $g_1(x, Q^2)$ structure function is related with

---

[4] For ^{3}He the orbital angular momentum of the 3-body system (2 protons and 1 neutron) is predominantly 0. In this state, due to Pauli exclusion principle, protons are anti-aligned. The spin effects observed in ^{3}He should therefore come from neutron. For studies on the deuteron both nucleons give contribution to the spin effects. However for deuteron the percentage of neutrons in the material is higher than for ^{3}He.

Flavour	Polarisation	Statistical and systematic errors
Δu	0.601	$0.039 \oplus 0.049$
Δd	–0.226	$0.039 \oplus 0.050$
$\Delta \overline{u}$	–0.002	$0.036 \oplus 0.023$
$\Delta \overline{d}$	–0.054	$0.033 \oplus 0.011$
Δs	0.028	$0.033 \oplus 0.009$
$\Delta u_{\text{valence}}$	0.603	$0.071 \oplus 0.040$
$\Delta d_{\text{valence}}$	–0.172	$0.068 \oplus 0.045$

Table 1.1: HERMES results for the quarks polarisation for different flavours, at Q^2=2.5 GeV^2 and in $0 \leq x \leq 1$. The sea quarks polarisation for u (d) is a difference between the total u (d) polarisation and the corresponding valence quarks polarisation. Taken from [48].

$\Delta\Sigma(x, Q^2)$, $\Delta q^{NS}(x, Q^2)$, $\Delta G(x, Q^2)$ through Eq. (1.28). Using DGLAP and Eq. (1.28) the predictions on $\Delta\Sigma(x, Q^2)$, $\Delta q^{NS}(x, Q^2)$, $\Delta G(x, Q^2)$ can be derived. The procedure is the following. First an initial parameterisation of the $\Delta\Sigma(x, Q^2)$, $\Delta q^{NS}(x, Q^2)$ and $\Delta G(x, Q^2)$ functions at a fixed reference value of $Q^2 = Q_0^2$ and at all x is made. Then the parameterised distributions are evolved according to DGLAP equations and the resulting values of $g_1(x, Q^2)$ are calculated for each (x_i, Q_i^2) where the experimental measurements of this structure function exist. The calculated and measured $g_1(x, Q^2)$ values are compared and using the χ^2 minimisation method the parameters of the initial parameterisation are optimised. The number of $g_1(x, Q^2)$ data points is presently about 230 (including data for proton, deuteron and helium targets). However as the lepton-nucleon polarised measurements were done exclusively by the fixed target experiments, they cover much smaller region of (x, Q^2) as compared with the unpolarised case, where also data from collider experiments are available (compare Figs. 1.3 and 1.4). As a consequence the predictions for $\Delta\Sigma$, Δq^{NS} and ΔG are only weakly constrained. In particular the uncertainty of the ΔG is large. In the recent COMPASS DGLAP evolution analysis [46] performed in the NLO, two solutions for ΔG were found, one positive and one negative. Both of them result in a rather small $|\Delta G| \sim 0.2 - 0.3$ for Q^2 =3 GeV^2, cf. Fig. 1.8.

There are two ways to improve the knowledge on ΔG. The first one is to enlarge the kinematic range of the g_1 measurements. This implies the data taking with the polarised beams at colliders. It would be possible within the polarised HERA project at DESY. Unfortunately the project was abandoned. There are plans for the upgrade of the RHIC at Brookhaven to eRHIC, where an additional polarised electron ring will be added to the existing hadron collider [52]. The timescale for this project is 10–20 years. Thus perspectives of the g_1 measurements in a wider x range are rather dim. The other method that leads to an improvement of the knowledge on ΔG is a direct measurement of this quantity in the process called Photon–Gluon Fusion.

1.6.3 Photon–Gluon Fusion

The **P**hoton–**G**luon **F**usion (PGF) process gives a direct insight into the gluon distribution in the nucleon. With an additional knowledge of $G(x, Q^2)$ coming from the unpolarised measurements, Fig. 1.9, the studies of the PGF process in the experiments with a polarised target and a polarised beam reveal the polarised gluon distribution

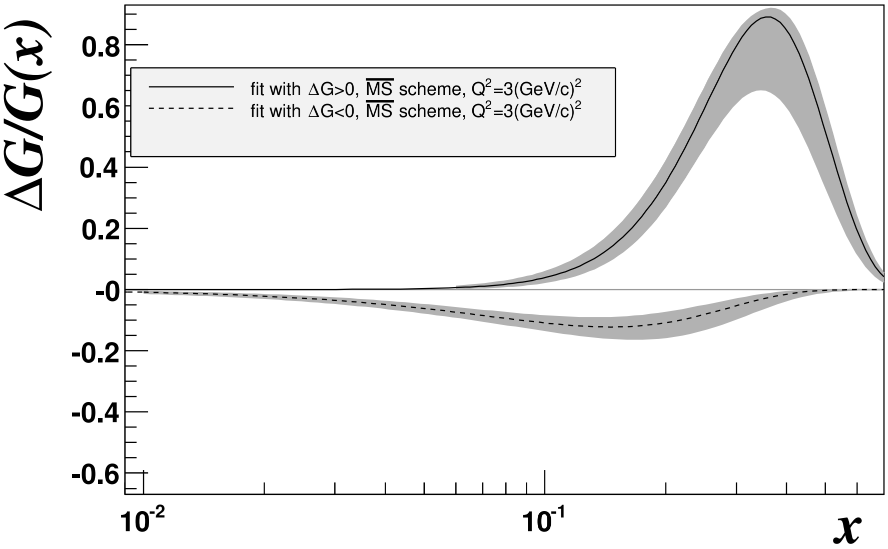

Figure 1.8: Distribution of the gluon polarisation $\Delta G/G(x)$ at $Q^2 = 3\text{GeV}^2$ from the recent COMPASS NLO QCD analysis [46]. Two solutions were found, one positive and one negative. The error bands correspond to the statistical error on $\Delta G(x)$ at a given x.

$\Delta G(x, Q^2)$. The PGF is an interaction of a virtual photon coming from the lepton with a gluon embedded in the nucleon, occurring through the exchange of a virtual quark and resulting in a $q\overline{q}$ pair production, Fig. 1.10. To enhance the amount of the PGF processes in the studied data sample two different methods can be used. The first one is based on the PGF tagging via the detection of the charmed quarks. It is called the open charm method as the tagging means reconstruction of the D^0 mesons in the final state. The other approach relies on the selection of hadron pairs with high transverse momenta with respect to the virtual photon direction [55]. The advantage of this method is a much higher statistics comparing to the open charm method, as it is not restricted to charmed quark pairs in the final state only. However, as it will be shown, it relies extensively on the Monte Carlo simulations.

1.6.4 The Open Charm Method

The mass of the charm quark, $m_c \approx 1.5$ GeV, is much larger than those of the u, d and s quarks. Therefore the charm content of the nucleon for the measurements at COMPASS kinematics can be neglected. Also the creation of the charm quarks in the fragmentation process is highly suppressed. Thus the only reaction that has a significant contribution to the charm production is the PGF process. The contribution from the resolved photon processes at COMPASS kinematics in the charm production was estimated with RAPGAP [56] Monte Carlo simulation, using different parameterisations of the photon structure. The contribution is of the order of a few percent [57] and is neglected in the analysis. The presented studies are performed in the LO QCD. Therefore also the description of the method will be limited to LO. The method for the introduction to the open charm analysis the NLO corrections is still a subject of studies in COMPASS. The impact of these corrections is not yet known.

The charmed quarks produced in the interactions, fragment subsequently into charmed

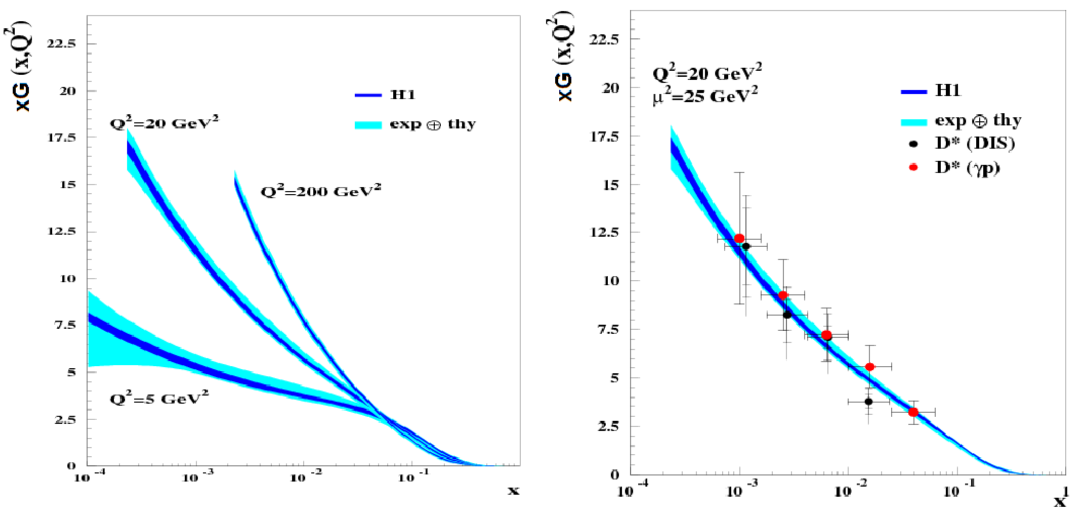

Figure 1.9: Left: determination of $xG(x, Q^2)$ in the NLO QCD by H1 at HERA using NMC and H1 lepton-proton data. Right: comparison of $xG(x, Q^2)$ obtained from scaling violation with the direct H1 measurement using the open charm method. Two subsamples were studied: DIS ($Q^2 > 2$ GeV^2) and photo–production ($Q^2 < 0.01$ GeV^2). The plot is taken from [53]. See also [54]

hadrons. The detection and identification of them provides a clear tag for the PGF process. From all known charmed particles, the one that can be most clearly reconstructed in the COMPASS kinematics, is a D^0, "open charm", meson ($c\bar{u}$ quark content). On average 1.2 D^0 mesons are produced per each $c\bar{c}$ pair [9]. The method of gluon polarisation measurement which base on the PGF tagging via charmed hadrons is for the first time implemented in COMPASS. It has never been used before in other experiments.

The observable that is measured in the experiment is the asymmetry defined as:

$$A^{exp} = \frac{N_{D^0}^{\overset{\leftarrow}{\Rightarrow}} - N_{D^0}^{\overset{\leftarrow}{\Leftarrow}}}{N_{D^0}^{\overset{\leftarrow}{\Rightarrow}} + N_{D^0}^{\overset{\leftarrow}{\Leftarrow}}} \tag{1.65}$$

where N_{D^0} are numbers of D^0 mesons produced with different relative target–beam spin orientations. The above experimental asymmetry can be translated into the spin dependent asymmetry of the lepton-nucleon interactions (A^{lN}) by dividing it by several dilution factors. These are: the beam polarisation P_B, the target polarisation P_T and the target material dilution factor f. The f factor accounts for the fraction of polarisable nucleons in the target material. All these factors will be discussed later. They give:

$$A^{lN} = \frac{1}{P_B P_T f} A^{exp} \tag{1.66}$$

The A^{lN} is related to the virtual photon-nucleon asymmetry $A^{\gamma^* N}$:

$$A^{\gamma^* N} = \frac{1}{D} A^{lN} = \frac{1}{P_B P_T f D} A^{exp} \tag{1.67}$$

where D is a depolarisation factor introduced in Sec. 1.5.1. Formula (1.67) holds only if the data sample contains exclusively the open charm events. If the background is also present, the formula should be rewritten as:

$$A^{\gamma^* N} = \frac{1}{P_B P_T f D \frac{S}{S+B}} A^{exp} - A^{BG} \tag{1.68}$$

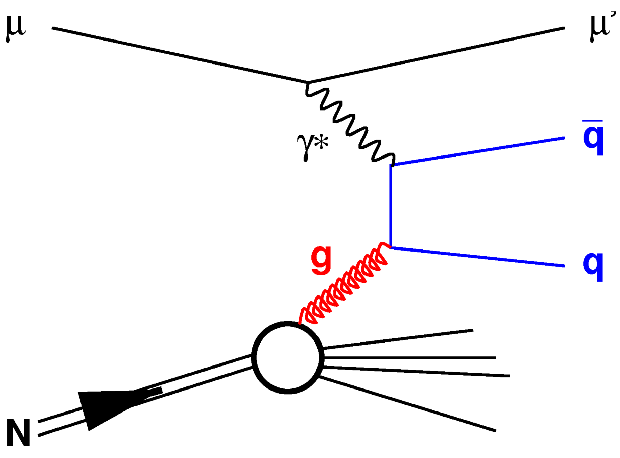

Figure 1.10: The Photon–Gluon Fusion process in LO.

The $S/(S+B)$ is an additional dilution factor with S and B being a number of signal and background events in the studied open charm sample. The A^{BG} is a background asymmetry arising from other spin dependent processes present in the sample. They are expected to have a negligible contribution comparing to the statistical error of the measurement, as discussed later in this work. Therefore the $A^{BG}=0$ is assumed.

The virtual photon-nucleon asymmetry can be presented as:

$$A^{\gamma^* N}(x_g) = \frac{\int_{4m_c^2}^{2M\nu} d\hat{s}\ \Delta\sigma^{\gamma^* g\to c\bar{c}X}(\hat{s})\Delta G(x_g,\hat{s})}{\int_{4m_c^2}^{2M\nu} d\hat{s}\ \sigma^{\gamma^* g\to c\bar{c}X}(\hat{s}) G(x_g,\hat{s})} \tag{1.69}$$

where the $\Delta\sigma^{\gamma^* g\to c\bar{c}X}(\hat{s})$ and $\sigma^{\gamma^* g\to c\bar{c}X}(\hat{s})$ are the cross-sections for the interactions leading to the PGF with $c\bar{c}$ production for the helicity dependent and helicity averaged cases. In the limit $Q^2 \to 0$ and in the LO, they are given by:

$$\Delta\sigma^{\gamma^* g\to c\bar{c}X}(\hat{s}) = \frac{4}{9}\frac{2\pi\alpha_e\alpha_s(\hat{s})}{\hat{s}}\left[3\beta - \ln\frac{1+\beta}{1-\beta}\right] \tag{1.70}$$

$$\sigma^{\gamma^* g\to c\bar{c}X}(\hat{s}) = \frac{4}{9}\frac{2\pi\alpha_e\alpha_s(\hat{s})}{\hat{s}}\left[-\beta(2-\beta^2) + \frac{1}{2}(3-\beta^4)\ln\frac{1+\beta}{1-\beta}\right] \tag{1.71}$$

In the above equations $\beta = \sqrt{1-4m_c^2/\hat{s}}$ and $\hat{s}$ is a centre-of-mass energy of the photon-gluon system[5]. The x_g variable is the fraction of the nucleon momentum carried by the gluon:

$$x_g = x\left(\frac{\hat{s}}{Q^2}+1\right) \approx \frac{\hat{s}}{2M\nu} \tag{1.72}$$

Where the approximation holds at low x, that is for instance for COMPASS. Integration limits in Eq. (1.69) are from the $c\bar{c}$ threshold energy squared ($4m_c^2$) to the square of the total energy available in the interaction at a given ν ($2M\nu$). The parton asymmetry for the photon-gluon interactions $\hat{a}_{LL}$ is defined as:

$$\hat{a}_{LL}(\hat{s}) = \frac{\Delta\sigma^{\gamma^* g\to c\bar{c}X}(\hat{s})}{\sigma^{\gamma^* g\to c\bar{c}X}(\hat{s})} \tag{1.73}$$

---

[5] Hats over variables, *e.g.* $\hat{s}$, mean that they are defined at the parton level of the interaction.

Substituting $\hat{a}_{LL}$ to Eq. (1.69) one gets:

$$A^{\gamma^* N}(x_g) = \frac{\int_{4m_c^2}^{2M\nu} d\hat{s}\ \hat{a}_{LL}(\hat{s}) \frac{\Delta G(x_g,\hat{s})}{G(x_g,\hat{s})} \sigma^{\gamma^* g \to c\bar{c}X}(\hat{s}) G(x_g,\hat{s})}{\int_{4m_c^2}^{2M\nu} d\hat{s}\ \sigma^{\gamma^* g \to c\bar{c}X}(\hat{s}) G(x_g,\hat{s})}$$

$$\approx \langle \hat{a}_{LL} \rangle \times \left\langle \frac{\Delta G}{G} \right\rangle (x_g) \tag{1.74}$$

The above equation together with formula (1.68) and $A_{BG} = 0$ give:

$$\left\langle \frac{\Delta G}{G} \right\rangle = \frac{1}{P_B P_T f D \langle \hat{a}_{LL} \rangle \frac{S}{S+B}} A^{exp} \tag{1.75}$$

where $\langle \frac{\Delta G}{G} \rangle$ and A^{exp} are the average values for the measured x_g range.

The differential cross-section for the $c\bar{c}$ production in a lepton-nucleon interactions is a product of a virtual photon flux (defined with a Hand convention [58]), Γ, and of the cross-section for the $\gamma^* N \to c\bar{c}X$ process:

$$\frac{d^2\sigma^{lN \to c\bar{c}X}}{dQ^2 d\nu} = \Gamma(E; Q^2, \nu) \sigma^{\gamma^* N \to c\bar{c}X}(Q^2, \nu) \tag{1.76}$$

where E is an incoming lepton energy. The virtual photon flux is:

$$\Gamma(E; Q^2, \nu) = \frac{\alpha_e}{2\pi} \frac{2(1-y) + y^2 + Q^2/2E^2}{Q^2 \sqrt{(Q^2 + \nu^2)}} \tag{1.77}$$

At a given ν and y, the flux increases when Q^2 decreases. Therefore a substantial fraction of D^0 mesons is produced at small Q^2. For the PGF process studied via the open charm mesons, the QCD scale of the interaction is set by a high mass of charmed quark and not by Q^2. The scale is equal to $4(m_c^2 + p_T^2)$, where p_T is the charmed quark transverse momentum with respect to the virtual photon. In what follows that scale is denoted with μ^2.

1.6.5 The Method of High–$\mathrm{p_T}$ Hadron Pairs

Another method to study the polarised PGF process is a measurement of the cross section asymmetries for the production of two hadrons of high transverse momenta relative to the virtual photon direction. In the $\gamma^* g$ centre-of-mass quarks are produced back-to-back. In the process where a quark is struck directly by a photon the quark inherits the direction of the momentum from the γ^*. After the fragmentation hadrons usually preserve the direction of motion of the quarks they originate from. Therefore selection of two high–$\mathrm{p_T}$ hadrons strongly enhances a fraction of PGF events. Simulations performed with PYTHIA and LEPTO showed that this fraction is about 30% in the COMPASS case.

The High–$\mathbf{p_T}$ Method for $\mathbf{Q^2 > 1}$ GeV$^\mathbf{2}$.

Apart from the PGF the high–$\mathrm{p_T}$ events with $Q^2 > 1$ GeV^2 contain a large fraction of the leading processes ($\gamma^* q \to q$) and of the QCD–Compton interactions ($\gamma^* q \to gq$). There are hints coming from the PYTHIA Monte Carlo simulation, that the contribution of the resolved photon processes in the region of high Q^2 is smaller than 10% [59].

Thus they are neglected. With the R_{PGF}, R_{LP} and R_{QCDC} being respectively fractions of events with PGF, leading and QCD–Compton scattering the asymmetry reads:

$$A^{\gamma^* N \to hh} = R_{PGF} \langle \hat{a}_{LL}^{PGF} \rangle \frac{\Delta G}{G} + \left[R_{LP} \langle \hat{a}_{LL}^{LP} \rangle + R_{QCDC} \langle \hat{a}_{LL}^{QCDC} \rangle \right] \frac{\Delta q}{q} \tag{1.78}$$

In this equation both sides are averaged over the experimentally accessible x_g range. In the analysis performed at COMPASS an additional cut rejecting events with $x > 0.05$ is imposed. This ensures that the measured A_1 asymmetry is small which corresponds to the smallness of the $\Delta q/q$. Therefore the terms describing leading and QCDC interactions can be dropped from the above equation retaining:

$$A^{\gamma^* N \to hh} \approx R_{PGF} \langle \hat{a}_{LL}^{PGF} \rangle \frac{\Delta G}{G} \tag{1.79}$$

The R_{PGF} cannot be extracted directly from the QCD. It has to be estimated from the simulations. Therefore its value is model dependent which introduces an additional systematic uncertainty to the analysis.

The High–$\mathbf{p_T}$ Method for $\mathbf{Q^2 < 1}$ GeV$^\mathbf{2}$.

For the fixed target experiments the bulk of events with two high–$\mathrm{p_T}$ hadrons is at small Q^2. At COMPASS about 90% of events have $Q^2 < 1$ GeV^2. In this kinematic region apart from the direct processes (PGF, LP and QCDC) an important contribution, more than 50%, comes from the resolved photon interactions. The asymmetry introduced with these interactions, A_{RP}, cannot be neglected in contrast to the $Q^2 > 1$ GeV^2 analysis. The measured asymmetry is thus:

$$A^{\gamma^* N \to hh} = R_{PGF} \langle \hat{a}_{LL}^{PGF} \rangle \frac{\Delta G}{G} + \left[R_{LP} \langle \hat{a}_{LL}^{LP} \rangle + R_{QCDC} \langle \hat{a}_{LL}^{QCDC} \rangle \right] \frac{\Delta q}{q} + A_{RP} \tag{1.80}$$

In the resolved photon interactions a photon first fluctuates into a hadronic structure, then a parton from this structure interacts with another parton coming from the nucleon. The interaction can occur in a number of channels each having its separate contribution to the $A^{\gamma^* N \to hh}$ asymmetry:

- $qq^\gamma \to qq$ where q is a nucleon quark and q^γ is a resolved photon quark. The contribution from this process to $A^{\gamma^* N \to hh}$ is:

$$R_{qq} \langle \hat{a}_{LL}^{qq} \rangle \frac{\Delta q}{q} \left(\frac{\Delta q}{q} \right)^\gamma \tag{1.81}$$

- $qg^\gamma \to qg$ where q is a nucleon quark and g^γ is a gluon coming from the hadronic structure of the photon. The contribution is given by:

$$R_{qg} \langle \hat{a}_{LL}^{qg} \rangle \frac{\Delta q}{q} \left(\frac{\Delta G}{G} \right)^\gamma \tag{1.82}$$

- $gq^\gamma \to qg$ where g is a gluon from a nucleon and q^γ is a quark coming from the hadronic structure of the photon. The contribution is given by:

$$R_{gq} \langle \hat{a}_{LL}^{qg} \rangle \frac{\Delta G}{G} \left(\frac{\Delta q}{q} \right)^\gamma \tag{1.83}$$

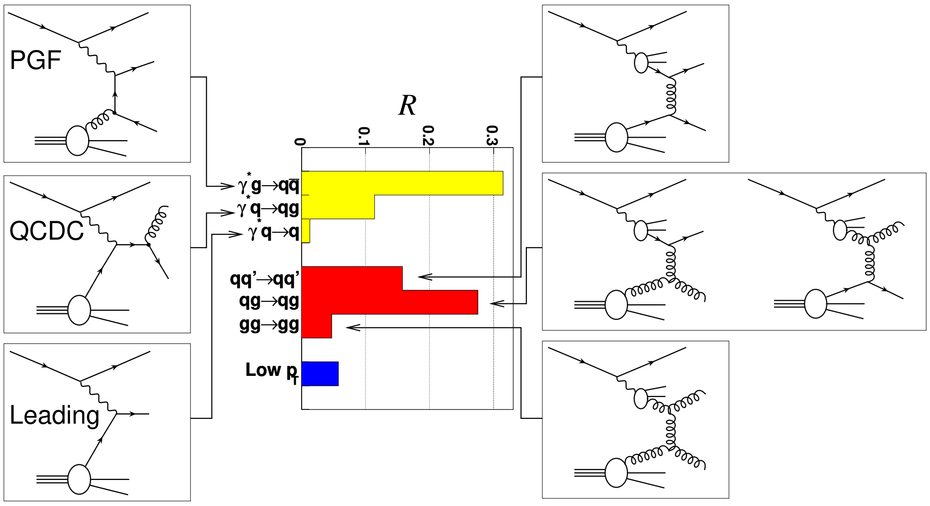

Figure 1.11: Processes contributing to the high–$\mathrm{p_T}$ sample with $Q^2 < 1$ GeV^2 as obtained for COMPASS analysis with PYTHIA. On the left the direct processes and on the right the resolved photon contributions are presented. Diagrams of processes with contributions smaller than 1% were omitted.

- $gg^\gamma \to gg$ where one gluon comes from the nucleon and the other from the resolved photon. The contribution to $A^{\gamma^* N \to hh}$ is equal to:

$$R_{gg} \langle \hat{a}_{LL}^{gg} \rangle \frac{\Delta G}{G} \left(\frac{\Delta G}{G} \right)^{\gamma} \tag{1.84}$$

- $q\overline{q}^\gamma \to q\overline{q}$, $\overline{q}q^\gamma \to qq$, $q\overline{q}^\gamma \to gg$, $\overline{q}q^\gamma \to gg$, $gg^\gamma \to q\overline{q}$ processes account only for a very small fraction of high–$\mathrm{p_T}$ events (0.6% in total) and can be neglected.

The total asymmetry produced by the interactions involving resolved photons is:

$$\begin{aligned} A_{RP} = & \left[R_{qq} \langle \hat{a}_{LL}^{qq} \rangle \left(\frac{\Delta q}{q} \right)^{\gamma} + R_{qg} \langle \hat{a}_{LL}^{qg} \rangle \left(\frac{\Delta G}{G} \right)^{\gamma} \right] \frac{\Delta q}{q} + \\ & \left[R_{gg} \langle \hat{a}_{LL}^{gg} \rangle \left(\frac{\Delta G}{G} \right)^{\gamma} + R_{gq} \langle \hat{a}_{LL}^{qg} \rangle \left(\frac{\Delta q}{q} \right)^{\gamma} \right] \frac{\Delta G}{G} \end{aligned} \tag{1.85}$$

where the superscript γ denotes the parton distributions describing the resolved photon hadronic structure. This structure is known only for the unpolarised case: q^γ and G^γ were measured experimentally while the Δq^γ and ΔG^γ polarised distributions are not known. They can only be estimated as theoretical considerations provide for them an upper and lower limits [60]. The uncertainty arising from this procedure has to be included in the systematic error of the final result. As it can be seen from Eq. (1.85) the resolved photon contributions not only dilute the measured $\Delta G/G$ but also through the $gg^\gamma \to gg$ and $gq^\gamma \to gq$ channels are sensitive to it. Finally the total asymmetry reads:

$$\begin{aligned} A^{\gamma^* N \to hh} = & \left[R_{PGF} \langle \hat{a}_{LL}^{PGF} \rangle + R_{qg} \langle \hat{a}_{LL}^{gg} \rangle \Big(\frac{\Delta G}{G} \Big)^{\gamma} + R_{gq} \langle \hat{a}_{LL}^{qg} \rangle \left(\frac{\Delta q}{q} \right)^{\gamma} \right] \frac{\Delta G}{G} + \\ & + \left[R_{LP} \langle \hat{a}_{LL}^{LP} \rangle + R_{QCDC} \langle \hat{a}_{LL}^{QCDC} \rangle + R_{qq} \langle \hat{a}_{LL}^{qq} \rangle \Big(\frac{\Delta q}{q} \Big)^{\gamma} + R_{qg} \langle \hat{a}_{LL}^{qg} \rangle \Big(\frac{\Delta G}{G} \Big)^{\gamma} \right] \frac{\Delta q}{q} \end{aligned} \tag{1.86}$$

Fractions of processes as well as average $\hat{a}_{LL}$ for each process have to come from simulation. A large number of parameters not measured directly but estimated from the simulation entails a strong model dependence of the resulting $\Delta G/G$ value. It is included in the systematic error.

1.7 Direct Measurements of $\Delta G/G$

Up to now the $\Delta G/G$ values for different x_g have been determined by the HERMES, SMC and COMPASS Collaborations. Measurements by the first two were based on the high–$\mathrm{p_T}$ approach. In HERMES the analysis was focused on the quasi–real photoproduction ($Q^2 \ll 1$ GeV^2) while in SMC on the DIS ($Q^2 > 1$ GeV^2) region. COMPASS is the first one to perform the measurements in both Q^2 ranges. In addition in COMPASS the $\Delta G/G$ is measured in the open charm channel. STAR and PHENIX experiments, located at RHIC, have also developed spin physics programmes and their first results are now available.

1.7.1 The HERMES Experiment

HERMES (**HERA ME**asurement of **S**pin) is an experiment situated in the DESY laboratory at the HERA collider. It is a fixed target setup with a forward spectrometer. The beam is either electrons or positrons of 27.5 GeV from HERA. It is polarised transversely to the beam plane in the Sokolov–Ternov process [61]. Before the interaction point the polarisation of the beam is rotated into the longitudinal direction. The polarisation is measured continuously with the Compton back-scattering process. Its average value is 0.55 ± 0.02. As the target HERMES uses a polarised gas. The gas is injected directly into a dedicated part of the beam pipe. As no target walls confining the gas are used, it leaks to the beam pipe from which it is pumped away by a set of high speed pumps. The vacuum in the HERA ring is not affected. The HERMES spectrometer is equipped with a magnet of 1.3 Tm integrated field used for the particles momenta measurement. The particle identification relies on a set of detectors, including the RICH and the calorimeter. A description of the detector setup can be found in [62].

The HERMES high–$\mathrm{p_T}$ hadron pairs analysis uses events registered on the hydrogen target and containing at least two oppositely charged hadrons. These hadrons are required to have momenta larger than 4.5 GeV and transverse momenta with respect to the beam exceeding 0.5 GeV. As a bulk of the selected events has $Q^2 \approx 0$ GeV^2 the transverse momenta from the above requirement are approximately equal to the transverse momenta calculated with respect to the photon direction. The invariant mass of the system of hadrons, assuming they are pions, has to be larger than 1 GeV. This cut removes the background arising from the ρ meson production. The fraction of the PGF process is estimated with the PYTHIA generator. This generator is also used for the estimation of the fractions of other direct processes: $\gamma^* q \to q$ and $\gamma^* q \to gq$, partonic asymmetries $\hat{a}_{LL}$ and the virtual photon depolarisation factor. Possible asymmetries arising from the resolved photon interactions are neglected.

The result of the analysis is:

$$\left\langle \frac{\Delta G}{G} \right\rangle = 0.41 \pm 0.18 \pm 0.03 \tag{1.87}$$

while the average x_g is 0.17 and the scale at which the nucleon structure was probed is given by the average p_T^2 equal to 2.1 GeV^2. For more details on the HERMES analysis see [63].

Recently HERMES presented a new result on $\Delta G/G$ [64]. It is based on the measurement of the inclusive hadron production asymmetry. The target was the deuteron and the events selected for the analysis had at least one high–$\mathrm{p_T}$ hadron of $1.05 < \mathrm{p_T} < 2.5$ GeV. The preliminary result of this analysis is:

$$\left\langle \frac{\Delta G}{G} \right\rangle = 0.071 \pm 0.034 \, {}^{+0.127}_{-0.105} \tag{1.88}$$

with the average x_g equal to 0.22 and the scale of 1.35 GeV^2.

1.7.2 The SMC Experiment

The SMC (**S**pin **M**uon **C**ollaboration) experiment, NA47, was the predecessor of COMPASS. It was located at CERN North Area and used the M2 positive muon beam of the energy 190 GeV. The beam was naturally polarised to –0.795 ± 0.019. The polarisation was measured in the $\mu e \rightarrow \mu e$ scattering and through the observation of the energy spectrum of the positrons from the muon decays. The SMC was a fixed target experiment. The target was composed of two solid state cells, each 60 cm long and filled with deuterated butanol or with ammonia. The first material was used for the studies of the interactions on the deuterium, the second on the hydrogen. The target material was polarised to 50% or 90% for deuterium and hydrogen, respectively. The cells were polarised in opposite directions enabling the measurement of interactions with both beam–target spin configurations at the same time. The SMC spectrometer was built around a 4.4 Tm magnet. The tracks were registered with over 100 multiwire proportional chamber detector planes. Scattered muons were identified detecting their tracks behind the 2 m thick iron filter. As no hadrons identification was done in SMC, efficient open charm reconstruction was not possible. Therefore the $\Delta G/G$ was determined only with the high–$\mathrm{p_T}$ hadron pairs. A description of the spectrometer can be found in [65].

The SMC analysis was restricted to the sample with $Q^2 > 1$ GeV^2. The subsample of the events with two hadrons was selected with the cuts:

- hadron candidates tracks were not found behind the muon filter;
- the contribution from the target fragmentation region was removed with $x_F > 0.1$ and $z > 0.1$ cuts for both hadron candidates[6].

A neural network was used to select the PGF events. The input information for the network were the global parameters describing an event (x, y, Q^2) and the parameters characterising hadronic tracks (transverse and longitudinal momenta, energy fractions etc.). The output of the network was a single number from the (0,1) range. Events described by a high value of this number were more likely to come from the PGF process, while these with a small value originated from the background. The choice of the cut-off value was done taking into account the purity (the ratio of the PGF to non–PGF processes) and the cut's efficiency (the fraction of PGF processes kept in the sample by the cut). The neural network was prepared and optimised on events generated with

---

[6] The $x_F \approx 2p_{Z'}^{\mathrm{cms}}/\sqrt{s}$, where $p_{Z'}^{\mathrm{cms}}$ is a hadron momentum along Z' axis pointing along the virtual photon momentum vector and $\sqrt{s}$ is the photon-nucleon centre-of-mass energy.

LEPTO. The Monte Carlo was also used for the partonic asymmetry $\langle \hat{a}_{LL}^{PGF} \rangle$ estimation.

The final value from the SMC analysis is [66]:

$$\left\langle \frac{\Delta G}{G} \right\rangle = -0.20 \pm 0.28 \pm 0.10 \tag{1.89}$$

The average x_g is 0.07 and the scale at which the nucleon structure was probed is 3 GeV^2.

1.7.3 The COMPASS Experiment

The basic layout of the COMPASS spectrometer is similar to that of the SMC. The main difference is a particle identification system consisting of a Cherenkov detector supplemented with electromagnetic and hadronic calorimeters. Also the structure of the tracking detectors is more complex, able to sustain much higher event rates compared to the SMC experiment. The particle identification together with the energy of interactions (the muon-nucleon centre-of-mass energy is ∼17 GeV) enable studies in the open charm channel. Apart of the open charm, COMPASS is also extracting $\Delta G/G$ using the high–$\mathrm{p_T}$ method. The analysis is performed separately in the DIS ($Q^2 > 1$ GeV^2) and in the quasi-real photoproduction ($Q^2 < 1$ GeV^2) kinematic regions. The cuts selecting high–$\mathrm{p_T}$ hadrons are the following:

- hadron candidates are detected in the hadronic calorimeters;
- $p_{T_1} > 0.7$ GeV, $p_{T_2} > 0.7$ GeV where p_{T_1} and p_{T_2} are hadron transverse momenta relative to the virtual photon direction;
- $p_{T_1}^2 + p_{T_2}^2 > 2.5$ GeV^2;
- invariant mass of the two hadron system, assuming the hadrons are pions, is larger than 1.5 GeV; this cut removes the resonances;
- contribution from the target fragmentation events is removed by demanding: $x_F > 0.1$ and $z > 0.1$ for both hadrons.

LEPTO 6.5.1 [67] generator is used to estimate the R_{PGF} and $\hat{a}_{LL}^{PGF}$ for $Q^2 > 1$ GeV^2. For the $Q^2 < 1$ GeV^2 events PYTHIA 6.2 [68] is used. In the latter case not only R_{PGF} but also the fractions of other processes are taken from simulation.

A preliminary result from the high–$\mathrm{p_T}$ analysis of the 2002–2003 data at $Q^2 > 1$ GeV^2 is:

$$\left\langle \frac{\Delta G}{G} \right\rangle = 0.06 \pm 0.31 \pm 0.06 \tag{1.90}$$

The fraction of R_{PGF} is equal to 0.34 ± 0.07, the average x_g for the sample is 0.13 with RMS of 0.08 while the scale is 3 GeV^2.

The result from the high–$\mathrm{p_T}$ analysis of the 2002–2003 sample at $Q^2 < 1$ GeV^2 is:

$$\left\langle \frac{\Delta G}{G} \right\rangle = 0.024 \pm 0.089 \pm 0.057 \tag{1.91}$$

The average x_g is $0.095^{+0.08}_{-0.04}$ and the scale is equal to 3 GeV^2 [69]. A preliminary result for the whole 2002–2004 data set is:

$$\left\langle \frac{\Delta G}{G} \right\rangle = 0.016 \pm 0.058 \pm 0.055 \tag{1.92}$$

with the same x_g and scale.

1.7.4 Experiments at RHIC

Relativistic **H**eavy **I**on **C**ollider (RHIC) is a hadron collider located at Brookhaven National Laboratory (BNL) in USA. Its primary goal is to explore the matter at the extreme conditions of temperature and density, *i.e.* to produce and probe the **Q**uark **G**luon **P**lasma (QGP). Another physics programme at RHIC is dedicated to the measurements of gluon polarisation. The programme is based on the observation of the polarised proton-proton collisions in two RHIC experiments: **S**olenoid **T**r**A**cker at **R**HIC (STAR) and **P**ioneering **H**igh **E**nergy **N**uclear **I**nteraction e**X**periment (PHENIX).

The protons in RHIC are accelerated to 100 or 250 GeV (other energies are also possible). They are polarised at an early stage of acceleration. Special magnets called Siberian Snakes are installed to overcome the proton depolarisation during acceleration. The magnetic field in the Snakes flips the protons polarisation and at the same time averages out the effects leading to the depolarisation. The proton spin orientation inside the rings is vertical. Before interaction points spins are rotated to the longitudinal orientation. For 2003–2006 data taking periods the polarisation of protons increased from 30% to the current 65%.

STAR is a detector which is optimised for the charged particles tracking and identification. It is well suited for the hadronic jet reconstruction. PHENIX specialises in the lepton and photon registration while the jet reconstruction is more difficult. A discussion of the STAR and PHENIX detectors can be found in [70] and [71].

In the RHIC experiments the gluon structure of the interacting protons can be probed through the reactions: $qg \to \gamma q$, $qg \to gq$, $gg \to gg$, cf. Fig. 1.12. In the final state either a photon accompanied by one jet or two jets are observed. The proton-proton interactions provide a much higher statistics of gluon interactions as compared to lepton-nucleon scattering. However, the background of other processes is large.

The observable measured in the experiments is a double spin cross-section asymmetry for a production of a given final state:

$$A^{exp} = \frac{\sigma^{++} - \sigma^{+-}}{\sigma^{++} + \sigma^{+-}} \tag{1.93}$$

where σ^{++} and σ^{+-} are the cross-sections for reactions with the colliding beams having polarisations mutually parallel or anti-parallel. A given final state (*e.g.* jet–jet) can be produced not only through the reactions in which a gluon from a proton is participating, but also through reactions with quarks only ($qq \to qq$). This second kind of reactions is considered a background. For a given partonic reaction the asymmetry, A_i, is given by:

$$A_i = \hat{a}_{LLi} \epsilon \frac{\Delta f_{i1}}{f_{i1}} \cdot \frac{\Delta f_{i2}}{f_{i2}} \tag{1.94}$$

where Δf_{i1-2} and f_{i1-2} are the polarised and unpolarised distributions of partons taking part in the interaction ($\Delta f = \Delta G$ and $f = G$ in case of gluons), $\hat{a}_{LLi}$ is a parton asymmetry for this reaction and ϵ stands for dilution factors. The experimental asymmetry, A^{exp}, is a sum of all A_i for reactions leading to a given final hadronic state. The asymmetries in the sum should be taken with weights corresponding to a fraction of a given reaction in the studied sample. Disentangling the $\Delta G/G$ from this sum is a complex and difficult task. Therefore another method is elaborated. Different scenarios of ΔG distribution are assumed and the corresponding expected experimental double

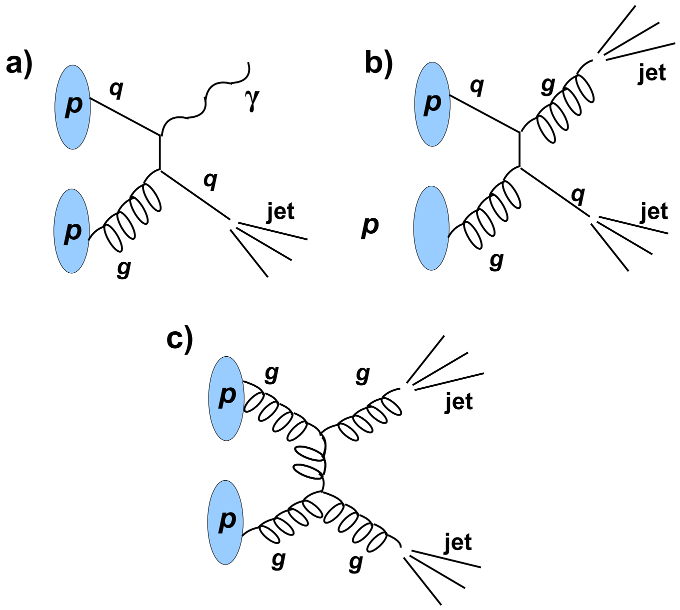

Figure 1.12: Partonic interaction channels in which $\Delta G/G$ can be probed at RHIC: a) $qg \rightarrow \gamma q$, b) $qg \rightarrow qg$, c) $gg \rightarrow gg$.

spin asymmetry for a production of a given final state are calculated. They are then compared with the measured value. Scenarios that do not agree with the measurement are discarded. The validation for the calculations used to interpret the observed spin asymmetries comes from the spin independent measurements of the cross-sections for production of different final states. The theory predictions and the data are here in a good agreement [72].

Measurements done at RHIC cover a wide x_g range, $0.01 < x_g < 0.3$. The final statistical errors are smaller than in the lepton-nucleon scattering. However the complexity of the hadron-hadron interactions makes the analysis extremely difficult and strongly model dependent.

The results from lepton-nucleon and nucleon-nucleon experiments are complementary. The measurements of $\Delta G/G$ in the former are much more direct, especially the open charm channel, but statistically limited, while the latter are based on a much larger event samples but have to take into account a greater number of the background processes.

Chapter 2

The COMPASS

The **CO**mmon **M**uon and **P**roton **A**pparatus for **S**tructure and **S**pectroscopy, COMPASS (NA58)[1], is a Collaboration of more than 250 physicists from 27 institutes from Europe, Russia, Japan and India. The experiment is a successor of a long chain of muon scattering experiments[2] located in the same hall in the previous 30 years. COMPASS is a result of merging two other originally planned experiments – HMC and CHEOPS. Consequently the COMPASS physics programme has two parts. The first is focused on the spin dependent observables and the other mainly on the hadron spectroscopy. In the former a polarised target and a polarised muon beam are used while the latter is based on different nuclear targets and hadron beams. The experiment was approved in 1998 and the spectrometer became operational in 2001 when a commissioning run was taken. In 2002 first physics data with a muon beam were recorded. The muon data taking programme continued in 2003 and 2004. In 2006 the muon programme was resumed after a one year break when the beam was not delivered due to the shutdown of the SPS at CERN. The analysis presented in this thesis concerns data taken in 2002–2004 with a muon beam. The main features of the spectrometer that was on the floor during that time are presented in this chapter. Also the software packages aiming at the reconstruction of the events and at the physics analysis are briefly described. Two topics are discussed in more details. The first one is the RICH detector and the particle identification based on it. Particle identification is crucial for the analysis presented here. The other topic is an example of Monte Carlo studies leading to the optimisation of the detector performance, here the studies of the Scintillating Fibers tracking station are presented. More specific information on the COMPASS detector configuration can be found in [73].

2.1 The Beam

The COMPASS detector is located in the CERN North Area, EHN2 hall. It uses a high-intensity muon M2 beam line (Fig. 2.1). The beam is produced in three subsequent steps. Protons of 400 GeV energy, coming from the **S**uper **P**roton **S**ynchrotron (SPS), collide with a solid, 500 mm thick, beryllium target (T6) generating a secondary beam which consists mainly of π^+, K^+, π^- and K^- mesons. Positive beam particles are then selected with bending magnets and directed into 600 meters long decay tunnel where about 7% of them decay into $\mu^+\nu_\mu$ pairs. At the end of the tunnel a heavy absorber is placed. It stops the remaining hadrons, while μ^+ pass it, loosing only a

---

[1] CERN code number of the experiment is NA58. COMPASS is a common name of both, the detector and the Collaboration.

[2] EMC (NA2, NA2', NA9, NA28), NMC (NA37) and SMC (NA47).

small fraction of their initial energy. Then the μ^+ beam enters a 400 meters long section where particles of a given energy are selected and focused in a set of magnets (B6–B9). This results in a final μ^+ beam of RMS ∼0.8 cm at target with $2 \cdot 10^8$ particles per spill (the SPS spill contains about $1.2 \cdot 10^{13}$ protons) and an angular divergence of 0.4×0.8 mrad. The contamination of hadrons is smaller than 10^{-6}. Spills last 4.8 s each and are separated by 12 s time windows when the beam is not delivered. The energy of the final beam can be selected in a range of about 60–200 GeV.

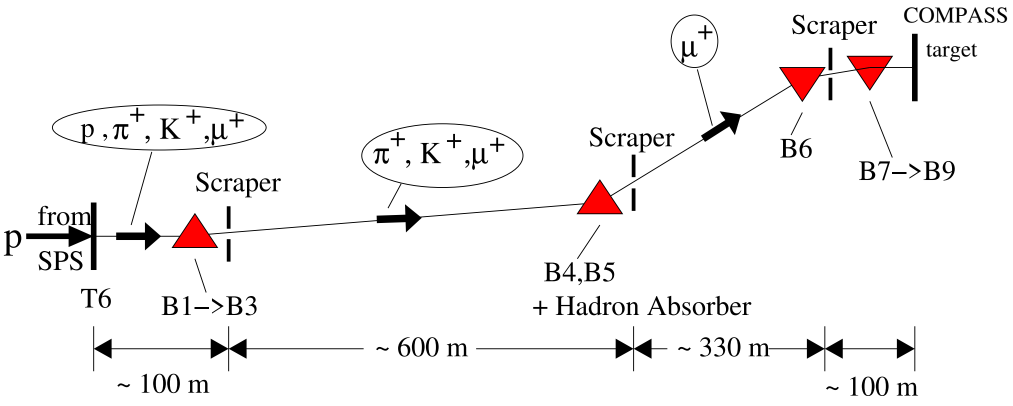

Figure 2.1: Sketch of the COMPASS M2 beam line. B1–9 are magnet stations, T6 is the hadron production target. Plot taken from [74]

Muons coming from the π and K decays are naturally polarised. In the rest frame of the decaying particle muons are 100% polarised and the μ^+ helicity is negative. This fact arises from the left-handedness of neutrinos and the angular momentum conservation. In the laboratory frame the polarisation of muons is no longer 100% due to the Lorentz boost. It depends on the ratio of the decaying meson energy ($E_{\pi,K}$) to the muon energy (E_μ) and is given by the formula:

$$P_\mu = -\frac{m^2_{\pi,K} + (1 - 2E_{\pi,K}/E_\mu)m^2_\mu}{m^2_{\pi,K} - m^2_\mu} \tag{2.1}$$

The highest polarisation ($P_\mu = -1$) is for $E_\mu = E_{\pi,K}$. There are three additional parameters that have to be taken into account when choosing the muon energy for the experiment: the beam intensity, the cross-section for the PGF process and the experimental acceptance which vary with the muon beam energy. Monte Carlo simulations prepared with the AROMA generator[3] were analysed to obtain the optimal beam energy for the studies of the spin dependent asymmetries [75]. For the 2002–2004 data taking the energy of 160 GeV was chosen. This corresponds to the beam polarisation of –0.76 (for 2002 and 2003) and –0.81 (for 2004 when the secondary π, K beam energy was changed). Momenta of the beam particles are measured to 0.5% accuracy with the **B**eam **M**omentum **S**tation (BMS) placed along the beam line. The RMS of the beam momentum spread is ∼3%.

Apart from the μ^+ beam also a hadron beam can be delivered via the M2 line to the COMPASS experimental hall. In this case the hadron filter is removed which lets the

---

[3] AROMA is a Monte Carlo generator tailored for the simulations of the heavy quark production through the PGF process. More details concerning this generator are given in Sec. 6.1.1.

π^+ and K^+ to reach the target. The identification of the beam hadrons is performed by Cherenkov CEDAR detectors placed along the beam line. The hadron programme of COMPASS is not covered by this thesis, therefore the details of its setup will be omitted.

For more information on the COMPASS beam line cf. [76].

2.2 The Target

For the muon programme in 2002–2004 COMPASS uses a target composed of two cylindrical cells each 60 cm long and 3 cm in a diameter separated by a 10 cm gap (cf. Fig. 2.2). Cells are filled with a solid lithium deuteride, ^{6}LiD. They are located inside a superconducting solenoid which provides a homogenous 2.5 T longitudinal magnetic field. The homogeneity $\Delta B/B$ in the cell region is of the order of $3.5 \cdot 10^{-5}$. The COMPASS solenoid magnet is the one used previously by the SMC Collaboration. It provides ±70 mrad angular acceptance. In 2006 it is replaced by a new one with an aperture of ±180 mrad.

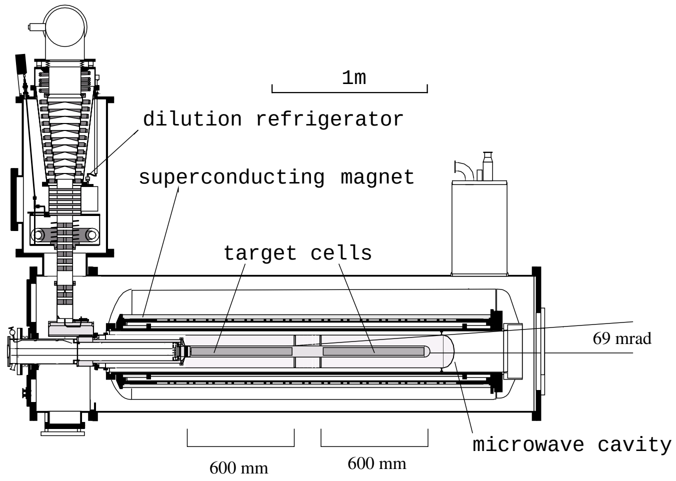

Figure 2.2: Setup of the COMPASS target that was used in 2002–2004 data taking period. Plot taken from [77].

The nuclear spins of the material in the two parts of the target are polarised in opposite directions – parallel and anti–parallel to the magnetic field direction. For the studies of the spin effects a very high level of the target nuclear polarisation is required. This cannot be achieved through the method based on a Zeeman effect. Using this method, even with a 2.5 T magnetic field and in 1 K temperature, polarisation of the deuterons would be only 0.05%[4] while in the same conditions the electrons polarisation is 96%. This difference is due to a much smaller magnetic moment of the nuclei in comparison with the electrons. In order to polarise nuclei a technique based on the **D**ynamic **N**uclear **P**olarization phenomenon (DNP) [78] is used. It may be described as an induced transfer of a large polarisation from the electrons to the nuclei. The electrons and the nuclei cannot be considered separately as they interact with each other via the electromagnetic field. Instead they should be treated as one complex quantum system.

---

[4] The level of polarisation for spin 1 target is defined as: $P = \frac{N_+ - N_-}{N_+ + N_0 + N_-}$ where N_+, N_- and N_0 are populations of a spin projection: +1, −1 and 0, respectively.

For simplicity let us consider a system composed of a spin $\frac{1}{2}$ nucleus and an electron. A target is then composed of the nucleus-electron pairs each being in one of the following states: $|A\rangle = (+\frac{1}{2}, +\frac{1}{2})$, $|B\rangle = (+\frac{1}{2}, -\frac{1}{2})$, $|C\rangle = (-\frac{1}{2}, +\frac{1}{2})$, $|D\rangle = (-\frac{1}{2}, -\frac{1}{2})$; where the first number corresponds to the nucleus and the second to the electron spin projection. In a strong magnetic field almost all the nucleus-electron pairs will be in the quantum states with given spin orientation of the electron, for instance in $|B\rangle$ and $|D\rangle$ (see Fig. 2.3). Then the target is irradiated with a microwave radiation. A frequency of the radiation is exactly equal to the frequency needed to a simultaneous flip of both spins from a given pair. By choosing a proper frequency, $\omega_e + \omega_p$ or $\omega_e - \omega_p$, $|C\rangle$ and $|A\rangle$ states can be filled selectively. Electron spins relax within milliseconds to a lower state and the nucleus-electron systems end in a state $|D\rangle$ or $|B\rangle$ (double spin transitions are highly suppressed) and thus the initial $|B\rangle$ states are transferred to $|D\rangle$ or $|D\rangle$ are transferred to $|B\rangle$, depending on the used microwave frequency. Once the microwave radiation is switched off the temperature of the target is lowered by an order of magnitude and the achieved nuclear polarisation level can be maintained for a long period.

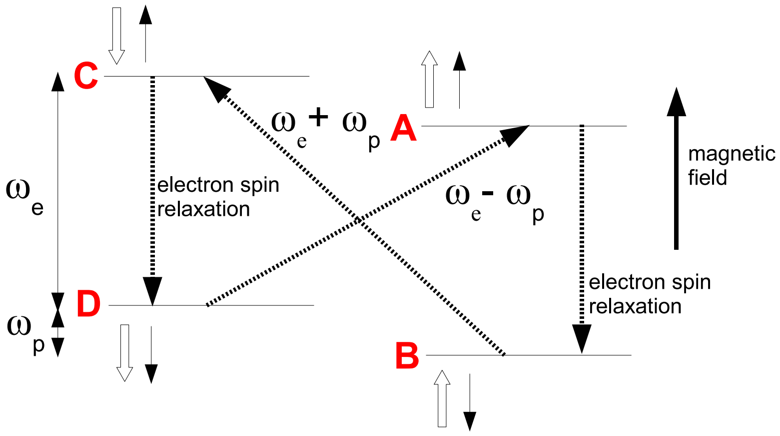

Figure 2.3: Energy levels and transitions between them used for the nucleus polarisation in the DNP method. The microwave frequencies are: $\omega_e + \omega_p$ or $\omega_e - \omega_p$. Arrows $\Uparrow$ and $\uparrow$ represent the nucleus and electron spin projections.

The DNP method requires the target cells to be enclosed in a microwave cavity and separated by a microwave stopper. Building up polarisation lasts for about 2–3 days. The maximal polarisation obtained was +57% and −53% (average about 50%). The polarisation is measured by the **N**uclear **M**agnetic **R**esonance method (NMR). The NMR is also used to estimate the amount of impurities in the ^{6}LiD material, especially the contamination coming from ^{7}Li and H isotopes. Another important contamination is due to the cooling system enclosing the ^{6}LiD material and consisting of ^{4}He and ^{3}He atoms. The amount of impurities has an influence on the spin asymmetry measurements. For the composition of the target material see Tab. 2.1. Directions of the target cells polarisation are flipped every 8 hours by applying an additional magnetic field of a maximal induction 0.5 T perpendicular to the solenoid field. The polarisation reversal lasts for about 30 minutes and preserves its initial level. The reversal is needed to cancel false asymmetries originating from different spectrometer acceptances for the two target halves. It also reduces the error from time dependent variations of the spectrometer efficiency. In order to sustain the polarisation level for a long time the target material is cooled down to the temperature of 50 mK. Cooling is done with a help of ^{3}He–^{4}He dilution refrigerator. For more information on the COMPASS target setup see [79].

Element	No. of mols	Atomic mass	Element	No. of mols	Atomic mass
H	0.1019	1	^{7}Li	1.7950	7
D	44.5370	2	C	0.0080	12
^{3}He	3.6207	3	F	0.0160	19
^{4}He	10.9118	4	Ni	0.0057	58.6
^{6}Li	42.8429	6	Cu	0.0136	63.6

Table 2.1: Composition of the target material in 2002.

The nucleons in a deuteron are in the spin triplet state. They can be in a mutual S-state ($L = 0$) or D-state ($L = 2$), with the probabilities of $P_S = 0.951$ and $P_D = 0.049$, respectively [80]. In the S-state the polarisation of the nucleons is simply parallel to that of the deuteron and both spins add up to form spin 1. For D-state the picture is more complex. If m, m_L and m_S denote the total, orbital and spin magnetic quantum numbers in the system, then the following states $|m_L, m_S; m\rangle$ are possible for $m = 1$: $|2, -1; 1\rangle$, $|1, 0; 1\rangle$ and $|0, 1; 1\rangle$. The corresponding Clebsch-Gordan coefficients are $\sqrt{3/5}$, $\sqrt{3/10}$ and $\sqrt{1/10}$. Therefore the nucleon spins are in net 50% cases aligned opposite to the deuteron polarisation. The total number of nucleons in the COMPASS target with spins parallel to the deuteron polarisation is thus:

$$N_{\uparrow\uparrow} = N_S - 1/2N_D = N - 3/2N_D = (1 - 3/2P_D)N = \Omega N = (0.926 \pm 0.016)N \quad (2.2)$$

where N_S and N_D are the numbers of nucleons in the S-state and D-state, while $N = N_S + N_D$. The nucleon polarisation in the target should be thus reduced by the Ω factor with respect to the deuteron polarisation. To be compatible with other COMPASS analyses, which use deuteron as a whole, it was decided to first calculate the $\Delta G/G$ for deuteron, *i.e.* without Ω, and then divide the final result of the analysis by 0.926 to get the $\Delta G/G$ for a nucleon.

2.3 The Spectrometer

The COMPASS detector consists of two separate spectrometers – **L**arge **A**ngle **S**pectrometer (LAS) and **S**mall **A**ngle **S**pectrometer (SAS), Fig. 2.4. This construction allows to perform accurate measurements of tracks of particles emitted at large and small angles with respect to the beam direction. LAS is optimised for angles larger than 30 mrad while SAS is made for smaller angle, high momentum tracks. Both spectrometers contain dipole magnets, SM1 and SM2, located in LAS and SAS respectively. The first magnet, 4 m downstream the target centre, has the field integral along the beam equal to 1 Tm. In order to have a wide angular acceptance it has a large, 2.29×1.52 m^2, central gap. This leads to a non–negligible fringe field in the zone between SM1 and the target solenoid. It is taken into account during track reconstruction. A charged particle has to carry momentum larger than 0.4 GeV to cross the magnet and be recorded downstream. For a particle slower than 0.4 GeV its momentum can be estimated from the measurement of the track deviation in the fringe field. The SM2 magnet is located 18 m downstream the target centre and has a field integral of 4.4 Tm. It has a central gap of 2×1 m^2. The minimal momentum for charged particles that can pass SM2 is 4 GeV. Zones before and after SM1 and SM2 are equipped with a number of tracking detectors which allow to reconstruct tracks in a magnetic field–free regions. Segments of the reconstructed tracks are then bridged through magnetic field and the final 3–momentum vectors are estimated.

The first spectrometer is equipped with a **R**ing **I**maging **CH**erenkov (RICH) detector which provides hadron identification in a wide momentum range. It measures particle velocity from the corresponding Cherenkov emission angle. Combining this information with the knowledge of momentum, the particle type can be determined. More detailed description of the RICH is presented in Sec. 2.5. The RICH detector is not well suited for the distinction between pions and muons. Therefore for muon identification the drift tubes detectors installed at the end of LAS and SAS are used. In front of them 60 cm iron and 2.4 m concrete walls are placed, respectively. The walls work as filters absorbing all charged particles but muons.

Both spectrometers contain hadronic calorimeters (HCAL1 and HCAL2). They have a sandwich construction of alternate scintillators and iron plates. Their task is to help the distinction between muons and hadrons. They are also used in the trigger system. SAS is additionally equipped with an electromagnetic calorimeter (ECAL2) made of lead glass blocks. Another electromagnetic calorimeter (ECAL1) has been added to the experiment setup in 2006. Both may be used for the detection and the energy measurement of neutral particles, *e.g.* photons.

Positions of all the detectors are defined in the COMPASS reference system. Its Z axis is along the beam direction, X axis is pointing horizontally towards the Jura mountains and Y axis is pointing upwards. The upstream target cell is placed between Z=–100 cm and Z=–40 cm while the downstream one between Z=–30 cm and Z=30 cm.

2.4 Tracking Detectors

Several kinds of tracking detectors are placed along both stages of the COMPASS. The purpose of using various detectors is to match different particle fluxes in different parts of the spectrometer. In general the detectors can be divided into three groups according to their position with respect to the beam axis. These are: **V**ery **S**mall **A**rea **T**rackers (VSAT), **S**mall **A**rea **T**rackers (SAT) and **L**arge **A**rea **T**rackers (LAT).

VSAT detectors work efficiently in a high particle intensity region, close to the beam. This group consists of eight **SCI**ntillating **FI**bers stations (SCIFI) [81] of various sizes (from 4×4 cm^2 up to 12×12 cm^2) and of the **SI**licon trackers (SI) [82]. Two SCIFI stations and all SI detectors are installed upstream the target and are responsible for a measurement of the direction of the incident muon (first detectors are placed 7.5 m upstream the target). The rest of SCIFI stations are located downstream the target. As the muon scattering angle is usually small these detectors are used for the muon track reconstruction. In Sec. 2.11 a more detailed discussion of SCIFI detectors is presented.

Further away from the beam region the SAT detectors are placed. Between the target and SM1 three **M**icro**M**egas stations (MM) [83], each equipped with three active layers, are located. These provide tracking in a zone highly populated with short hadron tracks outgoing from the primary interaction point. The active area of MM detectors is 40×40 cm^2 while the central part of 5 cm diameter is deactivated to avoid discharges caused by a high particle flux. Downstream SM1 ten stations of the **G**as **E**lectron **M**ultipliers

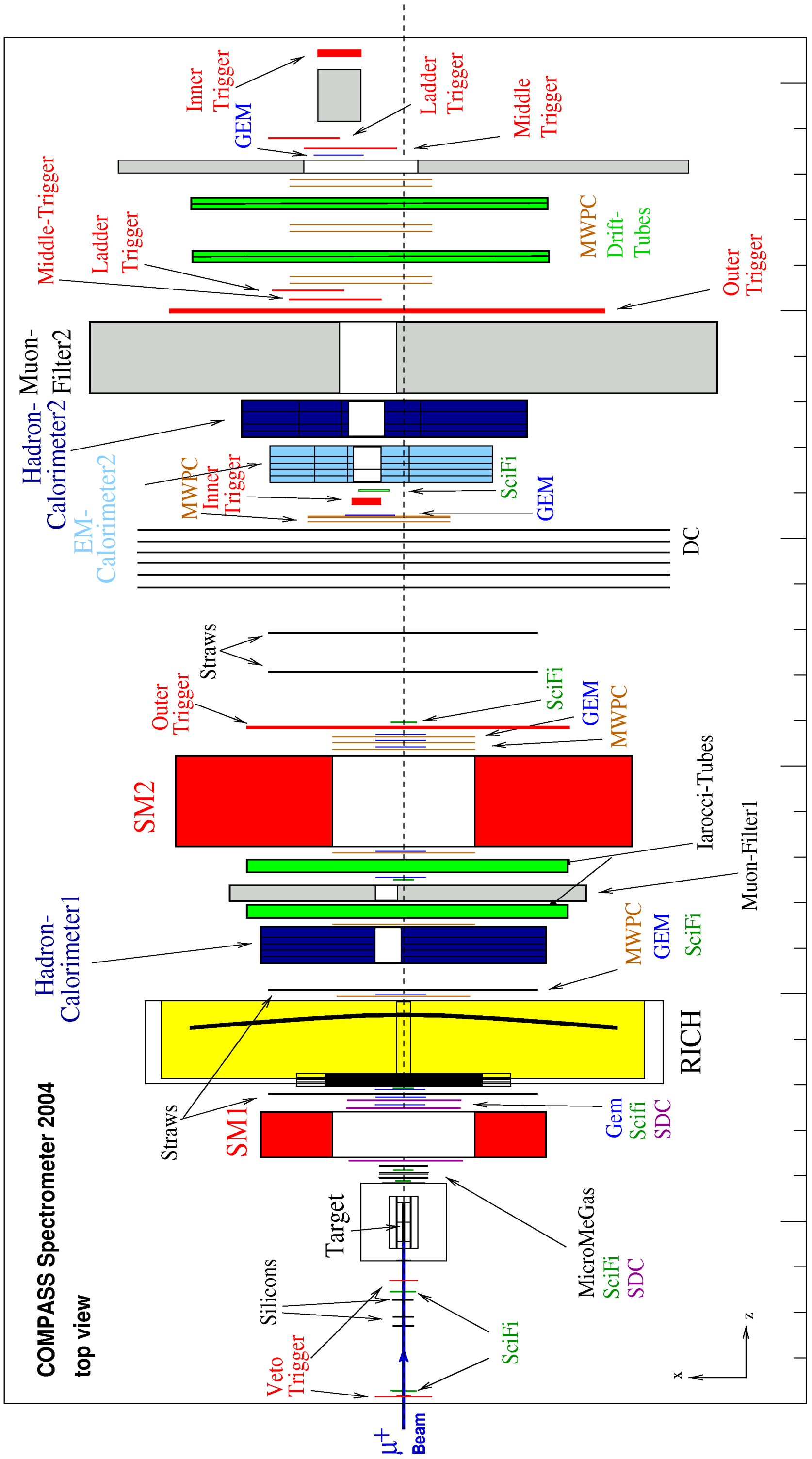

Figure 2.4: Sketch of the COMPASS spectrometer in 2004. The muon beam coming from the left and drawn in blue, before hitting the target is tracked by a set of Silicon and Scintillating Fiber stations. SM1 and SM2 magnets around which LAS and SAS spectrometers are built are marked red. The first spectrometer is equipped with RICH (yellow) while the second with Electromagnetic Calorimeter (light blue). Both stages contain Hadronic Calorimeters (dark blue) and Muon Filters (grey). A number of various tracking devices are also marked. In the SAS four pairs of trigger hodoscopes are placed: Inner, Middle, Outer and Ladder. Plot taken from [73].

(GEM) [84] trackers are installed. Each station consists of four planes rotated by 45° with respect to the other. Their dimensions are 31.6×31.6 cm^2 and the dead zones are the same as for the MM detectors.

The large area tracking is based on the **S**mall area **D**rift **C**hambers (SDC), **M**ulti **W**ires **P**roportional **C**hambers (MWPC) [85], **ST**raw drift chambers (ST) [86] and large area **D**rift **C**hambers (DC) [87]. There are three SDC stations each with eight active planes. One station is placed before SM1 and two just behind it. Their task is to enable track bridging of the particles outgoing from the interaction point at large angles with respect to the beam direction. The active area of SDC planes is 1.8×1.3 m^2 with a central dead zone of 30 cm diameter. The MWPC modules, 11 in total, provide the tracking in a region of a low track occupancy. The modules are installed throughout the SAS spectrometer. The last module is set about 46 m downstream the target. The size of MWPC is 1.8×1.2 m^2 while the dead zone diameter varies from 16 cm to 22 cm depending on the position of the module[5]. Tracking far from the beam area is also due to 15 double layer ST stations. Their sizes are 3.2×2.8 m^2 with the insensitive zones 20×20 cm^2 at the centres. Two of the modules are placed after SM1 and enable the tracking of slow hadrons which are strongly deflected in the magnetic field. The other two are placed after SM2 and help with the reconstruction of muon tracks, scattered at large angles. Downstream SM2 four DC modules are installed. They have active areas of 5×2.5 m^2 with diameters of the dead zones 0.5 m or 1.0 m. They provide tracking in the outermost regions of the spectrometer.

Detector	Active area [mm^2]	Dead zone [mm]	Resolution [mm]
SCIFI	39×39 ÷ 123×123	–	0.13 ÷ 0.21
SI	50×70	–	0.010
MM	400×400	r = 50	0.09
GEM	316×316	r = 50	0.07
SDC	1800×1275	r = 300	0.19
MWPC	1780×900 ÷ 1780×1200	r = 160 ÷ 220	1.6
ST	3230×2800	197×197	0.19
DC	5000×2500	r = 500 ÷ 1000	0.5

Table 2.2: Characteristics of tracking detectors.

2.5 The RICH

The first spectrometer is equipped with a **R**ing **I**maging **CH**erenkov detector (RICH)[6] responsible for the charged hadrons identification [88]. It is capable to separate pions kaons and protons in a wide range of their momenta starting from a threshold of a few GeV (2.5 GeV, 9 GeV, 17 GeV for π, K and p respectively) up to 50 GeV. It can work in a high–intensity particle environment and is able to register and record a great amount of data. It has a wide acceptance: ±250 mrad in horizontal and ±200 mrad in vertical directions in order to cover full acceptance range provided by the new COMPASS target solenoid that was installed in 2006. The amount of the material the particle has

---

[5] The sizes of the detectors are approximate. For actual sizes cf. Tab. 2.2 and [73].

[6] In what follows RICH detector configuration from 2002–2004 period is described. For 2006 run a number of RICH subsystems were upgraded.

to pass inside RICH was minimised so that the tracking and the energy measurement resolution (downstream the RICH the calorimeters are located) are not decreased significantly. In Fig. 2.5 the COMPASS RICH detector is sketched. Its vessel is 3.3 m long, 6.6 m wide and 5.3 m high (volume of about 80 m^3) and is filled with C_4F_{10} radiator at the atmospheric pressure. The contamination of oxygen in the radiator is smaller than 5 ppm. The downstream wall of the vessel is covered with 116 hexagonal and pentagonal segments of spherical, aluminised mirrors which reflect and focus the Cherenkov photons onto photodetectors located outside the region of the spectrometer acceptance. Multiwire Proportional Chambers with CsI photocatodes are used as photodetectors. They cover the area of 5.3 m^2 and are segmented in 8×8 mm^2 pads which gives a total number of 82 944 pixels. The read-out system consists of 192 front-end boards each connected to 432 pixels. The read-out can handle the trigger rate up to 100 kHz with the maximum pixel occupancy of 20%. This generates a data transmission rate of 6.64 Gb/s [90]. The RICH photon detectors are sensitive in UV region which corresponds to the wavelengths smaller than 200 nm. A typical path length of a photon inside the RICH vessel is 4.5 m. For this length the average medium transmittance is higher than 80%. The exemplary rings from the COMPASS RICH detector are presented in Fig. 2.6.

The COMPASS RICH detector can be compared with the ones used in HERMES and PHENIX. HERMES is equipped with two RICH modules [91], both with two radiators, silica areogel and C_4F_{10}. Such construction provides a clear identification of pions, kaons and protons in the momentum range from 2 to 15 GeV with the detector volume about 4 m^3 per each module. The number of photodetectors is 2×1934. The RICH used in PHENIX [92] is responsible for the e/π discrimination below the π Cherenkov threshold which is 4 GeV. It is not meant for the hadrons identification. There are two modules, 40 m^3 large and filled with CO_2 gas, each located in one of the central PHENIX spectrometer arms.

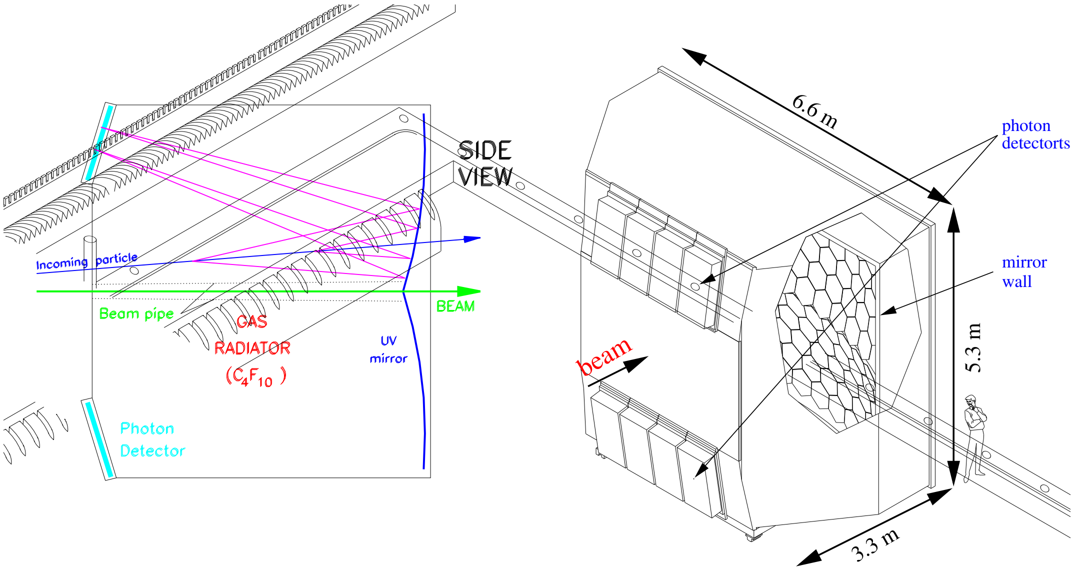

Figure 2.5: The COMPASS RICH detector [89].

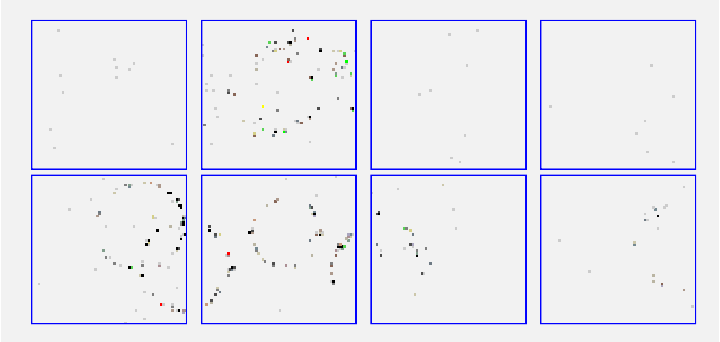

Figure 2.6: Exemplary rings from the RICH detector [89].

2.5.1 The Basic of Cherenkov Rings Finding

A particle travelling through the RICH radiator with velocity larger than the velocity of light in the medium ($v_{min} = c/n$), emits the Cherenkov radiation. The radiation is emitted along the whole path of the particle in the radiator and forms a cone of an opening angle $2\theta_C$ given by:

$$\cos\theta_C = \frac{1}{n\beta} = \frac{\sqrt{p^2 + m^2}}{np} \tag{2.3}$$

where:

$$\beta = \frac{v}{c} \tag{2.4}$$

Radiated photons are reflected by mirrors located at the downstream RICH wall and focused at the photon detectors placed at the upstream–top and upstream–bottom walls of the detector vessel (cf. Fig. 2.5). The signal of the particle created in the photodetectors has a form of a ring whose radius corresponds to the momentum and the mass of that particle. Knowing the momentum from the measurement of the track deflection in the SM1, the particle mass can be calculated. This procedure results in the particle identification. The identification is possible only if the momentum of a particle exceeds a certain threshold which is a function of the particle mass. The more massive a particle the higher the threshold. The thresholds vary from run–to–run as the refractive index of the RICH radiator fluctuates. In Tab. 2.3 the mean threshold values for different particles are presented.

Particle type	RICH momentum threshold [GeV]
muon	1.9
pion	2.5
kaon	9.0
proton	17.0

Table 2.3: The RICH thresholds for the identification of a given particle.

2.5.2 The χ^2 Method

Before the identification procedure an algorithm for the rings finding is used. At first clusters of fired photodetectors are searched. Each cluster corresponds to one Cherenkov photon that hit the detector plane and triggered a group of neighbouring photon cells. Then the clusterisation is performed. The most probable hit point of a photon is found calculating the weighted mean from positions of each photodetector from a cluster. Here a weight is an amplitude of a signal induced in a given detector. Finally the rings are searched for in the (θ, ϕ) coordinates, where θ and ϕ are a polar and an azimuthal angles with respect to the axis defined by the particle track. After rings are ascribed to tracks going through the RICH volume the particles identification procedure is applied.

A charged particle passing the RICH detector can be an electron, muon, pion, kaon or proton. All other charged particles produced in the target have too short life times to reach the detector before they decay. A distinction between those five kinds of particles is done by comparing the registered Cherenkov ring with rings expected for a given particle. For each mass hypothesis (below denoted with j) the expected Cherenkov angle is estimated. Then the χ^2 for each hypothesis is calculated:

$$\chi_j^2 = \sum_{i=1}^{N} \frac{(\theta_i - \theta_j^{hyp})^2}{\sigma_{\theta_i}^2} \tag{2.5}$$

In the equation the sum runs over all clusters ascribed to a ring. The σ_{θ_i} describes the resolution in θ for a given cluster. With the procedure five values of χ^2 are obtained: χ_e^2, χ_μ^2, χ_π^2, χ_K^2, χ_p^2. For the kaon identification, being crucial for the analysis presented in this thesis, only three last values of χ^2 are used. The reason is that the muons are identified more accurately with other detectors (calorimeters and muon filters), while the χ_e^2 does not improve the quality of the hadron identification[7]. It should be noted that the χ^2 procedure does not take into account the contribution of background photons which is different in various parts of the RICH photodetector planes. This drawback is absent in the *Likelihood* approach.

2.5.3 The *Likelihood* Method

Background in the RICH is a product of electronic noises and of the hardware memory of the cells that still remember signals from previous events. Distribution of the background is not uniform. The highest background level is in the region close to the beam axis as it is exposed to the highest muon beam flux. There are also photodetectors and their clusters that produce high electronic noises. Parameterisation of the background as a function of a photodetector position has been done in [93]. Based on this parameterisation the *Likelihood* method was introduced which takes into account expected shapes of the signal and of the background. Here the sketch of the method is presented. For more details see [93].

The likelihood value for a given mass hypothesis j is defined as:

$$L_j = \frac{e^{\lambda_j} \lambda_j^N}{N!} \prod_{i=1}^{N} P_j(\theta_i, x_i, y_i) \tag{2.6}$$

In this equation λ_j is the calculated expected number of photons (the number of expected signal photons varies with a mass of a particle, therefore index j was added), N is the number of registered photons, $P_j(\theta_i, x_i, y_i)$ is the probability density for a photon i to be found at some θ_i angle (for the signal) and with x_i and y_i coordinates in the photodetector

---

[7] Electrons and pions are hard to be distinguished in the RICH. The χ^2 for the two hypotheses are almost identical in nearly entire momentum range allowed.

plane system (for the background). The product runs over all the photons. The first part of the equation is a Poissonian term describing the detection probability of a given number of photons while the expected number of them is calculated theoretically. The remaining part of Eq. (2.6) is a total probability density for photons. It is calculated with an assumption that the particle is of the j kind. The probability density for a given photon can be written as a sum of terms describing the signal and the background distributions, normalised to the predicted number of photons:

$$P_j(\theta_i, x_i, y_i) = \frac{1}{\lambda_j}(S_j(\theta_i) + B(x_i, y_i)) \tag{2.7}$$

The signal part is assumed to be described by a Gaussian distribution centred at the predicted Cherenkov angle for a given mass hypothesis θ_j and with σ defined by the angular resolution of the ring reconstruction:

$$S_j(\theta_i) = \frac{A}{\sqrt{2\pi}\sigma} e^{-\frac{(\theta_i-\theta_j)^2}{2\sigma^2}} \tag{2.8}$$

where the normalisation factor A corresponds to the predicted density of photons in the Cherenkov ring. Finally the likelihood for a given mass hypothesis can be rewritten as:

$$L_j = e^{\lambda_j} \prod_{i=1}^{N} (\frac{A}{\sqrt{2\pi}\sigma} e^{-\frac{(\theta_i-\theta_j)^2}{2\sigma^2}} + B(x_i, y_i)) \tag{2.9}$$

In this equation multiplicative factors, same for different j, were omitted as for the particles identification only the ratios of the likelihoods are meaningful. Parameterisation of the background, that is included in the likelihood function, is the same for all mass hypotheses. Finally also a likelihood for the background hypothesis is given as:

$$L_{\mathrm{bg}} = e^{b} \prod_{i=1}^{N} (B(x_i, y_i)) \tag{2.10}$$

where b is the expected background strength.

2.5.4 The Refractive Index

The value of θ_C in Eq. (2.3) depend on the refractive index n of the radiator. The radiator is a mixture of a nominal C_4F_{10} ($\sim 95\%$) gas and of residual contaminations, mainly of gaseous nitrogen ($\sim 5\%$). This mixture changes composition with time as the gases constantly circulate through filters [94]. Moreover the temperature and the pressure (slightly higher than the atmospheric one to avoid the diffusion of air into the vessel) of the radiator gas vary with time, changing its refractive index. The variations of n are:

$$\frac{n - <n>}{<n> - 1} \sim 2\% \tag{2.11}$$

This effect may significantly lower the particle identification efficiency. Therefore for each run the refractive index is calculated separately. The refractive index is obtained from the reconstructed data using the fastest particle going through the RICH medium. For such a particle $\cos\theta_C \approx 1/n$ which gives an accurate estimation of n. However this procedure requires two passes of the data production[8]. After the first production the

---

[8] A production refers to the process of the raw data reconstruction. The procedure will be described in details in Sec. 2.8.

refractive indices are calculated for each run. They are later used in the second data production when particles identification is performed. The two–step procedure is very time consuming (one production takes a number of months). Therefore the so-called interpolation procedure was introduced. It requires the preproduction of just a few runs[9] for a given year. Then for those runs the refractive indices are calculated. They are then interpolated preparing the information needed in the production. For 2002 and 2003 this procedure is capable to predict the refractive indices with the precision:

$$\frac{n_{interpolated} - n_{true}}{n_{true} - 1} < 1\% \tag{2.12}$$

For the 2004 data the precision was increased to 0.1% due to the availability of information on temperature and pressure inside the RICH detector registered by newly added sensors. All of the 2002 and some of 2003 periods (each corresponding to approximately one week of the data taking) were produced for the second time. For them the true values of the refractive indices for each run were used in the second production. When this thesis was completed the rest of the 2003 periods still awaited to be produced for the second time.

2.5.5 The χ^2 Method Versus the *Likelihood* Method

The *Likelihood* method in comparison with the χ^2 approach is more robust as it takes into account the influence of the non–uniform RICH background. The gain in the statistics of the reconstructed open charm mesons, is indeed, for the former equal to about 10%, which favours this method of particle identification. However it requires a good background description $B(x, y)$ during data production. Such a description was prepared at the end of 2004 when the data for 2002 and 2003 had been already processed. Therefore presently the *Likelihood*-based particles identification can only be used for the 2004 data.

2.6 Triggers

The data acquisition starts when an event fulfils certain criteria defined by the scattering angle of the muon and by the energy deposited in the hadronic calorimeters. The scattering angle criterion corresponds to different regions of Q^2. The data acquisition is triggered starting from events with quasi–real photons ($Q^2 \ll 1$ GeV^2) up to inclusive deep inelastic scattering ($Q^2 > 1$ GeV^2), see Fig. 2.7. The triggers have to suppress efficiently the background induced by the radiative events and the muon-atomic electron scattering.

Four sets of hodoscopes, each covering different kinematical region of the interaction, provide information about the scattered muon track. Their aim is to give a crude but fast estimation of the track direction. Each set consists of two hodoscopes. If in a given set both detectors record hits, the trigger is formed. The sets of hodoscopes are called: Inner, Ladder, Middle and Outer. The Inner pair is sensitive to interactions with very small Q^2 ($Q^2 < 10^{-3}$ GeV^2) while the Outer forms triggers for $Q^2 > 1$ GeV^2. The veto detectors, placed before the target, are responsible for the background suppression. They reject events for which a set of hodoscopes was hit by a muon track not focused on the target (a beam halo track) and not by a scattered muon. The radiative and

---

[9] A run corresponds approximately to 30 minutes long data taking interval.

the μ-e events are removed if the energy deposit in the hadronic calorimeters is smaller than ~4 GeV. Hodoscopes cannot record all scattered muon tracks which can be reconstructed offline. Especially interactions with $Q^2 > 1$ GeV^2 often do not induce a signal in the hodoscopes. For that class of events a pure calorimetric trigger based on the amount of the energy deposited in HCAL1 and HCAL2 was introduced.

For 2002–2004 data taking seasons the number of triggers per spill varied from 20 000 to 40 000. It was limited by the data transfer speed. For more information about the triggers see [95].

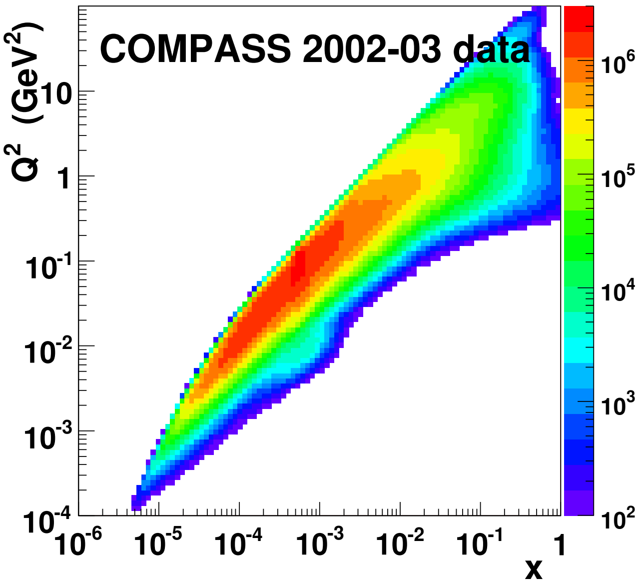

Figure 2.7: COMPASS kinematical acceptance in 2002 and 2003.

2.7 The Data AcQuisition (DAQ)

The COMPASS spectrometer has over 190 000 detector channels spread over different subsystems of the experiment. The total size of the data describing one event is 40–50 kB. In 2002, about $5 \cdot 10^9$ events were recorded. That gives around 260 TB of data written on disks. To cope with such an amount of information a special **D**ata **A**c**Q**uisition (DAQ) system was designed and implemented. The data flows from the frontend electronic boards to the mass storage disks in a few steps. The frontends of each detector are connected to the readout modules of two types: CATCH and GeSiCa. The aim of these modules is to collect the data from the detectors and transfer them via the optical links to the **R**ead **O**ut **B**uffers (ROB). ROBs are computers hosting special PCI[10] cards called Spillbufers which provide a buffering of the data coming from one spill. Then the data are sent through the Gigabit Ethernet line to the Event Builder computers. Once the data reach the Event Builders, the information from the different detectors is combined to construct a data block corresponding to a given event. The data blocks are transferred to the CERN data recording system and stored on tapes in the **C**ERN **A**dvanced **STOR**age Manager (CASTOR) infrastructure [96]. The DAQ

---

[10] PCI - Peripheral Component Interconnect standard specifies a computer bus for attaching peripheral devices.

design that includes Spillbufers, is especially useful in the COMPASS case because it takes advantage of the SPS spill structure. Each 4.8 s data taking period is followed by 12 s when the beam is not delivered. With the Spillbufers the data transfer can be uniformly distributed over the 16.8 s period which results in a decrease of the required transfer rate. The COMPASS DAQ system is widely presented in [97] and drawn in Fig. 2.8.

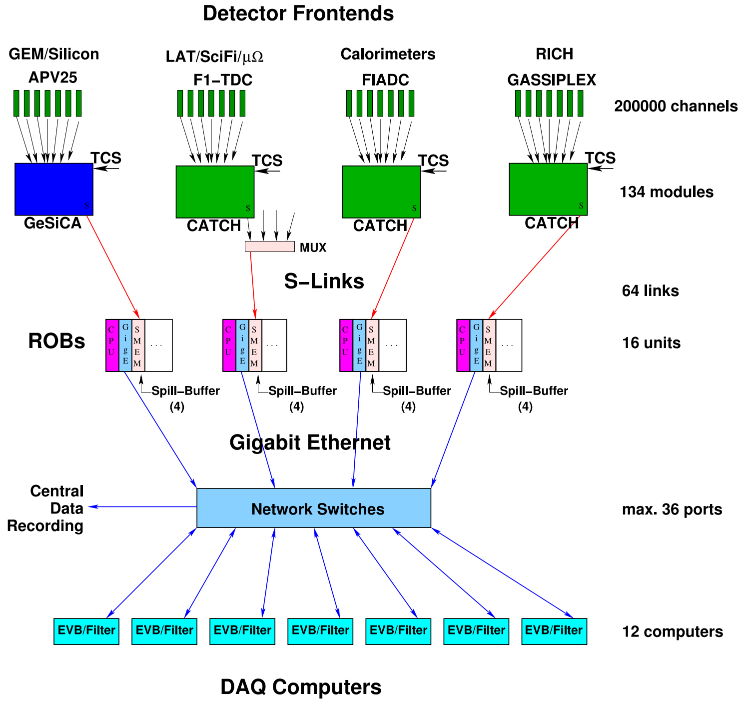

Figure 2.8: COMPASS DAQ system. For more information see text. Plot taken from [97].

2.8 Event Reconstruction

COmpass **R**econstruction and **A**na**L**ysis program (CORAL) is a software tool written mostly in C++ that enables a full reconstruction of events with the raw data stored at CASTOR. The reconstruction process can be decomposed into four steps:

- Decoding of the raw data. Information on the hits, recorded in a special format on the storage tapes, is mapped onto physical detectors in which they had appeared and the exact location in space of each hit is retrieved.
- Clusterisation. Hits that are at a close distance to each other in a given detector layer are combined. These hits are assumed to be produced by a single track which induced a signal in a group of neighbouring channels of one detector. A position of a combined hit is obtained using the weighted mean method where the weight is an amplitude of the signal in each channel.
- Tracks reconstruction. In this step the spectrometer is divided into zones in which the multiple scattering and the magnetic field are negligible. Inside these zones,

the tracks segments are assumed to be approximately straight. The zones are separated by the SM1, SM2, target and the second muon filter. The track finding algorithm reconstructs straight segments of the tracks in each zone separately. It is based on a combinatorial approach. Pairs of hits recorded in two different detectors in a given zone are used successively, defining a straight path in that zone. The width of the path changes from detector to detector depending on their spatial resolution. Along the path other hits are collected and ascribed to the track. At the end candidates for tracks segments are sorted according to the number of hits and the χ^2 criteria. Other more sophisticated methods are used to reject fake hits and low quality tracks. Also the low momenta segments that are curved in the fringe field or are highly affected by multiple scattering are looked for. After the straight segments are defined the bridging through zone boundaries takes place. During this procedure the neighbouring segments are connected and a full track is reconstructed. The bridging process is based on a very precise knowledge of the magnetic field through which a track is interpolated. A segment of a track located in one zone after bridging can be connected with several segments in another zone. In that case the quality function using a χ^2 value is used to evaluate which combination of track segments should be retained. Finally the back–tracking of track segments that were reconstructed after SM1 and not bridged successfully through the magnet takes place. In this procedure tracks that do not have segments before SM1 are propagated in the direction of the target picking up hits that are not associated to any other tracks or are associated to short tracks ending in the zone before SM1. These short tracks have a high probability to be "ghosts", *i.e.* tracks reconstructed accidentally. Once the tracks are reconstructed, the fitting procedure is applied. Its aim is to find the best estimation of the trajectory parameters for each particle and a corresponding error matrix. It is performed with a Kalman filter algorithm [98]. For each track it starts with parameters tentatively estimated during the track reconstruction procedure. Then the parameters and the error matrix are updated iteratively for each cluster found at the track's path, starting from the clusters that are the closest to the primary interaction point and moving downstream. The procedure takes into account the multiple scattering in the spectrometer material. When the Kalman filter procedure reaches the most distant cluster it starts again, this time going from the downstream end towards the upstream one. At the end the best estimation of parameters of each track at the first and the last measured points are saved.

- The fourth step of the CORAL reconstruction algorithm is vertexing, that is finding and fitting the primary interaction vertex. At first, vertex candidates are defined with geometrical cuts *e.g.* the closest approach of tracks. Then the parameters corresponding to the location of each vertex candidate are calculated, using an algorithm based on the Kalman filter. Since the location of a reconstructed vertex introduces additional information, the Kalman filter updates also the parameters of the tracks that are associated with that vertex. More details on the vertex fitting algorithm are presented in [99].

The reconstructed events are stored on the **D**ata **S**ummary **T**apes (DST). Apart from the DST files also files containing smaller amount of information are created. They are called mini-DST (mDST) and are used for performing the physics analysis of the data.

2.9 PHAST

PHysics **A**nalysis **S**oftware **T**ools (PHAST) [100] is a slave software package used for accessing data written on mDST for filtering and analysing them. It provides a set of C++ classes which correspond to physics objects that exist in the reconstructed data *e.g.* tracks, particles, vertices. It also provides a number of functions which can be used for extracting information on the detector setup (*e.g.* magnetic field maps, material maps, detectors geometry) for a given run. Special PHAST classes were prepared that enable working with Monte Carlo files. In this case additional information about the generated events is accessible.

The input for PHAST is a mDST file to be analysed and a C++ function prepared by a user – *UserEvent()*. PHAST is processing a mDST file by calling the *UserEvent()* function for each event. As an argument the function takes a block of information describing the event. From this block all reconstructed physics objects can be directly read in. In the *UserEvent()* a user specifies objects that are going to be analysed, introduces cuts and books histograms that are filled with the data during the mDST processing. Histograms are written to external files and can be viewed with the ROOT software (cf. Sec. 2.10). If a special function is called inside the *UserEvent()*, an output file containing filtered events satisfying given criteria may be created. The output file has a structure of a mDST and is sometimes referred to as a micro–DST. A reason for creating a file containing only filtered events is to save the CPU time for studies when different approaches or cuts are tried for a given subset of data. The analysis presented in the thesis was performed using the PHAST version 7.019.

2.10 ROOT

An Object-Oriented Data Analysis Framework ROOT is a C++ based software package dedicated to the HEP data analyses [101]. It has many features and tools which were prepared in order to solve common problems that arise during analysing data from different experiments. From a wide range of tools a few were chosen and used in the described analysis. These are tools which provide histograms and plots handling, function fitting and C++ classes for mathematical calculations. The input files for ROOT are produced with the help of PHAST and contain n-tuples and histograms. These can be viewed and analysed with a usage of ROOT visualisation tools. Plots may be saved for presentation as ROOT or PostScript files. For the presented studies ROOT version 4.03 was used.

2.11 Detector Optimisation – Tests of the Warsaw SCIFI detector

Reconstruction and identification of the scattered muons is crucial for the number of COMPASS analyses as it is needed for the calculation of the Q^2 and x variables. Most of the interacting muons are scattered at small angles with respect to the beam direction, and even after passing SM1 and SM2 their tracks pass the very inner parts of the spectrometer. Therefore the SCIFI detectors, which may work close to the beam, are the main detectors for the muon track reconstruction. The COMPASS SCIFI layers have various sizes ranging from 4×4 cm^2 to 12×12 cm^2, and are installed throughout the whole spectrometer. In 2004 there were eight SCIFI stations working. Six of them (cf. Tab. 2.4) were placed downstream the target and were used in the scattered muon track reconstruction, while the other two were responsible for the tracking of the incoming beam particles. Each station is composed either of two or three active detector planes. The fibres of a given plane are oriented horizontally (X planes), vertically (Y planes) or at the 45° (−45°) angle with respect to the perpendicular direction (U and V planes).

Name	Z position [cm]	Number of planes	Planes orientations
FI03	124	3	X,Y,U
FI04	213	3	X,Y,U
FI05	585	2	X,Y
FI06	1498	3	X,Y,V
FI07	2128	2	X,Y
FI08	3197	2	X,Y

Table 2.4: SCIFI planes used in 2004 for the outgoing muon reconstruction

For the interactions at small and medium Q^2, the scattered muons are going through the entire spectrometer, passing both SM1 and SM2, and finally hitting the detectors located after the second muon filter placed at the end of SAS. Reconstruction of those muon tracks relies on the successful bridging through both magnets. Therefore segments of a muon track have to be found simultaneously between the target and SM1, between SM1 and SM2 and after SM2. In the Monte Carlo detector studies it was found [102], that with the 2004 spectrometer setup a corresponding segment between SM1 and SM2 was missing for a few percent of events with a muon track segment reconstructed after SM2. The obvious solution to that problem was to place an additional SCIFI station between SM1 and SM2. This would increase the number of hits and improve the tracking efficiency in that zone. The Warsaw COMPASS group took the responsibility for the construction of this new station, which is thus called the Warsaw–SCIFI station.

The construction of each detector subsystem for the spectrometer is preceded by a number of Monte Carlo studies to optimise the configuration of the detector and thus to maximise the overall event reconstruction efficiency. The optimisation is focused on the events that are important for the main physics analysis foreseen for the experiment, that is on the events for $\Delta G/G$ studies in the open charm and high–$\mathrm{p_T}$ channels. The author contributed to the preparation of the Monte Carlo studies for the Warsaw–SCIFI station.

2.11.1 The Method

Optimisation of the SCIFI detector configuration was done using Monte Carlo samples produced with the AROMA generator. The events generated were processed through the GEANT based simulation of the COMPASS detector – a program called COMGEANT. The output of the COMGEANT may then be processed by the CORAL reconstruction program (cf. Sec 2.8).

There were three Monte Carlo samples produced with the AROMA–COMGEANT program chain. They are referred to as (I), (II) and (III). They were prepared to test various features of the SCIFI configuration. Each sample consisted of 50 000 simulated events containing interactions in which $D^*(2010)^+$ mesons were produced and decayed in the

$D^*(2010)^+ \to D^0\pi_S \to K\pi\pi_S$ chain[11]. For each test two separate CORAL reconstructions were performed: one with the new SCIFI station included in the tracking algorithm, the other without. This method enables studies of the reconstruction efficiency improvement with the spectrometer setup complemented with the Warsaw detector in a given configuration. The efficiency of the reconstruction is defined as a number of reconstructed tracks of a given type (*e.g.* muon tracks) divided by a number of reconstuctable tracks. The latter are all the tracks fulfilling the general requirement – they are within the acceptance of the first MicroMega station, that is at Z=142 cm they have -20 cm $< X <$ 20 cm and -20 cm $< Y <$ 20 cm. This requirement correspond to intrinsic cut included in the tracking algorithm in CORAL.

The first question addressed in the studies concerns the number of active layers in the planned SCIFI station. Two possible scenarios are considered: a single or a double layer station. The second question is the orientation of the layers. For a single layer station there are four possibilities: X, Y, U or V while for a double layer six configurations should be investigated: XY, XU, XV, YU, YV, UV. The third question is the position of the new detector in the spectrometer. From the discussion presented in Sec 2.11 it is obvious that this detector should be placed between SM1 and SM2 but it is not obvious, whether it should be closer to SM1 or to SM2.

2.11.2 Results on the Muon Reconstruction Efficiency

The Monte Carlo sample (I) was prepared in order to investigate the optimal number of layers and their orientations. The generation was done with a COMGEANT setup describing the 2004 COMPASS spectrometer complemented with four additional SCIFI layers (X, Y, U and V) at Z=1560 cm. Information from these layers could be taken into account in the CORAL reconstruction algorithm. Then a new single layer is simulated if one of these additional layers is included into reconstruction, and a double layer station, if two of them are included. The reconstruction efficiency of the scattered muons for each configuration (single or double layer with different orientations) was compared with the reconstruction efficiency for the same sample of events but with the reconstruction performed without the additional layers. The gain in efficiency for each studied configuration is presented in Tab. 2.5.

It is clear that for a single layer station the highest improvement is obtained for the layer oriented in the V direction. Also for the double layer station the highest improvement is for the detectors having one of the layers oriented in that direction. The orientation of the second layer plays a much smaller role, and the improvements for XV, YV and UV are almost the same.

Monte Carlo samples (II) and (III) were generated for the studies of the optimal location of the SCIFI station. In those generations there was only detector setup with two layers, U and V, used. The positions that were proposed for the detector, all of them between SM1 and SM2, are:

1. Z=975 cm;
2. Z=1355 cm;

---

[11] This decay chain is extensively studied in the analysis leading to the $\Delta G/G$ measurement with the open charm method.

Configuration	Gain [%]
single layer	
X	0.4
Y	0.5
U	0.4
V	1.2
double layer	
XY	1.1
XU	0.5
XV	1.5
YU	0.5
YV	1.4
UV	1.6

Table 2.5: The improvement in efficiency of the scattered muon reconstruction for a different number of layers and orientations of the Warsaw–SCIFI stations.

3. Z=1560 cm;
4. Z=1355 cm – reduced detector size;
5. Z=1560 cm – reduced detector size.

In the cases 1–3 the size of the SCIFI layers was 12.34 × 12.34 cm^2 (the standard size of the SCIFI detectors in COMPASS) and the number of wires for each layer was 176. For the cases 4 and 5 the size was 12.34 × 6.16 cm^2, where the first value is along the wire direction. The number of wires in these cases was reduced to 88. For each proposed configuration a reconstruction procedure with a SCIFI at a given position was performed. The results were compared with the efficiency for the reconstruction without the Warsaw detector. The gains in the muon reconstruction for each studied position are given in Tab. 2.6.

Configuration no.	Z position [cm]	Gain [%]
1.	975	1.8
2.	1355	1.8
3.	1560	1.7
4.	1355	2.1
5.	1550	1.6

Table 2.6: Improvement in the efficiency of the scattered muon reconstruction for different locations of the double layer Warsaw–SCIFI station.

The Monte Carlo sample (II) was used in cases 1 and 2, while the rest of the results were obtained for sample (III). Sample (II) was prepared after tuning the efficiencies of all the tracking detectors implemented in COMGEANT [103], while sample (III) was obtained for COMGEANT without tuning. As a consequence of tuning the overall performance of tracking increased by 2-3%. Therefore there is less space for improvement induced by the new Warsaw–SCIFI station and the efficiency increase for those cases is expected to be smaller. This explains why the gain for configuration 4 is larger than that for configuration 2, cf. Tab. 2.6.

The increase in the efficiency for the double layer station does not seem to depend significantly on its exact position between SM1 and SM2 (Tab. 2.6, rows 1–3). For detectors equipped with 88 wires only (rows 4 and 5) the gain is of the same order as for the nominally sized detector. This is expected, as the unbridged muon tracks are mostly located close to the beam axis and pass the area of the smaller SCIFI detector.

Numbers of hits generated for the muon tracks in the zone between SM1 and SM2, and in the zone between SM2 and second muon filter are shown in Fig. 2.9. The white histograms represent the generated and reconstructable scattered muon tracks; the yellow ones – the tracks reconstructed without hits from the Warsaw–SCIFI, and the red mark – the tracks reconstructed after adding information from this detector. The plots were obtained for the configuration no. 2 in Table 2.6. The gain in the number of the reconstructed scattered muon tracks is only for the tracks with less than 15 hits in the SM1–SM2 zone.

There were additional studies performed for a single SCIFI layer station located at Z=2130 cm, *i.e.* downstream SM2. This layer had a size of 12.34 × 12.34 cm^2 and the V orientation. The reconstruction efficiency with that configuration increased only by 0.03% which is in line with the predictions that the inefficiency of muon reconstruction is mainly due to the problems with tracking in the SM1–SM2 zone.

2.11.3 Increase in the Efficiency for Different y and Q^2 Regions

Warsaw–SCIFI detector improves tracking for muons scattered at small angles. This group of events is characterised with low Q^2. In Fig. 2.10 there are presented the distributions of y and Q^2 for events with a scattered muon reconstructed without (yellow) and with (red) Warsaw–SCIFI detector in configuration 2. Indeed there is the highest improvement in the reconstruction for interactions with $Q^2 < 0.1$ GeV^2 while the recovered events are more uniformly distributed in y. In Tab. 2.7 increase in the statistics for two different Q^2 cuts is shown.

Cut on Q^2	Gain [%]
no cut	1.8
<0.2 GeV^2	4.5
<0.1 GeV^2	5.4

Table 2.7: The gain in the muon reconstruction efficiency for different Q^2 regions.

2.11.4 Influence on the π and K Reconstruction

Apart from the improvement in the scattered muons reconstruction efficiency, the Warsaw–SCIFI station may in principle influence the reconstruction of other particles outgoing from the primary vertex. However this influence should be rather small, as the new detector is added far from the target and covers a very small scattering angle interval. The increase in the K and π reconstruction efficiency was checked with the open charm mesons Monte Carlo sample. The method employed was the same as the one for scattered muons. There was SCIFI configuration 2 used. It was found that the number of reconstructed K and π increased only by 0.04% and 0.03%, respectively.

2.11.5 Summary of the Warsaw–SCIFI Monte Carlo Studies

The tracks reconstruction in the COMPASS spectrometer with the Warsaw–SCIFI detector was studied using a Monte Carlo sample of open charm mesons. According to the expectations it was found that the highest increase in the efficiency was for tracks coming from the events with small Q^2 (< 0.1 GeV^2). For other particles the increase is marginal. The increase in the muon tracking efficiency does not depend significantly on the exact location of the detector in the SM1–SM2 zone. The analysis has shown that the smaller and cheaper station, equipped with only 88 instead of 176 wires in one plane, can also be used at a cost of loosing only a small fraction of recoverable events. It is important however to equip the station with two layers of the fibers, where one layer is in the V orientation.

The final decision on the Warsaw–SCIFI configuration was taken using the presented Monte Carlo studies. It was decided that the detector would be equipped with two active layers, U and V, but of reduced size. The station was constructed in 2005; in spring 2006 it was added to the spectrometer setup at the position of Z=1400 cm and took an active part in the 2006 data taking. When this thesis was completed a small part of the 2006 data was ready for the analysis. This allowed to check if the introduction of the Warsaw–SCIFI indeed increased the efficiency for muon reconstruction. The improvement that was found [104] is a 4.2% gain in the number of muons reconstructed in a sample of events with $Q^2 < 0.1$ GeV^2. This should be compared with 5.4% increase predicted. Both numbers are in a fair agreement, taking into account that the simulations were done for the 2004 setup, and in 2006 the spectrometer was equipped with a number of new detectors that also influenced the muon reconstruction efficiency.

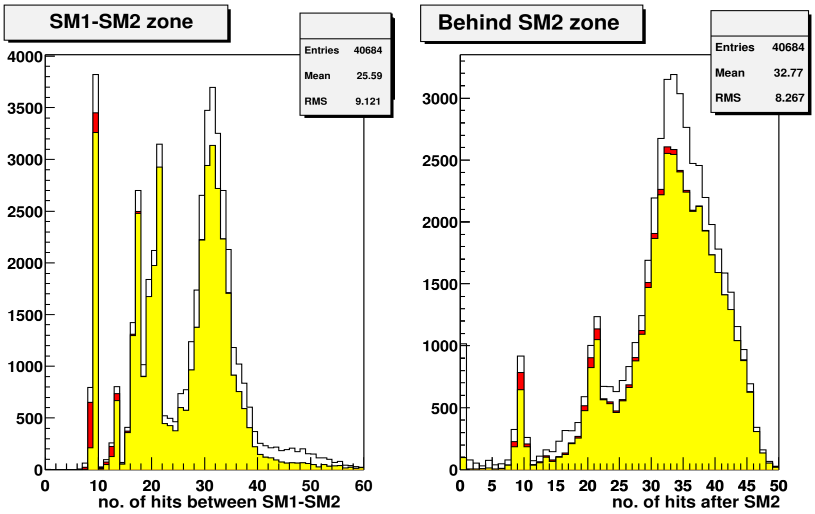

Figure 2.9: Number of hits in the zones SM1–SM2 (left) and SM2–muon filter (right) for all generated and reconstructable muon tracks (white), reconstructed without (yellow) and with (red) Warsaw–SCIFI station at Z=1355 cm and equipped with two active planes.

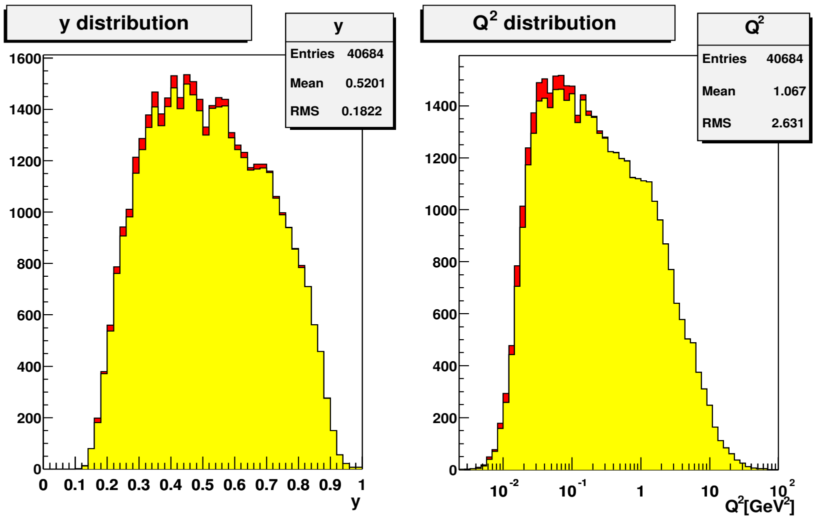

Figure 2.10: Distributions of y and Q^2 for events with reconstructed scattered muon without (yellow) and with (red) Warsaw–SCIFI station at Z=1355 cm and equipped with two active planes.

Chapter 3

Hadron Spectroscopy

Studies of the production asymmetries require strong confidence in the stability of the spectrometer. An efficient reconstruction of the rare D^0 mesons additionally demands a very good calibration for a precise particles momenta measurement. Both aims, the monitoring of the stability and the calibration, can be achieved studying the "V^0" vertices. A V^0 vertex is registered in a spectrometer when a neutral particle weakly decays into two charged particles of opposite signs. The decaying object is called a V^0 particle. There are two V^0 states that can be reconstructed in COMPASS, namely K^0 mesons[1] and Λ baryons.

Studies of the D^0 were preceded by the analysis of the data stability using V^0 vertices. Also the spectrometer efficiency check, and the evaluation of the COMGEANT detector simulation were performed using those secondary vertices [105]. These activities led to the optimisation of the cuts selecting V^0 particles. The cuts were then adopted to search for the open charm mesons decaying into $K^0\pi^+\pi^-$. It was shown that the signal in the $K^0\pi^+\pi^-$ indeed appears, however its strength and purity are poor [106] and thus it is presently not used for the gluon polarisation extraction. Due to a high number of V^0 particles reconstructed in the data, they can also be used to search for rare hadronic states decaying into V^0.

This chapter is dedicated to the studies of V^0 states. An invariant mass scan for resonances, that are predicted to appear in the K^0K^0 and $K^0\Lambda^0$ combinations, is described. Also an analysis leading to the reconstruction of the Ξ baryon and the studies of the $\Xi\pi^\pm$ and $\Xi(1530)^0\pi^\pm$ invariant masses are presented. Then, reconstruction of the triple strange Ω baryon and its excited states is outlined. Finally, the search for the double strange ϕ^{--} pentaquark is described. That last study performed on the 2002–2003 data has been already published [13]. Here the analysis includes also the 2004 data.

3.1 Motivation for Spectroscopy Studies

Several mass states predicted by the QPM have not been found until now. There is also a number of states which wait to be confirmed by new measurements. The most interesting of these are the states that might correspond to particles which have quark content other than two-quark mesons or three-quark baryons. This group includes glueballs, tetraquarks and pentaquarks, *i.e.* objects composed of gluons only, four and five quarks,

---

[1] The K^0 and $\overline{K}^0$ mesons are eigenstates of strong (production) interactions. Eigenstates of decays are K^0_S and K^0_L. In the COMPASS a V^0 is a K^0_S and is denoted simply by K^0.

respectively. Those states are predicted by the lattice QCD and by different effective theories applicable in the low energy regime.

3.1.1 The States in the K^0K^0 Mass Spectrum

There has been a number of states observed in the K^0K^0 mass spectrum. Among them there are a few produced copiously: $f_0(980)$, $a_0(980)$, $f_2(1270)$, $f_0(1370)$, and $f'(1525)$ [25]. Also other states with larger masses, above 1900 MeV, were reported. However most of them are weak and broad. This makes them difficult to be resolved from background. Three other states are of the special interest: $f_0(1500)$, $f_0(1710)$ and $f_J(2220)$, since they are considered to be the glueball candidates. From these, the first one, with the precision of the COMPASS muon data and with the studies limited to the invariant mass scan, cannot be separated from strong $f'(1525)$ resonance. The other two may be visible in COMPASS. In particular, the $f_J(2220)$ state is characterised by a small width, (23±8 MeV), and may be searched for in the COMPASS muon data. It is the only state reported above 1900 MeV having such a small width.

QCD calculations on the lattice predict the lightest glueball to appear in the mass range of 1400÷1800 MeV and have $J^{PC} = 0^{++}$. The lightest tensor glueball, $J^{PC} = 2^{++}$, is expected to have a mass of about 2200 MeV. The quantum numbers of these two glueball candidates are non-exotic and they mix with ordinary $q\overline{q}$ mesons having the same quantum numbers. For a detailed discussion of the lightest glueball states see [107].

The $f_0(1710)$ resonance is considered to be a state with a large glue component. It was observed in a number of experiments and produced in a glue-rich environment, that is in the radiative decays of the J/ψ meson and in the pomerons central interactions. For an overview of the experiments examining the $f_0(1710)$ state see [107]. More recently a report of a possible $f_0(1710)$ observation in the electron-proton interactions was published by the ZEUS Collaboration [108]. Also the L3 experiment at LEP reported an observation of a state centred at the mass of 1760 MeV [109]. However it is not certain if the state observed in L3 can be interpreted as $f_0(1710)$, since it was produced in the $\gamma\gamma$ interactions, where the formation of a glueball should be suppressed. According to PDG [25], the mass of the $f_0(1710)$ is (1718±6) MeV while its width is (137±8) MeV. These values were calculated after excluding a large number of dubious signals in a mass range of 1650–1800 MeV and of widths between 30 and 200 MeV. A lot of controversy on the origin of those signals still remains. Further studies of this mass range are needed. The only data coming from the μN scattering that can be used for such studies is the K^0K^0 pair production at COMPASS. Such analysis has never been done in a muon experiment before, and therefore it is presented here.

Another resonance, $f_J(2220)$, may be related to the lightest tensor glueball as its mass is close to the lattice QCD predictions for that state. However, there are also many doubts: the resonance width is much smaller than the predicted for a glueball, and there are indications that its $J^{PC} = 4^{++}$ [107].

Yet another relevant issue concerning the K^0K^0 mass spectrum is the status of the $f_0(980)$ and $a_0(980)$. Their masses are approximately equal to that of the $K\overline{K}$ threshold and a strong coupling to the $K\overline{K}$ channel suggests that these states are bound systems of two kaons. This awaits a final confirmation [25, 107].

3.1.2 The Non-Exotic States in the ΛK^0, $\Xi^-\pi^+$, $\Xi(1530)^0\pi^-$ Mass Spectra

Double strange baryons (quark content *uss* or *dss*) are called cascade hyperons and labelled Ξ. In comparison to the non-strange three quark states (N^* or Δ) and single strange states (Λ or Σ), the cascade hyperons spectrum is very poorly examined. Assuming the $SU(3)$ symmetry, the number of the Ξ mass states should be equal to the number of N^* and Δ together [110]. Presently there are 24 non-strange resonances measured accurately (status: 3 or 4 stars[2] in the PDG tables [25]) and about 20 that wait to be confirmed (1 or 2 stars in [25]). This should be compared to 11 Ξ states reported so far.

The ground state cascade hyperons, decaying through weak interactions, are denoted as Ξ^0 and Ξ^-. The mass of the first one is ~1315 MeV while the second is 6 MeV heavier. The Ξ^0 decays almost exclusively in the $\Lambda\pi^0$ channel. The reconstruction of the π^0 particle in COMPASS requires information from the electromagnetic calorimeter. During the preparation of this thesis, the calorimeter tuning for the π^0 reconstruction was still going on. Therefore studies of the decay channels with the neutral pion were not possible. The Ξ^- decays almost exclusively in the $\Lambda\pi^-$ mode. With a high Λ reconstruction efficiency in COMPASS, a signal from this resonance can easily be resolved from the background.

The $\Xi(1530)$ resonance is the first excited state of the cascade hyperons family. Both, charged and neutral $\Xi(1530)$ particles were observed and measured in a number of experiments. The neutral state has a mass ~1532 MeV and the charged one ~1535 MeV. Their widths are about 10 MeV. The $\Xi(1530)$ states decay into pairs of ground state cascade hyperons and pions. From these only the $\Xi^-\pi^+$ combination can be studied in COMPASS. This allows to reconstruct $\Xi(1530)^0$. The ground state and the $\Xi(1530)$ are the only cascade hyperon resonances that are of the four stars status in the PDG tables. Observations of other candidates for the excited cascade states are much less pronounced.

Apart from the above two well known states, there are four cascade hyperon resonances of the three stars status: $\Xi(1690)$, $\Xi(1820)$, $\Xi(1950)$, $\Xi(2030)$; two of the two stars: $\Xi(2250)$, $\Xi(2370)$; and three of the one star: $\Xi(1620)$, $\Xi(2120)$, $\Xi(2500)$[3]. Information on these states is collected in Tab. 3.1. Their properties, *e.g.* partial widths and decay channels, are poorly known. However all the determined widths are rather small. Assuming that all the signals listed in the PDG tables correspond to real resonances, there are still 33 cascade hyperons missing (44(N^*, Δ)–11(Ξ)). Therefore a simple scan of the invariant mass spectra in their apparent decay channels may turn out an important tool for the double strange baryons spectroscopy. COMPASS can exploit three different decay channels of possible resonances. These are: ΛK^0, $\Xi^-\pi^+$, $\Xi(1530)^0\pi^-$ and their charge conjugates.

---

[2] According to the PDG: **** - existence is certain and properties are at least fairly well explored; *** - existence ranges from very likely to certain, but further confirmation is desirable; ** - evidence for existence is only fair; * - evidence for existence is poor.

[3] During the workshop on the cascade baryon spectroscopy organised at the Jefferson Laboratory in December 2005 [110], it was proposed to reduce the number of stars for the $\Xi(1950)$ and $\Xi(2250)$ to two and one respectively. It was also suggested to drop the $\Xi(2120)$ from the tables.

State	Status	Mass [MeV]	Width [MeV]
$\Xi(1620)$	*	∼1620	?
$\Xi(1690)$	***	1690±10	<30
$\Xi(1820)$	***	1823±5	24^{+15}_{-10}
$\Xi(1950)$	***	1950±15	60^{+20}_{-20}
$\Xi(2030)$	***	2025±5	20^{+15}_{-5}
$\Xi(2120)$	*	∼2120	?
$\Xi(2250)$	**	∼2250	?
$\Xi(2370)$	**	∼2370	?
$\Xi(2500)$	*	∼2500	?

Table 3.1: Status, masses and widths of all cascade hyperon candidates, except for the four star $\Xi(1530)$ and the ground state, according to the PDG.

3.1.3 The $\phi(1860)$ Pentaquark State

According to the static quark model proposed in 1964 by Gell-Mann and Zweig and later developed by other theorists, the known spectrum of hadrons can be understood assuming that they are composed either of three valence quarks or of a pair of a valence quark and anti-quark. The much more complex picture of the internal hadron structure was introduced by the QCD. The hadrons are now considered as clusters of confined quarks and gluons. The confinement rule requires that hadrons are described by colour-singlet wave functions. Standard baryons and mesons obviously fulfil this requirement, but clearly, they are not the only possible colour-singlet states. An alternative is a pentaquark, combined of four quarks and one anti-quark. Baryon pentaquarks should form multiplets similarly to the standard three quark baryons. One of them, an anti-decuplet, is presented in Fig. 3.1.

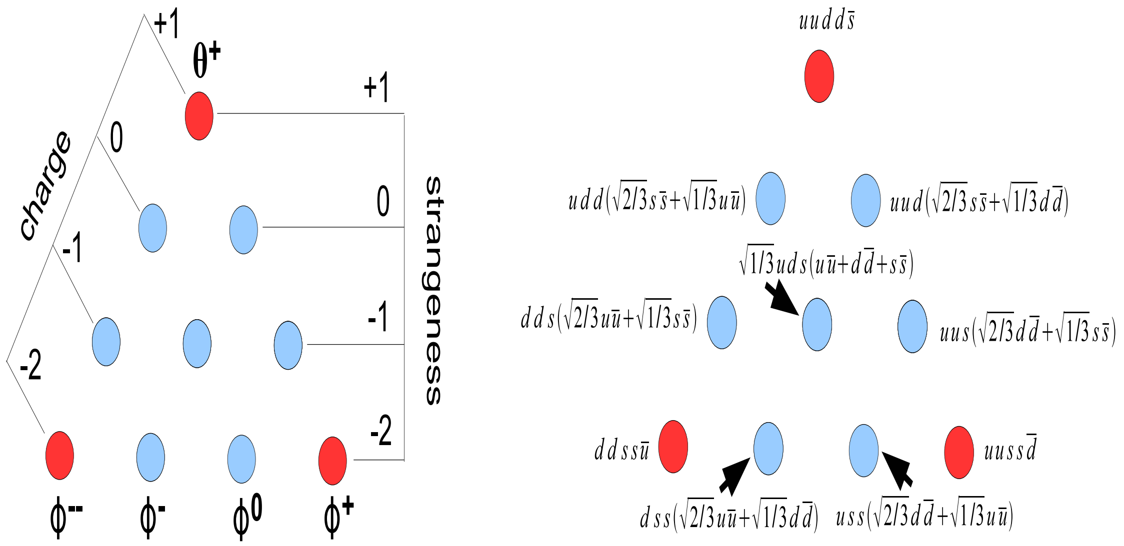

Figure 3.1: The pentaquark anti-decuplet. Left: the charge and the strangeness of particles; right: their quark content. Only the particles in the corners of the triangle (Θ, ϕ^{--}, ϕ^+) have exotic quantum numbers.

First theoretical estimates of the pentaquarks masses were derived from the bag model in the late seventies [111]. These predictions are ruled out by the present experimental data. In 1987 Praszałowicz [112] using the chiral soliton model of the nucleon postulated an existence of a pentaquark with a quark content $uudd\overline{s}$ and a mass of 1540 MeV. In 1997 Diakonov, Petrov and Polyakov [113] using a similar approach and identifying $N^*(1710)$ as one of the non-strange pentaquarks from the anti-decuplet were able to predict masses and widths of all particles from that decuplet. The lightest state, called Θ^+ ($uudd\overline{s}$), would have the mass of 1530 MeV and the width smaller than 15 MeV. In this picture the pentaquark states with one strange quark would have masses of 1890 MeV and the cascade pentaquarks, with two strange quarks, masses of 2070 MeV. It should be stressed that only three five-quark states, laying in the corners of the anti-decuplet triangle, Fig. 3.1, carry exotic quantum numbers. The other states contain a pair of a quark and an anti-quark of the same flavour and therefore the quantum numbers introduced by these two additional quarks cancel out.

Between 2001–2004 several experiments claimed to observe the lightest pentaquark state, $\Theta(1540)^+$. These reports were followed by a number of negative results coming from experiments which collected much higher statistics of events in the channels where the $\Theta(1540)^+$ resonance should be visible. This made the discovery of the lightest pentaquark state questionable [114]. At the moment the situation is still not clear and more experimental studies are needed. Information on the COMPASS search for the $\Theta(1540)^+$ state may be found in [105]. This study gave a negative result.

Reports on the observation of the $\Theta(1540)^+$ were followed by a claim of the discovery of another exotic pentaquark: ϕ^{--}. A candidate for ϕ^{--} state was observed by NA49 experiment at CERN in the proton-proton interactions at 160 GeV (~17 GeV in the centre-of-mass system). Peaks in $\Xi^-\pi^-$ and $\Xi^-\pi^+$ spectra were found at masses of about 1860 MeV [115]. The signal in the $\Xi^-\pi^-$ was interpreted as a ϕ^{--} while the one in $\Xi^-\pi^+$ as ϕ^0. An enhancement of events was also observed in the $\overline{\Xi}^+\pi^+$ channel, a possible $\overline{\phi}^{++}$ exotic state, while no evidence of a signal corresponding to $\overline{\phi}^0$ was found in $\overline{\Xi}^+\pi^-$ mass spectrum. After summing up events from all four channels the signal had a statistical significance of 5.6 σ and a width of 17 MeV, consistent with the detector resolution. The four mass spectra as well as their sum are presented in Fig. 3.2. In connection with the NA49 observation, a critical overview of analyses investigating the $\Xi^-\pi^+$ invariant mass distribution from previous experiments was performed [116]. Only the experiments of statistics comparable or greater than NA49 were examined. None of them reported a peak in the mass region around 1860 MeV.

Until summer 2005, when the negative COMPASS result based on the analysis of the 2002–2003 data was published [13], other nine experiments had presented their results of search for the $\phi(1860)$ state: ALEPH [117], BaBar [118], CDF [119], E690 [120], FOCUS [121], HERA-B [122], HERMES [123], WA-89 [124] and ZEUS [125]. Despite that in most of them the statistics was higher than that of NA49, all the results were negative. A graphical compilation of them is presented in Fig. 3.3. Circles and squares on the plot give the observed numbers of Ξ^- and $\Xi(1530)^0$ particles, respectively. The triangle indicates the yield of the $\phi(1860)^{--}$ observed by the NA49 Collaboration [115]. The arrows show the upper limits reported by various experiments. Some of the results were obtained at the 95% and some at the 99% confidence level. Also the widths of the examined mass windows around the 1860 MeV value varied as the experimental resolutions were different. Thus a direct comparison of the limits has to consider possible

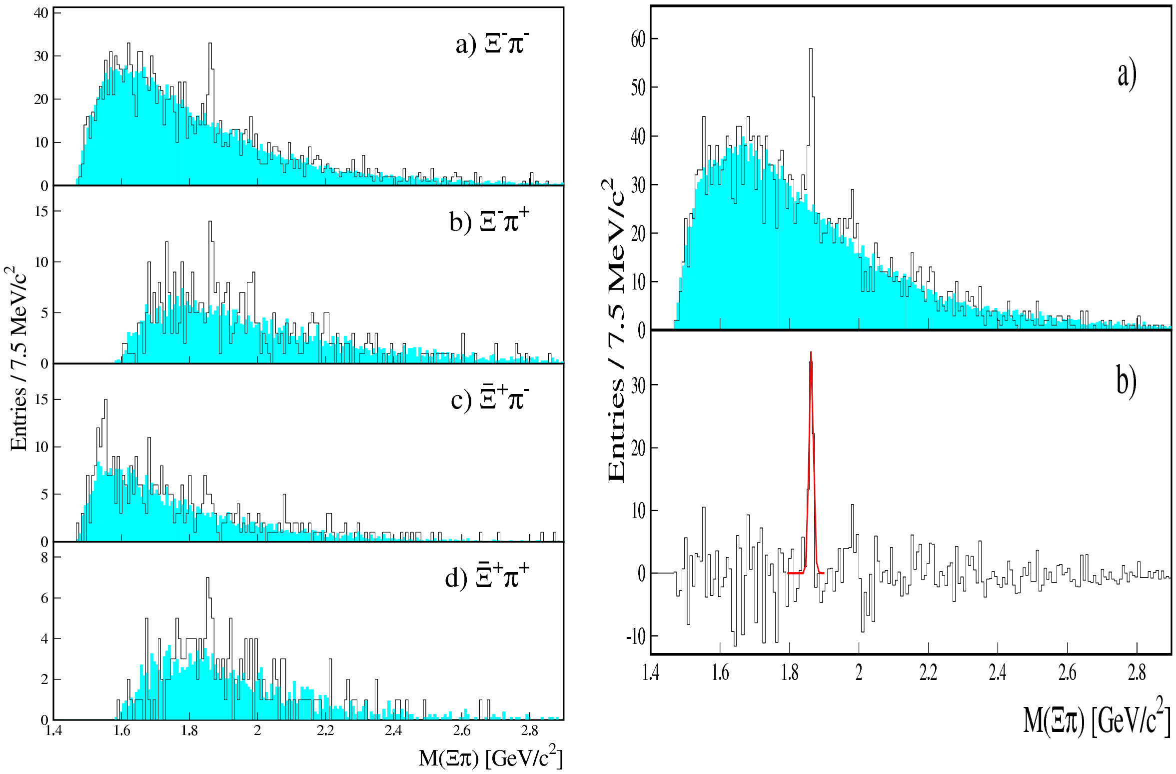

Figure 3.2: Left: invariant mass spectra in NA49 analysis for $\Xi^-\pi^-$ (a), $\Xi^-\pi^+$ (b), $\overline{\Xi}^+\pi^-$ (c) and $\overline{\Xi}^+\pi^+$ (d). The blue histograms are the mix-event normalised background. Right: the sum of the four mass spectra (a), background subtracted spectrum with the Gaussian function fitted (b). Plot taken from [115].

shifts by a factor of 2.5 between the results [126]. Assuming that the relative detection efficiency for various resonances was similar in all experiments and ignoring possible differences in the production mechanism of the pentaquarks, one can estimate the expected yields of $\phi(1860)^{--}$ by scaling the observed numbers of Ξ^- with the $\phi(1860)^{--}/\Xi^-$ ratio reported by NA49. The result is shown in Fig. 3.3 as a dashed line. The comparatively large $\phi(1860)^{--}/\Xi^-$ production ratio presented in [115] is not supported by other experiments. The existence of $\phi(1860)^{--}$ therefore seems to be doubtful. In this thesis the COMPASS analysis presented in [13] is updated to encompass the statistics of 2004 and a new CORAL reprocessing of part of 2002 and 2003 data where the track reconstruction efficiency was improved. The upper limits for the $\phi(1860)$ pentaquark state production at COMPASS are also recalculated here.

3.1.4 The Ω States

In the PDG tables [25] there are three candidates for the excited Ω states: Ω(2250), Ω(2380) and Ω(2470). For their characteristics see Tab. 3.2. Despite the two and three star status ascribed to them, evidence for their existence is not strong. The Ω(2250) was observed in two experiments while the remaining two only by one experiment. An independent confirmation of the existence of these baryons is needed. In the thesis the $\Xi(1530)^0K^-$ invariant mass spectrum obtained from the COMPASS data is presented. It may reveal the excited Ω baryons.

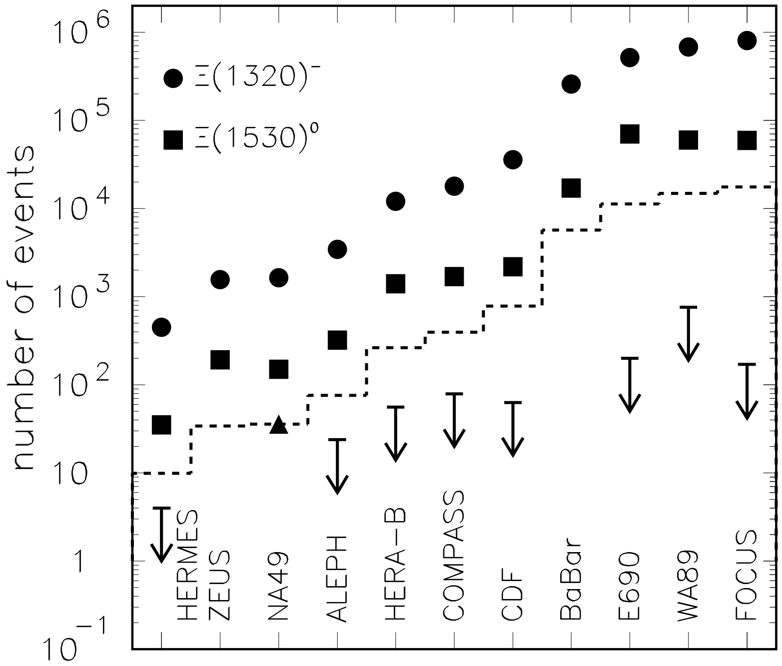

Figure 3.3: The results of the $\phi(1860)^{--}$ pentaquark search in different experiments. The COMPASS result presented here was obtained from the 2002-2003 data [13]. See text for details.

State	Status	Mass [MeV]	Width [MeV]
$\Omega(2250)$	***	2250±9	55±18
$\Omega(2380)$	**	≈2380	?
$\Omega(2470)$	**	2474±12	72±33

Table 3.2: Status, masses and the widths of the candidates for the excited Ω baryons according to PDG [25].

3.2 Data Selection

All data taken in 2002, 2003 and 2004 are included in the analysis presented in this chapter. It is assumed that any possible polarisation dependence would average out. Only events with the primary vertex reconstructed and containing both the incoming and the scattered μ^+ are studied. A cut on the primary interaction point to be within the geometrical target limits is imposed: $Z_{\text{prim}} \in [-100, -40] \cup [-30, 30]$ cm and $\sqrt{X^2_{\text{prim}} + Y^2_{\text{prim}}} < 1.5$ cm. All positive particles with momenta larger than 140 GeV are assumed to be misidentified beam muons and removed from the analysed sample.

3.3 K^0, Λ and $\overline{\Lambda}$ Selection

Reconstruction of the K^0, Λ and $\overline{\Lambda}$ particles is performed through their V^0 decay vertices with two outgoing particles of opposite charges:

$$K^0 \to \pi^+\pi^- \qquad \Lambda \to p\pi^- \qquad \overline{\Lambda} \to \overline{p}\pi^+ \tag{3.1}$$

These V^0 vertices are well separated from the primary interaction points due to the long life-time of the above particles. In order to perform a safe charge identification and a momentum measurement, tracks corresponding to both particles outgoing from a V^0 vertex should have hits recorded at the tracking detectors located at $Z > 360$ cm, that is after SM1. With this cut all tracks reconstructed only in the fringe field of SM1 are rejected. To reduce the background originating mainly from the V^0 vertices reconstructed inside the target volume and endowed with a large reconstruction uncertainty due to the multiple Coulomb scattering, a demand that a V^0 vertex has $Z >$30 cm and is downstream the target cells is imposed. Vertices mimicking a V^0 and corresponding to the photon conversions, $\gamma \to e^+e^-$, are removed by the requirement that the transverse momenta of the decay products with respect to the flight direction of the mother particle are larger than 23 MeV. The quality of the V^0 reconstruction is described by the χ^2. All vertices with $\chi^2 >$4 are discarded. Finally the mass of the mother particle is reconstructed from the decay products. Three different hypotheses are assumed: K^0, Λ or $\overline{\Lambda}$. For the K^0 pion masses are assigned to both tracks outgoing the V^0 vertex. For the Λ a positive particle is assigned a proton mass and a negative a pion mass. For $\overline{\Lambda}$ the assignment is opposite. Then the differences:

$$\Delta M_{K^0} = |M(\pi^+\pi^-) - M_{K^0}| \tag{3.2}$$

$$\Delta M_{\Lambda} = |M(p\pi^-) - M_{\Lambda}| \tag{3.3}$$

$$\Delta M_{\overline{\Lambda}} = |M(\pi^+\overline{p}) - M_{\Lambda}| \tag{3.4}$$

are computed where $M(ab)$ is an effective mass of a and b and M_X is a PDG mass of particle X [25]. The K^0, Λ and $\overline{\Lambda}$ samples are defined through:

$$\Delta M_{K^0} < \Delta M_{\Lambda} \qquad \Delta M_{K^0} < \Delta M_{\overline{\Lambda}} \tag{3.5}$$

$$\Delta M_{\Lambda} < \Delta M_{K^0} \qquad \Delta M_{\Lambda} < \Delta M_{\overline{\Lambda}} \tag{3.6}$$

$$\Delta M_{\overline{\Lambda}} < \Delta M_{K^0} \qquad \Delta M_{\overline{\Lambda}} < \Delta M_{\Lambda} \tag{3.7}$$

An additional cut: $|\cos\theta^*| < 0.9$, with θ^* being the V^0 centre-of-mass emission angle of the negative particle with respect to the $\Lambda(\overline{\Lambda})$ flight direction is imposed for Λ and $\overline{\Lambda}$. For a detailed discussion of the cuts optimisation for the K^0 and Λ selection see [105].

Mass spectra of K^0, Λ and $\overline{\Lambda}$ candidates are presented in Fig. 3.4. They are fitted with a sum of two Gaussian functions for each peak and a straight line for the background. The number of particles inside the peaks obtained with fits is shown[4] in Tab. 3.3. In Tab. 3.4 these numbers are normalised to the numbers for 2002. From the tables one can see that the improvement of the statistics in each year for different hadrons is roughly the same.

For the studies of states decaying into V^0V^0 hadrons, the K^0 candidates with masses

---

[4] A possible modification of the background shape under the peaks due to the selection cuts imposed is neglected. This effect can change the numbers of V^0 particles at most by a few percent.

inside the 8 MeV windows around the centre of each peak are taken. For the Λ and $\overline{\Lambda}$ candidates this cut is 6.8 MeV. These windows correspond to about 2 σ of a Gaussian function having a smaller width.

The above way of the V^0 reconstruction does not use the information from the RICH. Particle identification may improve the purity of the sample albeit significantly reducing the statistics. It was thus decided to keep the statistics high rather than to increase the signal-over-background ratio, which is already very high.

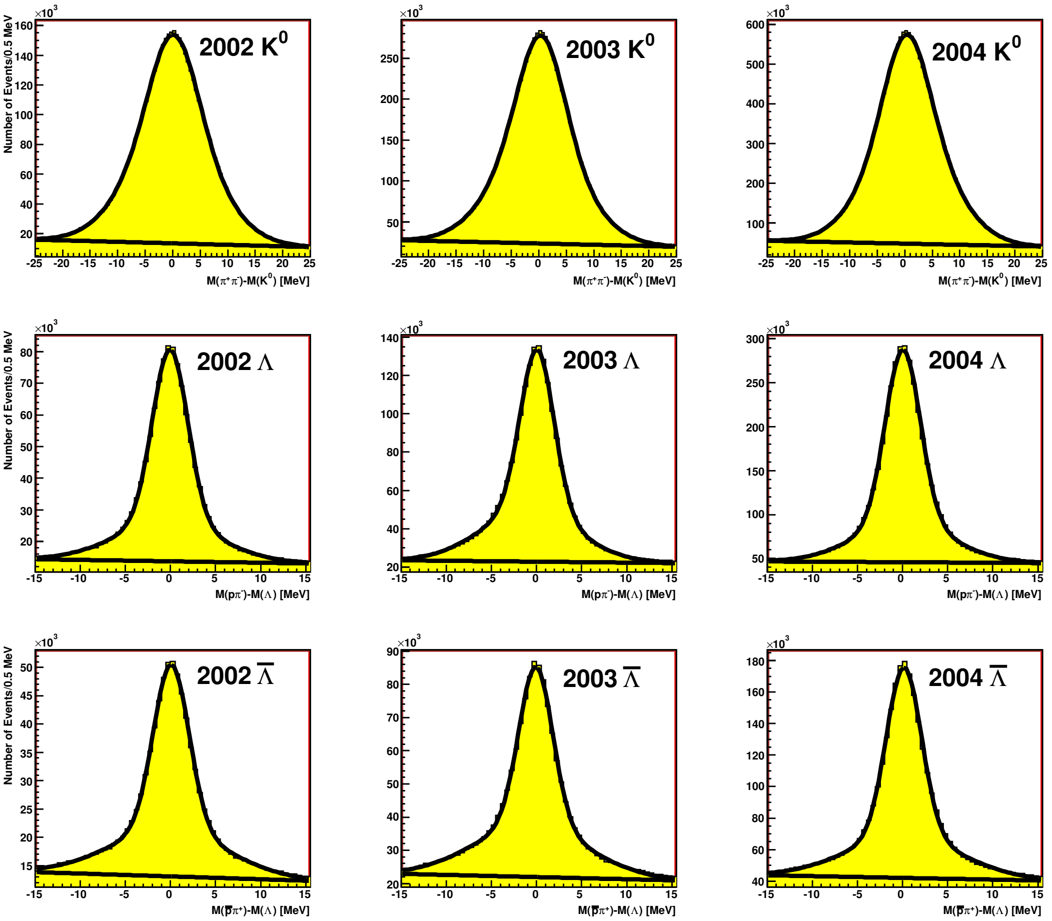

Figure 3.4: Rows from top to bottom: ΔM_x distributions for $X = K^0$, Λ, $\overline{\Lambda}$. Columns from left to right: data from 2002, 2003 and 2004. Straight lines correspond to the background.

	2002	2003	2004
K^0	4 295 000	7 480 000	15 292 000
Λ	881 000	1 484 000	3 086 000
$\overline{\Lambda}$	545 000	923 000	1 850 000

Table 3.3: Number of the V^0 particles reconstructed in a given year.

	2002	2003	2004
K^0/K^0_{2002}	1.0	1.7	3.6
Λ/Λ_{2002}	1.0	1.7	3.5
$\overline{\Lambda}/\overline{\Lambda}_{2002}$	1.0	1.7	3.4

Table 3.4: Number of the V^0 particles reconstructed in a given year normalised to the 2002 statistics.

3.4 The V^0V^0 Pairs

The total statistics of the K^0 mesons in the 2002–2004 data is over 27 million while the number of Λ and $\overline{\Lambda}$ baryons reaches almost 9 million. Such a large number of the V^0 hadrons permits to study the decay chains in which they are produced. These studies are restricted to the search for the neutral particles decaying into pairs of the V^0 mesons:

$$X^0 \to K^0K^0 \qquad Y^0 \to K^0\Lambda \qquad \overline{Y}^0 \to K^0\overline{\Lambda} \tag{3.8}$$

Combinations where a charged particle decays into a V^0 particle and into charged K or π are much more difficult to study. The reason is that the reconstruction of those states requires a precise reconstruction of momentum of charged K or π. This is difficult since the experimental setup does not include a vertex detector and since the momentum of a charged meson can be changed due to a strong multiple Coulomb scattering inside the target volume.

3.4.1 The K^0K^0 Spectrum

Selection of the K^0 sample was discussed in Sec. 3.3. For the K^0K^0 spectrum studies the events containing two K^0 candidates are chosen. It is checked that both particles are reconstructed using two independent pairs of tracks of the pion candidates. Then the both V^0 states are assigned the PDG mass of the kaon. Finally the invariant mass of the K^0K^0 pair is calculated, cf. Fig. 3.5.

In the 2002–2004 data, 220 000 events containing two kaons were found. This number should be compared to 2553 pairs reported in the ZEUS analysis [108]. In the mass spectrum an enhancement of events is seen close to the threshold for the K^0K^0 production. This corresponds to the expected $f_0(980)$ and $a_0(980)$ resonances that are suspected the KK bound states. The mass spectrum between 1100 and 1400 MeV is dominated by the wide $f_2(1270)$ and $f_0(1370)$ mesons. The former state has a PDG width of 185 MeV while the width of the latter is between 200 and 500 MeV. In the COMPASS data $f_2(1270)$ had been previously seen in the $\pi^+\pi^-$ decay mode for which its branching ratio is much larger, cf. [105].

A broad maximum at about 1530 MeV corresponds to the $f'(1525)$ resonance. The mass spectrum above 1370 MeV is fitted with a sum of a Gaussian plus an exponential which describe the signal and the background respectively. The values of parameters returned by the fitting procedure are (1532±4) MeV for the centre of the Gaussian and (91±11) MeV for its width, in qualitative agreement with the PDG values: (1525±5) MeV and (73±6) MeV for the mass and the width of $f'(1525)$ resonance.

No enhancements are visible in the spectrum above 1600 MeV even if between 1800 and 2400 MeV certain resonances were claimed to exist.

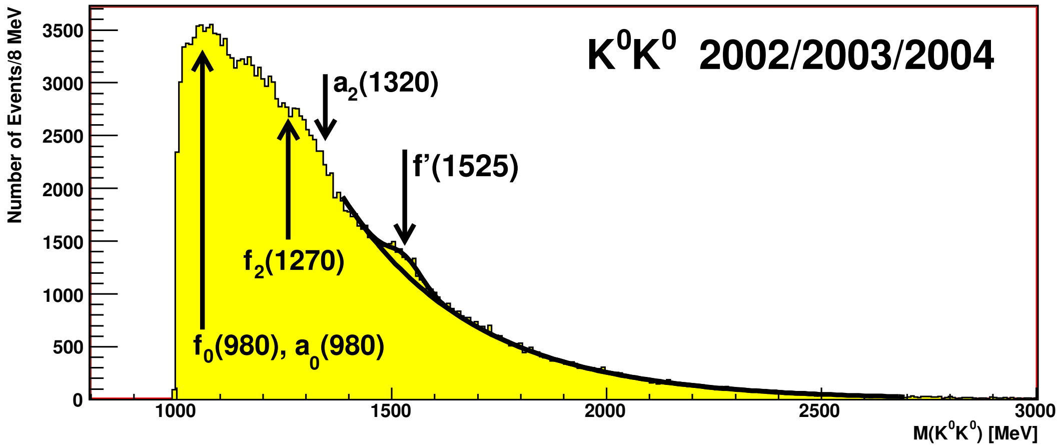

Figure 3.5: K^0K^0 invariant mass spectrum.

Studies of mesons that decay into the K^0K^0 pairs are complicated by the presence of a strong background. The background appears mainly due to the K^0K^0 pairs that do not come from the decays of the mesons produced in the fragmentation of the struck quark but originate from the target remnants. This background can be suppressed by a cut on the x_F variable. The x_F is defined as:

$$x_F = \frac{p_{Z'}}{p_{Z'\,\max}} \approx \frac{2p_{Z'}^{CMS}}{\sqrt{s}} \tag{3.9}$$

where the Z' axis is along the virtual photon momentum vector, $p_{Z'}$ is the momentum of the K^0K^0 system along Z', $p_{Z'\,\max}$ is a maximum allowed $p_{Z'}$ for a given interaction. The *CMS* is the photon-nucleon centre-of-mass while $\sqrt{s}$ is the photon-nucleon invariant mass. The cut on x_F was optimised requiring the strongest enhancement of the well visible $f'(1525)$ state. Finally the cut $x_F > 0.7$ was chosen. The invariant mass spectrum with this cut is plotted in Fig. 3.6. Only 22 800 K^0K^0 pairs survive that cut but all the signals seen without the cut (Fig. 3.5), are now much more pronounced. Furthermore a new bump appeared in a mass range around 1700 MeV which may correspond to $f_0(1710)$. However the significance of the peak is small. Searches for signals at M(K^0K^0)>2000 MeV may only be done after substantial increase of statistics. The improvement is expected to come with the 2006 data.

3.4.2 The ΛK^0 and $\overline{\Lambda}K^0$ Spectra

For the ΛK^0 and $\overline{\Lambda}K^0$ spectra one V^0 should come from the K^0 meson and the other from Λ or $\overline{\Lambda}$. It is checked that both V^0 particles were reconstructed using two independent pairs of charged tracks. The V^0 states are then assigned the PDG masses of the kaon and lambda respectively. Finally the invariant masses of the ΛK^0 and $\overline{\Lambda}K^0$ pairs are calculated, cf. Fig. 3.7. The sum for both channels is also presented at that figure. Masses at which the three stars Ξ states: $\Xi(1690)$, $\Xi(1820)$, $\Xi(1950)$, $\Xi(2030)$ should be visible are marked with arrows. The first of these, $\Xi(1690)$, is located in the mass region where the background is raising very steep probably masking it. Other states are not visible either, not even after the x_F cut. Data from 2006, doubling the 2002–2004 statistics, may help to clarify this problem.

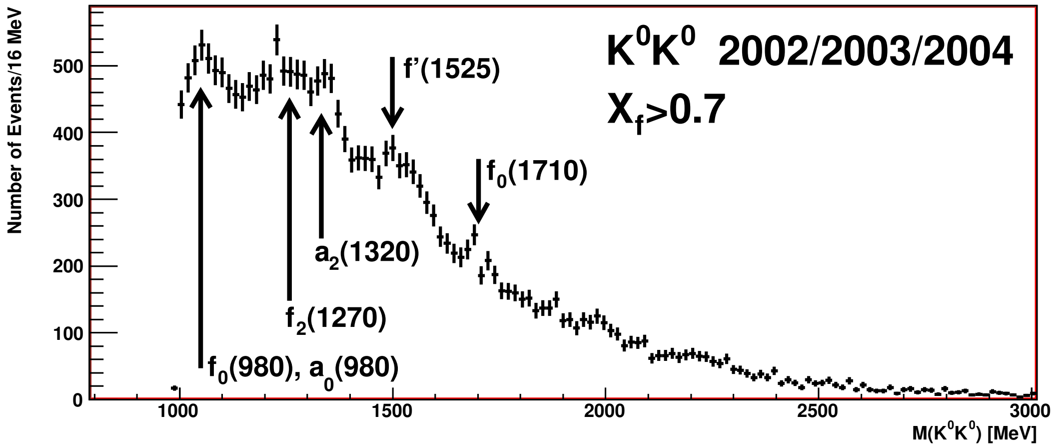

Figure 3.6: K^0K^0 invariant mass spectrum with $x_F > 0.7$. Errors are statistical.

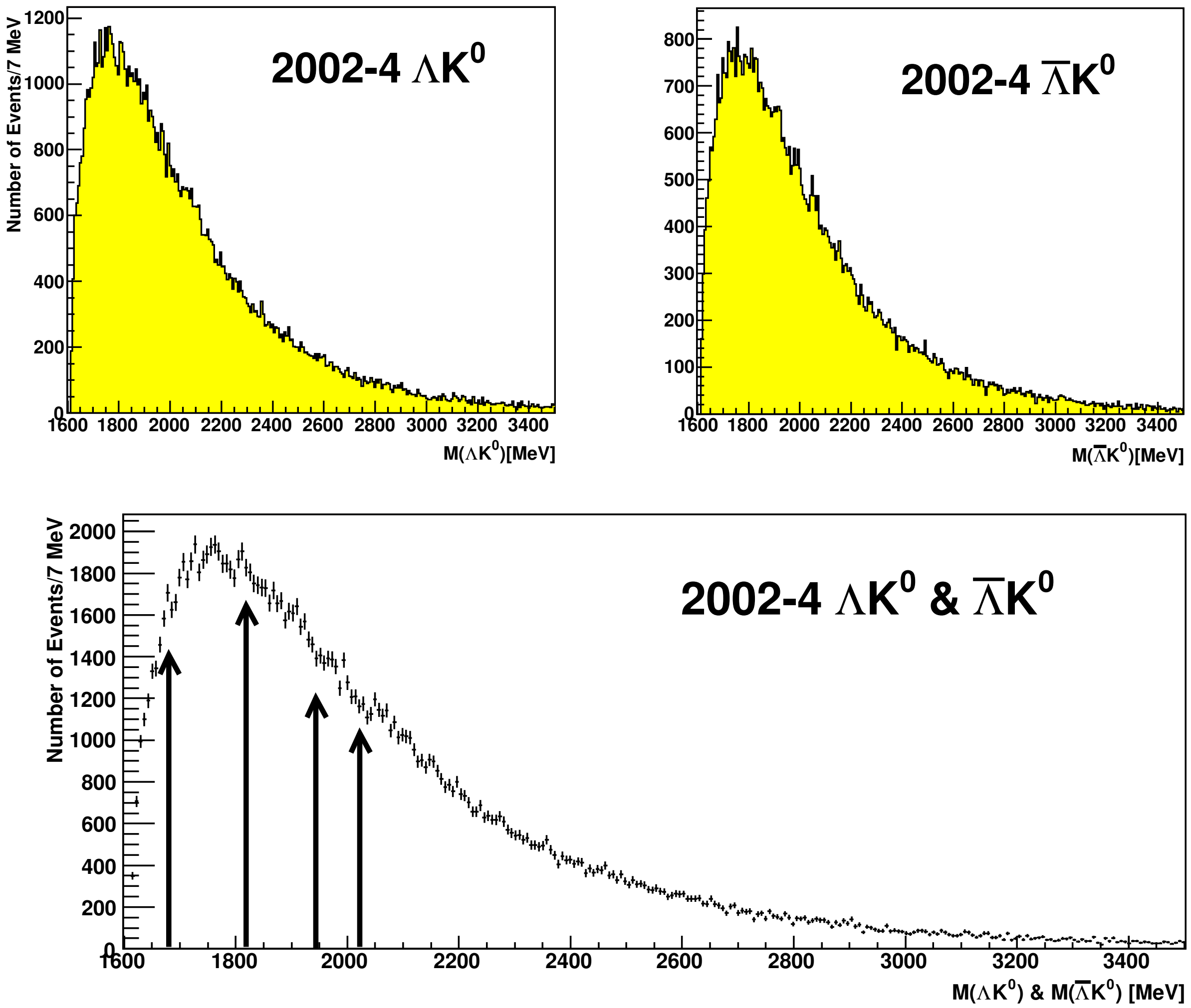

Figure 3.7: Top left: ΛK^0 spectrum from 2002/2003/2004 COMPASS data. Top right: $\overline{\Lambda}K^0$ spectrum from 2002/2003/2004 COMPASS data. Bottom: the sum of both channels. Errors are statistical, arrows mark positions of the expected $\Xi(1690)$, $\Xi(1820)$, $\Xi(1950)$, $\Xi(2030)$ states.

3.5 Ξ^- and $\overline{\Xi}^+$ Selection

In order to obtain the $\Xi^-(\overline{\Xi}^+)$ sample the $\Lambda(\overline{\Lambda})$ candidates assigned with a nominal mass of this particle are paired in turn with all the candidates for pions coming from Ξ decay. They are denoted as π_Ξ and defined as tracks not used in the $\Lambda(\overline{\Lambda})$ reconstruction, having an appropriate charge (negative for Ξ^- and positive for $\overline{\Xi}^+$) and not attached to the primary vertex[5] by the CORAL reconstruction procedure. The distance of the closest approach between the reconstructed $\Lambda(\overline{\Lambda})$ and π_Ξ tracks is calculated. The pairs for which it is greater than 0.8 cm are discarded. Additionally the Z-coordinate of the point at the π_Ξ track for which the distance between the tracks is the smallest has to be downstream the primary and upstream the $\Lambda(\overline{\Lambda})$ decay vertex, see Fig. 3.8. The π_Ξ are assigned a pion mass and $\Xi^-(\overline{\Xi}^+)$ state candidates are reconstructed, cf. Fig. 3.9. The invariant mass spectra are then fitted with a sum of two Gaussians for each peak and a straight line for the background. The numbers of the reconstructed $\Xi^-(\overline{\Xi}^+)$ cascade hyperons, obtained from the fits, are collected in Tab. 3.5. In Tab. 3.6 these numbers are normalised to the numbers coming from 2002. The ratios agree well with values from Tab. 3.4. For the further analysis cascade hyperons in the ±10 MeV windows around the centre of each peak are taken.

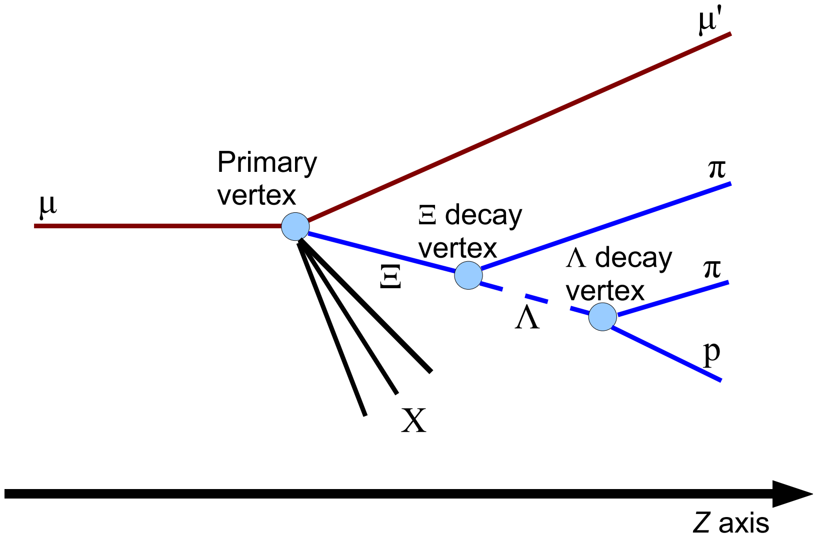

Figure 3.8: Sketch of Ξ^- decay.

	2002	2003	2004
Ξ^-	9 900	16 600	35 300
$\overline{\Xi}^+$	5 700	10 100	20 700

Table 3.5: Number of the Ξ^- and $\overline{\Xi}^+$ hyperons reconstructed in a different data samples.

---

[5] The mean life-time of Ξ^- is $1.6{\cdot}10^{-10}$ s. Thus its decay vertex can be easily distinguished from the primary one.

	2002	2003	2004
Ξ^-/Ξ^-_{2002}	1.0	1.7	3.6
$\overline{\Xi}^+/\overline{\Xi}^+_{2002}$	1.0	1.8	3.6

Table 3.6: Number of the Ξ^- and $\overline{\Xi}^+$ hyperons reconstructed in a different data samples normalised to 2002 statistics.

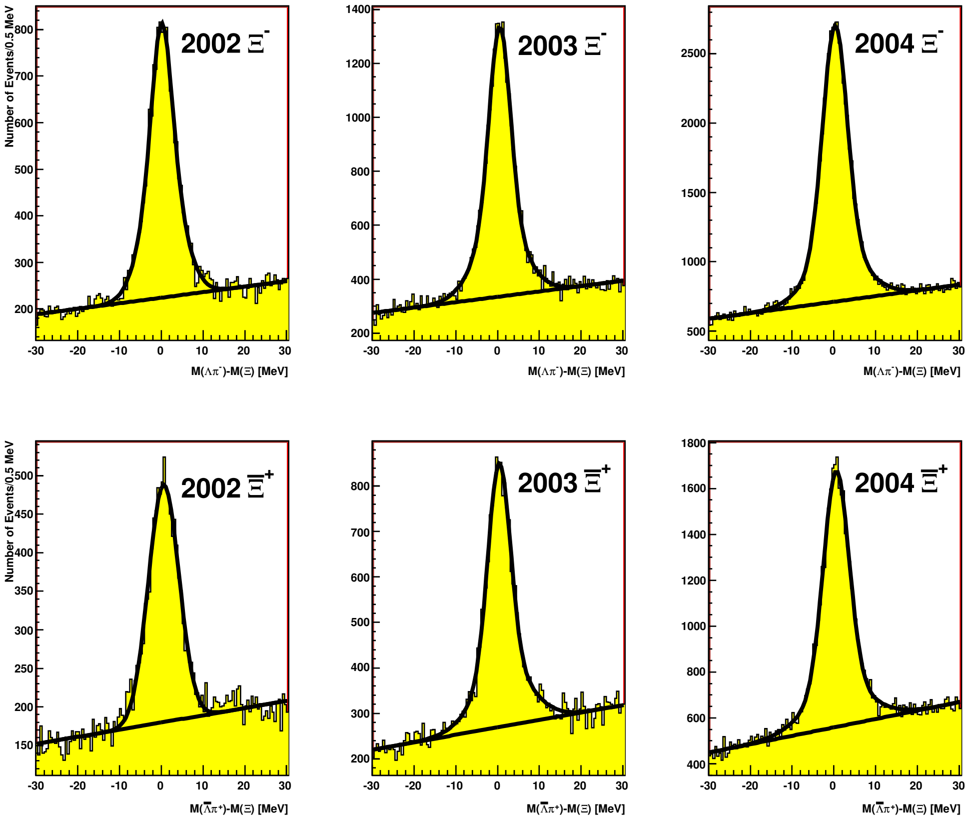

Figure 3.9: Top row: Ξ^- hyperons, bottom row: $\overline{\Xi}^+$ hyperons. Columns from left to right: data from 2002, 2003 and 2004. Curves are the fitted signal and background.

3.6 The $\Xi^-\pi^\pm$ and $\overline{\Xi}^+\pi^\mp$ Spectra

To obtain the invariant masses of the $\Xi^-\pi^-$, $\Xi^-\pi^+$, $\overline{\Xi}^+\pi^+$ and $\overline{\Xi}^+\pi^-$ systems, particles attached to the primary vertex and not used in the previous steps of the analysis leading to the Ξ^- ($\overline{\Xi}^+$) reconstruction are assigned a pion mass and paired with a Ξ^-($\overline{\Xi}^+$) candidate. The invariant masses of the combinations are calculated assuming the nominal mass for the Ξ^-($\overline{\Xi}^+$).

In the two charge combinations, $\Xi^-\pi^+$ and $\overline{\Xi}^+\pi^-$, the well known $\Xi(1530)^0$ and $\overline{\Xi}(1530)^0$ resonances are clearly visible, Fig 3.10. These states decay via the strong interactions and thus their decay points coincide with the primary interaction vertex. The signals are fitted with the Voigtian function (a convolution of the Gaussian and the Lorentzian functions) and the background is parameterised as $(m-p_0)^{p_1}\cdot\exp(-p_2\cdot m - p_3\cdot m^2)$. The numbers of $\Xi(1530)^0$ and $\overline{\Xi}(1530)^0$ returned by the fit are 4940±180 and 3000±130 respectively.

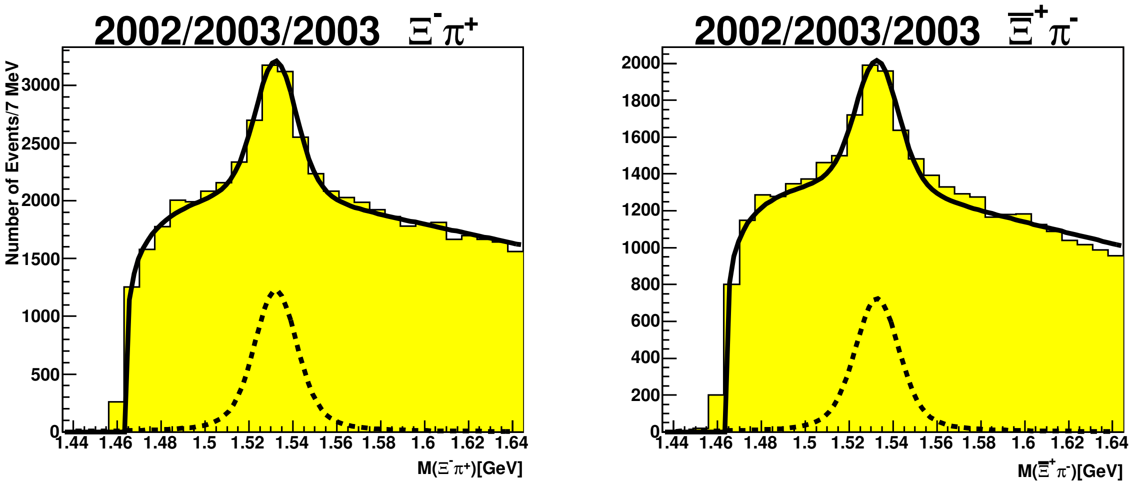

Figure 3.10: The $\Xi^-\pi^+$ and $\overline{\Xi}^+\pi^-$ mass spectra with $\Xi(1530)^0$ and $\overline{\Xi}(1530)^0$ well visible. Curves are the fit, see text.

Invariant mass spectra of the four different charge systems are shown in Fig. 3.11. The arrows indicate the positions where the NA49 signal of ϕ^{--} was seen. No signal is observed in COMPASS. The upper limit for the ϕ^{--} production is obtained as follows. The estimation of the background is done via the exponential fit to the mass spectrum excluding the region from 1825 MeV to 1895 MeV. Then three intervals, each 28 MeV wide, staggered by 14 MeV, with the central interval centred at 1860 MeV are investigated. The numbers of entries in these intervals are n_1, n_2, n_3 while the estimated background for each interval is b_1, b_2, b_3. The upper limit of a possible excess of events can be thus calculated as $\max_{i=1,2,3}(3\sqrt{b_i} + \max(0, n_i - b_i))$. This procedure gives the upper limit of 195 for ϕ^{--} state and 170 for $\overline{\phi}^{++}$ at the 99% confidence level. The estimate of the number of ϕ^{--} that should be observed in COMPASS is 1360 if the ϕ^{--}/Ξ^- ratio reported by NA49 is taken.

No other states except the $\Xi(1530)^0$ cascade hyperon are found on the plots.

3.7 The $\Xi(1530)^0\pi^-$ Spectra

A large number of the reconstructed $\Xi(1530)^0$ and $\overline{\Xi}(1530)^0$ particles allows a search for the resonances that decay into the $\Xi(1530)^0$. For instance a channel in which excited cascade hyperon is accompanied by a charged pion can be studied. In these studies heavier excited cascade hyperons may be revealed, cf. Sec. 3.1.2. A full decay chain looks like:

$$\Xi^{*-} \to \Xi(1530)^0\pi^- \to \Xi^-\pi^+\pi^- \to \Lambda\pi^-\pi^+\pi^- \to p\pi^-\pi^-\pi^+\pi^- \tag{3.10}$$

$$\overline{\Xi}^{*+} \to \overline{\Xi}(1530)^0\pi^+ \to \overline{\Xi}^+\pi^-\pi^+ \to \overline{\Lambda}\pi^+\pi^-\pi^+ \to \overline{p}\pi^+\pi^+\pi^-\pi^+ \tag{3.11}$$

A method for reconstructing the $\Xi(1530)^0$ ($\overline{\Xi}(1530)^0$) was discussed in the previous section. For this part of the analysis the $\Xi(1530)^0$ ($\overline{\Xi}(1530)^0$) candidates having an invariant mass in the ±17 MeV window around the 1530 MeV value are taken. All charged particles outgoing from the primary vertex that were not used for the $\Xi(1530)^0$

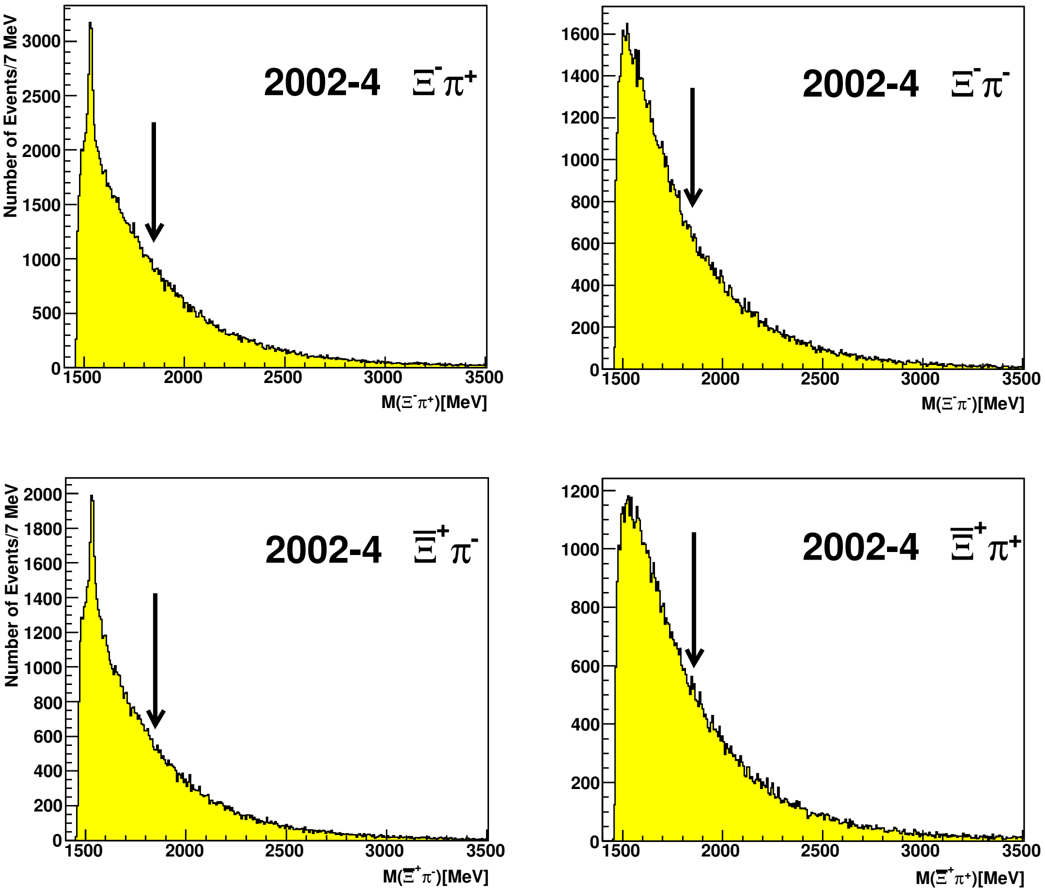

Figure 3.11: Mass spectra of $\Xi^-\pi^+$, $\Xi^-\pi^-$, $\overline{\Xi}^+\pi^-$ and $\overline{\Xi}^+\pi^+$ combinations. The arrows indicate positions where the pentaquark signal was reported by NA49 (cf. Fig. 3.2).

($\overline{\Xi}(1530)^0$) reconstruction are assigned a pion mass and paired consecutively with the $\Xi(1530)^0$ ($\overline{\Xi}(1530)^0$) candidate. The obtained spectra of $\Xi(1530)^0\pi^-$ and $\overline{\Xi}(1530)^0\pi^+$ are shown in Fig. 3.12. No indication of any signal is found there.

3.8 The Ω Baryon

The Ω baryon decays similarly to the Ξ^- cascade hyperon: into a Λ and a charged particle, and forming a secondary vertex. Contrary to the Ξ^- decay the charged particle is not a pion but a kaon. An efficient selection of the charged kaons requires the RICH detector. The RICH cuts defining the kaons sample are the following:

- $\chi^2_{\rm K} < \chi^2_\pi$
- $\chi^2_{\rm K} < 5$

The same cuts are used for the data coming from different data taking periods. No likelihood method is applied. Other selection requirements are identical with those used for the pion selection for the Ξ^- reconstruction. The same concerns the selection of the Λ ($\overline{\Lambda}$) sample. The ΛK^- and $\overline{\Lambda}K^+$ spectra are shown in Fig. 3.13. The Ω signal is visible. Also in the mass region of $\overline{\Omega}$ an enhancement of events indicates the presence of $\overline{\Omega}$.

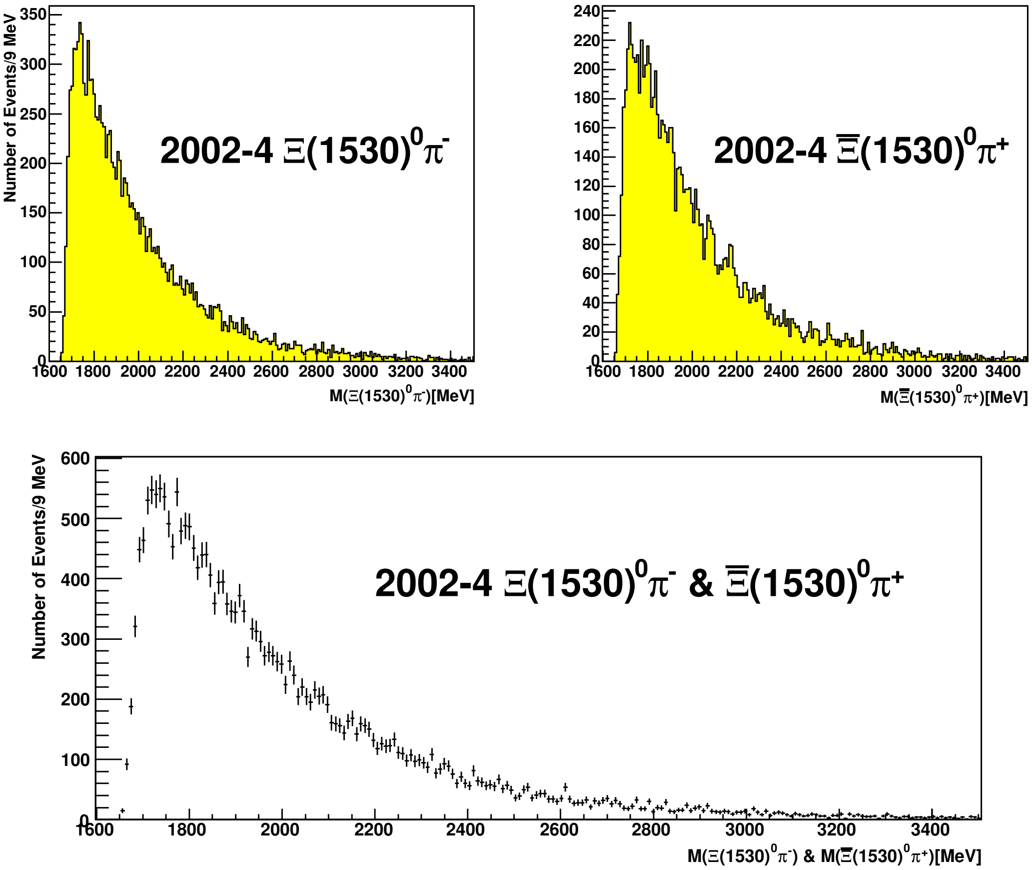

Figure 3.12: Top left: $\Xi(1530)^0\pi^-$ spectrum from 2002/2003/2004 COMPASS data. Top right: $\overline{\Xi}(1530)^0\pi^+$ spectrum from 2002/2003/2004 COMPASS data. Bottom: the sum of both channels; errors are statistical.

The excited Ω states can be looked for in the $\Xi(1530)^0K^-$ and $\overline{\Xi}(1530)^0K^+$ combinations. Selection of the $\Xi(1530)^0$ ($\overline{\Xi}(1530)^0$) was described in Sec. 3.7. For the kaons the RICH identification is required. It is the same as discussed above for the Ω ground state reconstruction. In Fig. 3.14 the sum of both channels, $\Xi(1530)^0K^-$ and $\overline{\Xi}(1530)^0K^+$, is presented. Also the sum of the charge conjugated channels, $\Xi(1530)^0K^+$ and $\overline{\Xi}(1530)^0K^-$, where the peaks are not expected is shown. In the first plot a sharp spike at the mass of around 2250 MeV is observed, absent in the second one. A sum of a Gaussian and a second degree polynomial was fitted to the mass range 2150–2700 MeV. The fit returned (2270±7) MeV and (43±28) MeV for the centre and the width of the Gaussian function. These results are compatible with the PDG values for the $\Omega(2250)$ state: (2250±9) MeV and (55±18) MeV respectively. The number of the signal events in the two most occupied bins is S=17. The background under the peak comprises B=31 events. These numbers can be translated into the statistical significance of the peak using the following formula:

$$\sigma = \frac{S}{\sqrt{B}} \tag{3.12}$$

According to that equation the significance of the signal is 3.1 σ. A more conservative approximation of a peak significance is given by an expression:

$$\sigma = \frac{S}{\sqrt{S+B}} \tag{3.13}$$

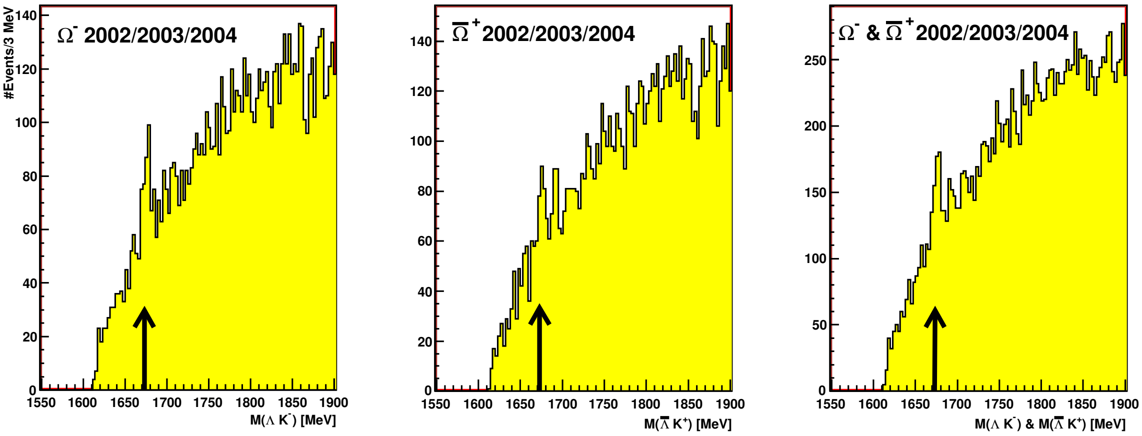

Figure 3.13: The ΛK^- and $\overline{\Lambda}K^+$ invariant mass spectra and their sum. The Ω baryon is marked with an arrow.

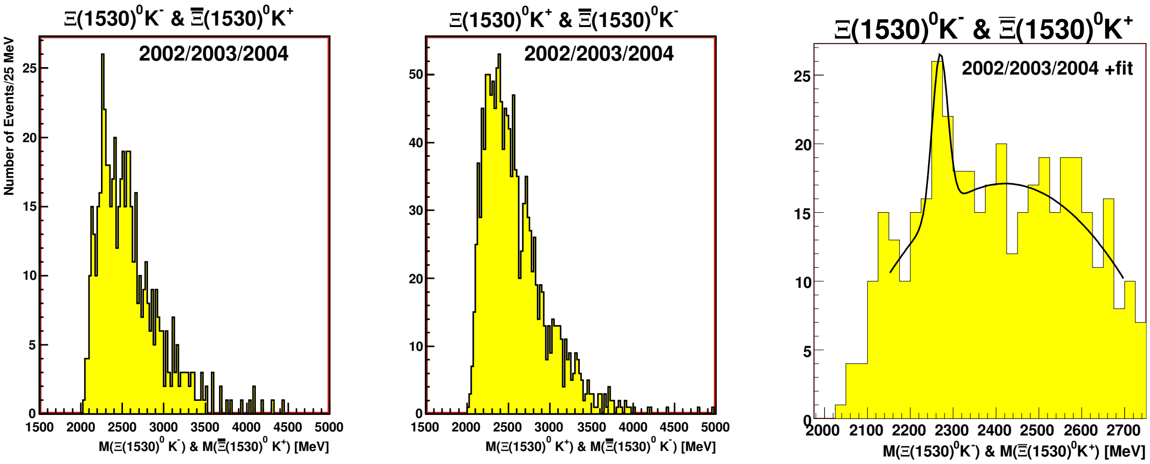

Figure 3.14: Left: the sum of $\Xi(1530)^0K^-$ and $\overline{\Xi}(1530)^0K^+$ mass spectra; centre: the sum of $\Xi(1530)^0K^+$ and $\overline{\Xi}(1530)^0K^-$ mass spectra; right: the sum of $\Xi(1530)^0K^-$ and $\overline{\Xi}(1530)^0K^+$ mass spectra with a fit.

Now a statistical significance of the peak is 2.5 σ. Both values are low and not sufficient to claim the observation of the $\Omega(2250)$ state. The new data from 2006 will double the statistics, and if the peak indeed corresponds to the excited Ω mass state the significance should rise to about 4 σ which will make the observation much more credible.

3.9 Summary

In this chapter reconstruction of the V^0 particles in the 2002–2004 data sample was presented. Very high statistics of events were obtained for both neutral mesons (K^0) and baryons (Λ, $\overline{\Lambda}$) decaying into pairs of charged particles. They were selected without particle identification by the RICH. Final states containing the following particles were considered:

- K^0K^0
- ΛK^0 and $\overline{\Lambda}K^0$

- $\Xi^-\pi^+$, $\Xi^-\pi^-$, $\overline{\Xi}^+\pi^-$ and $\overline{\Xi}^+\pi^+$
- $\Xi(1530)^0\pi^-$ and $\overline{\Xi}(1530)^0\pi^+$
- ΛK^- and $\overline{\Lambda}K^+$
- $\Xi(1530)^0K^-$ and $\overline{\Xi}(1530)^0K^+$

In the K^0K^0 channel a number of well known states was found, in particular a strong signal from the $f'(1525)$ meson. Selecting the K^0K^0 pairs with $x_F > 0.7$ gave an enhancement of events around 1700 MeV. It may correspond to the $f_0(1710)$ state that is expected to have a large content of the glue.

The ΛK^0, $\overline{\Lambda}K^0$, $\Xi^-\pi^+$, $\overline{\Xi}^+\pi^-$, $\Xi(1530)^0\pi^-$ and $\overline{\Xi}(1530)^0\pi^+$ invariant mass spectra were searched for the excited cascade hyperons. No clear signal (except for $\Xi(1530)^0$) was found in any mass spectrum.

Careful studies were dedicated to a signal observed by the NA49 experiment at CERN and interpreted as $\phi(1860)$ pentaquark. With statistics of Ξ^- and $\overline{\Xi}^+$ 45 times larger than NA49, the COMPASS data does not support the existence of the $\phi(1860)$ state. This result is in line with analysis conducted by other collaborations.

Finally the signal coming from the Ω baryon was reconstructed. The $\Xi(1530)^0K^-$ and $\overline{\Xi}(1530)^0K^+$ channels were used to perform a search for the excited triple strange states. A weak indication of the $\Omega(2250)$ state was found.

Results presented here are only a demonstration of the spectrometer potential for the mass spectroscopy studies in the muon programme. Further work, including the 2006 data, is needed to establish the observation of the $f_0(1710)$ and $\Omega(2250)$ states in COMPASS. In 2007 COMPASS will start the hadron physics programme dedicated *inter alia* to mass spectroscopy.

Chapter 4

The Selection of the Open Charm Mesons

This chapter is dedicated to events containing open charm mesons. First a characteristic of such events is presented and then the cuts leading to their most efficient selection are discussed. A selection efficiency is defined through the introduction of a parameter called **F**igure **O**f **M**erit (FOM):

$$\mathrm{FOM} = \frac{S}{1 + B/S} \tag{4.1}$$

where yields of the signal (S) and the background (B) are extracted from a fit to the invariant mass spectrum of the open charm candidates. Only events inside the [–47,47] MeV range around the nominal D^0 mass are counted. This range corresponds to about 2 σ interval of the D^0 signal reconstructed in COMPASS. The inverse square root of FOM is proportional to the error on the $\Delta G/G$ value calculated using the so called **F**irst **O**rder **U**nweighted **M**ethod (FOUM):

$$\delta(\Delta G/G)_{\mathrm{FOUM}} \sim \frac{1}{\sqrt{\mathrm{FOM}}} \tag{4.2}$$

Different methods applied for the $\Delta G/G$ extraction from the open charm signal are discussed in details in the next chapter.

Cuts described in this part of the thesis result from long studies that began in 1995 and last until now. At the end of the chapter two additional methods for FOM increasing are presented. They were investigated but finally not used in the analysis.

4.1 Open Charm Mesons in COMPASS

The D^0 meson, a spin 0 particle, has a quark content $c\bar{u}$, mass M_{D^0}=(1864.5±0.4) MeV and a mean life time τ=(410.1±1.5)·10^{-15} s [25]. The mean path it travels in the laboratory frame before the decay is:

$$L = c\tau\gamma = c\tau\frac{E}{M_{D^0}} \tag{4.3}$$

where E is the meson's energy. In the COMPASS data, average energy of D^0 produced in μN interactions is approximately 40 GeV, spreading from 20 to 90 GeV. The average flight length is thus around 2.6 mm.

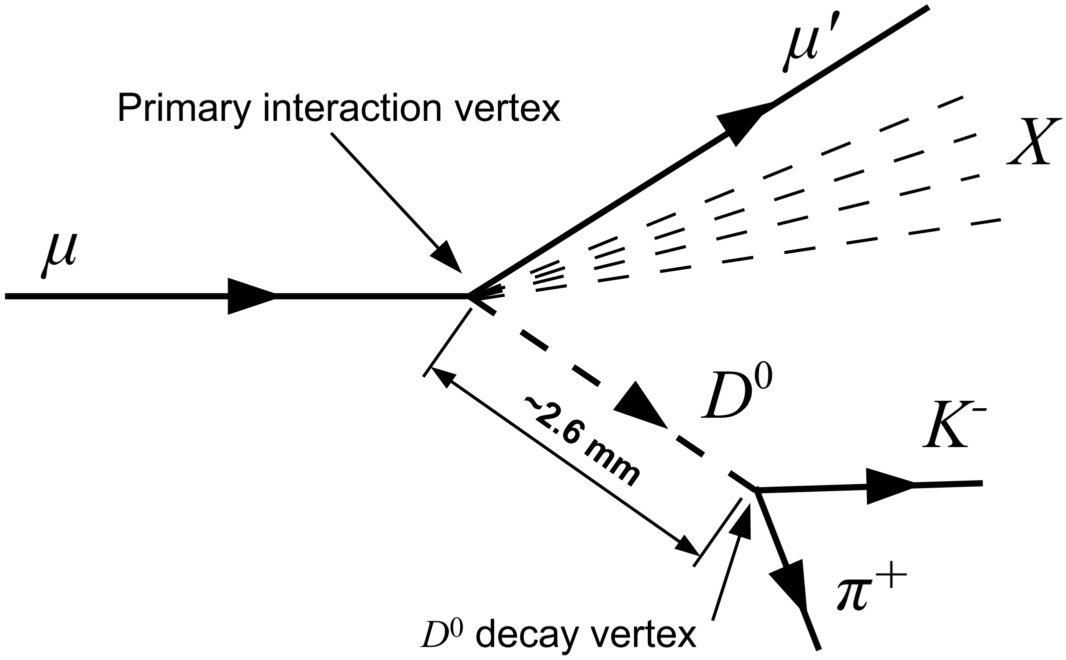

Figure 4.1: A μN interaction in which a D^0 meson decaying in the golden channel is produced.

Interactions leading to the open charm production take place inside one of the 60 cm long solid state target cells (cf. Sec. 2.2). Construction of the cells and the vessel in which they are enclosed prevents to employ dedicated silicon detectors to separate the production and the decay vertices of the D^0 mesons. For the reconstruction of the primary vertex position and the tracks of the charged particles outgoing from the target, a set of the tracking detector planes located between the target and the first magnet is used. These are Scintillating Fibers, MicroMegas and Drift Chambers (see Sec. 2.4). They provide a 1-2 cm resolution of the primary vertex reconstruction in the Z direction. Therefore the D^0 mesons cannot be selected through the observation of their decay vertices. Instead the selection has to be done via the identification and reconstruction of their decay products.

The D^0 mesons can decay in various channels [25]. Out of these the $K^-\pi^+$ decay channel, Fig. 4.1, is the one that is relatively easy to reconstruct as only two charged hadrons in the final state have to be measured. The branching ratio for this mode is (3.80±0.07)%. It will be referred to as the "golden channel".

$$\begin{aligned} \mu N \longrightarrow \mu' X D^0 & \\ \hookrightarrow K^-\pi^+ & \end{aligned} \tag{4.4}$$

Apart from the golden channel also other decay modes can be used for the open charm selection to accumulate larger statistics and improve the accuracy of the production asymmetry measurement. Attempts to reconstruct D^0 mesons were indeed made for various channels: $K^0\pi^+\pi^-$ [106], $K^-\pi^+\pi^0$ [127] and others [128, 129]. Results of these studies were that either no significant D^0 signal was visible or a weak signal was accompanied by an overwhelming background. The channels with a π^0 in the final state probably will give a significant contribution to the D^0 statistics after the 2006 data taking period when the electromagnetic calorimeters will be fully operational. For the data from 2002, 2003 and 2004 it was decided to focus only on the open charm decays in the golden channel.

For the D^0 reconstruction in the golden channel two charged tracks corresponding to the decay products have to be measured. Reconstruction of the incoming and the scattered muons is also required in order to obtain information on the interaction kinematics. The combinatorial background for the studied reaction is high. It can be partially suppressed using particle identification by the RICH. In particular identification of kaons is especially useful as it rejects a large number of $\pi\pi$ pairs that otherwise would be classified as $K\pi$ pairs and used for the open charm candidates reconstruction.

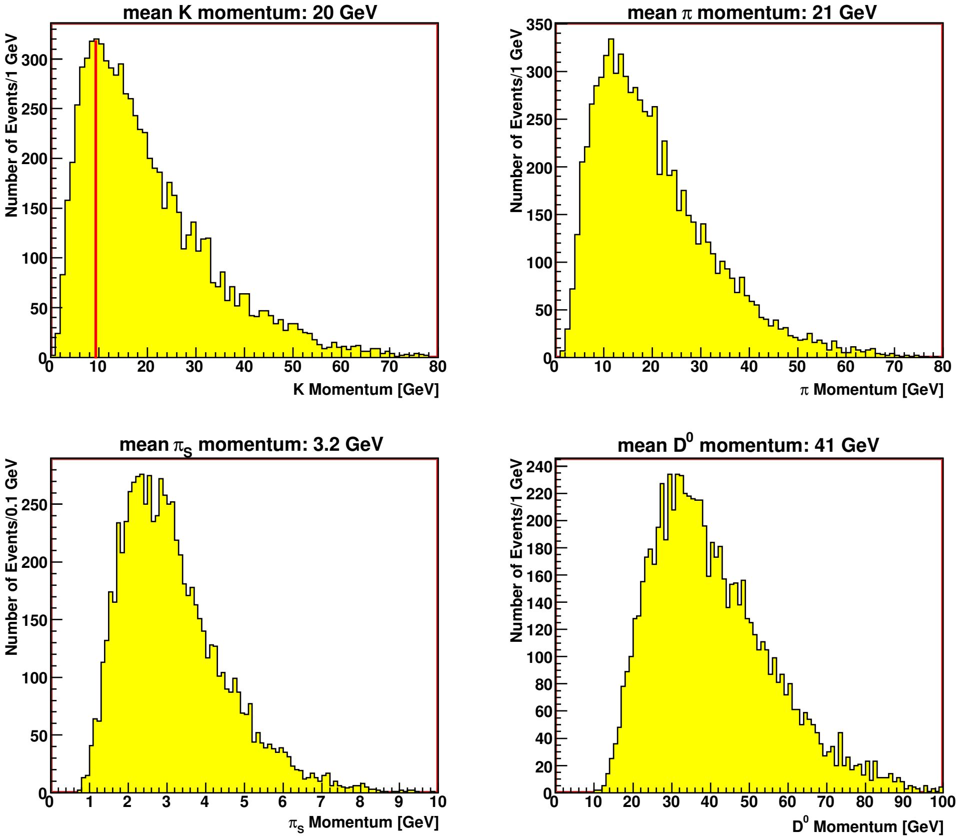

Figure 4.2: Momentum distributions for K, π, π_S and D^0 from the $D^* \to D^0\pi_S \to K\pi\pi_S$ decays. The red line marks the momentum of a kaon above which the RICH identification is possible. The distributions come from AROMA sample reconstructed with CORAL.

About 40% of D^0 particles originate from decays of $D^*(2010)^+$ mesons (later called D^*). The mass of the D^* meson is (2010±0.4) MeV and its width is (96±22) keV. In 67.7% of cases the D^* decay into $D^0\pi^+$ pairs. The average laboratory momentum of the pion from that decay is about 3 GeV, Fig. 4.2, a small value as compared with momenta of other particles produced in the interaction. Therefore such a pion is called a soft pion and will be denoted as π_S.

$$\begin{aligned}\mu N \longrightarrow \mu' X D^* \quad & \\ \hookrightarrow \pi_S^+ D^0 & \\ \hookrightarrow K^-\pi^+ &\end{aligned} \tag{4.5}$$

In this decay more constraints can be imposed on the selection procedure. This results in a much higher signal-over-background ratio. A sketch of such a two step process is shown in Fig. 4.3.

It was decided to divide the sample containing selected D^0 events into two subsamples. In the first one for each event a soft pion is found and a D^* candidate is reconstructed in a given mass window centred at the meson PDG mass. The second sample comprises the events where no D^* candidate is present. The former subsample is called the D^0–tagged sample as the D^0 mesons are tagged with the reconstruction of the D^* candidates. The latter is called the D^0–untagged sample. Cuts leading to the optimal selection of both samples will be discussed in this chapter.

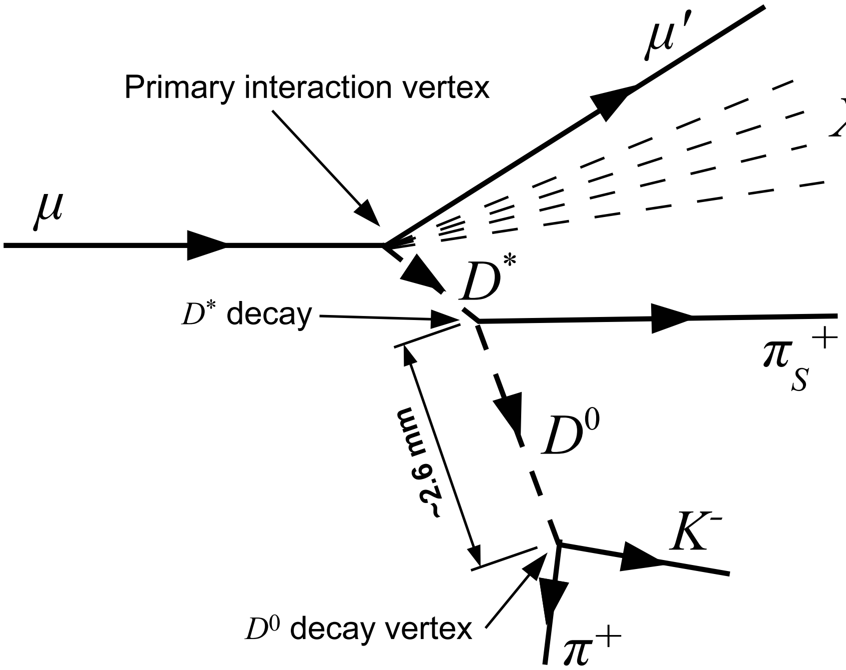

Figure 4.3: Sketch of an interaction in which a D^* decaying subsequently to a $D^0\pi_S^+$ pair is produced (not to scale).

4.2 Basic Selection of Events

In the analysis the data taken in 2002, 2003 and 2004 with the longitudinal target polarisation are used. They are grouped into several periods, each corresponding to about one week of the data taking. A list of periods used in the analysis is given in Tab. 4.1. Each period consists of a number of thirty-minute-long runs, while runs comprise spills corresponding to the 16.8 s long cycles of the SPS (cf. Sec. 2.1).

4.2.1 Stability of the Data

Stability of the spectrometer conditions during the data taking is a basic requirement for studies of the cross-section asymmetries. The stability is monitored on the spill-by-spill bases. Spills for which there are indications that they were taken during the

Year	Period name
2002	P1C02, P2A02, P2D02, P2E02, P2F02, P2G02
2003	P1A03, P1B03, P1C03, P1D03, P1E03, P1F03, P1I03, P1J03
2004	W2204, W2304, W2604, W2704, W2804, W2904, W3004, W3104, W3204, W3704, W3804, W3904, W4004

Table 4.1: List of data taking periods used in the analysis.

time period when the spectrometer was unstable enter the “bad spills list” [130] and are discarded from the analysis. Preparation of the list is based on the monitoring of variables characterising each spill. These are:

- average number of primary vertices per event;
- average number of incoming muon tracks per event;
- average number of reconstructed tracks per event;
- average number of tracks outgoing from the primary interaction per vertex;
- integrated beam flux in a given spill.

If at least one of these variables deviates more than 5 σ from the average value, a spill is marked as bad. Additionally, if the statistics of events in a spill is more than 3 times lower than the nominal one, it is also put on the list. Finally, groups of spills for which the above parameters differ systematically from those for the neighbouring spills are considered as bad. Percentage of spills that are excluded in a given period varies from 3% to about 30%.

Apart from the bad spills a number of full runs that were taken under unstable spectrometer conditions are excluded from the used data. These are:

- runs from the beginning of the P2A02 – where the detector performance was not stable;
- runs from the beginning of the P1A03 – after the excluded runs there was a two days break in the SPS operation, during which some changes to the spectrometer setup were introduced;
- runs from the middle of the P1E03 – in the excluded interval some detector tests were performed causing instabilities in the spectrometer work.

4.2.2 Primary Vertex Cuts

A poor spatial resolution for the Z-coordinate of an interaction point inside the dense target material, makes it impossible to separate the D^0 decay vertex from the primary interaction point where the meson was born. Thus in what follows the “primary vertex” indicates a sum of the primary interaction and the D^0 decay vertex.

Only events containing a reconstructed primary vertex qualify for the analysis. The primary vertex is defined as a vertex with which an incoming muon track and at least one outgoing charged track are associated. The latter may correspond to a scattered muon or to a particle produced in the interaction. Given event may contain more than one vertex fulfilling this demand. Most of those additional primary vertices originate from random combinations of tracks outgoing from the target. If an event contains more than one primary vertex, the one with the highest number of outgoing tracks is treated as the real interaction point. If there are two or more vertices with the same number of tracks, the one with the smallest χ^2 is taken. The χ^2 corresponds to the accuracy of the Kalman procedure for the primary vertex fitting. The vertex chosen with those requirements is called the best primary vertex. Distributions of the number of primary vertices per event, the number of outgoing tracks associated with the best primary vertex and of the χ^2 for the best primary vertex are presented in Fig. 4.4.

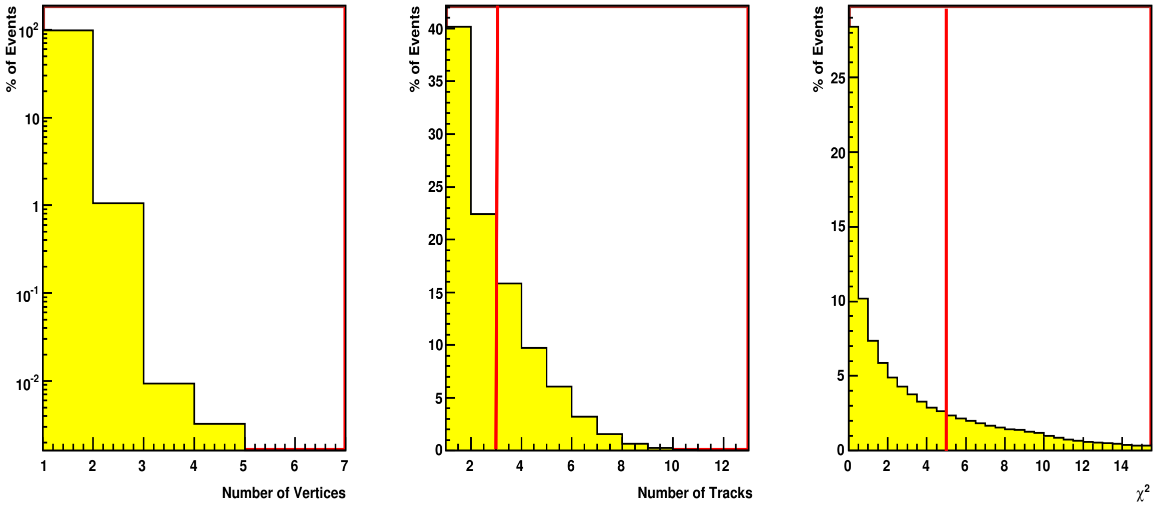

Figure 4.4: From left to right: number of primary vertices reconstructed in a given event, number of charged tracks outgoing from the best primary vertex, χ^2 of the best primary vertex. All plots are normalised to 100%. The red lines mark the cuts used in the analysis: events with more than two outgoing tracks and events with $\chi^2 < 5$ were selected.

For the open charm studies it is required that at least three charged tracks originate from the best primary vertex. One of these tracks has to be identified as a scattered muon while the other two are candidates for a pion and a kaon that emerge from the D^0 decay. The electric charges of those two tracks have to be opposite. Additionally the χ^2 of the vertex is required to be smaller than 5.

4.2.3 Vertex Position

For the asymmetry studies it is crucial to accurately attribute interaction vertices to one of the two target cells. For interactions in which a D^0 is reconstructed, at least three charged particles are associated with the best primary vertex. With such a high number of outgoing tracks, the position of the vertex can be reconstructed with a precision better than average. A mean uncertainty of the Z-coordinate is only 0.9 cm (for an average event: 2 cm). This value should be compared with a 10 cm gap separating both cells. An unambiguous attribution of the interaction point to one of the target halves can be thus performed accurately.

A second important issue concerning the primary vertices is a selection of those interactions which took place inside the target material and for instance not in the target vessel. Any significant admixture of events coming from such non-target interactions may systematically bias the asymmetry. In the nominal detector setup the (X=0, Y=0, Z) line defines the central axis of the target cylinders. In the real setup the target is slightly tilted with respect to that line. The tilt is described by coordinates (x_U, y_U) of the centre of the upstream border of the upstream cell and by (x_D, y_D) of the centre of the downstream border of the downstream cell, cf. Fig. 4.5. These coordinates are different for 2002, 2003 and 2004 data taking periods. Their values are shown in Tab. 4.2.

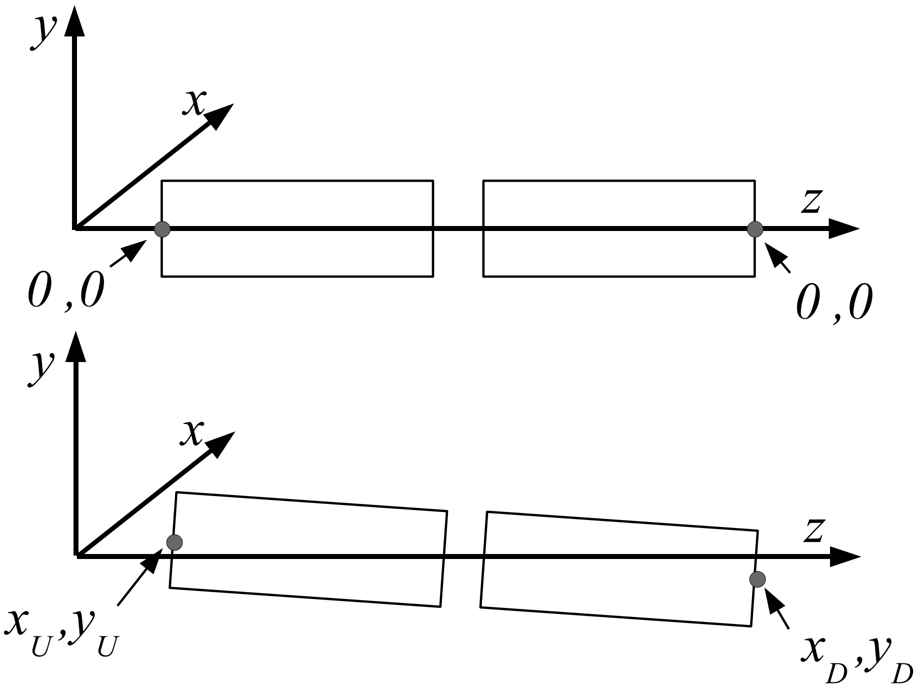

Figure 4.5: The nominal (top) and real (bottom) orientations of the target.

Period	$x_U[cm]$	$y_U[cm]$	$x_D[cm]$	$y_D[cm]$
2002	–0.2	0.1	–0.3	–0.15
2003	0	–0.1	–0.1	–0.25
2004 (W22–W32)	0	–0.1	0	–0.3
2004 (W37–W40)	0	–0.13	0	–0.3

Table 4.2: Position of the target in different data taking periods.

Cuts selecting interactions located inside the target are defined in the tilted coordinate system, also called the target reference system. For a primary vertex at (v_x, v_y, v_z) in the target reference system, the following cuts are used:

- vertex inside the upstream cell: -100 cm $< v_z < -40$ cm
  or inside the downstream cell: -30 cm $< v_z <$ 30 cm.
- $r = \sqrt{v_x^2 + v_y^2} < 1.4$ cm.

To avoid the influence of the inhomogeneities of the target material close to its borders and to prevent the migration of the interactions from outside into the target caused by reconstruction uncertainties (in the r direction it is of the order of 0.2 mm), the cut on r is tighter than the radius of the target. A distribution of primary vertices is plotted in Fig. 4.6. The right plot shows that less interactions occur in the upper part of the target ($Y > 0$ cm). This effect is due to the beam axis shift with respect to the centre of the target. It should not bias the asymmetry measurement. A more precise scan of the target material disclosed also that the cylinders are not uniformly filled with ^{6}LiD. Upper parts of the cells contain less material. To avoid the influence of this inhomogeneity on the measurement it was decided to reject events with primary vertices located in that part of the target. The following cut is therefore used:

- $v_y < 1$ cm.

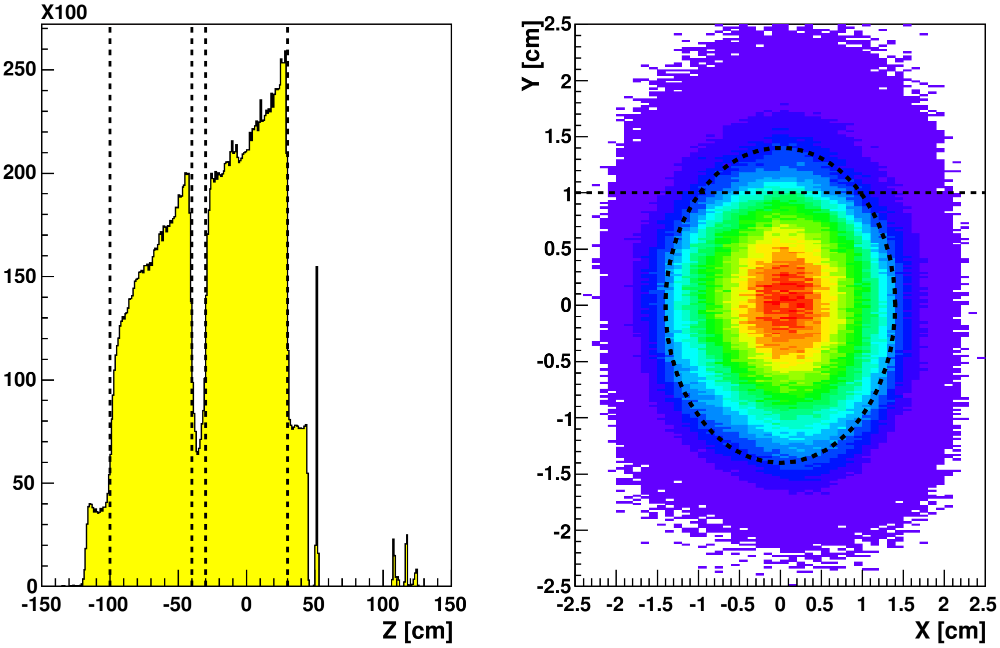

Figure 4.6: The distribution of primary vertices with at least three outgoing charged tracks. Left: the distribution in Z direction, two target cells are clearly visible as well as the first detector stations at Z=110 cm where some interactions took place. Right: distribution in XY plane. Dashed lines at both pictures represent the cuts described in text.

4.2.4 Beam Flux Equalisation

Extraction of the asymmetry relies on the assumption that the beam fluxes going through both target cells are exactly the same. As the beam axis is not parallel to the target symmetry axis, this assumption is no longer valid. The upstream and the downstream cells are in fact exposed to slightly different fluxes. This effect has to be corrected by an additional set of cuts. The incoming muon track that induced the interaction in the target is extrapolated to the beginning of the upstream cell and to the end of the downstream cell (as if it did not interact), cf. Fig. 4.7. With this extrapolation two points are obtained (x_1,y_1) and (x_2,y_2). It is checked if:

- $r_i = \sqrt{x_i^2 + y_i^2} < 1.4$ cm, i=1,2.
- $y_i < 1$ cm, i=1,2.

When the above requirements are fulfilled, a muon causing an interaction would travel equal paths through each cell if the interaction did not happen. All events with incoming muon tracks outside the above cuts are discarded from the analysis. This procedure is called the beam flux equalisation.

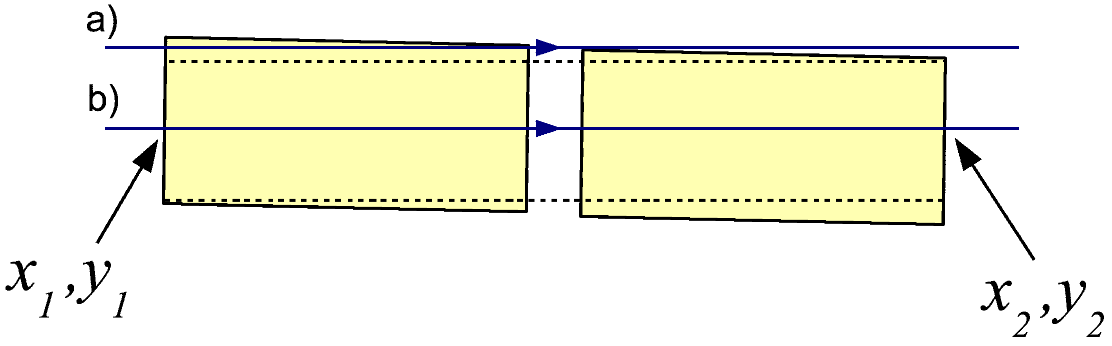

Figure 4.7: Equalisation of the beam flux. Dashed lines mark the limits of the target not affected by different beam fluxes. Beam track a) is rejected as it does not go through both target cells. Beam track b) is accepted since the (x_1,y_1) and (x_2,y_2) are inside the cuts and the track is passing both cells.

4.3 Kinematic Cuts

Apart from the cuts on the global characteristic of events (primary vertex location, number of outgoing tracks etc.), cuts on the kinematical properties of particles forming D^0 and D^* candidates are imposed. These cuts are important for suppressing a large combinatorial background.

4.3.1 Cut on z_{D^0}

In the PGF process a pair of charmed quarks is produced. Each of the quarks carry a large fraction of the virtual photon energy (about half of this energy per each quark). In the charm quark fragmentation process this large energy is subsequently transferred to the charm hadrons. The D^0 mesons are thus characterised with a large value of the z variable (cf. Eq. (1.8)). The background in the D^0 sample arises mainly from the random combinations of charged particles which do not come from the open charm meson decays. These particles come mostly from the target fragmentation region and thus did not have a direct contact with the photon. The corresponding D^0 candidates are characterised by a rather small z. Therefore a cut on the energy fraction of the D^0 meson candidates results in a significant reduction of the background events, cf. Fig. 4.8. For the analysis two cuts are chosen:

- $z_{D^0} > 0.2$
- $z_{D^0} > 0.25$

The first one is used for the selection of the D^0–tagged mesons. The second, stricter, rejects more efficiently the background in the D^0–untagged sample.

4.3.2 Cut on θ^*_K

Another kinematic variable that is used for the background suppression is an angle between the flight direction of K in the D^0 centre-of-mass frame and the direction of the D^0 velocity in the laboratory system. The angle is called θ^*_K. For a decay of a spin 0 particle, such as D^0, the distribution of $\cos\theta^*_K$ should be flat. The combinatorial background is formed by particles coming from the target fragmentation region where they get only a small amount of the transverse momentum. Therefore the $\cos\theta^*_K$ values for the D^0 candidates arising from combinatorial background are close to ±1, cf. Fig. 4.8. For the selection of the open charm sample two cuts on $\cos\theta^*_K$ are imposed:

- $|\cos\theta^*_K| < 0.85$
- $|\cos\theta^*_K| < 0.50$

They are used for the D^0–tagged and D^0–untagged samples, respectively. The cuts on the RICH identification, discussed later, remove the kinematical range of high $|\cos\theta^*_K|$ values, making the above cuts redundant. However they are kept in the analysis as the cuts on the particles identification are still subjects of intensive studies. For those studies a well defined sample of the D^0 events with suppressed background is required.

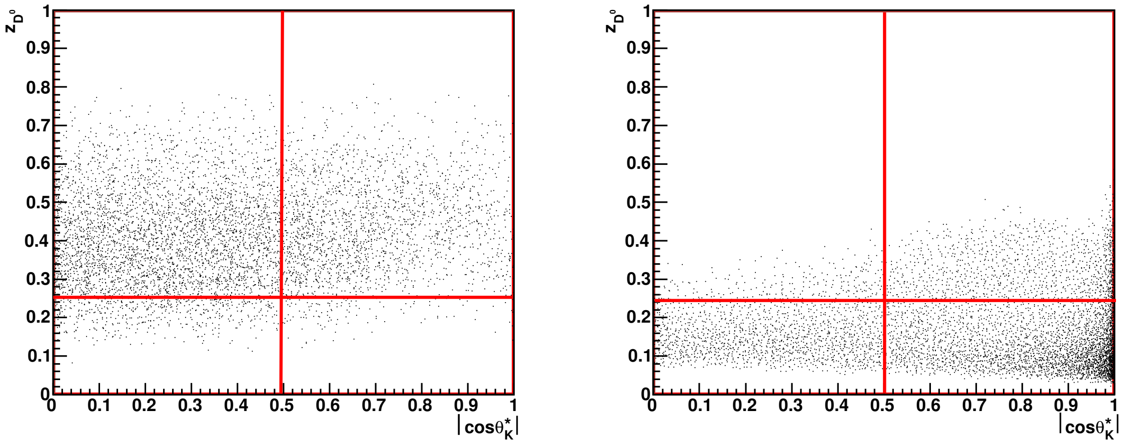

Figure 4.8: The z_{D^0} and $|\cos\theta^*_K|$ distributions for the D^0 signal (left) and the background (right). The signal sample was obtained from AROMA-COMGEANT-CORAL. The background sample comes from the data, where the signal contribution, much smaller than background, was neglected. Both were obtained for the D^0–untagged channel. Red lines mark cuts used for the signal selection in that channel. The two samples are not normalised to each other.

4.3.3 Cut on the $\Delta M = M_{K\pi\pi_S} - M_{K\pi} - M_\pi$

For the D^0–tagged sample another, robust kinematical cut is applied. It is a consequence of a difference between the invariant masses of the $K\pi\pi_S$ and $K\pi$ combinations:

$$\delta M = M_{K\pi\pi_S} - M_{K\pi} \tag{4.6}$$

If these systems correspond to D^* and D^0 mesons, δM is about 145 MeV. The bulk of the energy released in a D^* decay is transferred into the mass of π_S which is 139.6 MeV.

Thus the momentum of the soft pion is small, about 40 MeV in the D^* rest frame. For the selection used in the analysis the following variable is introduced:

$$\Delta M = M_{K\pi\pi_S} - M_{K\pi} - M_\pi \tag{4.7}$$

In the two dimensional plot, Fig. 4.9, a distribution of ΔM versus $M_{K\pi} - M_{D^0}$ is plotted with a clearly visible region of D^* decaying to D^0. A projection of that plot on the ΔM axis is also presented. The cut defining D^* tagging is chosen as:

- 3.1 MeV $< \Delta M <$ 9.1 MeV

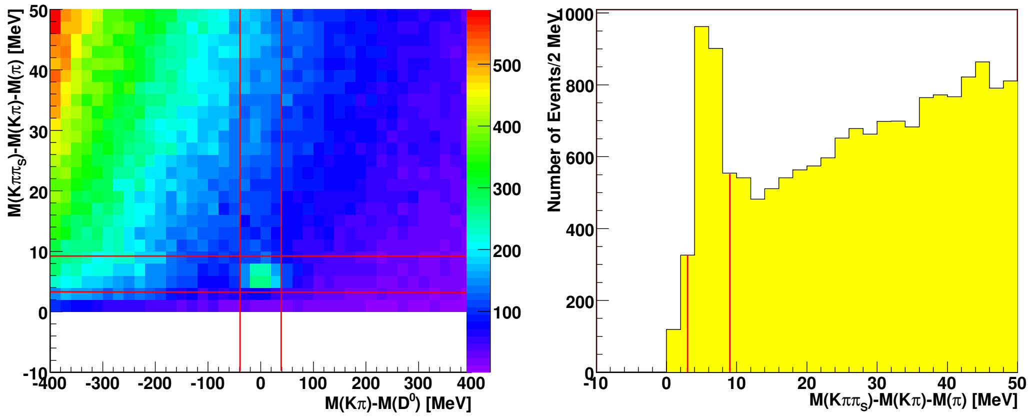

Figure 4.9: Left: plot of $K\pi$ *vs* $K\pi\pi_S$ invariant masses. A maximum in the distribution corresponds to the $D^* \to D^0$ decays. Right: the projection of the previous plot on the y-axis. Only the bins from the band marked with vertical red lines, *i.e.* 50 MeV $< M_{K\pi} - M_{D^0} <$ 50 MeV, were projected. The red horizontal lines at the left plot as well as the lines at the right one mark the cut selecting the D^0–tagged sample.

4.4 Identification of Particles in the RICH

Identification of particles in the RICH detector is crucial for the selection of the open charm mesons. In case of the D^0–untagged (tagged) decays two (three) particles can undergo identification. For the former it was indeed found that using the information from the RICH for both tracks improves FOM, while for the latter only the information on the kaon is essential. Optimisation of the cuts based on the RICH was studied by several groups in COMPASS. Final cuts are described in the following sections.

4.4.1 Identification of Kaons

Methods of identification differ for 2002–2003 and 2004 data sets. Kaons from the former sample are identified with a χ^2 technique while in the latter a more sophisticated *Likelihood* approach is used, cf. Sec. 2.5.

The χ^2 cuts defining kaons in 2002–2003 data sample are the following:

- A track is considered as that of kaon only if the momentum associated with it is lower than 50 GeV. For the particles with larger momenta, the RICH performance decreases and the identification becomes unreliable.

- The χ^2 for the kaon mass hypothesis is smaller than that for the pion mass hypothesis: $\chi^2_K < \chi^2_\pi$.
- An additional quality cut: $\chi^2_K < 5$ for D^0–tagged and $\chi^2_K < 4$ for D^0–untagged samples is imposed. The stricter cut for the D^0–untagged channel is more efficient in suppressing the background that dominates this sample.

There are the following *Likelihood* cuts for the 2004 data sample:

- The kaon candidate momentum is lower than 50 GeV. This cut is the same as for the 2002–2003 χ^2 selection.
- The *Likelihood* of the kaon mass hypothesis is larger than the *Likelihood* of the pion mass hypothesis by a factor A:
$$\frac{L_K}{L_\pi} > A \tag{4.8}$$
- The *Likelihood* of the kaon mass hypothesis is larger than the *Likelihood* of the background hypothesis by a factor B:
$$\frac{L_K}{L_{\mathrm{bg}}} > B \tag{4.9}$$
- The *Likelihood* of the kaon mass hypothesis is larger than the *Likelihood* of the proton mass hypothesis:
$$L_K > L_p \tag{4.10}$$

The parameters A and B were tuned in order to obtain the highest FOM. It was found that there are two pairs of optimal parameters, applicable for separate groups of periods produced with different RICH background parameterisations in CORAL. For periods W22, W23, W26, W27, W32, W38, W39 and W40, $A = 1.24$ and $B = 0.98$ while for periods W28, W29, W30, W31 and W37, $A = 1.06$ and $B = 1.02$.

The highest background level on the RICH photocathode planes is for the region close to the beam axis as it is exposed to the highest muon flux. Identification of particles going through this region is therefore least efficient. For the D^0–untagged sample all the kaon candidates passing the RICH detector at distances smaller than 12 cm from the beam axis are rejected.

4.4.2 Identification of Pions

Pions are the most common hadrons produced in the high energy interactions. The number of pions per event is significantly larger than that of kaons and protons together. With a simple assumption that all hadron tracks outgoing from the primary vertex are $\pi^\pm$, only a minor contamination of kaons and protons is neglected. Therefore the RICH identification of pions from the D^0 decays is not as important as in the case of kaons. However for a sample of events that already contain an identified kaon track the probability that there is a second track corresponding to another charged kaon is large, a consequence of strangeness conservation in the strong and electromagnetic interactions. Thus the RICH information on a pion candidate provides additional means of suppressing the combinatorial background and increasing the FOM. It was found that for the D^0–tagged and the D^0–untagged samples different approaches for the pions identification should be used.

For the D^0–tagged channel the sample of π candidates is restricted to the particles with momenta below 50 GeV. Then for each pion candidate it is checked if its momentum is larger than the threshold for the kaon RICH identification. If this is true, the kaon hypothesis is verified according to the set of cuts defined in Sec. 4.4.1. If the particle is identified as a kaon, it is removed from the pion sample.

For the D^0–untagged channel stricter criteria defining the π candidates sample are imposed. In case of 2002–2003 data they are based on the χ^2 method and read:

- A π candidate has to have momentum larger than the momentum threshold for the kaon identification and smaller than 50 GeV.
- A χ^2 for the pion mass hypothesis is smaller than that for the kaon mass hypothesis: $\chi^2_\pi < \chi^2_K$.
- A χ^2 for the pion mass hypothesis has to be lower than 5: $\chi^2_\pi < 5$.

For the 2004 data the cuts on the *Likelihood* are used:

- A momentum of a π candidate has to be larger than the threshold for kaons RICH identification and smaller than 50 GeV.
- *Likelihoods* of the π, K, p and background hypothesis have to fulfil the following conditions:

$$L_\pi > L_K, L_\pi > L_\mathrm{p}, L_\pi > L_\mathrm{bg} \tag{4.11}$$

4.5 Other Cuts

In addition to the cuts listed above there are others used for the selection of optimal samples and for the subsequent asymmetry calculations.

Many of the low energy π_S tracks do not cross SM1. Their momenta have to be determined from the deflection in the magnetic fringe field spreading between the target and SM1. For the tracks measured only in the fringe field the momentum estimate has a much larger uncertainty than for the tracks passing through the magnet centre. Therefore the $D^* \to D^0$ reconstruction with those π_S reconstructed only in fringe field is also much less reliable. It was checked if the removal of such soft pions from the analysis increases the FOM for the D^0–tagged sample. Indeed, for 2003 data such improvement is clearly visible while for 2002 and 2004 the FOM remains at the same level. This difference is probably caused by different CORAL versions used for the data reconstruction. For 2003 the data were produced with the older, and the less efficient, version of CORAL. For 2002 and 2004, newer versions, able to reconstruct fringe field tracks more accurately, were used. Finally it was decided to remove the fringe field tracks only from the 2003 data sample.

There can be more than one combination of tracks fulfilling all the requirements for the D^0 candidate in an event. These combinations do not have to be independent, as a kaon or a pion from one may also belong to another combination. If both candidates are taken for the asymmetry extraction the final result might be biased since it will be equivalent to a double counting of some events. On the other hand if one combination is selected, and the others from the same event are dismissed, the relevant choice should be well justified. Different criteria may be proposed to define the retained combinations, *e.g.* the minimal difference between the reconstructed invariant mass and the D^0 nominal mass, the smallest error of the reconstructed mass, etc. It is not clear which criterion should be taken and how to prevent a possible systematic shift of the final result due to a choice of given combinations. Therefore it was decided to remove the events containing more than one D^0 candidate from the studied sample.

4.6 The Final Mass Spectra

The cuts presented above define the D^0–tagged and the D^0–untagged meson samples. The samples are independent of each other, which means that if an event is ascribed to the D^0–tagged sample it is automatically excluded from the D^0–untagged one. This prevents the double counting of events. The signal-to-background ratio for each sample can be obtained directly from the invariant mass spectrum. The spectra are fitted with a sum of functions describing the background and the signal distributions. For the signal distribution it was chosen to use a single Gaussian function in both samples. The background was fitted with a sum of two exponential functions in the D^0–untagged sample, while for the D^0–tagged sample a sum of a single exponential and an additional Gaussian distribution was applied. This second Gaussian describes a bump observed in the invariant mass spectrum around $M_{D^0} - 240$ MeV. It corresponds to a reflection of a $D^0 \to K^-\pi^+\pi^0$ decay mode which has a branching ratio of $(14.1 \pm 0.5)\%$. Actually it was considered to use events from this bump for the $\Delta G/G$ extraction too. However, as it will be shown in chapter 6, the accurate knowledge of the D^0 meson kinematics is very important for the $\Delta G/G$ calculation. For the decay mode, where the π^0 remains unmeasured, this accuracy is small. Further, the number of events in that bump is about 10 times lower than the number of events in the main peak. Therefore a decrease of a statistical uncertainty of the $\Delta G/G$ measurement would be small, while an additional systematic error would be very difficult to control. It was thus decided to treat this second decay mode as a background.

In Figs. 4.10 and 4.11 the final mass spectra for both channels are plotted for each year separately. In Tab. 4.3 numbers of D^0 obtained from fits are presented. In Tab. 4.4 these numbers are normalised to the numbers coming from 2002. A direct comparison with values for K^0, Λ and $\overline{\Lambda}$ in Tab. 3.4 is not possible as for the D^0 selection different cuts are used for each year. However the numbers in 2003 are about 1.9 and in 2004 3.5 larger than in 2002, similar ratios were observed for K^0, Λ, $\overline{\Lambda}$, Ξ^- and $\overline{\Xi}^+$ states.

The total number of D^0 in the tagged sample as obtained from fit is:

$$\mathbf{3870 \pm 100}$$

and in the untagged one:

$$\mathbf{14\,630 \pm 560}$$

	2002	2003	2004
D^0–tagged	644	1152	2076
D^0–untagged	2113	4241	8277

Table 4.3: The numbers of D^0 particles reconstructed in each year.

	2002	2003	2004
D^0/D^0_{2002} –tagged	1.0	1.8	3.2
D^0/D^0_{2002} –untagged	1.0	2.0	3.9

Table 4.4: The numbers of D^0 particles reconstructed in each year, normalised to the numbers from 2002.

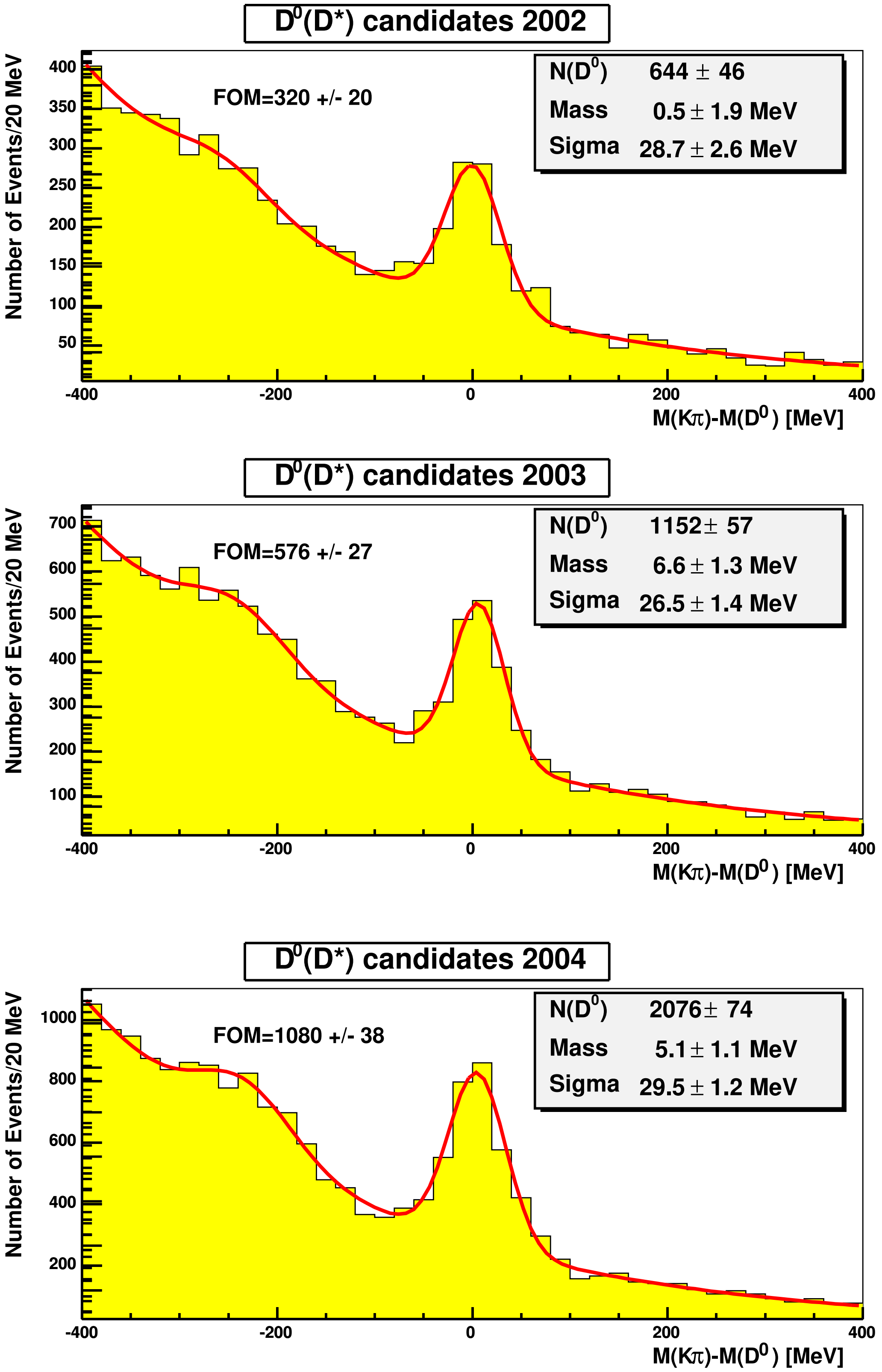

Figure 4.10: The D^0–tagged sample in each year. The numbers of D^0, the centre and the Gaussian dispersion of each peak are given. Also the FOM is presented.

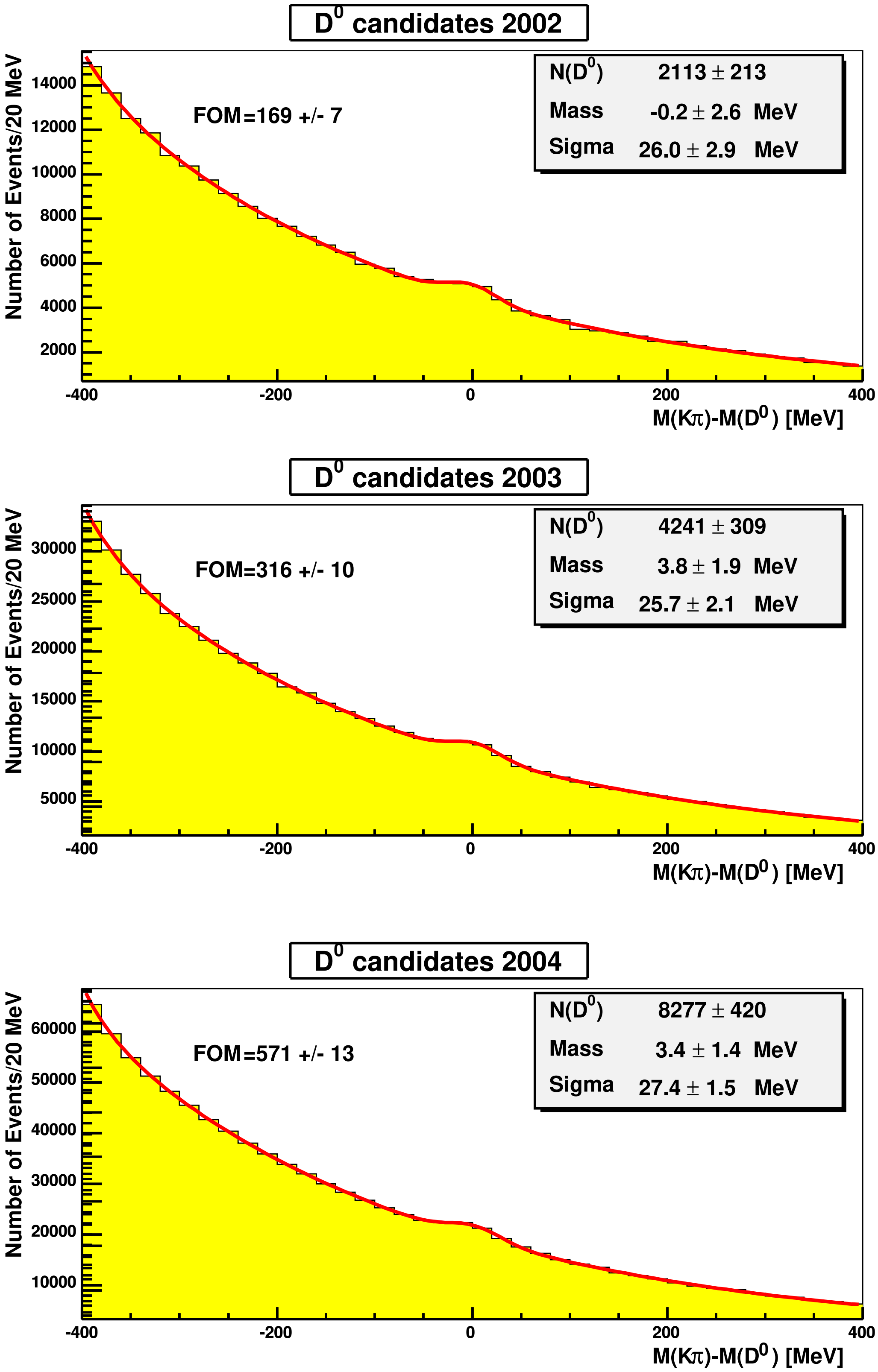

Figure 4.11: As 4.10 but for the D^0–untagged sample.

4.7 The Invariant Mass Cuts

The background underlying the D^0 signal is mainly a product of random combinations of kaons and pions that do not originate from the open charm meson decays. They may come from the target fragmentation region directly or may be decay products of different resonances created in an interaction. These resonances may be identified in the invariant mass distributions. The cuts removing them from the data sample will remove the kaons and pions from the background increasing the FOM of the D^0 signal.

The procedure is as follows. The kaons and pions forming D^0 candidates according to the presented cuts are paired consecutively with another charged track emerging from the primary vertex, cf. Fig. 4.12. That track is assumed to be a pion, kaon or proton. For each assumption an invariant mass is calculated and possible resonances are looked for. In Figs. 4.13 and 4.14 the invariant mass spectra of $\pi_{D^0}\pi$, $\pi_{D^0}K$, $\pi_{D^0}p$, $K_{D^0}\pi$, $K_{D^0}K$, $K_{D^0}p$ are plotted, where the first particle in a given pair, marked with a D^0 subscript, corresponds to a track forming a D^0 candidate. Some of the plots were obtained using the particle identification procedure for the tracks not coming from D^0 decays. In this case the identification is based on a comparison of χ^2_π, χ^2_K, χ^2_p for a given track. A particle type is defined by the smallest χ^2.

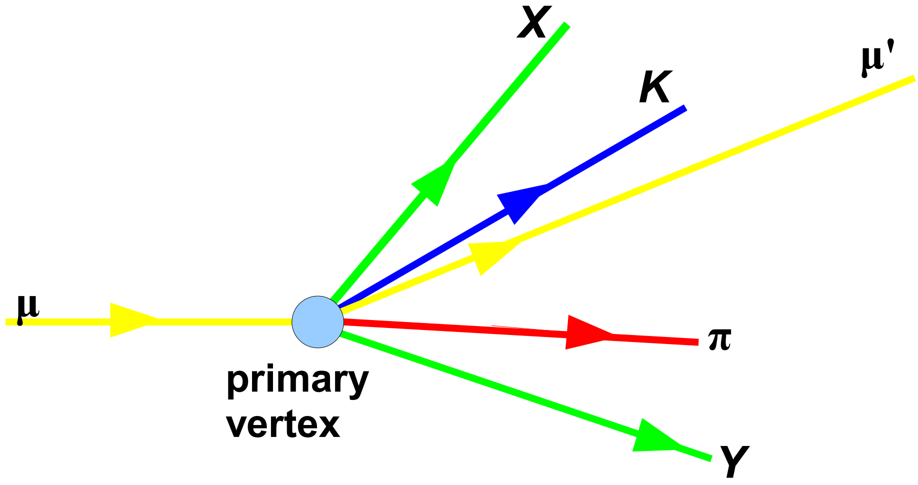

Figure 4.12: The kaon (blue) and the pion (red) candidates are paired with X and Y particles (green) consecutively. Invariant masses of the KX, KY, πX, πY systems are calculated with assumptions X, $Y = \pi$, K, p.

In the mass spectra where no additional RICH identification of the second particle is required, the following resonances are clearly visible:

- $K^*(892)$ in the $K_{D^0}\pi$ spectrum in both D^0–tagged and D^0–untagged samples.
- $\phi(1020)$ in the $K_{D^0}K$ spectrum in both D^0–tagged and D^0–untagged samples.
- $\rho(770)$ in the $\pi_{D^0}\pi$ spectrum in the D^0–untagged sample.

All these resonances are also present in the spectra with the RICH identification for the track not coming from the D^0 decay. In that case an additional signal appears:

- $K^*(892)$ in the $\pi_{D^0}K$ spectrum in the D^0–untagged sample.

Cut	Combination	Mass range [MeV]	Resonance excluded	Identification in RICH
D^0–tagged				
1.	$K_{D^0}K$	1111–1128	$\phi(1020)$	K without identification
2.	$K_{D^0}K$	1111–1128	$\phi(1020)$	K identified
3.	$K_{D^0}\pi$	849–945	$K^*(892)$	π without identification
4.	$\pi_{D^0}\pi$	662–854	$\rho(770)$	π without identification
D^0–untagged				
5.	$K_{D^0}K$	1111–1128	$\phi(1020)$	K without identification
6.	$K_{D^0}K$	1111–1128	$\phi(1020)$	K identified
7.	$\pi_{D^0}\pi$	662–854	$\rho(770)$	π without identification
8.	$\pi_{D^0}\pi$	662–854	$\rho(770)$	π identified
9.	$K_{D^0}\pi$	849–945	$K^*(892)$	π without identification
10.	$K_{D^0}\pi$	849–945	$K^*(892)$	π identified

Table 4.5: Cuts removing resonances.

Mass cuts that exclude the strongest resonance signals are presented in Tab. 4.5. The cuts are done independently. For each of them a new mass spectrum of the D^0–tagged or untagged candidates is obtained and a new FOM is calculated. If a given cut affects only the background for the D^0 signal the FOM should increase. However this is not the case, as resonance signals are accompanied by a significant background, which may belong to the D^0 peak itself. Therefore the FOM increases or decreases, depending on the fractions of background and signal events removed with a given cut. The summary of the results obtained for each case is presented in Tab. 4.6.

Cut	FOM increase [%]	Cut	FOM increase [%]
1.	–0.7	6.	+0.25
2.	+0.2	7.	–35.0
3.	+1.5	8.	–4.0
4.	–3.0	9.	–0.3
5.	–1.25	10.	+0.6

Table 4.6: Results of different cuts on the invariant mass. See text for the details.

As it is seen from the table, most of the cuts decrease the FOM. A small enhancement is observed for three cuts, 2., 6. and 10., while only for one cut, no. 3., this increase is larger than 1%. The statistical error on the final $\Delta G/G$ value is approximately equal to the inverse square root of FOM. With the increase of FOM by 1.5% the gain on the statistical error is of the order of 0.7%, thus negligible. Finally, it was decided not to add any additional cuts on the invariant mass distributions.

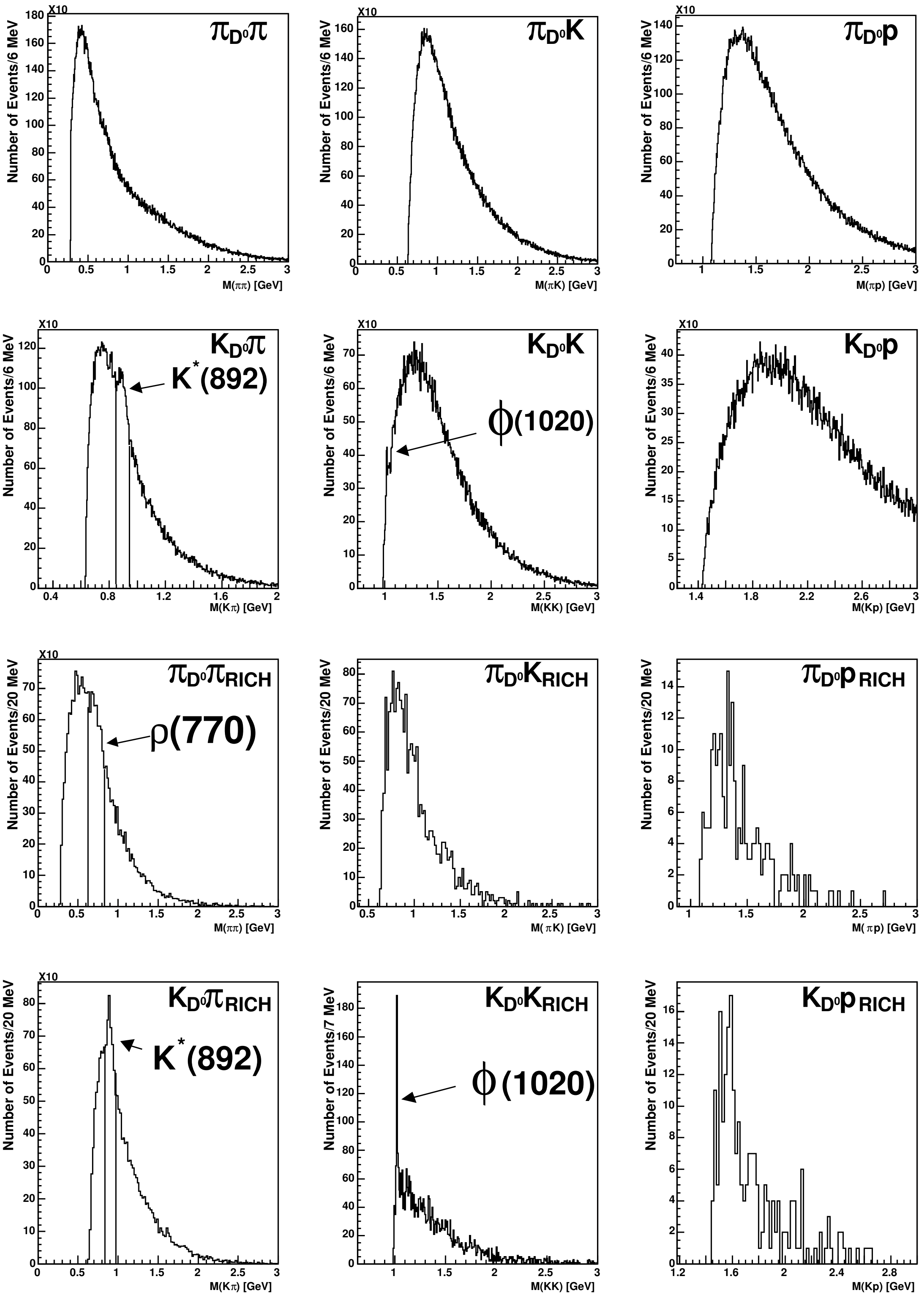

Figure 4.13: Mass spectra of a pair containing a pion or a kaon from the D^0 decay and another charged particle from the primary vertex, assumed to be a pion, a kaon or a proton. Two top rows present the mass spectra when this additional particle is not identified in the RICH. Two bottom rows are for the case when the RICH identification of the particle is performed. The mass ranges of different resonances are marked with arrows and with vertical lines. The plots are for the D^0–tagged sample.

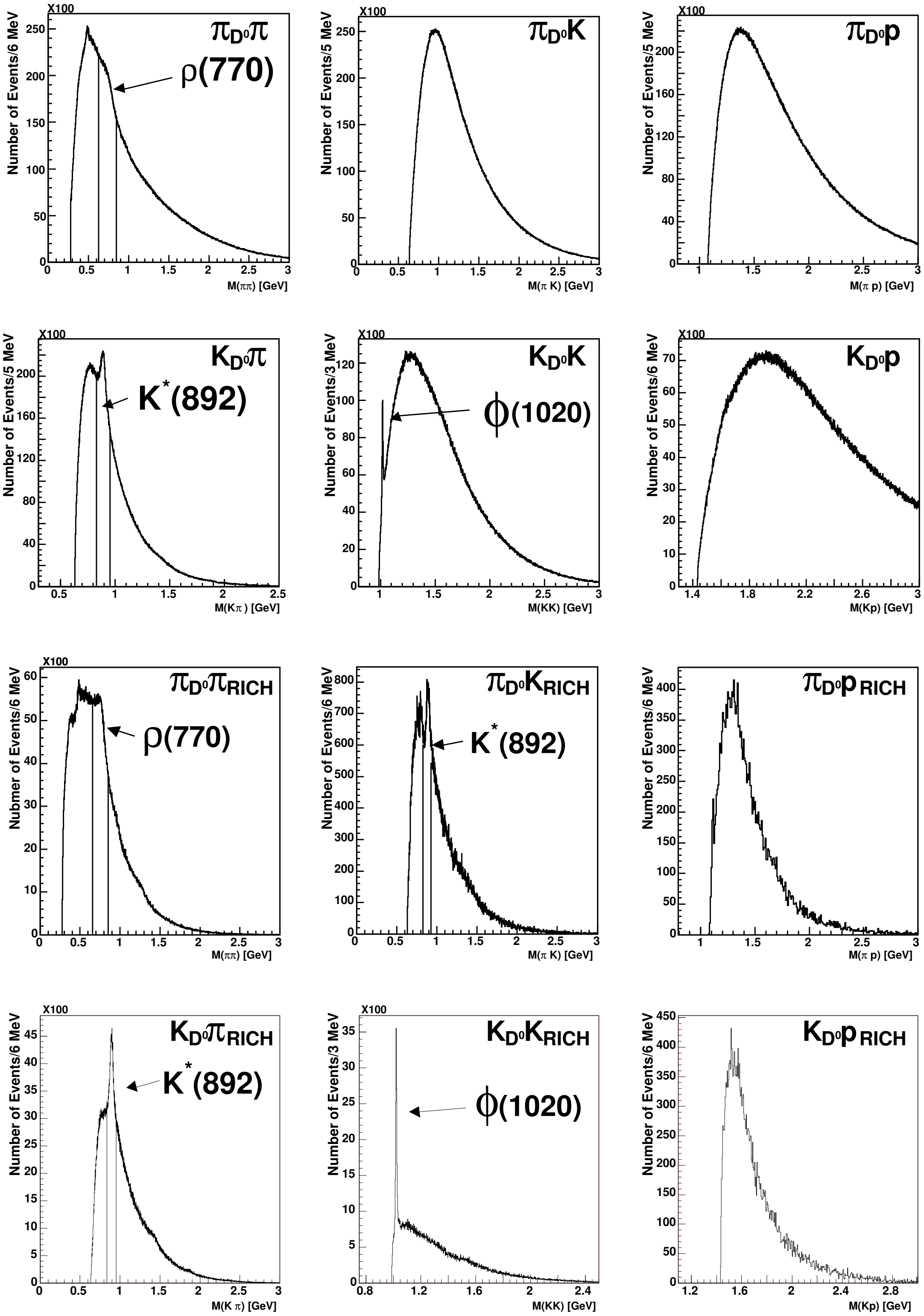

Figure 4.14: As 4.13 but for the D^0–untagged sample.

4.8 Soft Pion Studies

For the D^0–tagged mesons selection, a reconstruction and identification of three particles is required: K, π and π_S. Out of these, the efficient reconstruction of π_S is the most difficult, as its momentum is the lowest and its measurement may be highly affected by the solenoid magnetic field and the multiple Coulomb scattering inside the target material. Therefore the soft pions reconstruction efficiency was studied more profoundly.

4.8.1 Soft Pions in the Monte Carlo

An AROMA generated sample consisting of events with $D^* \to D^0\pi_S \to K\pi\pi_S$ decay chains was prepared. The events were processed through the COMGEANT and reconstructed with CORAL. During the Monte Carlo generation, information on the origin of each track was saved. PHAST allowed to perform a scan over all the tracks that were reconstructed in a given event. The scan was extended for tracks that were generated but failed to be reconstructed by CORAL. During the scan also the information on the track origin was read out allowing an unambiguous identification of the soft pion tracks.

The studies were limited to the subsample of events with a soft pion track within an acceptance of the first MicroMega station, that is at $Z = 142$ cm, X and Y were smaller than 20 cm and larger than –20 cm. The tracks that were outside these limits were regarded as unreconstructable. In this subsample it was found that 80.2% of the generated soft pion tracks are in the reconstructed data. This large fraction shows that the efficiency of the soft pions reconstruction is very good.

A fraction of the soft pion tracks not attributed to primary vertices was found to be about 5.7%. Such tracks are not used for the D^* mesons selection.

4.8.2 The Soft Pion Recovery Procedure

The selection procedure of the D^0–tagged sample can be extended to encompass events with a soft pion candidate not ascribed to a primary vertex. All the selection cuts remain the same, while the only change is that when searching for a soft pion candidate all charged tracks for which the closest distance of approach to a primary vertex is smaller than 2 cm are now accepted. These tracks are added to a primary vertex. Their parameters are also used for the reduction of the primary vertex position uncertainty. This requires a vertex fitting procedure to be repeated.

The Kalman filter for the vertex fitting is implemented as a part of the CORAL package and is used during the data production, see Sec. 2.8. At the level of PHAST there is no possibility to modify the objects, *e.g.* tracks and vertices, created during production. Therefore a special C++ extension to the PHAST package was prepared. It is a function that needs the following information as an input: a set of the parameters describing the primary vertex, all the tracks ascribed to it, and a track that is going to be added. Then the Kalman fitting is performed and a new object corresponding to a refitted vertex is created. The object has the same structure as the initial one describing the primary vertex, but encompasses also the additional track. The parameters of the primary vertex and all the tracks belonging to it after refitting are changed. The new object can be accessed during analysis and may be used for the D^0 selection. The algorithm was tested at the Monte Carlo sample. It was found that the refitting procedure improves the parameters of the added track. They deviate on average 40% less from the ones generated by AROMA comparing to the parameters of tracks from before the refitting.

The subsample of events containing tracks not attached to primary vertices, but having the closest distance of approach smaller than 2 cm was selected from the data. Then for each event the refitting procedure was executed and the D^0–tagged selection, using the refitted primary vertex, was performed. Assuming that 5.7% of D^* events have a soft pion track not attached to a primary vertex, the expected signal of the open charm mesons in the studied subsample should reach 200. However this estimate neglects two issues:

- The scan of the Monte Carlo sample did not take into account the cuts that are made for the selection of the open charm events in the real data. It may happen that events for which a soft pion track is not attached to a primary vertex occupy preferentially the kinematical range that is excluded by the cuts.
- No background Monte Carlo studies were done. It may happen that with the above procedure used for the real data, the background is strongly enhanced, and the final FOM for the sample is small.

It was decided not to perform additional Monte Carlo studies but focus directly on the real data. An invariant mass of the $K\pi$ pairs selected with the cuts for the D^0–tagged sample in the group of events for which the refitting procedure was used, is shown in Fig. 4.15. No significant enhancements are seen in the $D^0 \to K\pi$ signal range and the background in the sample is high. This may point onto the issues mention above.

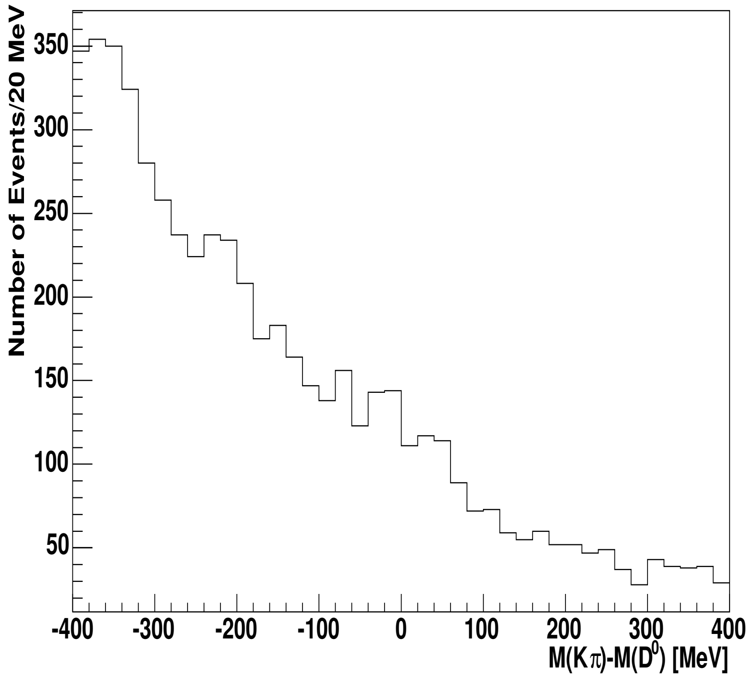

Figure 4.15: Invariant mass distribution of the $K\pi$ pairs selected with the cuts for the D^0–tagged sample in the group of events for which the refitting procedure was imposed.

Chapter 5

Methods of the Asymmetry and $\Delta G/G$ Extraction

In this chapter methods of the asymmetry and $\Delta G/G$ extraction are presented. First, the dilution factors that enter the formulas leading to the result on the gluon polarisation are discussed. Then different methods for the calculation of the $\Delta G/G$ are reviewed. The discussion starts with the simplest method, that takes into account only the numbers of the open charm events registered in both target cells, and concludes with a method which encompasses different spectrometer acceptances for the events from the target cells, and takes into account the fact that some of the events carry more information on the $\Delta G/G$ quantity than the others. These methods have already been presented in details in a number of elaboration [131–135]. Therefore here their description will be limited to the most important features.

5.1 Factors Diluting the Asymmetry Measurement

Five quantities dilute the measurement of the spin dependent cross-section asymmetry, (see Sec. 1.6.4): the material dilution factor f, the level of the beam polarisation P_B, the level of the target polarisation P_T, the depolarisation factor D and the signal-to-background ratio $S/(S+B)$. An additional factor appears in a transformation from the asymmetry to the $\Delta G/G$: a partonic asymmetry, $\hat{a}_{LL}$. In this section general description of f, P_B, P_T, D and $\hat{a}_{LL}$ will be presented. A more detailed discussion of the methods leading to the $\hat{a}_{LL}$ and the $S/(S+B)$ estimation for each open charm event will be given in the next chapter.

5.1.1 Dilution Factor f

A dilution factor f is a fraction of all the muon scatterings that occur on the deuterons. The ^{6}LiD material had been chosen as a target, since it is characterised by a high deuteron content. The ^{6}LiD system can be treated as a combination of two D and one ^{4}He nuclei [136]. Both deuterons can be polarised in the DNP process while the helium nucleus stays unpolarised (its spin is zero). Therefore the amount of the deuterons in the ^{6}LiD material is 50%. Apart from the ^{6}LiD, the target material contains many other elements which enrich the fraction of the material that can not be polarised. Information on these impurities is given in Tab. 2.1. With n_{pol} being a number of the polarisable nuclei (deuteron) inside the target material, and n_i a number of the unpolarisable nuclei of the i kind, the dilution factor is defined as:

$$f = \rho \frac{n_{pol}\sigma_{pol}}{n_{pol}\sigma_{pol} + \sum_i n_i \sigma_i} \tag{5.1}$$

In this equation the sum runs over all the unpolarisable elements while σ_{pol} and σ_i are the cross-sections for interactions between a muon and a nucleus of a given kind. The cross-sections depend on the kinematics of the interaction. Therefore the dilution factor is a function parameterised with x and y variables, $f(x, y)$ [137]. The unpolarised radiative correction are taken into account in the ρ factor. The corrections were calculated with a TERAD program [138] and take into account only the inelastic tail which corresponds to the inelastic lepton-nucleon scaterrings accompanied by radiative photons emissions. The elastics and quasi-elastic tails are not used as a reconstruction of hadrons in the final state proofs that an inelastic interaction took place. In Fig. 5.1 the f factor is plotted as a function of x and y variables. Also the distribution of f in the D^0–tagged sample is presented. The mean value for that distribution is 0.41.

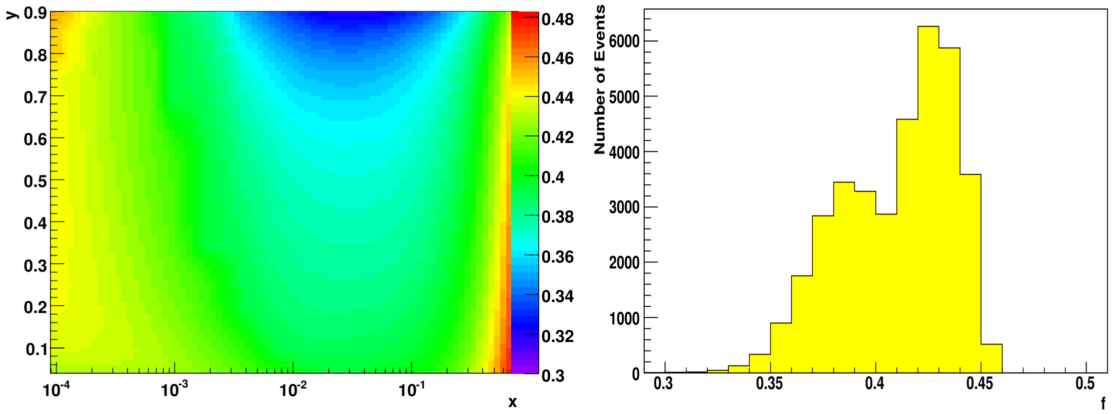

Figure 5.1: Left: parameterisation of f in terms of x and y. Right: f distribution in the D^0–tagged sample.

5.1.2 Beam Polarisation

Polarisation of the incoming muons is not measured in COMPASS. It was precisely determined by the SMC. As the beamlines used by the two experiments are the same, the SMC measurements are used in the current programme. The polarisation of muons is a function of their momentum. In Fig. 5.2 (left) the dependence between the polarisation and the momentum is presented for 2002–2003 and 2004 data taking periods. As it was described in Sec. 2.1 the polarisation in 2004 was slightly higher due to different selection of the secondary beam hadrons. The average muon polarisations were: -0.76 for 2002–2003 and -0.81 for 2004. The negative signs of the above values mean that the muons were polarised opposite to their flight direction, that is anti-parallel to the Z axis. The distributions of the muon polarisation for the samples with D^0–tagged events are presented in Fig. 5.2 (right).

5.1.3 Target Polarisation

The target polarisation is determined by ten NMR coils equally spaced and spirally distributed along both target cells. The polarisation is measured every 5–15 minutes during the run. Then it is averaged over the whole run and a given target cell. Finally for each run two values are stored and are accessible by PHAST, one for the upstream and one for the downstream cell. The distributions of the target polarisations for both cells for the sample of events with D^0–tagged candidates are presented in Fig. 5.3. The average absolute polarisations for this group of events are 51.9% and 49.8% for the upstream and the downstream cells, respectively. The polarisations of the cells are inverted every 8 hours. The level of polarisation is retained in that process. The data recorded during the inversion are excluded from the analysis, as they may be biased by an additional systematic error, difficult to estimate.

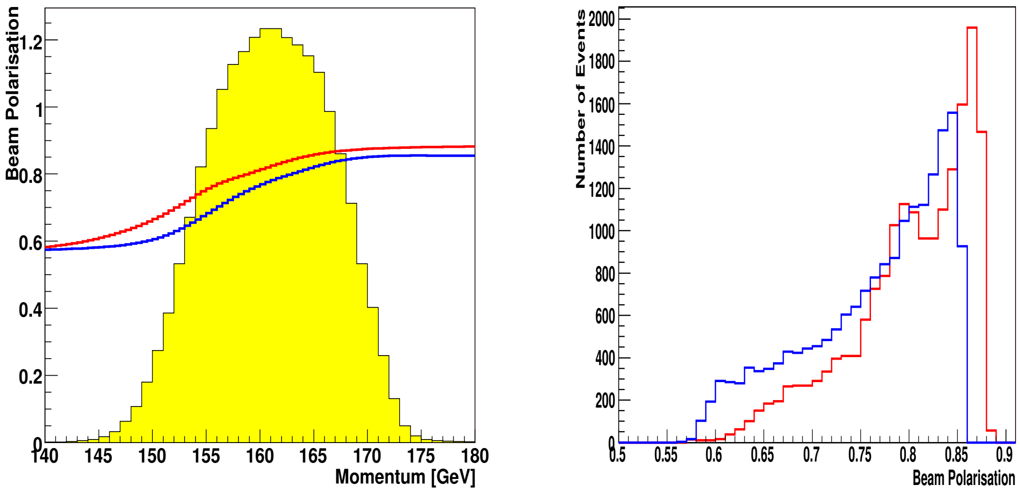

Figure 5.2: Left: momentum dependence of the muon polarisation for 2002–2003 (blue) and for 2004 (red). The momentum profile of the COMPASS beam is also plotted. Normalisation is arbitrary. Right: beam polarisation distribution for the D^0–tagged sample, for 2002–2003 (blue) and for 2004 (red).

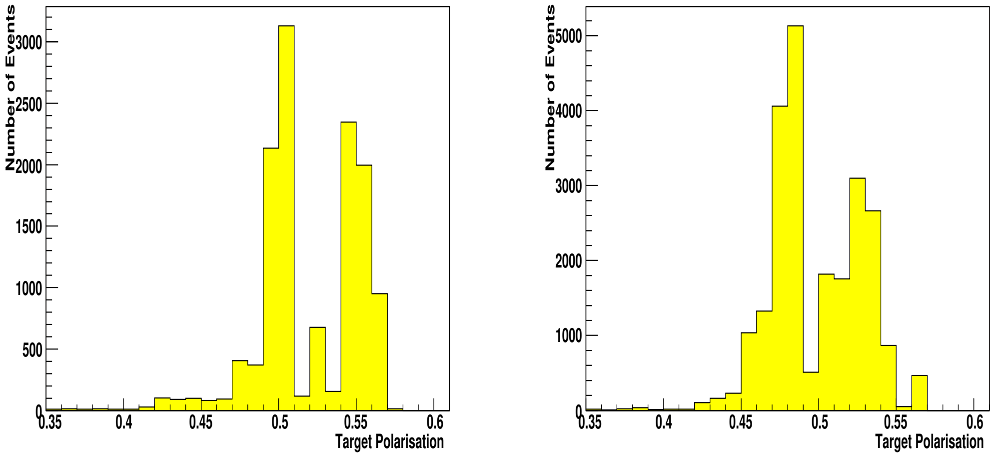

Figure 5.3: Absolute polarisation values of the upstream (left) and downstream (right) target cells for the events with D^0–tagged candidates.

5.1.4 Depolarisation Factor and Partonic Asymmetry

The depolarisation factor D describes the polarisation transfer from a polarised muon to a virtual photon that is interacting with a target. It can be expressed through kinematical variables Q^2 and y and is in a range [0,1], see Sec. 1.5.2.

The partonic asymmetry $\hat{a}_{LL}$ relates the virtual photon-nucleon cross-section asymmetry to the gluon polarisation, Eq. (1.74). It is a function of the inclusive variables defining the kinematics of the virtual photon-nucleon scattering, Q^2 and x, and other variables that characterise the parton kinematics [139, 140]. These are:

$$x_p = \frac{x}{x_g} \tag{5.2}$$

$$z_q = \frac{\mathbf{P} \cdot \mathbf{P_q}}{\mathbf{P} \cdot \mathbf{q}} \tag{5.3}$$

$$\cos\phi = \frac{(\overrightarrow{P} \times \overrightarrow{k}) \cdot (\overrightarrow{P} \times \overrightarrow{P_q})}{|\overrightarrow{P} \times \overrightarrow{k}| \cdot |\overrightarrow{P} \times \overrightarrow{P_q}|} \tag{5.4}$$

where $\mathbf{P}$, $\mathbf{k}$, $\mathbf{q}$ and $\mathbf{P_q}$ are the four vectors describing the target nucleon, interacting muon, virtual photon and the produced charm quark, respectively. Additionally, the mass of the charm quark has to be used as an input for the $\hat{a}_{LL}$ calculation. Finally:

$$\hat{a}_{LL} = \hat{a}_{LL}(x, Q^2, x_p, z_q, \cos\phi, m_c) \tag{5.5}$$

The formula for $\hat{a}_{LL}$ is known to the first order in α_S.

The parton kinematics of each event cannot be calculated exactly, as the measurement is limited to only one charmed meson per event. In most cases the second meson escapes from the reaction undetected. Therefore $\hat{a}_{LL}$ is not a direct observable. There are two possible methods to overcome this. The first one is to use the mean value of $\hat{a}_{LL}$ obtained from the Monte Carlo simulation. The other is to create a parameterisation of $\hat{a}_{LL}$ based on the kinematical variables that are measured for each event. Such parameterisation will not predict the accurate value of $\hat{a}_{LL}$, but will give its better estimate than a simple average. The parameterisation can be obtained using a Monte Carlo sample where for each event the true $\hat{a}_{LL}$ is known. In this analysis, such parameterisation was indeed created and used. The procedure applied for its preparation will be discussed in Sec. 6.1.

5.2 The First Order Unweighted Method

In 2002–2004 COMPASS used the target divided into two separate cells, upstream and downstream, which here will be denoted by subscripts u and d. The polarisations of the two cells were opposite. They were reversed every 8 hours. The variables that will be used for the description of the target setup with the polarisation of the upstream cell pointing in the direction of the beam polarisation will be marked with primes. In Fig. 5.4 the two setups are shown.

The beam fluxes going through both target cells are equal. This was assured by the beam flux equalisation cut presented in Sec. 4.2.4. The process of the polarisation reversal may change slightly the target localisation. Therefore two fluxes, Φ and Φ', corresponding to two target setups, are used here. The polarisation of the muon beam is independent of the targets and is described by one variable, P_B.

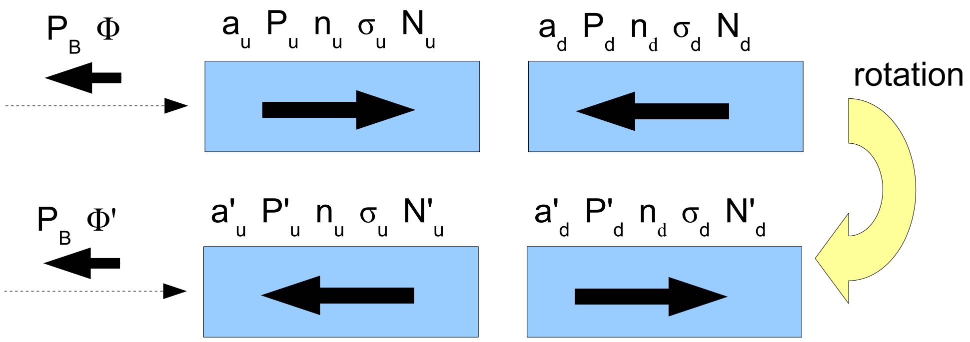

Figure 5.4: Polarisations of the target cells. Listed are variables essential for the analysis.

Spectrometer acceptances for the open charm mesons produced in the upstream and downstream target cells are different. In addition the acceptance for the events coming from a given cell may be slightly changed during the polarisation reversal. Therefore four independent variables, a_u, a_d, a'_u and a'_d describing the acceptance for the open charm events are introduced.

A parameter that is important for the description of the target material is the number of scattering centres. This number depends on the target cell and is described by two values n_u and n_d.

The σ_u and σ_d denote the average cross-sections for the interactions in the upstream and the downstream target cells, respectively. They are defined as:

$$\sigma_{u,d} = \frac{n_{pol\ u,d}\,\sigma_{pol} + \sum_i n_{i\ u,d}\,\sigma_i}{n_{pol\ u,d} + \sum_i n_{i\ u,d}} \tag{5.6}$$

In the unweighted methods presented in this and in the next section, the values of f, P_B, D, $S/(S+B)$ and targets polarisations are averaged over a whole data taking season. This is of course not the optimal approach, as all these quantities vary from one event to another. This drawback will be removed in the weighted methods, later in this chapter.

Numbers of the open charm meson candidates registered in the spectrometer and coming from a given target cell polarised in a given direction are denoted by N_u, N_d, N'_u and N'_d. They fulfil the equations:

$$N_u = \Phi a_u n_u \sigma_u (1 + kfP_B P_u D A^{\gamma^* N}) \tag{5.7}$$

$$N_d = \Phi a_d n_d \sigma_d (1 + kfP_B P_d D A^{\gamma^* N}) \tag{5.8}$$

$$N'_u = \Phi' a'_u n_u \sigma_u (1 + kfP_B P'_u D A^{\gamma^* N}) \tag{5.9}$$

$$N'_d = \Phi' a'_d n_d \sigma_d (1 + kfP_B P'_d D A^{\gamma^* N}) \tag{5.10}$$

where $A^{\gamma^* N}$ is the photon-nucleon asymmetry, to be extracted in the analysis and $k = S/(S+B)$. The asymmetries that are accessible directly at the measurement level are the counting rate asymmetries for the production of the open charm mesons:

$$A_I^{exp} = \frac{N_u - N_d}{N_u + N_d} \tag{5.11}$$

$$A_{II}^{exp} = \frac{N'_d - N'_u}{N'_d + N'_u} \tag{5.12}$$

These asymmetries can be rewritten using Eq. (5.7–5.10):

$$A_I^{exp} = \frac{a_u n_u \sigma_u - a_d n_d \sigma_d + kfP_B D A^{\gamma^* N}(P_u a_u n_u \sigma_u - P_d a_d n_d \sigma_d)}{a_u n_u \sigma_u + a_d n_d \sigma_d + kfP_B D A^{\gamma^* N}(P_u a_u n_u \sigma_u + P_d a_d n_d \sigma_d)} \tag{5.13}$$

$$A_{II}^{exp} = \frac{a'_d n_d \sigma_d - a'_u n_u \sigma_u + kfP_B D A^{\gamma^* N}(P'_d a'_d n_d \sigma_d - P'_u a'_u n_u \sigma_u)}{a'_d n_d \sigma_d + a'_u n_u \sigma_u + kfP_B D A^{\gamma^* N}(P'_d a'_d n_d \sigma_d + P'_u a'_u n_u \sigma_u)} \tag{5.14}$$

Assuming that both target cells are equally filled with the material of the same composition: $n_d \sigma_d = n_u \sigma_u$ and introducing a variable $\beta = kfP_B D P_T$, where P_T is an average target polarisation given with:

$$P_T = \frac{1}{2}\Big(\frac{P_u a_u - P_d a_d}{a_u + a_d} + \frac{P'_d a'_d - P'_u a'_u}{a'_d + a'_u}\Big) \tag{5.15}$$

the Eq. (5.13) and (5.14) can be put in a form:

$$A_I^{exp} = \frac{a_u - a_d + \beta A^{\gamma^* N}(a_u + a_d)}{a_u + a_d + \beta A^{\gamma^* N}(a_u - a_d)} \tag{5.16}$$

$$A_{II}^{exp} = \frac{a'_d - a'_u + \beta A^{\gamma^* N}(a'_d + a'_u)}{a'_d + a'_u + \beta A^{\gamma^* N}(a'_d - a'_u)} \tag{5.17}$$

Especially for the open charm analysis the acceptance for the downstream cell is considerably larger than the acceptance for the upstream one. This arises for instance from the soft pion reconstruction efficiency which is much smaller for the D^* states produced in the upstream cell. The ratio of acceptances is described by variables r and r': $r = a_u/a_d$ and $r' = a'_u/a'_d$. It may be assumed that these ratios are constant and independent of the polarisation of the target cells, $r = r'$. With this assumption:

$$A_I^{exp} + A_{II}^{exp} = \frac{8r^2\beta}{(1+r)^2} A^{\gamma^* N} \tag{5.18}$$

As asymmetries are expected to be small, terms proportional to $(A^{\gamma^* N})^2$ were neglected in the above equation. Thus:

$$A^{\gamma^* N} = \frac{(1+r)^2}{4r^2} \frac{1}{kfP_B D P_T} \frac{(A_I^{exp} + A_{II}^{exp})}{2} \tag{5.19}$$

If the acceptances were equal for both cells, $r = 1$, the formula would be further simplified and given by:

$$A^{\gamma^* N} = \frac{1}{kfP_B D P_T} \frac{(A_I^{exp} + A_{II}^{exp})}{2} \tag{5.20}$$

However for the open charm studies the acceptance difference is of the order of 40% and Eq. (5.19) has to be used instead. In the equations for P_T and r the ratios of acceptances can be approximated by the ratios of the number of events registered in a given cell. This leads to the following approximation of P_T and r:

$$P_T \approx \frac{1}{2}\Big(\frac{P_u N_u - P_d N_d}{N_u + N_d} + \frac{P'_d N'_d - P'_u N'_u}{N'_d + N'_u}\Big) \tag{5.21}$$

$$r \approx \frac{N_u}{N_d} \tag{5.22}$$

The $A^{\gamma^* N}$ calculated with Eq. (5.19) can be translated into $\Delta G/G$ dividing it by the average $\hat{a}_{LL}$ value which can be obtained from the Monte Carlo simulation.

$$\left(\frac{\Delta G}{G}\right)_{\text{FOUM}} = \frac{1}{\langle \hat{a}_{LL} \rangle} \frac{(1+r)^2}{4r^2} \frac{1}{kfP_B D P_T} \frac{(A_I^{exp} + A_{II}^{exp})}{2} \tag{5.23}$$

The method presented here is called the **F**irst **O**rder **U**nweighted **M**ethod (FOUM) for the $\Delta G/G$ extraction. It is not correct if the asymmetry is large and the terms with $(A^{\gamma^* N})^2$ are not negligible. To properly treat the not equal acceptances for the two target cells the **S**econd **O**rder **U**nweighted **M**ethod (SOUM) has to be introduced.

5.3 The Second Order Unweighted Method

In the Second Order Unweighted Method a new variable is used. It is a ratio of the counting rates, defined as:

$$\delta = \frac{N_u N'_d}{N_d N'_u} \tag{5.24}$$

With the same assumption as previously, *i.e.* $\sigma_d n_d = \sigma_u n_u$, the above definition can be rewritten as:

$$\delta = \frac{a_u a'_d (1 + kfP_B P_u D A^{\gamma^* N})(1 + kfP_B P'_d D A^{\gamma^* N})}{a_d a'_u (1 + kfP_B P_d D A^{\gamma^* N})(1 + kfP_B P'_u D A^{\gamma^* N})} \tag{5.25}$$

Further, imposing also an assumption that the double ratio of acceptances, $a_u a'_d / a_d a'_u$, is equal to 1, a second order equation for the $A^{\gamma^* N}$ is obtained:

$$a(A^{\gamma^* N})^2 + bA^{\gamma^* N} + c = 0 \tag{5.26}$$

with:

$$a = \delta \beta'_u \beta_d - \beta_u \beta'_d \tag{5.27}$$

$$b = \delta(\beta'_u + \beta_d) - (\beta_u + \beta'_d) \tag{5.28}$$

$$c = \delta - 1 \tag{5.29}$$

Here $\beta_h = kfP_B P_h D$ and h denotes a given target cell with a given polarisation orientation. The second order equation (5.26) leads to:

$$A^{\gamma^* N} = \frac{\pm\sqrt{b^2 - 4ac} - b}{2a} \tag{5.30}$$

A sign before the square root depends on the sign of the polarisation P_u. As the f, D, P_B and the target cell polarisations are different for different events, a mean value of β should be taken, and $\beta_h \rightarrow \langle \beta_h \rangle$ with:

$$\langle \beta_h \rangle \approx \frac{\sum_i f_i P_{B\,i} P_{h\,i} k D_i}{N_h} \tag{5.31}$$

Here index i runs over all events registered in a given target cell with a given polarisation direction. The $\Delta G/G$ value is then calculated as before, that is dividing the asymmetry by the $\langle \hat{a}_{LL} \rangle$ obtained from the Monte Carlo simulation. The Second Order Unweighted Method treats properly the not equal acceptances for the two target halves. However it is still not the optimal method for the $\Delta G/G$ calculation, as it is based on the average values of $\langle \beta_h \rangle$ and $\langle \hat{a}_{LL} \rangle$. With the knowledge of β and $\hat{a}_{LL}$ on an event–by–event basis the Weighted Methods can be introduced.

5.4 The First Order Weighted Method

The experimental asymmetries given by Eqs (5.11–5.12) and the procedure leading to the $\Delta G/G$ calculation with the FOUM treat all the events from the open charm sample in exactly the same way. However this is not the optimal approach as for each event f, D, P_B and polarisation of a target cell may be different. Also the $\hat{a}_{LL}$ value differs for different PGF events. Additionally the reconstructed mass of the D^0 can be closer or further away from the centre of the D^0 signal and therefore the k parameter is mass dependent:

$$k \equiv k(m) = \frac{S(m)}{S(m) + B(m)} \tag{5.32}$$

These features of the open charm meson sample inspired the introduction of the weighted method which takes into account the fact that events carry various amount of information on the $\Delta G/G$. In the weighted method, with each event i a weight w_i is associated. The asymmetry may now be calculated in a number of bins into which the open charm sample can be divided, according to the weight value. In each bin marked with j the asymmetry is approximated with:

$$A_j^{\gamma^* N} = \frac{1}{2R}\frac{1}{w_j}(A_{I\,j}^{exp} + A_{II\,j}^{exp}) \tag{5.33}$$

where $A_{I\,j}^{exp}$ and $A_{II\,j}^{exp}$ are the counting rate asymmetries introduced with the FOUM but calculated for the events from a given bin j. The w_j is the mean weight for a given bin, while R is a quantity, described later, independent on the bin number. Each $A_j^{\gamma^* N}$ has a statistical error equal to:

$$\sigma_{A_j^{\gamma^* N}} \approx \frac{1}{2R}\frac{1}{w_j}\sqrt{\frac{1}{N_{u\,j} + N_{d\,j}} + \frac{1}{N'_{d\,j} + N'_{u\,j}}} \tag{5.34}$$

The above approximation holds if $N_{u\,j} \approx N_{d\,j}$ and $N'_{u\,j} \approx N'_{d\,j}$. The total asymmetry of the sample is calculated as the weighted mean of all $A_j^{\gamma^* N}$ values:

$$A^{\gamma^* N} = \frac{\sum\limits_j A_j^{\gamma^* N} \cdot \left(\frac{1}{\sigma_{A_j^{\gamma^* N}}}\right)^2}{\sum\limits_j \left(\frac{1}{\sigma_{A_j^{\gamma^* N}}}\right)^2} \tag{5.35}$$

$$\sigma_{A^{\gamma^* N}} = \sqrt{\frac{1}{\sum\limits_j \left(\frac{1}{\sigma_{A_j^{\gamma^* N}}}\right)^2}} \tag{5.36}$$

Inserting Eq. (5.33) and (5.34) into (5.35) the formula for $A^{\gamma^* N}$ reads:

$$A^{\gamma^* N} = \frac{1}{2R}\left(\frac{\sum_j w_j (N_{u\,j} - N_{d\,j})}{\sum_j w_j^2 (N_{u\,j} + N_{d\,j})} + \frac{\sum_j w_j (N'_{d\,j} - N'_{u\,j})}{\sum_j w_j^2 (N'_{d\,j} + N'_{u\,j})}\right) \tag{5.37}$$

The number of bins can be enlarged until each bin encompasses only one event. Then the above formula can be rewritten as follows:

$$A^{\gamma^* N} = \frac{1}{2R}\left(\frac{\sum_i^{N_u} w_i - \sum_i^{N_d} w_i}{\sum_i^{N_u} w_i^2 + \sum_i^{N_d} w_i^2} + \frac{\sum_i^{N'_d} w_i - \sum_i^{N'_u} w_i}{\sum_i^{N'_d} w_i^2 + \sum_i^{N'_u} w_i^2}\right) \tag{5.38}$$

and the uncertainty is given by:

$$\sigma_{A^{\gamma^* N}} = \frac{1}{2R}\sqrt{\frac{1}{\sum_i^{N_u} w_i^2 + \sum_i^{N_d} w_i^2} + \frac{1}{\sum_i^{N'_d} w_i^2 + \sum_i^{N'_u} w_i^2}} \tag{5.39}$$

In Eq. (5.38–5.39) summations run over all the weights corresponding to events recorded in a given target cell polarised in a given direction. The form of the weights should be optimised to best describe the amount of information on the $\Delta G/G$ carried by a given event. For this purpose the weight including all the variables, P_B, f, D, k and the target polarisation, seems to be appropriate. However the polarisation of the target is not constant, neither its value is changing randomly. After the maximal polarisation is obtained in the DNP procedure, its value is decreasing with time. If the monotonically decreasing function is included in the weight, it will lead to the systematic bias of the asymmetry. Therefore the target polarisation was excluded from w. Finally for a given open charm event with a reconstructed mass m_i, the weight is defined as:

$$w_i = f_i|P_{B\,i}|D_i\frac{S(m_i)}{S(m_i)+B(m_i)} \tag{5.40}$$

The target polarisation enters the Eq. (5.38) through R:

$$R = |P_T| \tag{5.41}$$

where P_T, Eq. (5.21), is a mean target cells polarisation for the data taking season.

The final goal of the measurement is the determination of the $\Delta G/G$ value. The **F**irst **O**rder **W**eighted **M**ethod (FOWM) can be extended to lead directly to the $\Delta G/G$ evaluation. The weight should be just supplemented by the $\hat{a}_{LL}$ variable. Then:

$$(\Delta G/G)_{\text{FOWM}} = \frac{1}{2|P_T|}\left(\frac{\sum_i^{N_u} W_i - \sum_i^{N_d} W_i}{\sum_i^{N_u} W_i^2 + \sum_i^{N_d} W_i^2} + \frac{\sum_i^{N'_d} W_i - \sum_i^{N'_u} W_i}{\sum_i^{N'_d} W_i^2 + \sum_i^{N'_u} W_i^2}\right) \tag{5.42}$$

with:

$$W_i = f_i|P_{B\,i}|D_i\hat{a}_{LL\,i}\frac{S(m_i)}{S(m_i)+B(m_i)} \tag{5.43}$$

The approach presented in this section does not take into account different acceptances for events coming from upstream and downstream cells. This can be partially included by introducing the acceptance ratio, cf. [135], and proceeding similarly to the FOUM approach. However the more proper way of encompassing both, the weights and the various acceptances, is through the **S**econd **O**rder **W**eighted **M**ethod (SOWM).

5.5 The Second Order Weighted Method

A yield of events in a given target cell is a function of a number of variables such as the position of the primary vertex, the kinematics of the interaction etc. All these variables can be combined in a vector $\overrightarrow{X}$. Then the yield can be written as:

$$N_{u,d}(\overrightarrow{X}) = \alpha_{u,d}(\overrightarrow{X})(1 + A^{\gamma^* N}\beta_{u,d}(\overrightarrow{X})) \tag{5.44}$$

with:

$$\alpha_{u,d}(\overrightarrow{X}) = (\Phi a_{u,d} n_{u,d}\sigma_{u,d})(\overrightarrow{X}) \qquad \beta_{u,d}(\overrightarrow{X}) = (kP_B P_{u,d} f D)(\overrightarrow{X}) \tag{5.45}$$

The total number of events is obtained through the integration over $\overrightarrow{X}$:

$$N_{u,d} = \int N_{u,d}(\overrightarrow{X})d\overrightarrow{X} \tag{5.46}$$

For the weighted method this equation is modified into:

$$p_{u,d} = \int w(\overrightarrow{X})N_{u,d}(\overrightarrow{X})d\overrightarrow{X} \tag{5.47}$$

Substituting Eq. (5.44) into (5.47) one gets:

$$\begin{aligned} p_{u,d} &= \int w(\overrightarrow{X})\alpha_{u,d}(\overrightarrow{X})(1 + A^{\gamma^* N}\beta_{u,d}(\overrightarrow{X}))d\overrightarrow{X} \\ &= \int (\Phi n_{u\ d}\sigma_{u\ d})(\overrightarrow{X})d\overrightarrow{X} \cdot \langle a_{u\ d}\rangle(1 + A^{\gamma^* N}\langle\beta_{u,d}\rangle) \end{aligned} \tag{5.48}$$

where:

$$\langle a_{u\ d}\rangle = \frac{\int(\Phi n_{u\ d}\sigma_{u\ d}a_{u,d}w)(\overrightarrow{X})d\overrightarrow{X}}{\int(\Phi n_{u\ d}\sigma_{u\ d})(\overrightarrow{X})d\overrightarrow{X}} \qquad \langle\beta_{u\ d}\rangle = \frac{\int(\alpha\beta w)(\overrightarrow{X})d\overrightarrow{X}}{\int(\alpha w)(\overrightarrow{X})d\overrightarrow{X}} \tag{5.49}$$

The double ratio of events numbers, Eq. (5.24), can now be transformed into a double ratio of p:

$$\delta = \frac{p_u p'_d}{p'_u p_d} \tag{5.50}$$

With an assumption that the double ratio of weight averaged acceptances is equal to unity:

$$\frac{\langle a_u\rangle\langle a'_d\rangle}{\langle a'_u\rangle\langle a_d\rangle} = 1 \tag{5.51}$$

the δ can be written in a form:

$$\delta = \frac{(1 + A^{\gamma^* N}\langle\beta_u\rangle)(1 + A^{\gamma^* N}\langle\beta'_d\rangle)}{(1 + A^{\gamma^* N}\langle\beta'_u\rangle)(1 + A^{\gamma^* N}\langle\beta_d\rangle)} \tag{5.52}$$

and the second order equation for $A^{\gamma^* N}$ is now obtained as:

$$a(A^{\gamma^* N})^2 + bA^{\gamma^* N} + c = 0 \tag{5.53}$$

with:

$$a = \delta\langle\beta'_u\rangle\langle\beta_d\rangle - \langle\beta_u\rangle\langle\beta'_d\rangle \tag{5.54}$$

$$b = \delta(\langle\beta'_u\rangle + \langle\beta_d\rangle) - (\langle\beta_u\rangle + \langle\beta'_d\rangle) \tag{5.55}$$

$$c = \delta - 1 \tag{5.56}$$

and:

$$A^{\gamma^* N} = \frac{\pm\sqrt{b^2 - 4ac} - b}{2a} \tag{5.57}$$

The weight that should be used in the Second Order Weighted Method is a product of P_B, f, D, $k(m)$ and a mean value of target polarisation $|P_T|$ (Eq. (5.21)):

$$w_i = P_{Bi} f_i D_i k(m_i)|P_T| \tag{5.58}$$

In the analysis $\langle\beta\rangle$ is approximated as:

$$\langle\beta_{u,d}\rangle = \frac{\sum_i^{N_{u,d}} w_i\beta_i}{\sum_i^{N_{u,d}} w_i} \tag{5.59}$$

The SOWM approach is the optimal method for the asymmetry extraction as it takes explicitly into account difference of acceptances for the two target cells and the resulting value has the smallest statistical error. As it was presented in Sec. 5.4 the weight (5.58) can be extended to include also the $\hat{a}_{LL}$ parameter and thus the method can be used for the direct calculation of the $\Delta G/G$:

$$W_i = P_{B\,i} f_i D_i \frac{S(m_i)}{S(m_i)+B(m_i)} \hat{a}_{LL\,i} |P_T| \tag{5.60}$$

With this weight:

$$(\Delta G/G)_{\mathrm{SOWM}} = \frac{-\sqrt{b^2-4ac}-b}{2a} \tag{5.61}$$

The sign before the square root is selected by taking into account the sign of the P_u. The Second Order Weighted Method is the one chosen for this analysis. In the next section the statistical error of the method is briefly discussed.

5.6 The Statistical Error for the Second Order Weighted Method

The Second Order Weighted Method for the $\Delta G/G$ extraction is the approach that minimises the statistical error of the measurement. The error is given by [133]:

$$\sigma^2_{\Delta G/G} = \left(\frac{\partial \Delta G/G}{\partial \delta} \sigma_\delta\right)^2 \tag{5.62}$$

It can be calculated with the formula:

$$\sigma^2_{\Delta G/G} = \left(\frac{\partial \Delta G/G}{\partial a}\right)^2 \sigma_a^2 + \left(\frac{\partial \Delta G/G}{\partial b}\right)^2 \sigma_b^2 + \left(\frac{\partial \Delta G/G}{\partial c}\right)^2 \sigma_c^2 \tag{5.63}$$

where σ_a, σ_b and σ_c are:

$$\sigma_a^2 = \left(\frac{\partial a}{\partial \delta}\right)^2 \sigma_\delta^2 \qquad \sigma_b^2 = \left(\frac{\partial b}{\partial \delta}\right)^2 \sigma_\delta^2 \qquad \sigma_c^2 = \left(\frac{\partial c}{\partial \delta}\right)^2 \sigma_\delta^2 \tag{5.64}$$

The error on the δ can be calculated with the following equation:

$$\sigma_\delta^2 = \left(\frac{\partial \delta}{\partial p_u}\right)^2 \sigma^2_{p_u} + \left(\frac{\partial \delta}{\partial p_d}\right)^2 \sigma^2_{p_d} + \left(\frac{\partial \delta}{\partial p'_u}\right)^2 \sigma^2_{p'_u} + \left(\frac{\partial \delta}{\partial p'_d}\right)^2 \sigma^2_{p'_d} \tag{5.65}$$

Finally the errors of p_u, p_d, p'_u and p'_d read:

$$\sigma^2_{p_u} = \sum_i^{N_u} w_i^2 \qquad \sigma^2_{p_d} = \sum_i^{N_d} w_i^2 \qquad \sigma^2_{p'_u} = \sum_i^{N'_u} w_i^2 \qquad \sigma^2_{p'_d} = \sum_i^{N'_d} w_i^2 \tag{5.66}$$

In [133–135] and [141] a profound discussion of the statistical error is presented. All the assumptions, that were made to obtain the estimate presented above, are examined. The conclusion is that the equations for both, $\Delta G/G$ and $\sigma_{\Delta G/G}$, as shown here are sufficiently accurate for this analysis, despite some simplifications in their derivation.

Chapter 6

The Results

In this chapter the result on $\Delta G/G$ obtained with 2002/3/4 COMPASS data is presented. At first a procedure leading to the estimation of the partonic asymmetry $\hat{a}_{LL}$ on an event-by-event bases is described. The procedure is founded on the Neural Network that was created using a sample prepared with a Monte Carlo generator. It will be shown, that the chosen approach reproduces the $\hat{a}_{LL}$ with a correlation factor exceeding 80%. The other topic discussed in this chapter is a correlation between the partonic asymmetry and the strength of the open charm signal. If neglected this effect leads to an underestimation of the statistical error of the measurement and may also induce a systematical bias of the obtained $\Delta G/G$ value. A solution is presented, which is based on the so called binning procedure.

6.1 Estimation of the Partonic Asymmetry

The partonic asymmetry, $\hat{a}_{LL}$, is defined as the ratio of $\gamma^* g$ cross-sections for the interactions leading to the PGF for the helicity dependent and helicity averaged cases, see Eq. (1.73). The $\hat{a}_{LL}$ cannot be calculated directly on an event–by–event basis since the exact parton kinematics is not known, cf. Sec. 5.1.4. However for the Second Order Weighted Method the knowledge of the $\hat{a}_{LL}$ for each event is crucial. The solution to that problem was found in an approximate parameterisation that relates the partonic asymmetry to a number of kinematic variables that are measured for each event. The parameterisation was prepared using a Monte Carlo sample, in which for each event a true $\hat{a}_{LL}$ value was available. In the search for the optimal parameterisation a Neural Network was used. As the $\hat{a}_{LL}$ parameterisation is the only part of the analysis leading to the $\Delta G/G$ calculation where a Monte Carlo input is needed, a more detailed discussion of the procedure is in place.

6.1.1 The Monte Carlo Sample

The AROMA Monte Carlo generator is tailored for the simulation of heavy quarks production through the PGF process. The program was prepared for the lepton-nucleon collisions and encompasses full description of the electroweak lepton-nucleon interactions. The QCD structure of the interactions is described in the Leading Order, while the higher order QCD radiation from the initial and final states are simulated with the parton shower processes. The hadronisation is described by the Lund string model.

The AROMA generator is based on the procedures and numerical algorithms inherited from other Lund Monte Carlo packages. These are LEPTO 6.5 [67], JETSET 7.4[1] [68] and PYTHIA 5.7 [68]. AROMA is also exploiting default parameters that are set in those packages. The option files that are passed as an input to the generator allow to modify those values and tune them for a given purpose. The AROMA generator is described in [142].

For studies leading to the $\hat{a}_{LL}$ parameterisation, AROMA was used to generate a sample of events. During the generation, a pair of the charmed quarks was required to be produced in each event. It was assured that at least one of those quarks fragmented subsequently into a D^* meson. The main modifications introduced to the AROMA default parameters were the following:

- The charm quark mass was set to 1.5 GeV. Other values from the 1.3–1.6 GeV range are also considered as possible. Dependence of the final result of the analysis on the chosen charmed quark mass will be included into systematic error.
- **P**arton **D**istribution **F**unctions (PDF) are probability densities for finding a parton with a given x and Q^2. As mentioned in Sec. 1.6.2, these densities cannot be derived theoretically. They have to be extracted from the experimental results. Various groups work on PDF extraction: CTEQ [143], GRV [144] and MRST [145]. It was decided to use the GRV98 parameterisation in Leading Order.
- The parton shower mechanism was switched off to comply with the Leading Order approach.

A sample prepared with AROMA was processed by the COMGEANT package, where a response of the detector was simulated. The geometrical description of the spectrometer was as in 2004 detector setup. Finally, the sample was reconstructed with CORAL. After all the above steps the sample contained 20 000 events.

For generated events the variables describing parton kinematics are directly accessible. This enables to calculate the $\hat{a}_{LL}$ on an event–by–event basis. A comparison between $\hat{a}_{LL}$ and a set of the kinematical variables, $\overrightarrow{K}$, that are reconstructed in a given event allows to construct a parameterisation:

$$\hat{a}_{LL} \leftrightarrow \overrightarrow{K} = (x, Q^2, ...) \tag{6.1}$$

This parameterisation cannot be accurate as the kinematical variables that are available after reconstruction do not contain full information on the parton kinematics. A method that has the best performance in finding the most efficient parameterisation for a given set of kinematical variables employs a Neural Network.

6.1.2 Basis of the Neural Network

The **N**eural **N**etwork (NN) is a group of software simulated neurons that are interconnected and form a special structure. Artificial neurons are functions receiving a set of numbers, I_j, as an input. The numbers are then weighted by individual weights R_j, summed up and the result is transformed by a non-linear function, Φ. The outcome of the function is an output of the neuron:

$$O = \Phi(\sum_j R_j I_j) \tag{6.2}$$

---

[1] JETSET is a Lund string model for parton hadronisation used both in PYTHIA and LEPTO.

The NN is composed of many neurons grouped into layers. A neuron from a given layer is interconnected with all neurons from a subsequent layer and transfers its output to them. The first layer, called an input layer, receives a set of parameters from the outside. Then, after each neuron processed the input numbers and produced the output, the second layer is activated. This layer is called a hidden layer, as it does not have a direct contact with the outside. The last (output) layer in the network returns the final response. A sketch of a NN is presented in Fig. 6.1.

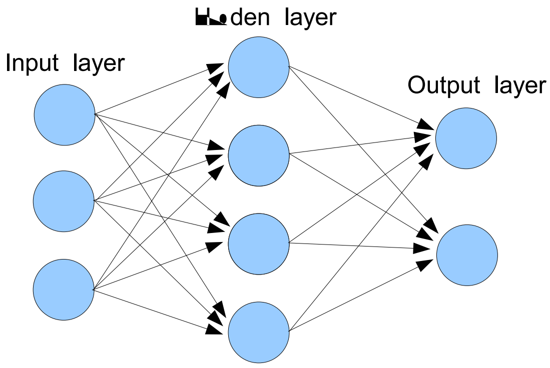

Figure 6.1: Sketch of a Neural Network composed of three layers of neurons. Marked are information spread directions.

Information in the network spreads only in one direction through the layers: from the input layer, through the hidden one, to the output layer. No loops are allowed in this structure. Such network is called feedforward.

The most important feature of the NN is a possibility of learning. The learning is supervised. The network is given a set of pairs (A, B). The aim of the process is to find the best weights for each neuron in such a way that giving an input A from a given pair, a network produces B' at the output, and the mismatch between the output value and the true value from a given pair, B, is the smallest. Here the goal is to match a set of kinematic observables, $\overrightarrow{K}$, with $\hat{a}_{LL}$ value. The criterion defining the optimal weights is the smallest difference between the NN output and the exact value of $\hat{a}_{LL}$. During learning this difference is minimised. In a given moment of learning the difference depends on weights ascribed to neurons. This dependence is called a cost function. The minimisation of the cost function is done by calculating its derivative with respect to the weights. Then the weights are changed in a gradient direction. This procedure is repeated for all the $(\overrightarrow{K}, \hat{a}_{LL})$ pairs from the sample. The process of learning leads to the reduction of the global cost function calculated for the whole sample. The process should be stopped when the reduction becomes slow, as a too long learning may lead to the over–learning, when the NN starts to learn the sample "by heart" and will be useless for other inputs.

The process of NN learning in the studied case is based on two samples. The first one is the main learning sample, which is used to optimise the weights of the network. The other one is a control sample, used to assure that the network is not starting to learn "by heart". Moreover during the learning procedure the network can evolve, that is the number of neurons can be changed. This additionally improves the final mapping of $\hat{a}_{LL}$ with $\overrightarrow{K}$.

6.1.3 Neural Network Parameterisation

The Neural Network for the COMPASS $\hat{a}_{LL}$ parameterisation is prepared using the NetMaker package [146]. The package was implemented for COMPASS and for ICARUS neutrino experiment. The program is written in the C#[2] language and optimised for working with large data sets. It provides a graphical interface for a network preparation and for controlling the learning process. After the process is finalised, a file containing the description of the structure of the network, including all the weights, is prepared. It is a text file written in an XML[3] standard. A special C++ class, that simulates the Neural Network based on the XML file, was prepared and added to the PHAST package. The class allows to run during the analysis the Neural Network obtained with the NetMaker, and predict $\hat{a}_{LL}$ on an event–by–event basis. In Fig. 6.2 the chain leading to the $\hat{a}_{LL}$ estimation in the real data is presented.

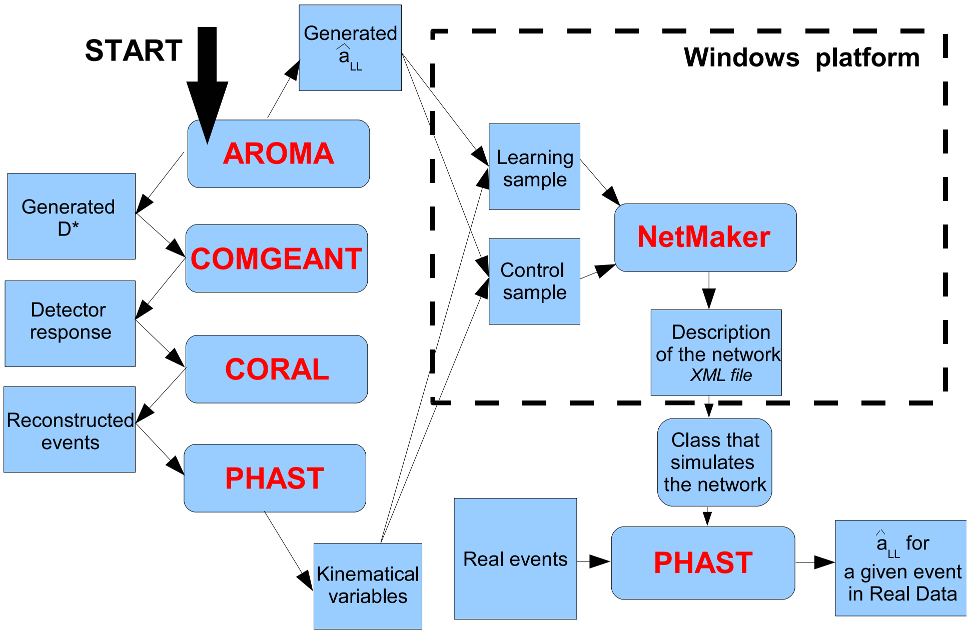

Figure 6.2: Sketch of a procedure leading to the estimation of the $\hat{a}_{LL}$ on an event–by–event basis. The procedure starts with a generation of a Monte Carlo sample in the AROMA–COMGEANT–CORAL chain (left). Then the generated pairs of $(\overrightarrow{K}, \hat{a}_{LL})$ are passed to the NetMaker in two separate samples (centre). The NetMaker prepares the NN (right-top). It is then used in PHAST to estimate the $\hat{a}_{LL}$ for real data events (right-bottom). The whole procedure uses two platforms: Windows and Unix.

A remaining question is a choice of kinematic variables that should be used for the parameterisation. In the previous studies of the open charm channel [131] two variables, namely the fraction of the photon energy carried by D^0 meson, z_{D^0}, and its transverse momentum with respect to the virtual photon direction, p_{TD^0}, were used. In those studies the mapping was done first generating a large Aroma Monte Carlo sample and then determining an average $\hat{a}_{LL}$ values on a grid in z_{D^0} and p_{TD^0}. The main advantage of the NN approach is that the parameterisation is not only optimised, but also it is

---

[2] C# (C *sharp*) is an object-oriented programming language developed by Microsoft and based on C++ syntax.

[3] XML – the Extensible Markup Language is a general-purpose markup language. It provides a set of rules based on markups according to which an information, *e.g.* a structure of network, is described.

prepared faster than using other methods. Therefore it can be based on a larger set of kinematic parameters. Also a comparison of parameterisations obtained with different sets of these parameters can be done. The following sets were tried:

- p_{TD^0}, z_{D^0}
- p_{TD^0}, z_{D^0}, Q^2, x
- p_{TD^0}, z_{D^0}, Q^2, y
- p_{TD^0}, z_{D^0}, Q^2, W^2
- p_{TD^0}, z_{D^0}, Q^2, x, y

Evaluation of a given parameterisation is done using a correlation factor defined as:

$$R = \frac{C}{\sigma_{\mathrm{rec}}\sigma_{\mathrm{gen}}} \tag{6.3}$$

where:

$$C = \frac{1}{N}\sum_{i}^{N}(\hat{a}^{i}_{LL\,\mathrm{rec}} - \langle\hat{a}_{LL\,\mathrm{rec}}\rangle)(\hat{a}^{i}_{LL\,\mathrm{gen}} - \langle\hat{a}_{LL\,\mathrm{gen}}\rangle) \tag{6.4}$$

In this equation $\hat{a}_{LL\,\mathrm{gen}}$ and $\hat{a}_{LL\,\mathrm{rec}}$ are the generated and the reconstructed partonic asymmetries. The summation goes over the whole sample that is used for the NN learning. The σ_{gen} and σ_{rec} are the standard deviations of $\hat{a}_{LL\,\mathrm{gen}}$ and $\hat{a}_{LL\,\mathrm{rec}}$ calculated in the sample. Higher R corresponds to a higher correlation between the $\overrightarrow{K}$ and $\hat{a}_{LL}$ sets.

It appeared that the correlation factors for all the parameterisations are of the same order. Differences between them are not larger than 2%. The highest R, 82%, was obtained for the parameterisation based on p_{TD^0}, z_{D^0}, Q^2, x, y variables. This parametrisation was thus selected for the analysis.

6.1.4 The $\hat{a}_{LL}$ Parameterisation

In Fig. 6.3 the $\hat{a}_{LL}$ parameterisations obtained with the Neural Network method is presented (left) and compared with the one prepared in [131] (right). The correlation factor for the NN parameterisation is 4% higher than that calculated for the other approach. The improvement in the correlation is clearly visible especially for the region of large $\hat{a}_{LL}$, around +0.8, and of small $\hat{a}_{LL}$, around -0.4. The events from both regions are especially important for the $\Delta G/G$ calculation, as the weights ascribed to them have large absolute values. Therefore the Neural Network method has two advantages – it gives a higher correlation factor and it performs much better in the regions important for the analysis.

6.2 Correlation Between $\hat{a}_{LL}$ and $\frac{S}{S+B}$

The Second Order Weighted Method, on which the $\Delta G/G$ extraction is based, requires weights calculated for each event individually. As discussed in Sec. 5.5 the optimal weight is given by:

$$W_i = P_{Bi}(E_\mu)f_i(x,y)D_i(y,Q^2)\frac{S}{S+B}(m_i)\hat{a}_{LLi}(\overrightarrow{K})|P_T| \tag{6.5}$$

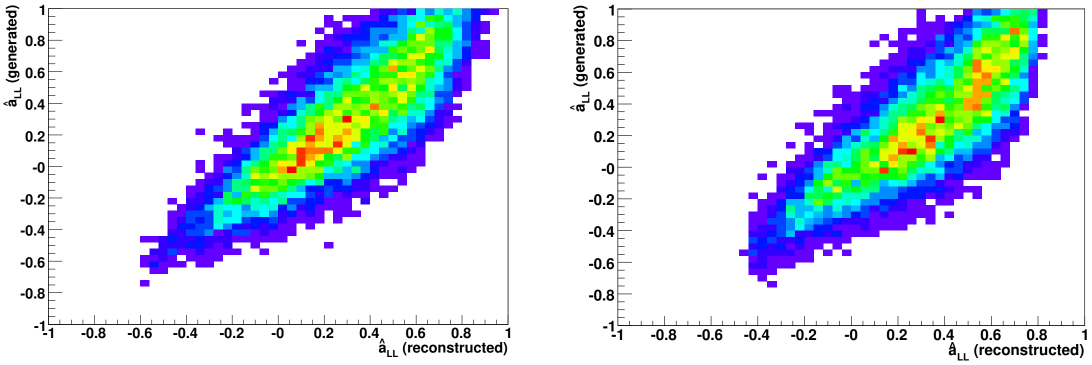

Figure 6.3: Left: the parameterisation of $\hat{a}_{LL}$ obtained with the Neural Network. Right: the parameterisation used before the Neural Network approach was developed [131].

In Sec. 4.3 it was shown that the signal–to–background ratio can be enhanced with specific kinematic cuts. This indicates that $S/(S+B)$ is also a function of a set of kinematic variables:

$$\frac{S}{S+B}(m) \rightarrow \frac{S}{S+B}(m, \overrightarrow{K'}) \tag{6.6}$$

The weight given with Eq. (6.5) contains $S/(S+B)$ averaged in $\overrightarrow{K'}$ over the studied sample:

$$W_i = P_{Bi}(E_\mu) f_i(x,y) D_i(y,Q^2) \Big\langle \frac{S}{S+B}(\overrightarrow{K'}) \Big\rangle (m_i) \hat{a}_{LLi}(\overrightarrow{K}) |P_T| \tag{6.7}$$

This procedure does not take into account a possible correlation between the $\hat{a}_{LL}$ and the $S/(S+B)$ factors due to common variables in $\overrightarrow{K}$ and $\overrightarrow{K'}$ sets. If the correlation is strong, the final result for gluon polarisation may be biased. The problem disappears if the signal–to–background ratio is parameterised not only as a function of mass but also as a function of the most important kinematic variables common for both sets, that is z_{D^0} and $p_{T\,D^0}$. The parameterisation may be based on the open charm signal in the real data or on the signal in the Monte Carlo sample. The former approach cannot be used, as the statistics of the open charm mesons is too small for the multivariable parameterisation, whereas the latter would introduce an additional dependence on the Monte Carlo. Therefore yet another method, not removing the correlation entirely but minimising its influence, is implemented. It is called a binning approach.

The binning method uses a W^0 variable defined as:

$$W_i^0 = f_i P_{Bi} D_i \hat{a}_{LLi} \tag{6.8}$$

The sample of the open charm events is divided into several intervals of W^0, denoted with n. In each interval an independent mass fit is performed. The result of the fit is then used to estimate the $S/(S+B)$ in a given interval. Finally the weight is:

$$W_i = P_{Bi}(E_\mu) f_i(x,y) D_i(y,Q^2) \frac{S}{S+B}(m_i, n) \hat{a}_{LLi}(\overrightarrow{K}) |P_T| \tag{6.9}$$

The number of intervals should be high enough to minimise the $\hat{a}_{LL}$ and $S/(S+B)$ correlation but also small enough to have sufficient number of open charm events in each to obtain reliable mass fits. It was decided to use five and three W^0 bins for the D^0-tagged and the D^0-untagged channels, respectively. The choice of the smaller number of bins for the latter is caused by the worse signal–to–background ratio which results in the less reliable mass fits. The widths of intervals are such that the events are distributed evenly among them.

In Fig. 6.4 it is clearly seen that the two variables, $\hat{a}_{LL}$ and $S/(S+B)$, are correlated: increasing one decreases the other. It is better visible in Fig. 6.5 where mass distributions for the open charm tagged sample for each of the five W^0 bins are presented. The signal deteriorates as the interval is shifted to the higher W^0 values (that is to the higher $\hat{a}_{LL}$): in the first bin it is significantly stronger than in the last one.

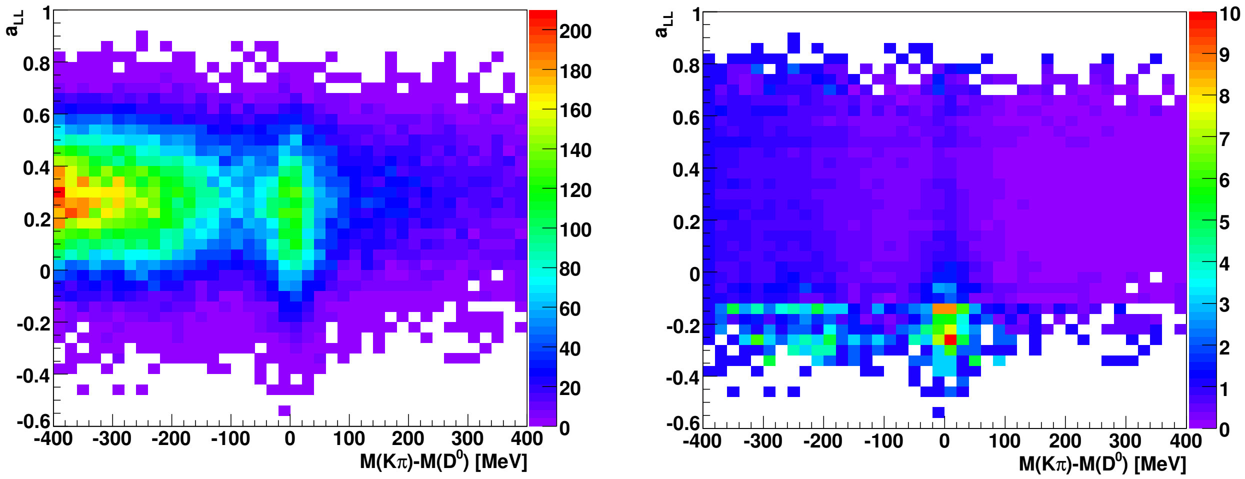

Figure 6.4: Left: distribution of the $a_{LL} = D\hat{a}_{LL}$ estimated with the NN method as a function of mass of the open charm candidates. Right: distribution of the a_{LL} as a function of mass of the open charm candidates normalised to the number of events in the first bin in each row (occupied with at least one event). From the left plot it is visible that the highest number of the open charm candidates is for the a_{LL} of about 0.2, while the highest S/B is for the group of events with a_{LL} below 0, right plot.

The correlation, if neglected, would artificially decrease the error of the $\Delta G/G$ measurement. This would happen as in the weights the $S/(S+B)$ factor averaged over all bins would be used. It is larger than the one calculated in bins of high W^0. Therefore the weights of events characterised with large W^0 would be artificially increased. The correlation may also shift the measured $\Delta G/G$ value, and even change its sign. The binning procedure minimises those effects, but they are not removed completely. Estimation of the residual influence of the correlation, still present inside each bin, will be discussed in chapter 7.

6.3 Result on $\Delta G/G$

For the $\Delta G/G$ calculation, the Second Order Weighted Method, described in Sec. 5.5, is used. The $\hat{a}_{LL}$ values obtained on an event–by–event basis with the NN parameterisation, Sec. 6.1.4, enter the weights. The sample of the open charm events used for the calculations was defined in Sec. 4.6.

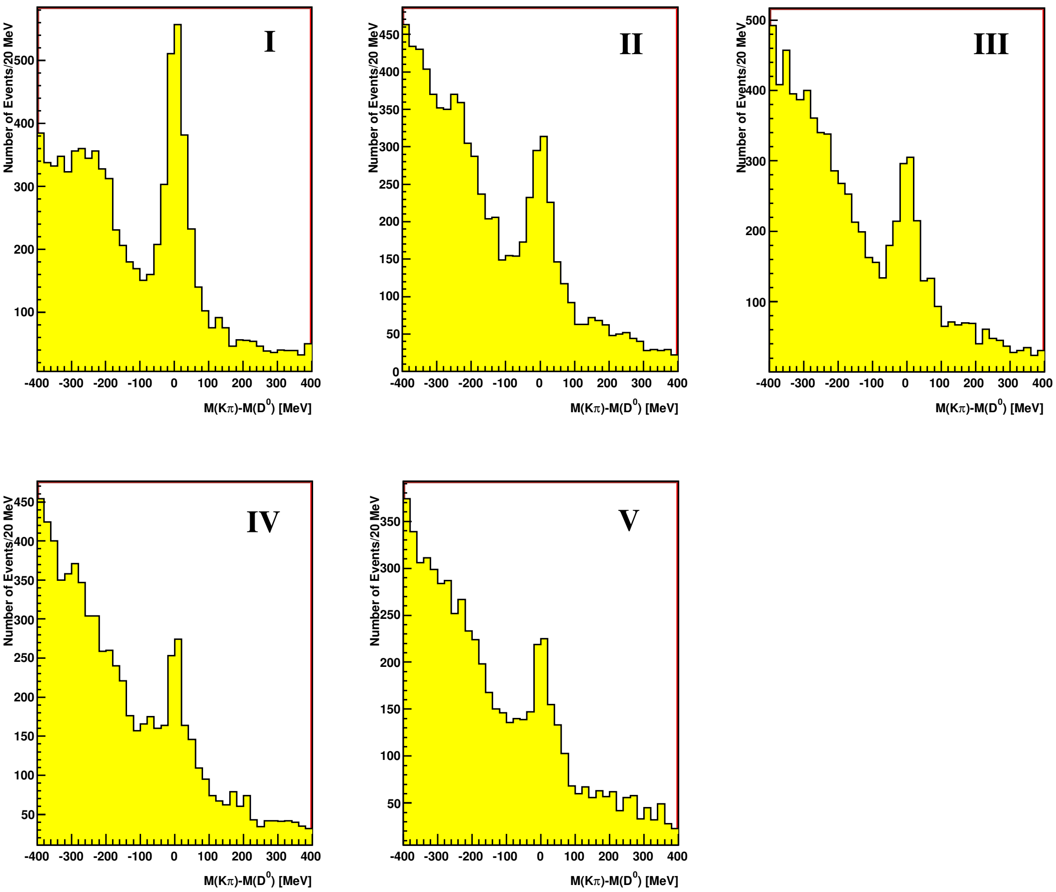

Figure 6.5: The mass distributions of the tagged sample for five W^0 bins.

The $\Delta G/G$ determination relies on the assumption that the spectrometer efficiency remains stable in time. This is however not true, the efficiencies are different in various time intervals. With this in view the gluon polarisation is calculated individually for intervals where the changes in the detector can be neglected. Then the average value is calculated. The procedure is as follows:

- the $(\Delta G/G)_p$ is calculated individually for each data taking period[4]. Subscript p denotes period number.
- The $(\Delta G/G)_y$ is calculated for each year separately as a weighted mean of values obtained for all periods during that year:

$$(\Delta G/G)_y = \frac{\sum_p \frac{(\Delta G/G)_p}{\delta(\Delta G/G)_p^2}}{\sum_p \frac{1}{\delta(\Delta G/G)_p^2}} \tag{6.10}$$

$$\delta(\Delta G/G)_y = \sqrt{\frac{1}{\sum_p \frac{1}{\delta(\Delta G/G)_p^2}}} \tag{6.11}$$

where subscript y denotes a given year.

---

[4] Two periods, P2G02 and P1D03, are artificially divided into two subgroups of runs. The division line for the former is when the repolarisation of the target cells took place. Splitting of the latter corresponds to changes in triggers and detector setup that occurred in the middle of this period.

- The $\Delta G/G$ is calculated for the whole data taking (2002–2004) by taking the average of values obtained for each year.

These three steps are performed separately for both open charm samples, tagged and untagged. The final result of the analysis is obtained as a weighted mean of them. The results for each year and the final $\Delta G/G$ for the 2002–2004 period are presented in Fig. 6.6 and in Tab. 6.1.

The final result for the $\Delta G/G$ from the COMPASS experiment for 2002–4 data taking and for deuteron (that is not correcting for D-state) is:

$$\mathbf{-0.57 \pm 0.41}$$

The error quoted above is statistical. A detailed discussion of the systematic effects on the result is presented in the next chapter.

	D^0–tagged channel		D^0–untagged channel	
Year	$\Delta G/G$	$\delta(\Delta G/G)$	$\Delta G/G$	$\delta(\Delta G/G)$
2002	–2.33	1.43	–0.17	1.68
2003	–0.90	1.04	0.04	1.15
2004	–1.00	0.70	0.38	0.82
Weighted mean:	–1.17	0.54	0.21	0.62
Final result:	$\mathbf{-0.57 \pm 0.41}$			

Table 6.1: The $\Delta G/G$ results year–by–year for both channels, the weighted mean of the values in each channel and the final result for $\Delta G/G$. Errors are statistical.

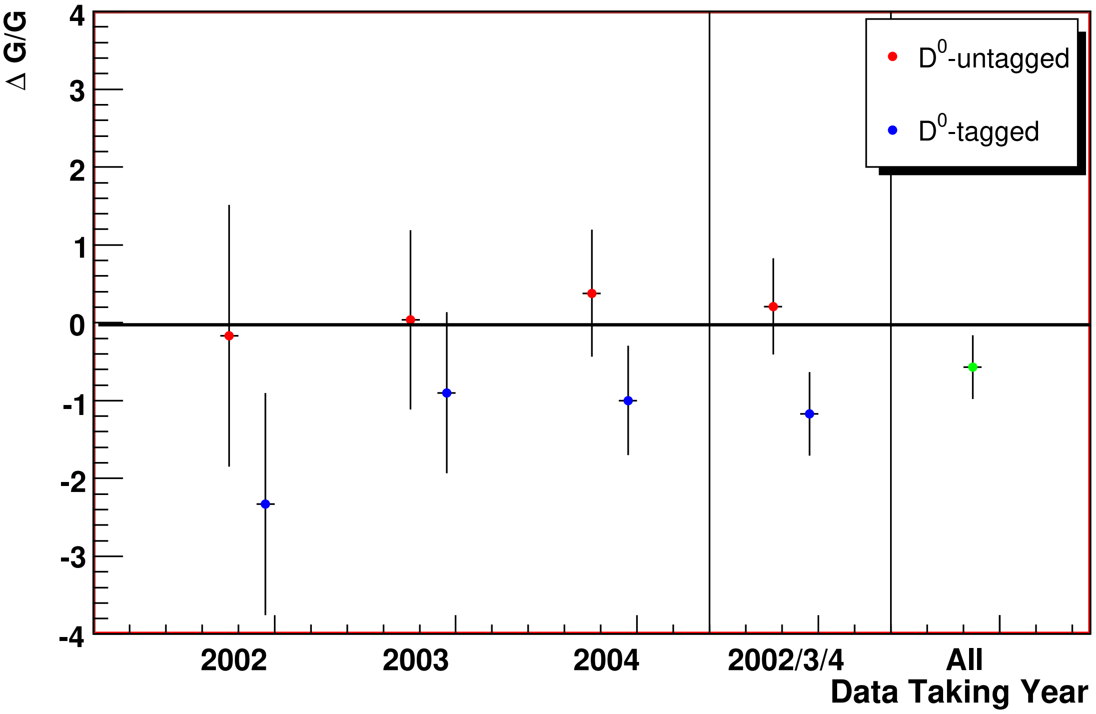

Figure 6.6: The $\Delta G/G$ calculated separately for each year and for the whole 2002–2004 data taking period. Errors are statistical.

The QCD scale for the PGF with $c\bar{c}$ creation is given by the mass of the charm quark and its transverse momentum with respect to the virtual photon:

$$\mu^2 = 4(m_c^2 + p_T^2) \tag{6.12}$$

Here it is of the order of 13 GeV^2, high enough to justify the perturbative treatment of the process. This value was obtained from the sample simulated by AROMA.

To calculate the value of $\Delta G(x_g, \mu^2 = 13\ \mathrm{GeV}^2)$ the distribution of $G(x_g)$ corrected for the COMPASS acceptance is needed. The $G(x_g)$ distribution is obtained using four different sets of parton distribution functions: GRV98, MRST2004 and two versions of CTEQ (CTEQ5M and CTEQ6L), all of them at the LO QCD. The Monte Carlo sample of D^0 events, generated in AROMA–COMGEANT–CORAL chain, is used to obtain the x_g distribution in the sample selected for the analysis, $\zeta(x_g)$ (cf. Fig. 6.7). The $G(x_g)$ corrected with the acceptance is:

$$G_{\mathrm{cor}} = \frac{\int_0^1 \zeta(x_g) G(x_g) dx_g}{\int_0^1 \zeta(x_g) dx_g} \tag{6.13}$$

For the selected sample the average fraction of the nucleon momentum carried by the gluon in the PGF resulting in D^0 production in the final state is $x_g = 0.15$ with RMS of 0.08.

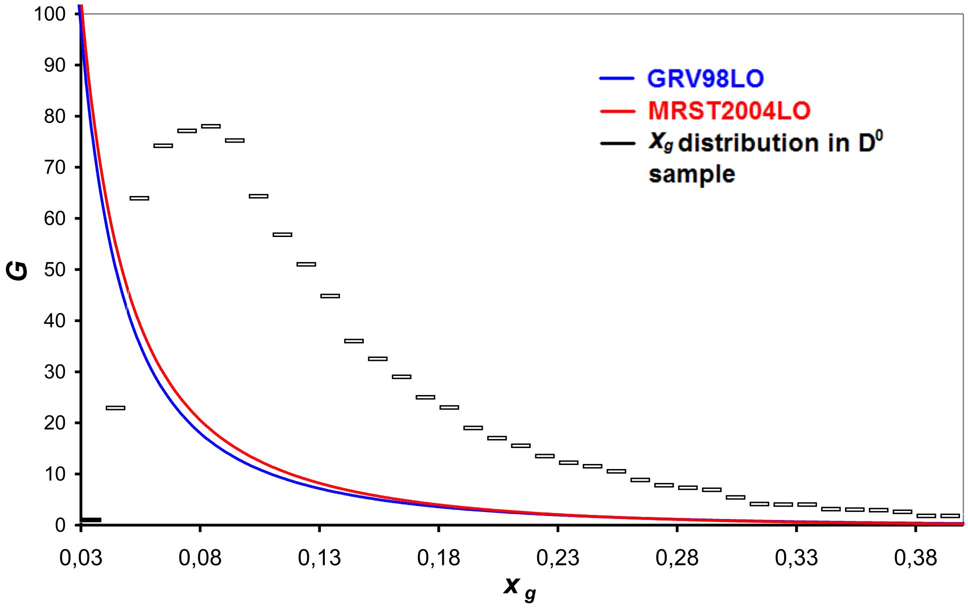

Figure 6.7: The $G(x_g)$ distribution given by GRV98 (blue) and MRST2004 (red). The x_g distribution in the D^0 selected sample (black), normalisation arbitrary.

Finally the $\Delta G(x_g = 0.15, \mu^2 = 13\ \mathrm{GeV}^2)$ is calculated multiplying the value -0.57 ± 0.41 by G_{cor}. The results for different parton distribution functions used for G_{cor} calculation are presented in Tab. 6.2.

The GRV98 was previously used for the $\hat{a}_{LL}$ studies, Sec. 6.1.1. It was thus decided to quote the $\Delta G(x_g = 0.15, \mu^2 = 13\ \mathrm{GeV}^2)$ value obtained for the $G(x_g)$ distribution given with GRV98 as a final result. The difference between the two most distant values, for GRV98 and MRST2004, is treated as a systematic error arising from different G parameterisations. Then:

$$\boldsymbol{\Delta}\mathbf{G}(\mathbf{x_g} = \mathbf{0.15}, \boldsymbol{\mu}^{\mathbf{2}} = \mathbf{13}\ \mathrm{GeV}^{\mathbf{2}}) = -\mathbf{7.4} \pm \mathbf{5.3} \pm \mathbf{1.0}(G\ \text{distribution})$$

PDF	$\Delta G(x_g = 0.15, \mu^2 = 13\ \mathrm{GeV}^2)$	Error
GRV98	-7.4	5.3
MRST2004	-8.4	6.0
CTEQ5M	-8.0	6.7
CTEQ6L	-8.2	5.9

Table 6.2: The $\Delta G(x_g = 0.15, \mu^2 = 13\ \mathrm{GeV}^2)$ calculated from the measured $\Delta G/G$ with $G(x_g)$ given by different parton distribution functions.

Chapter 7

Systematic Effects in the Open Charm Analysis

The sample of the open charm events for the $\Delta G/G$ extraction is small. It is thus expected that the statistical error will contribute substantially to the total uncertainty of the measurement. Different systematic effects may also play a significant role. This chapter is dedicated to the discussion of these effects. In certain cases only qualitative results are possible and in others also numerical estimates of the effects are given.

7.1 Methods for the Systematic Effects Minimisation

Several methods are implemented in the COMPASS analysis chain which aim at minimisation of the influence of the systematic effects on the asymmetry measurement. These are:

1. The stability of the data is monitored on the spill–by–spill bases. The spills that do not satisfy certain criteria, see Sec. 4.2.1, are excluded from the analysis.

2. Reversing the target polarisation induce small shifts in the spectrometer setup. These are reflected in a difference between the ratios of the acceptances for events coming from the upstream and the downstream cells in the two spin configurations. The method for the asymmetry extraction relies on an assumption that this ratio is constant for both configurations, cf. Sec. 5.5. Any deviation from this assumption results in a false asymmetry which biases the measured $\Delta G/G$. There are two known effects induced by spin reversals:

    - movement of the target by about 600 μm;
    - change in the efficiencies of the tracking detectors located close to the target.

    Both effects are caused by the target solenoid field, whose direction changes by 180° during the spin reversal. If the direction of the solenoid field with respect to the polarisation of the target remains the same during the whole data taking period, the above effects will accumulate. The relative direction of the solenoid field with respect to the polarisation should be thus reversed periodically, Fig. 7.1. During the reversal, the old polarisation of the target is lost, and then the new polarisation is built. After re-polarisation a relative direction of the solenoid field and the polarisation is changed. The procedure takes approximately 2–3 days. Therefore it is repeated 1–2 times in the data taking season only.

3. The air temperature in the experimental hall fluctuates with an amplitude of a few degrees and a period of twenty four hours. This reflects the day–night changes in the air temperature outside the hall. The efficiencies of certain detectors may depend on those variations. To decrease a possible influence on the asymmetries, the spin rotation is done 3 times a day, every 8 hours. Therefore every next day, at a given time, the data are taken with an opposite spin configuration.

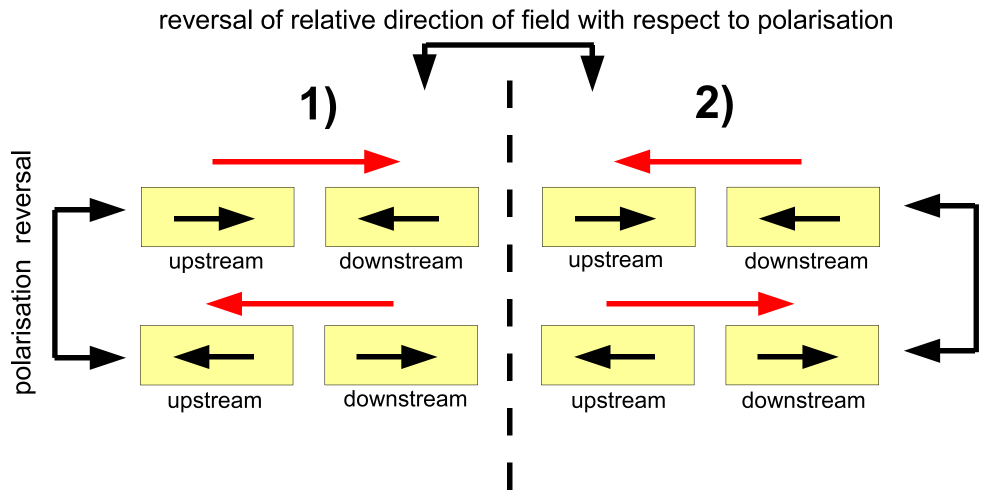

Figure 7.1: Two different relative directions of the solenoid field (red arrow) with respect to polarisation (black arrow). In the left configuration the field is always parallel to the polarisation of the upstream cell, in the right one it is anti-parallel.

7.2 Background Asymmetries

The $K\pi$ pairs that form a background diluting the D^0–tagged or the D^0–untagged signals, can be divided into three categories. There are pairs for which one particle is coming from a D^0 decay and the other does not, pairs coming from decays of resonances like $K^*(892)$, $\rho(770)$, $\phi(1020)$, cf. Sec. 4.7, and finally, random combinations of charged particles outgoing from the primary vertex. All three groups may induce the background asymmetry, A^{BG}.

7.2.1 Sidebands Studies

The sideband method is based on an asymmetry extraction using D^0 candidates selected with the standard cuts but having mass outside the mass range of the open charm signal. For the D^0–untagged sample the mass range under consideration is $[-400,-100]\cup[100,400]$ MeV while for the D^0–tagged sample it is $[-400,-150]\cup[150,400]$ MeV[1].

The studies are based on a quantity calculated in a similar way as the $\Delta G/G$ – using a Second Order Weighted Method with a weight[2]:

$$w = f P_B D \hat{a}_{LL} \tag{7.1}$$

---

[1] All the mass ranges in this chapter are quoted in a scale where 0 MeV corresponds to the D^0 nominal mass.

[2] As the weight does not contain the $S/(S+B)$ factor, the calculated values are marked with primes: $(\Delta G/G)'$. Also to distinguish the calculated value from a real $\Delta G/G$ a subscript is added, here subscript BG is used. These notations will be used also later in this chapter.

In the case of the D^0–tagged sample a second Gaussian, describing the reflection of the $K\pi\pi^0$ decay channel, should be rejected by an additional mass cut. Such cut would largely limit the studied sample, therefore it was not used. The asymmetry resulting from the PGF events from this second Gaussian should not be significant as the $K\pi\pi^0$ bump contains ten times less events than the main D^0 signal.

A dependence of the background asymmetry on the mass range is also studied. The asymmetry may change sign and give an overall background asymmetry equal to zero, while in a given mass range it is large and positive and in another – large and negative. To study this possibility the sideband samples are divided into several mass bins. For the D^0–untagged case the bins are 100 MeV wide. For the D^0–tagged sample, due to the limited statistics, only two bins are used: $[-400, -150]$ and $[150, 400]$ MeV. Moreover, since the experimental setup differs for each data taking season, which may reflect in different background properties, the background asymmetries are calculated separately for the 2002, 2003 and 2004 data. The resulting values are presented in Figs. 7.2 and 7.3. All background asymmetries are consistent with zero. No significant year or mass dependence is visible and therefore it is safe to sum up events from all years of the data taking (cf. Fig. 7.4) and from all mass bins (cf. Fig. 7.5).

The mean values for both channels are (errors are calculated using the formulas for the SOWM with weights defined with Eq. 7.1):

$$(\Delta G/G)'_{\mathrm{BG}}(D^0) = -0.012 \pm 0.016 \tag{7.2}$$

$$(\Delta G/G)'_{\mathrm{BG}}(D^*) = 0.05 \pm 0.14 \tag{7.3}$$

These values should now be divided by the average $S/(S+B)$ ratios for the signal ranges calculated in each channel. The average $S/(S+B)$ values are extracted in [-90, 90] MeV mass ranges, corresponding to approximately $3\,\sigma$ of the D^0 signal. Finally a weighted average of the results on $(\Delta G/G)_{\mathrm{BG}}$ in both channels is calculated. The following estimate for the upper limit of the systematic effects induced by the background asymmetry is obtained:

$$(\Delta G/G)_{\mathrm{BG}}(D^* + D^0) = -0.04 \pm 0.24 \tag{7.4}$$

7.2.2 Wrong Charge Combinations

In the wrong charge combinations studies it was required that both particles forming a D^0 candidate have the same electric charge. Remaining selection cuts were the same as for the standard analysis. For such sample of events, the D^0 meson signal vanishes and a pure background can be analysed.

For the studies the Second Order Weighted Method is employed, where the event weight is of the form:

$$w = f P_B D \hat{a}_{LL} \frac{S}{S+B}(m) \tag{7.5}$$

The $S/(S+B)(m)$ factor is taken from the standard analysis, that is from the samples where the D^0 signals are present.

In case of the D^0–untagged sample for the wrong charge pairs analysis, $K^+\pi^+$ and $K^-\pi^-$ combinations are used. For the D^0–tagged channel four different samples are

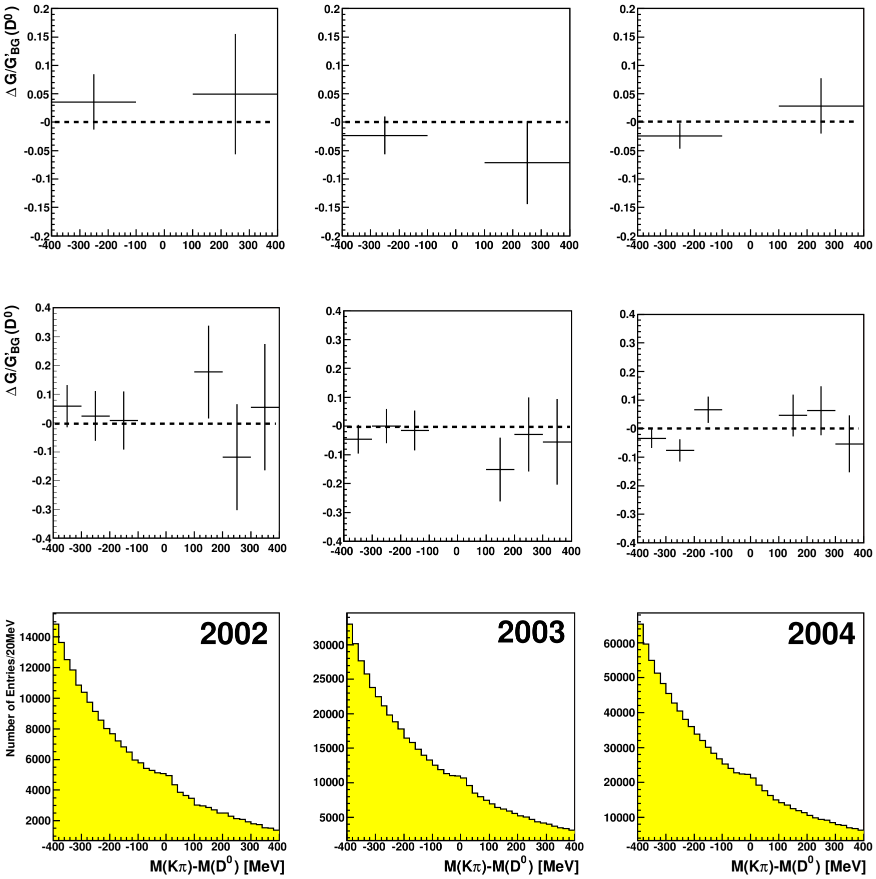

Figure 7.2: The $(\Delta G/G)'_{\rm BG}(D^0)$ in the sidebands. The top row presents the results for $[-400,-100]$ and $[100,400]$ MeV mass bins, the middle row for 100 MeV wide mass bins, while the bottom presents the mass spectra for D^0–untagged channel. Errors are statistical.

taken: $K^+\pi^+\pi_S^-$, $K^+\pi^+\pi_S^+$, $K^-\pi^-\pi_S^-$, $K^-\pi^-\pi_S^+$. Assuming that there may exist small differences in kinematical variables distributions for combinations with two and three particles of the same charge, the background asymmetries are estimated separately for $K^+\pi^+\pi_S^-$, $K^-\pi^-\pi_S^+$ and for $K^+\pi^+\pi_S^+$, $K^-\pi^-\pi_S^-$. The resulting values for different channels are presented in Tab. 7.1. The weighted mean of the results is:

$$(\Delta G/G)_{\rm WCC} = 0.21 \pm 0.47 \tag{7.6}$$

Channel	Result
$K^+\pi^+$ and $K^-\pi^-$	-0.01 ± 0.77
$K^+\pi^+\pi_S^-$ and $K^-\pi^-\pi_S^+$	-0.41 ± 0.79
$K^+\pi^+\pi_S^+$ and $K^-\pi^-\pi_S^-$	1.35 ± 0.94
Weighted mean:	0.21 ± 0.47

Table 7.1: Results for $(\Delta G/G)_{\rm WCC}$ calculated in different channels.

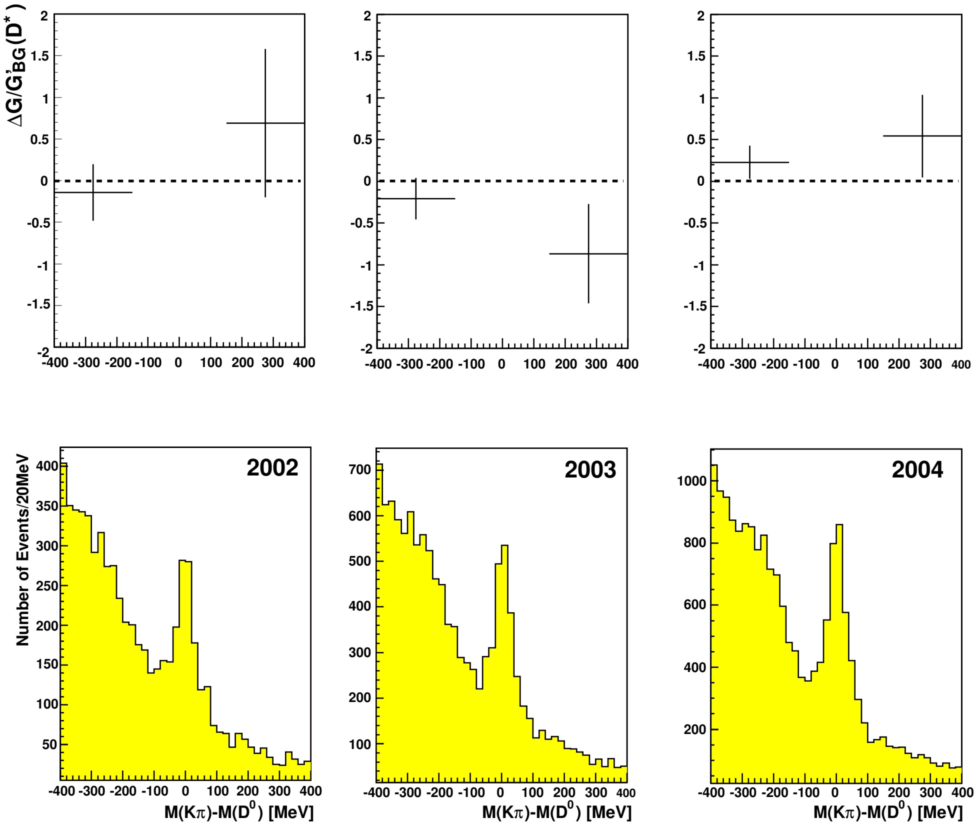

Figure 7.3: Top row: $(\Delta G/G)'_{\mathrm{BG}}(D^*)$ in the sidebands in $[-400,-150]$ and $[150,400]$ MeV bins. Bottom row: mass spectra for D^0–tagged channel. Errors are statistical.

7.2.3 Studies with PID Cut Released

The sidebands and the wrong charge combinations studies rely on the assumption that the background under the signal has exactly the same properties as the events used in these two methods. This is not exactly true. For instance most of the resonances that enter the D^0 background are absent in the sample of events with pairs of tracks having charges of the same sign. To check if the asymmetry of the background in the signal region is not significantly greater than the asymmetry in the sidebands or in the wrong charge combinations, the cut on the RICH particles identification was relaxed in a number of steps. As a result the number of signal events increased totally by about 20%, while the amount of the background events increased approximately two times. For each step the $(\Delta G/G)'_{\mathrm{PID}}$ and its error were calculated. The events taken for the calculation were located inside the $[-50,50]$ MeV mass window and the Second Order Weighted Method was used with a weight: $w = fP_B D\hat{a}_{LL}$. With the assumption that the background under the peak has no asymmetry, the $(\Delta G/G)'_{\mathrm{PID}}$ calculated for different cuts should approach zero as more background events are accumulated. At the same time the statistical error will decrease. This effect should be well visible for the D^0–tagged sample, where with the standard cuts the $(\Delta G/G)'_{\mathrm{PID}}$ is negative. On the contrary, if the background asymmetry is significant, it will result in a non-vanishing $(\Delta G/G)'_{\mathrm{PID}}$.

The results are plotted in Fig 7.6. On the horizontal axis the numbers of events accepted with the chosen set of RICH cuts and located in the $[-50,50]$ MeV mass window are

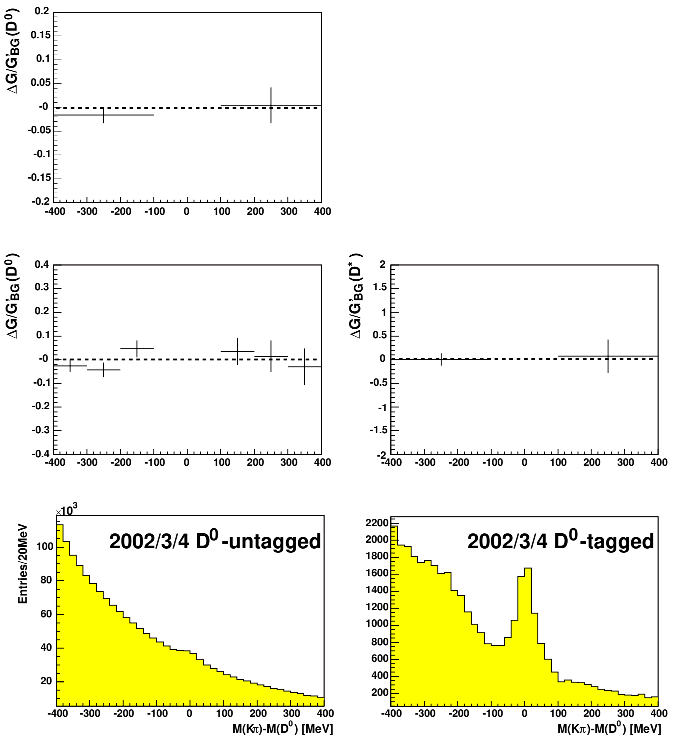

Figure 7.4: The $(\Delta G/G)'_{\rm BG}(D^0)$ and $(\Delta G/G)'_{\rm BG}(D^*)$ in the sidebands for different mass bins for summed 2002, 2003 and 2004 data. Errors are statistical.

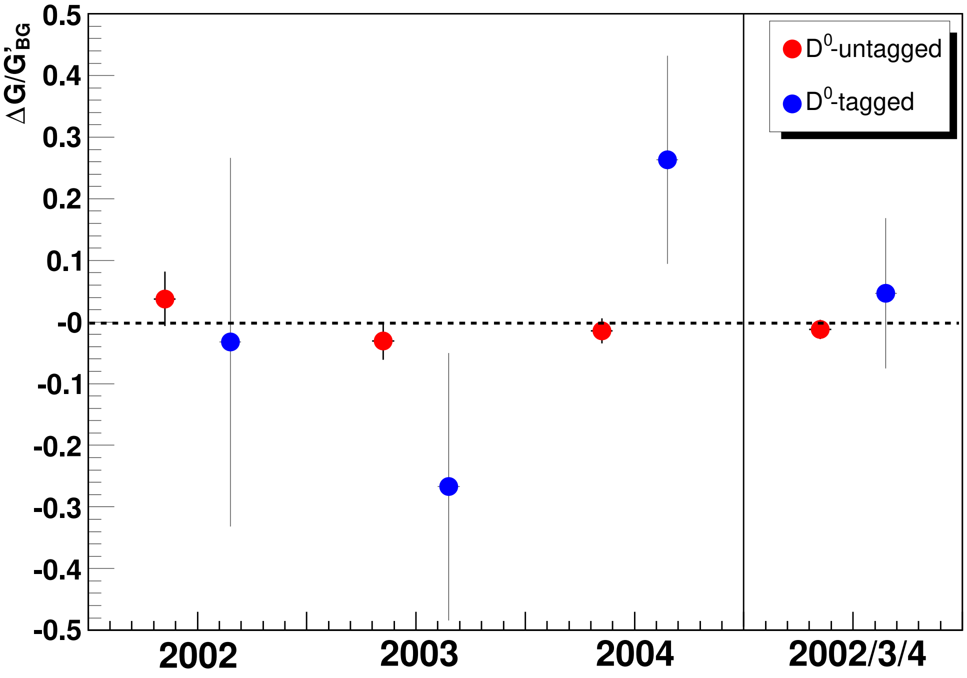

Figure 7.5: The $(\Delta G/G)'_{\rm BG}(D^0)$ and $(\Delta G/G)'_{\rm BG}(D^*)$ in each year and their weighted average. Errors are statistical.

presented. The vertical axis represent the $(\Delta G/G)'_{\rm PID}$ value. For the D^0–tagged sample the $(\Delta G/G)'_{\rm PID}$ approaches zero as the number of background events increases. For the D^0–untagged sample it stays compatible with zero for different number of background events.

7.2.4 Summary of the Background Asymmetry Studies

The three complementary studies presented above do not reveal any significant background asymmetry. The first and the second method provide with upper limits. Those limits are high as the studies were performed on limited samples of the background events. A competitive approach for the estimation of the influence of the background asymmetry was proposed in [134, 147]. It is based on a simultaneous fitting the signal and the background asymmetries to the data. The $\Delta G/G$ calculated with this method is –0.50±0.40 [148]. A difference between the $\Delta G/G$ obtained with the standard method (cf. Sec 6.3) and the above value is 0.07. This shift may arise from the background asymmetry or from uncertainties of fits in that method. It was decided to take the 0.07 shift as an estimation of a possible influence of the background asymmetry on the $\Delta G/G$ measurement:

$$\delta(\Delta G/G)_{\rm BG} = 0.07 \tag{7.7}$$

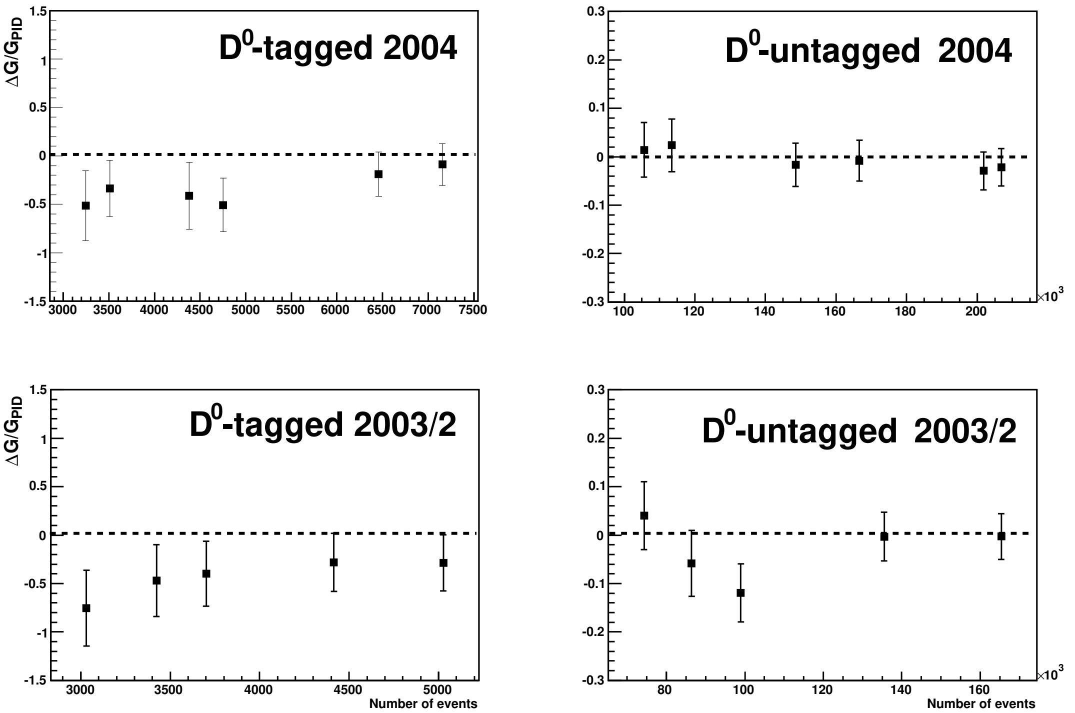

Figure 7.6: The $(\Delta G/G)'_{\rm PID}$ value for different numbers of events in the $[-50, 50]$ MeV mass window, left: for D^0-tagged channel, right: for D^0-untagged channel. The first point at each plot corresponds to the events selected with the nominal RICH cuts. Errors are statistical, and correlated.

7.3 The Binning Procedure

The correlation between the $S/(S+B)$ ratio and the $\hat{a}_{LL}$ was described in Sec. 6.2. The $S/(S+B)$ decreases when $\hat{a}_{LL}$ increases. This may affect the result on the $\Delta G/G$ biasing its value and changing significantly its statistical error. The problem may be removed parametrising the $S/(S+B)$ not only as a function of mass but also as a function of those kinematical variables on which the $\hat{a}_{LL}$ depends. Unfortunately this cannot be done since statistics of the data is too low to perform a multivariable fit. On the other hand, a parameterisation based on a Monte Carlo sample would introduce an additional model dependence to the analysis. Therefore it was decided to use the binning method described in Sec. 6.2. In the procedure the D^0–tagged sample is divided into five bins of $fP_BD\hat{a}_{LL}$ while the D^0–untagged sample into three. In each bin a separate mass fit is performed and then used in the weight. This procedure reduces the correlation effects, but does not suppress them entirely.

Estimation of residual effects of the correlation is done dividing the open charm sample in number of bins different from the one used in the analysis, and repeating the extraction of the $\Delta G/G$. For the D^0–tagged sample ten values of $\Delta G/G$ are calculated, corresponding to 1 (no binning) up to 10 bins containing equal numbers of the open charm events. For the D^0–untagged channel only three different values are calculated corresponding to the division into 1, 2 and 3 intervals. It is not possible to divide the untagged sample into more than 3 bins and still obtain reliable mass fits. The resulting values are presented in Fig. 7.7 as functions of the number of bins used for the calculation. The values are also collected in Tab. 7.2.

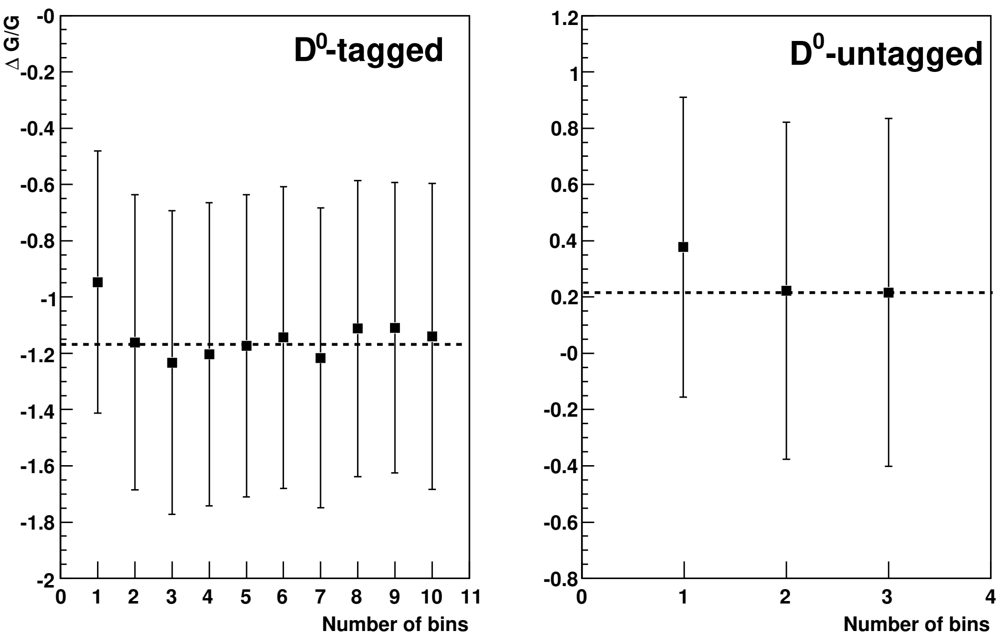

Figure 7.7: The $\Delta G/G$ values for the D^0–tagged and the untagged samples calculated with different number of bins in $fP_BD\hat{a}_{LL}$. Dashed lines mark the $\Delta G/G$ values for 5 (left plot) and 3 (right plot) bins, respectively. These are the final values obtained for the open charm analysis. Errors plotted for each point are the statistical uncertainties. Note that all the points in a given plot are fully statistically correlated and variations between them are caused exclusively by using different number of bins.

For the D^0–tagged sample it is clear that all values of $\Delta G/G$ are very similar, except for the case where no bins are used (the first point). The conclusion is that it is enough to use even a small number of bins to minimise the correlation influence. The average

D^0–tagged		D^0–untagged	
Number of bins	$\Delta G/G$	Number of bins	$\Delta G/G$
1	–0.95 ± 0.47	1	0.38 ± 0.53
2	–1.16 ± 0.52	2	0.22 ± 0.60
3	–1.23 ± 0.54	3	**0.21 ± 0.62**
4	–1.20 ± 0.54		
5	**–1.17 ± 0.54**		
6	–1.14 ± 0.54		
7	–1.22 ± 0.53		
8	–1.11 ± 0.53		
9	–1.11 ± 0.52		
10	–1.14 ± 0.54		

Table 7.2: The $\Delta G/G$ values for the D^0–tagged and the D^0–untagged samples calculated with different number of bins in $fP_BD\hat{a}_{LL}$. Values in bold are the final values for the open charm analysis for a given channel.

value for $\Delta G/G$ calculated using the results obtained for 2–10 bins is –1.17, which is equal to the final value presented in this thesis for the tagged channel, cf. Sec 6.3. To quantify the variations between different $\Delta G/G$ values, a standard deviation for 9 results (2–10 bins) was calculated. It is 0.04. This number will be treated as an uncertainty introduced to the $\Delta G/G$ analysis in the D^0–tagged channel due to the binning procedure.

For the D^0–untagged sample the above procedure of the uncertainty estimation cannot be performed. However it can be noticed that values of $\Delta G/G$ for the cases with 2 and 3 bins are in a perfect agreement. Therefore it may be assumed that the uncertainty introduced with the binning procedure is small also in this channel.

As the final estimation of the systematic error associated with the binning procedure, the one calculated for the D^0–tagged channel, is used. Thus the uncertainty due to the binning is:

$$\delta(\Delta G/G)_{\text{binning}} = 0.04 \tag{7.8}$$

7.4 Stability of the Detector

Stability of the detector efficiency is a key assumption of the analysis. Therefore a number of consistency checks of the data recorded in different parts of the detector are performed. The checks are based on samples containing events characterised by kinematics resembling the one of the open charm mesons. Tests are performed for two such samples:

- a sample selected with cuts identical to those for the D^0–untagged case, with the restriction that the mass of the open charm candidate is in the range $[-50, +50]$ MeV around the centre of the D^0 signal;
- a sample selected with cuts identical to those for the D^0–tagged case, with the restriction that the mass of the open charm candidate is in the range $[-400, +400]$ MeV around the centre of the D^0 signal.

For each test a given sample is divided into two groups of similar statistics. The division is done taking into account *e.g.* a direction of a momentum vector or its value for a given particle in an event. Then for each of the two groups $(\Delta G/G)'_{\mathrm{F}}$ is derived using the Second Order Weighted Method with a weight defined by Eq. (7.1). Finally the difference between $(\Delta G/G)'^{1}_{\mathrm{F}}$ and $(\Delta G/G)'^{2}_{\mathrm{F}}$ values obtained for the two groups is calculated:

$$(\Delta G/G)'^{1-2}_{\mathrm{F}} = (\Delta G/G)'^{1}_{\mathrm{F}} - (\Delta G/G)'^{2}_{\mathrm{F}} \tag{7.9}$$

This difference should be compatible with zero within the accuracy of a statistical error:

$$\delta((\Delta G/G)'^{1-2}_{\mathrm{F}}) = \sqrt{\delta((\Delta G/G)'^{1}_{\mathrm{F}})^2 + \delta((\Delta G/G)'^{2}_{\mathrm{F}})^2} \tag{7.10}$$

7.4.1 Top–Bottom and Left–Right Stability

If a given part (top, bottom, left or right) of the spectrometer for the whole data taking period works with efficiency different than the other parts, the $\Delta G/G$ measurement should not be biased since data coming from both spin configurations will be affected in the same way. If, for some reason, inhomogeneities in the detector efficiency influence only events from one spin configuration, the $(\Delta G/G)'_{\mathrm{F}}$ calculated for the events reconstructed in this part will be shifted with respect to the $(\Delta G/G)'_{\mathrm{F}}$ obtained for the events from other parts.

To analyse the consistence of results obtained using events reconstructed with different parts of the detector, the samples are divided into several pairs of subsamples as follows:

- the K candidate is outgoing from the primary vertex in the direction of positive or negative X values;
- the π candidate is outgoing from the primary vertex in the direction of positive or negative X values;
- the π_S candidate is outgoing from the primary vertex in the direction of positive or negative X values;
- the K candidate is outgoing from the primary vertex in the direction of positive or negative Y values;
- the π candidate is outgoing from the primary vertex in the direction of positive or negative Y values;
- the π_S candidate is outgoing from the primary vertex in the direction of positive or negative Y values.

Calculations of $(\Delta G/G)'^{1-2}_{\mathrm{F}}$ are performed for each year separately. Then the weighted means over all years are derived. The results are presented in Fig. 7.8. No significant inconsistencies of the results obtained with the data reconstructed with different detector parts are seen. All points at the plots are compatible with zero within at most two standard deviations.

7.4.2 Studies of the Momentum Dependence

For these studies the samples are divided according to the momentum of a given particle. Three different possibilities are investigated:

- momentum of K candidate below or above 19.5 GeV;
- momentum of π candidate below or above 16.0 GeV;

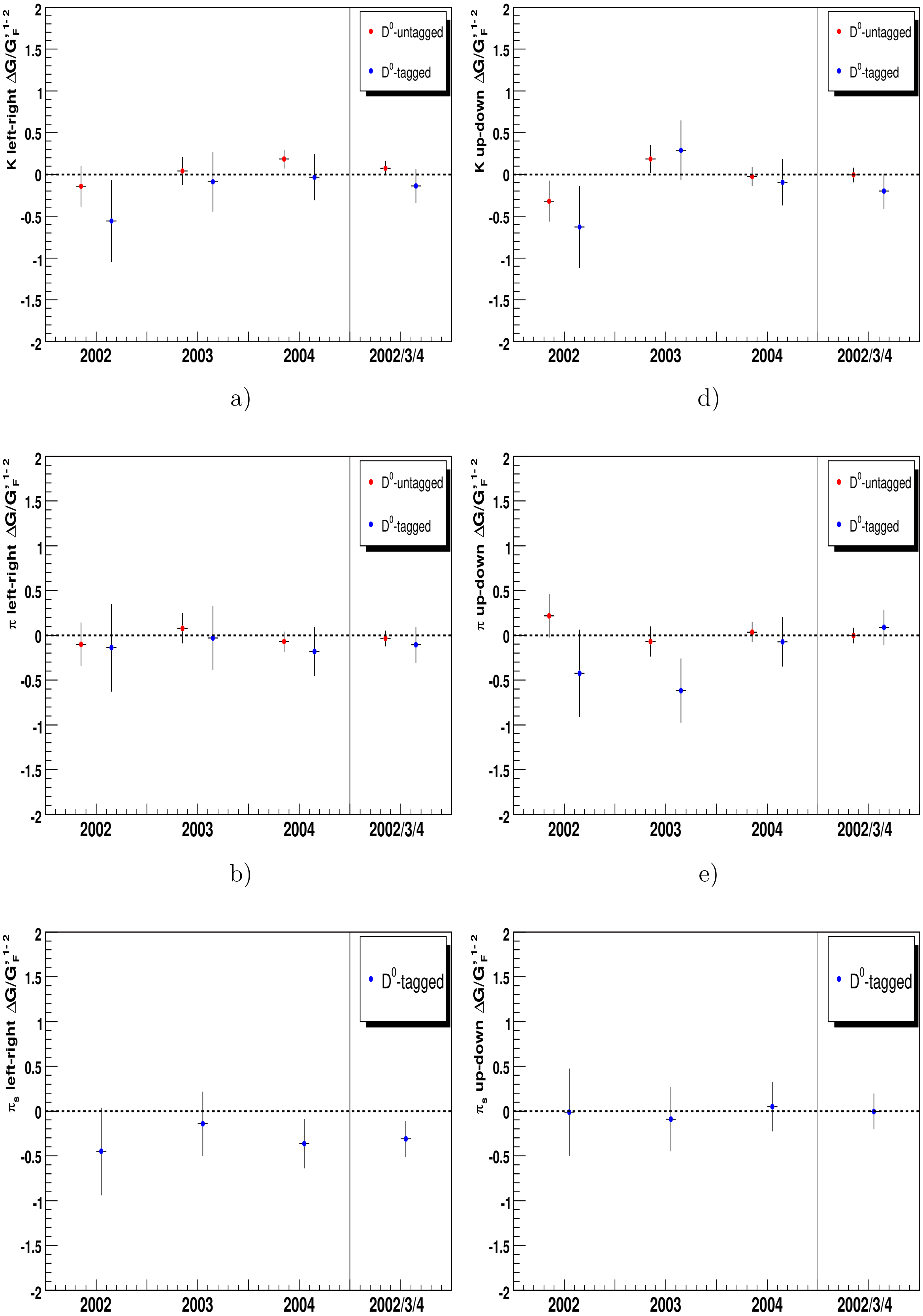

a) d)

b) e)

c) f)

Figure 7.8: The $(\Delta G/G)'^{1-2}_{\rm F}$ calculated for the subsamples selected according to: a) the horizontal direction of kaon, b) the horizontal direction of pion, c) the horizontal direction of soft pion, d) the vertical direction of kaon, e) the vertical direction of pion, f) the vertical direction of soft pion.

- momentum of π_S candidate below or above 2.8 GeV.

The values of the above momenta were chosen to divide in each case the sample into two subsamples of similar statistics. Studies of K in two momentum bins could reveal systematic effects introduced by the momentum dependent RICH acceptance. In the π_S case, events from the first bin that corresponds to smaller momenta, are more sensitive to the influence of the target solenoid field.

The left column in Fig. 7.9 presents the outcome of these studies. No indication of a systematic shift on either plot is noticeable. The largest deviations from zero value occur for 2002 in the sample divided according to K and to π_S momenta. These deviations are however at the level of ∼2 σ and may have a statistical origin. They do not appear neither for the 2003 nor for the 2004 data.

7.4.3 The ζ Angle Dependence

The ζ angle is defined as an angle between the Z direction and a direction of a given particle track at the primary vertex. The samples are divided into pairs of subsamples with criteria defined for the ζ angle for K, π and π_S:

- the ζ of kaon smaller or larger than 0.045 rad;
- the ζ of pion smaller or larger than 0.055 rad;
- the ζ of soft pion smaller or larger than 0.023 rad.

The values of the above angles were chosen to divide in each case the sample into two subsamples of similar statistics. The studies concerning two bins in ζ check the consistency of the data recorded by the outer and the inner parts of the spectrometer. The results are presented in Fig. 7.9. No discrepancy is seen.

7.4.4 Day–Night Effect

Within the period of 24 hours the temperature in the experimental hall fluctuates by a few degrees, reflecting the weather changes outside the building. This may induce small movements of the detector planes, changing their overall efficiency. The effect is minimised by the odd number of spin reversals taken during the day–night period. However if the effect is large and the fluctuations are not periodic (the daily averaged temperature changes in time), the residual impact on the measured asymmetries remains.

The existence of the day–night effect can be verified by dividing the data into two subsamples according to the temperature in the COMPASS experimental hall. The first one contains events recorded between noon and midnight, the other between midnight and noon – usually the highest temperature in the hall is at 7 p.m., and the lowest at 6 a.m. In Fig. 7.10 the $(\Delta G/G)'^{1-2}_{\mathrm{F}}$ calculated for those subsamples is presented. It is consistent with zero, proving that the influence of the day–night effect is small.

7.4.5 Solenoid Field Direction

To minimise the influence of the solenoid magnetic field on the stability of the detector, during data taking two settings were used, see Sec. 7.1. They correspond to opposite relative directions of the spin and the solenoid magnetic field. The amount of the data collected with both settings are approximately equal. Therefore the influence of the

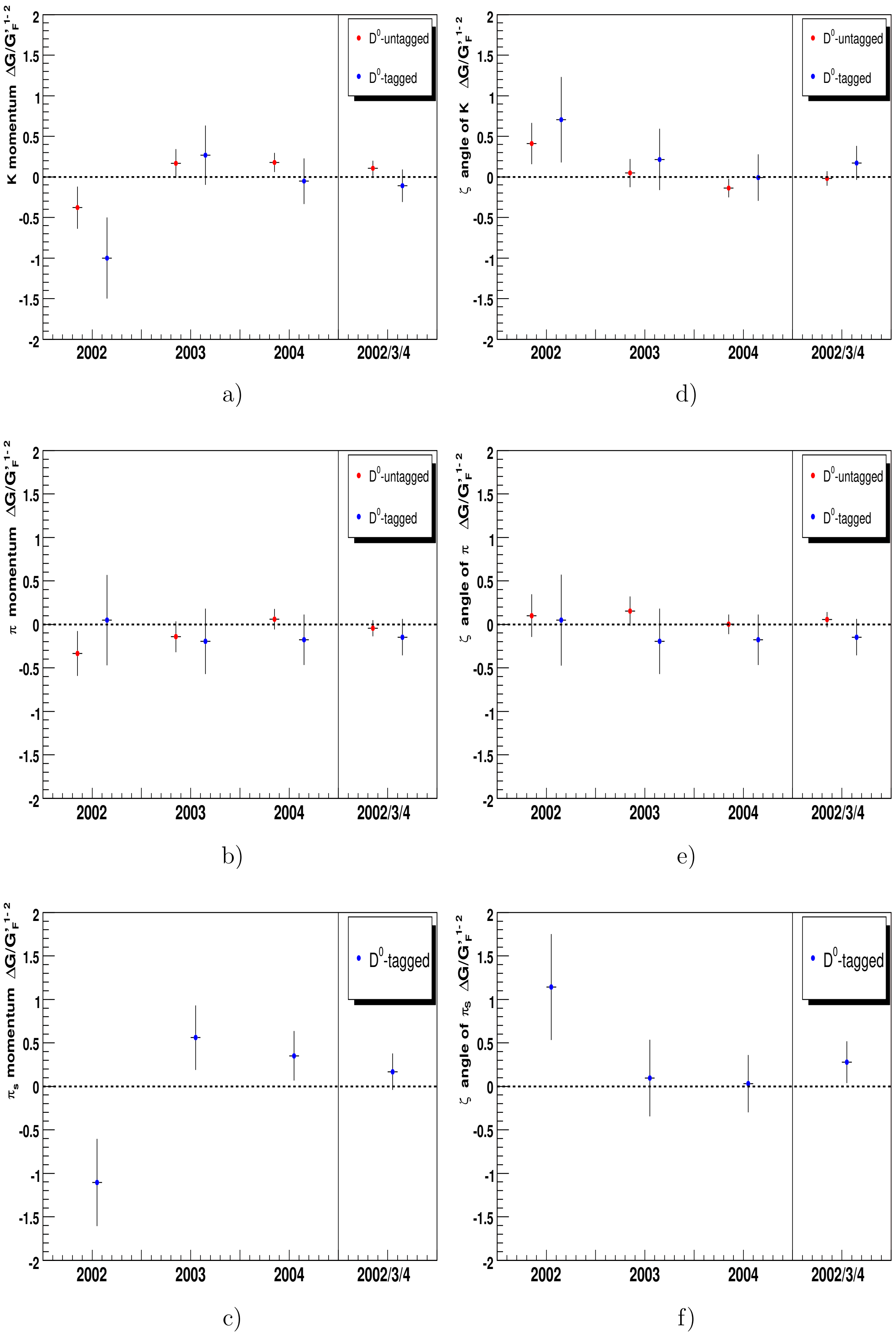

a) d)

b) e)

c) f)

Figure 7.9: The $(\Delta G/G)'^{1-2}_{\rm F}$ calculated for the subsamples selected according to: a) the momentum of kaon, b) the momentum of pion, c) the momentum of soft pion, d) the ζ angle of kaon, e) the ζ angle of pion, f) the ζ angle of soft pion.

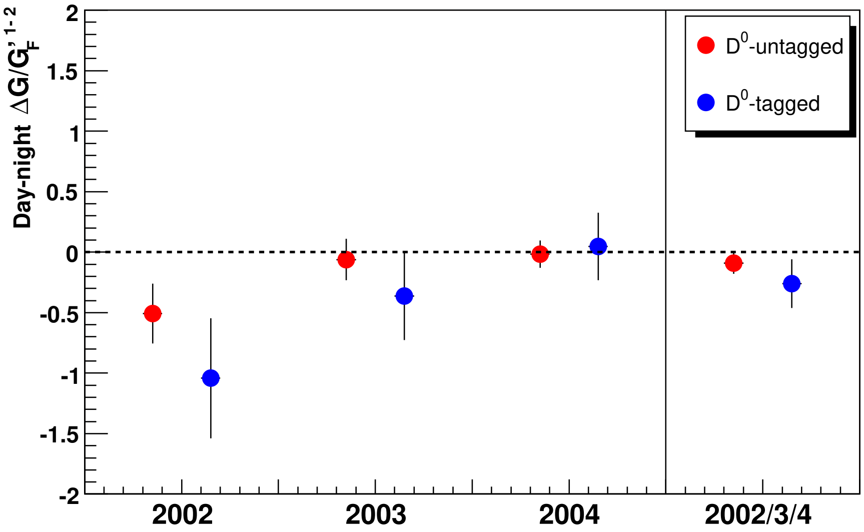

Figure 7.10: The $(\Delta G/G)'^{1-2}_{\mathrm{F}}$ calculated for the subsamples selected according to time: first with events recorded between noon and midnight, the other between midnight and noon.

solenoid field direction should to a large extent cancel out. It is interesting to check what is the size of the total effect and how it would bias the result, if the changes of the relative spin–field directions were not done. For this the samples are divided into two groups, each corresponding to the data taken with a given setting. Then the $(\Delta G/G)'^{1-2}_{\mathrm{F}}$ for these groups is calculated. The results are presented in Fig. 7.11. Most of the values are positive, which may indicate a slight false asymmetry induced by the solenoid magnetic field. However taking into account the statistical errors of the points, they are all consistent with zero. Therefore it is assumed that any residual false asymmetry introduced with the solenoid magnetic field can be neglected.

7.4.6 One Cell Studies

The target is susceptible to the influence of the magnetic field produced by the target solenoid and by the SM1. Both may cause fluctuations of the target position during the data taking and thus change the acceptance for D^0 events.

The simplest method of testing the target instabilities influencing the asymmetry measurement is through a division of the events according to the primary vertex location, to those with a primary vertex in the downstream and in the upstream cell. Then each cell is divided into two equal subcells, Fig. 7.12. The $(\Delta G/G)'_{\mathrm{F}}$ are calculated for each cell separately. For the calculation the asymmetries between the number of events with a primary vertex located inside a given subcell are used, cf. Fig. 7.12b. As the material inside a cell is polarised in one direction, the expected $(\Delta G/G)'_{\mathrm{F}}$ values should be zero. The results are presented in Fig. 7.13. They prove that the target is fairly stable.

7.4.7 Up-Upstream–Down-Downstream Combination

Another test is performed using the same concept of subdivided target cells. This time two $(\Delta G/G)'_{\mathrm{F}}$ values are calculated – first for the events with a primary vertex located

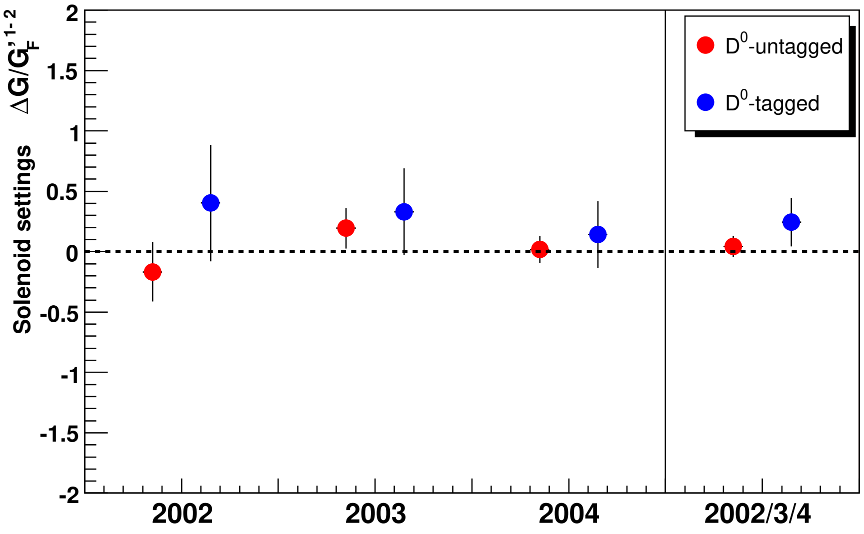

Figure 7.11: The $(\Delta G/G)'^{1-2}_{\rm F}$ calculated for the subsamples divided according to the solenoid magnetic field relative direction.

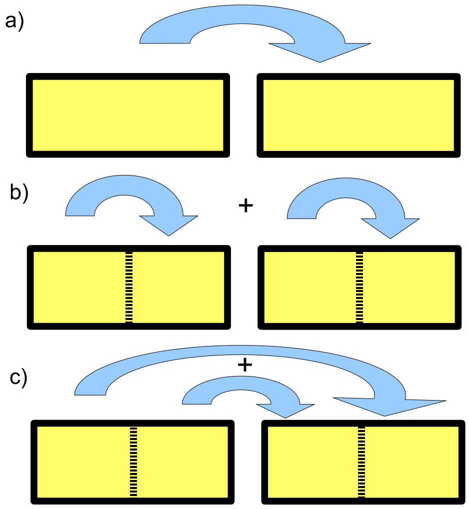

Figure 7.12: Combinations used for a) calculation of $\Delta G/G$, b) studies of the systematic effects inside one cell, c) studies of the systematic effects in up-upstream–down-downstream combination.

inside the upstream part of the upstream cell and the downstream part of the downstream cell, and the second for the events with a primary vertex inside the downstream part of the upstream and the upstream part of the downstream cell, cf. Fig. 7.12c. In Fig. 7.14 the $(\Delta G/G)'^{1-2}_{\rm F}$ values are plotted. All of them are consistent with zero.

7.4.8 Dependence on the Target Radius

To check the possible dependence of the asymmetry on the location of the primary vertex in the radial coordinate two subsamples are prepared. The first one is composed of events with a primary vertex within $r < 0.8$ cm, and the second of events with this vertex within $r < 1.3$ cm. For the events included in those subsamples the beam flux

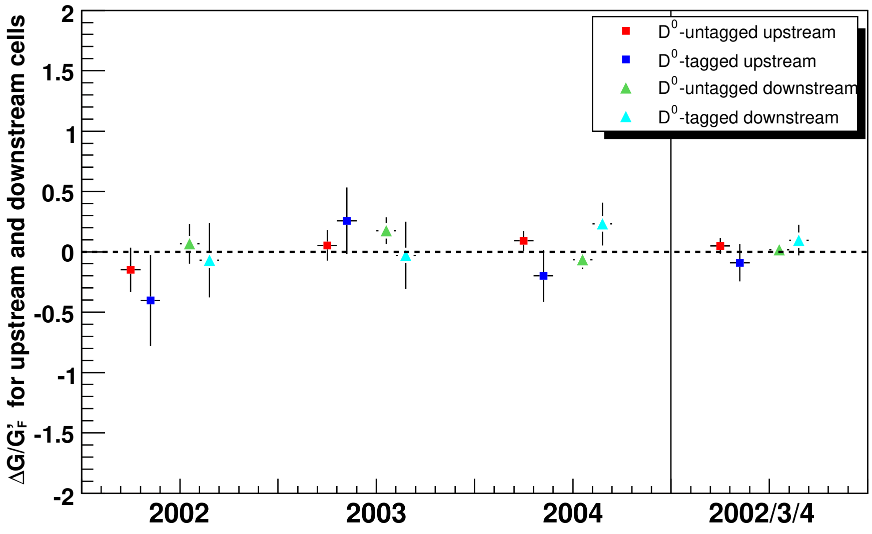

Figure 7.13: The $(\Delta G/G)'_{\mathrm{F}}$ calculated for events inside a given target cell. Note that $(\Delta G/G)^{1-2}_{\mathrm{F}}$ difference is not calculated here.

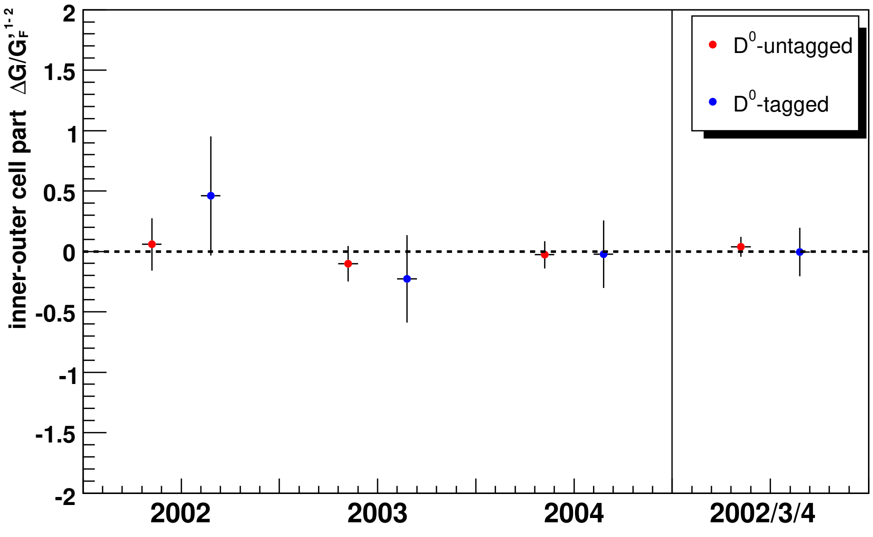

Figure 7.14: The $(\Delta G/G)^{1-2\prime}{}_{\mathrm{F}}$ calculated for the subsamples divided according to a primary vertex location in the inner or the outer halves of both cells.

equalisation requirement (Sec. 4.2.4) has to be fulfilled with $r_i < 0.8$ cm and $r_i < 1.3$ cm, respectively. In both cases the $\Delta G/G$ value is calculated using the standard Second Order Weighted Method and compared with the $\Delta G/G$ measured for the whole data sample (cut $r < 1.4$ cm). For this comparison the difference between the $\Delta G/G$ values is calculated. The error of the difference is given by:

$$\delta((\Delta G/G)_{r<1.4} - (\Delta G/G)_{r<0.8\ \vee\ 1.3}) = \sqrt{|\delta(\Delta G/G)^2_{r<1.4} - \delta(\Delta G/G)^2_{r<0.8\ \vee\ 1.3}|} \quad (7.11)$$

as the samples are correlated (events with $r < 0.8$ cm or $r < 1.3$ cm belong also to the sample with $r < 1.4$ cm cut). In Fig. 7.15 results for both samples are presented. All values are consistent with zero.

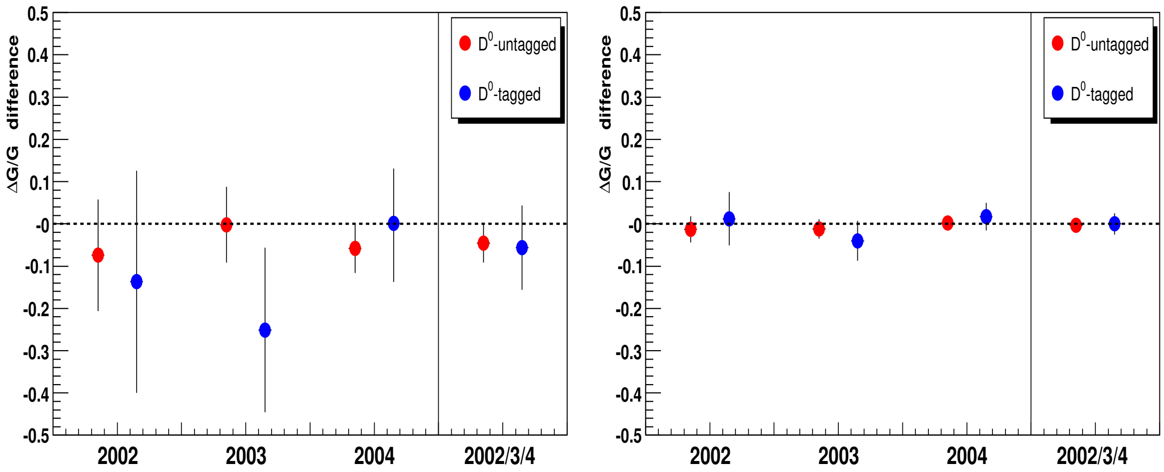

Figure 7.15: Difference between $\Delta G/G$ calculated for the whole sample and the sample restricted to the events with a primary vertex within $r < 0.8$ cm (left) and $r < 1.3$ cm (right) cuts.

7.5 The Pulls Method for the False Asymmetries Estimation

In this section a standard approach, used in different analyses in COMPASS, for the estimation of the upper limits of the systematic error related to the false asymmetries is described. It is called a pulls method and with improvements, presented here, can be used to obtain the upper limit for the false asymmetries in the open charm analysis.

There are two kinds of false asymmetries, reproducible and unreproducible. The former kind corresponds to the false asymmetries due to changes in the spectrometer induced by variation of one particular parameter that is easily accessible in the offline analysis, *e.g.* the temperature in the experimental hall. The influence of these is small, as it has been shown in the previous sections. The latter type of false asymmetries arises from the random fluctuations of the spectrometer efficiency in time. These can be studied with the usage of the pulls method.

For the pulls method the background in the range $[-400, -90]$ and $[90, 400]$ MeV around each D^0 peak, tagged and untagged, is taken. An assumption is made that events from the background region populate the spectrometer in the same way as the events from the signal range. This assumption will be discussed later. Then the set of events is divided according to the "configurations", [149]. Each configuration contains events from a few subsequent runs, where in the middle the polarisation was reversed. For each configuration the $(\Delta G/G)_{\mathrm{F}}$ is calculated with the Second Order Weighted Method. The weight used for the calculation is defined as:

$$w = f P_B D \hat{a}_{LL} \left\langle \frac{S}{S+B} \right\rangle \tag{7.12}$$

The average value of the S/(S+B) is calculated for the mass range enclosing the signal, that is $[-90, 90]$ MeV. The $(\Delta G/G)_{\mathrm{F}}$ for each configuration is calculated separately for the D^0 tagged and untagged samples:

$$\begin{aligned}&(\Delta G/G)^i_{\mathrm{F}}(D^*) \pm \delta((\Delta G/G)^i_{\mathrm{F}}(D^*))\\ &(\Delta G/G)^i_{\mathrm{F}}(D^0) \pm \delta((\Delta G/G)^i_{\mathrm{F}}(D^0))\end{aligned} \tag{7.13}$$

where the index i counts configurations. Then for each configuration the weighted mean of the values for both channels is calculated. A weight corresponds to the statistical uncertainty of the measured $\Delta G/G$ in a given channel, cf. Sec. 6.3. The procedure results in a set of values (cf. Fig. 7.16 (top)):

$$(\Delta G/G)^i_{\mathrm{F}}(D^* + D^0) \pm \delta((\Delta G/G)^i_{\mathrm{F}}(D^* + D^0)) \tag{7.14}$$

Then for each configuration a pull is calculated. It is defined as:

$$P_i = \frac{(\Delta G/G)^i_{\mathrm{F}}(D^* + D^0) - \langle(\Delta G/G)_{\mathrm{F}}(D^* + D^0)\rangle}{\delta((\Delta G/G)^i_{\mathrm{F}}(D^* + D^0))} \tag{7.15}$$

In the absence of false asymmetries, the distribution of pulls should be Gaussian with a mean value zero and RMS equal to 1. Random fluctuations of the spectrometer efficiency would enlarge the RMS, here denoted by ρ. Having the $\rho \pm \sigma_\rho$ and $\langle(\Delta G/G)_{\mathrm{F}}(D^* + D^0)\rangle \pm \delta\langle(\Delta G/G)_{\mathrm{F}}(D^* + D^0)\rangle$ a limit for the systematic error due to the false asymmetries can be calculated according to the formula:

$$\delta(\Delta G/G)_{\mathrm{FA}} = \sqrt{(\rho + 2\sigma_\rho)^2 - 1} \cdot \delta\langle(\Delta G/G)_{\mathrm{F}}(D^* + D^0)\rangle \tag{7.16}$$

In Fig. 7.16 (bottom) a distribution of pulls is plotted. It is fitted with a Gaussian function with the following parameters:

$$\begin{aligned}\langle(\Delta G/G)_{\mathrm{F}}(D^* + D^0)\rangle &= 0.11\\ \delta\langle(\Delta G/G)_{\mathrm{F}}(D^* + D^0)\rangle &= 0.22\\ \rho &= 1.02\\ \sigma_\rho &= 0.06\end{aligned}$$

These numbers are translated into:

$$\delta(\Delta G/G)_{\mathrm{FA}} = 0.12 \tag{7.17}$$

The procedure presented above can be applied only if the background events from the $[-400, -90]$ and $[90, 400]$ MeV range populate the parts of the spectrometer in the same way as the events from the signal region $[-90, 90]$ MeV. Only with this assumption the false asymmetries produced by the spectrometer inefficiencies are the same for both groups of events. In Figs. 7.17–7.20 the momentum and ζ angle distributions for the pion, kaon and soft pion tracks from the background and the signal ranges are compared. To the 15% accuracy the distributions look similar. This result proves that both classes of events populate the spectrometer in a similar way, and the presented procedure for the false asymmetries estimation can indeed be used.

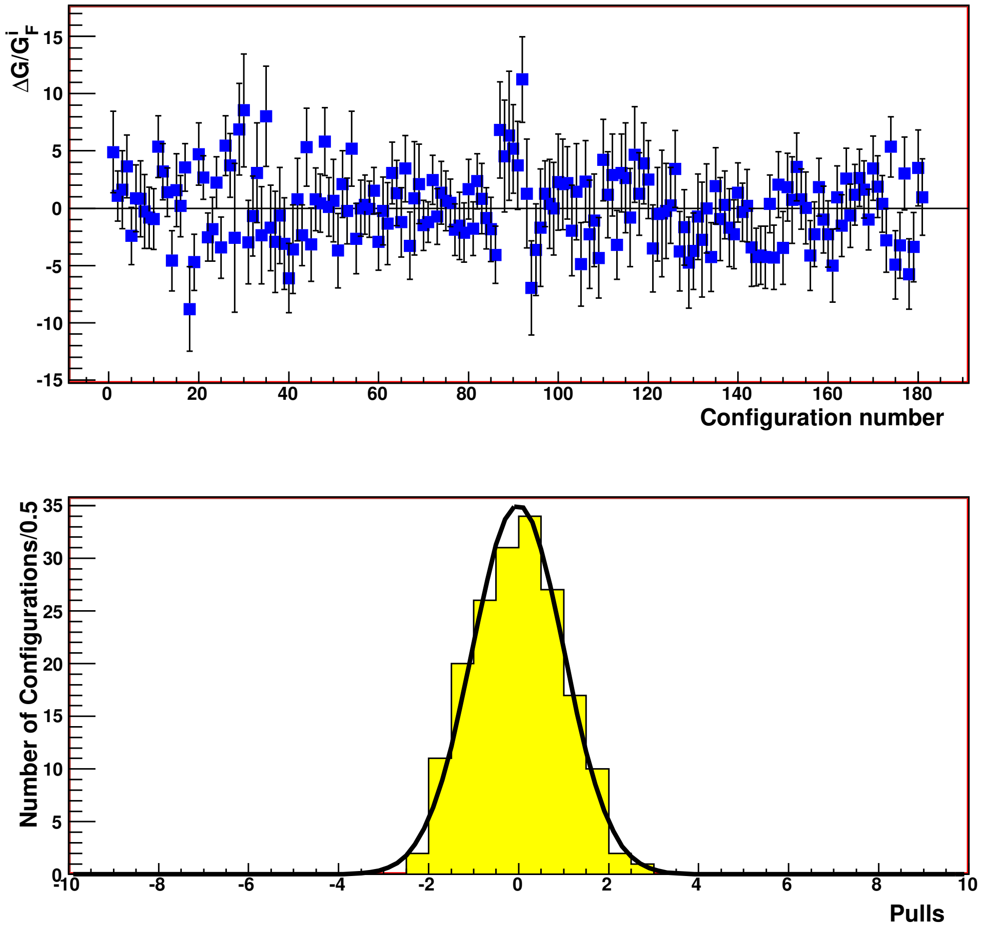

Figure 7.16: Top: the $(\Delta G/G)^i_{\mathrm{F}}(D^* + D^0)$ values corresponding to different configurations. No significant fluctuations are seen. Groups of values, for instance around 90, may be suspected to be biased due to systematic effects, however the statistical errors are large and the final conclusion cannot be drawn. Possible fluctuations are averaged and not seen at the pulls distribution. Bottom: the pulls distribution, the curve is a fitted Gaussian.

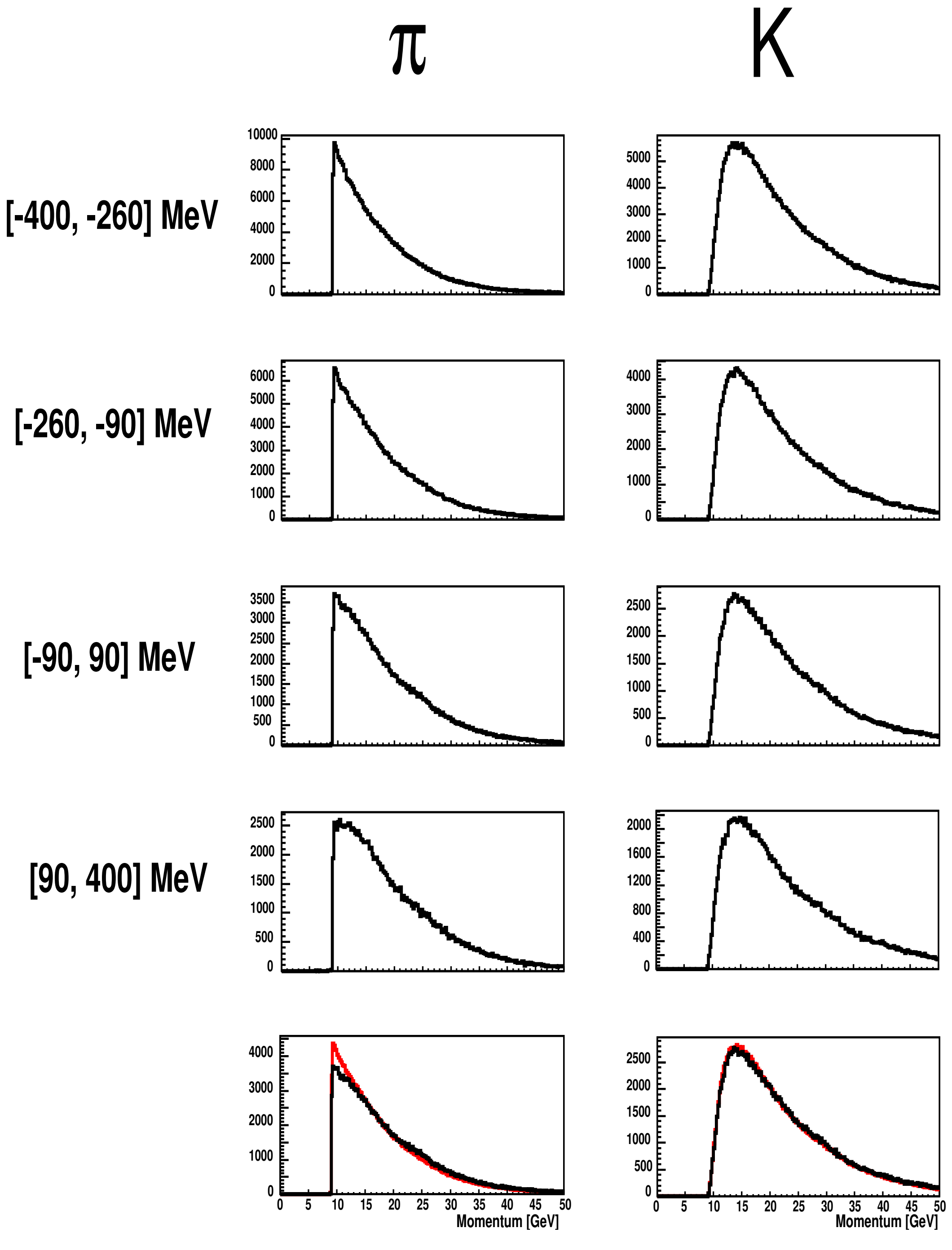

Figure 7.17: Distributions of momenta for pion and kaon candidates for events for which D^0 candidates are reconstructed in different mass ranges. The row [-90, 90] MeV corresponds to the signal range, while [-400, -260], [-260, -90] and [90, 400] MeV to the background. In the bottom row the signal distribution (black) is compared to the sum of the background distributions, normalised to the number of signal events (red). The plots are for the D^0–untagged sample.

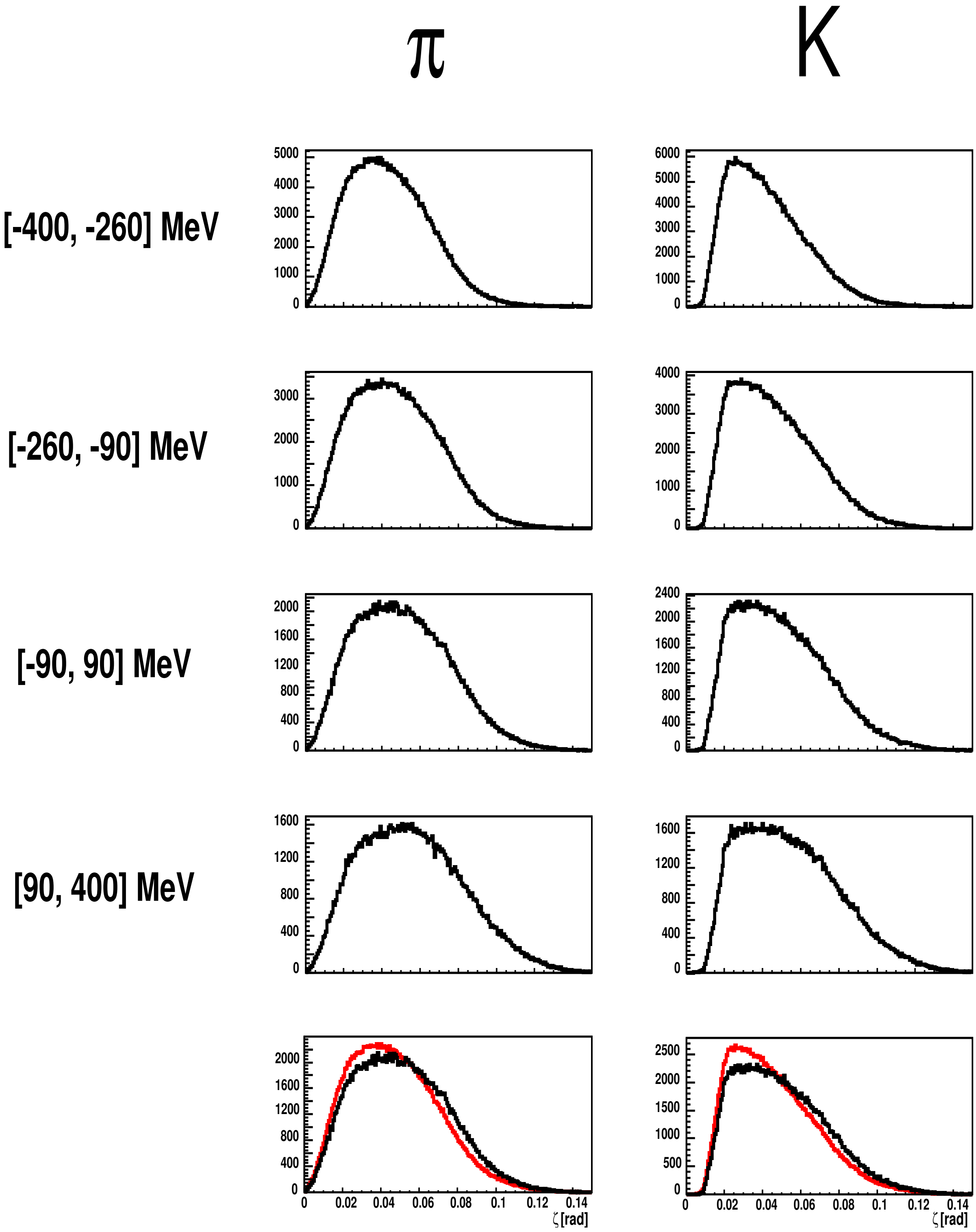

Figure 7.18: Same as in 7.17 but for the ζ angle distribution.

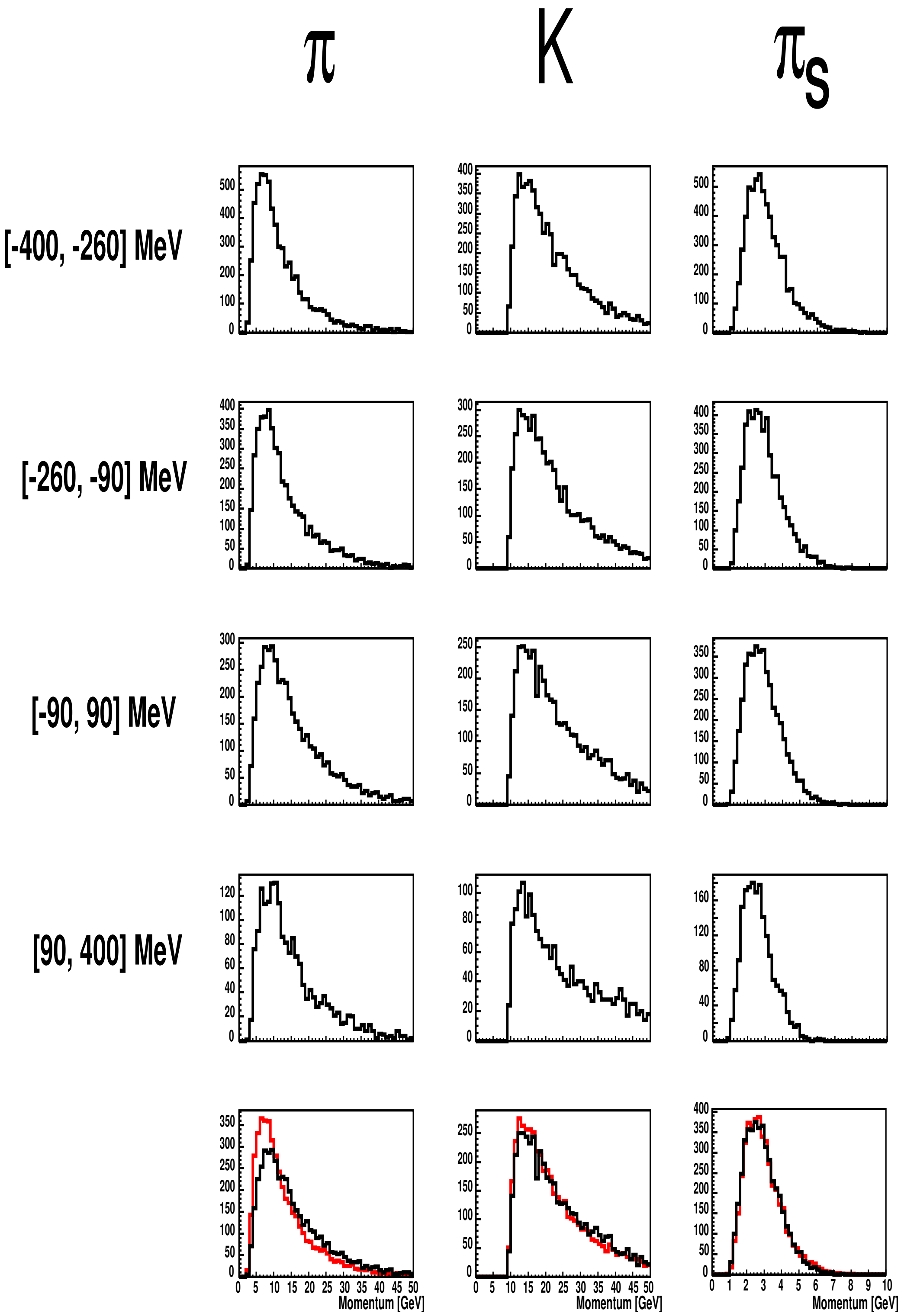

Figure 7.19: Same as in 7.17 but for the D^0–tagged sample.

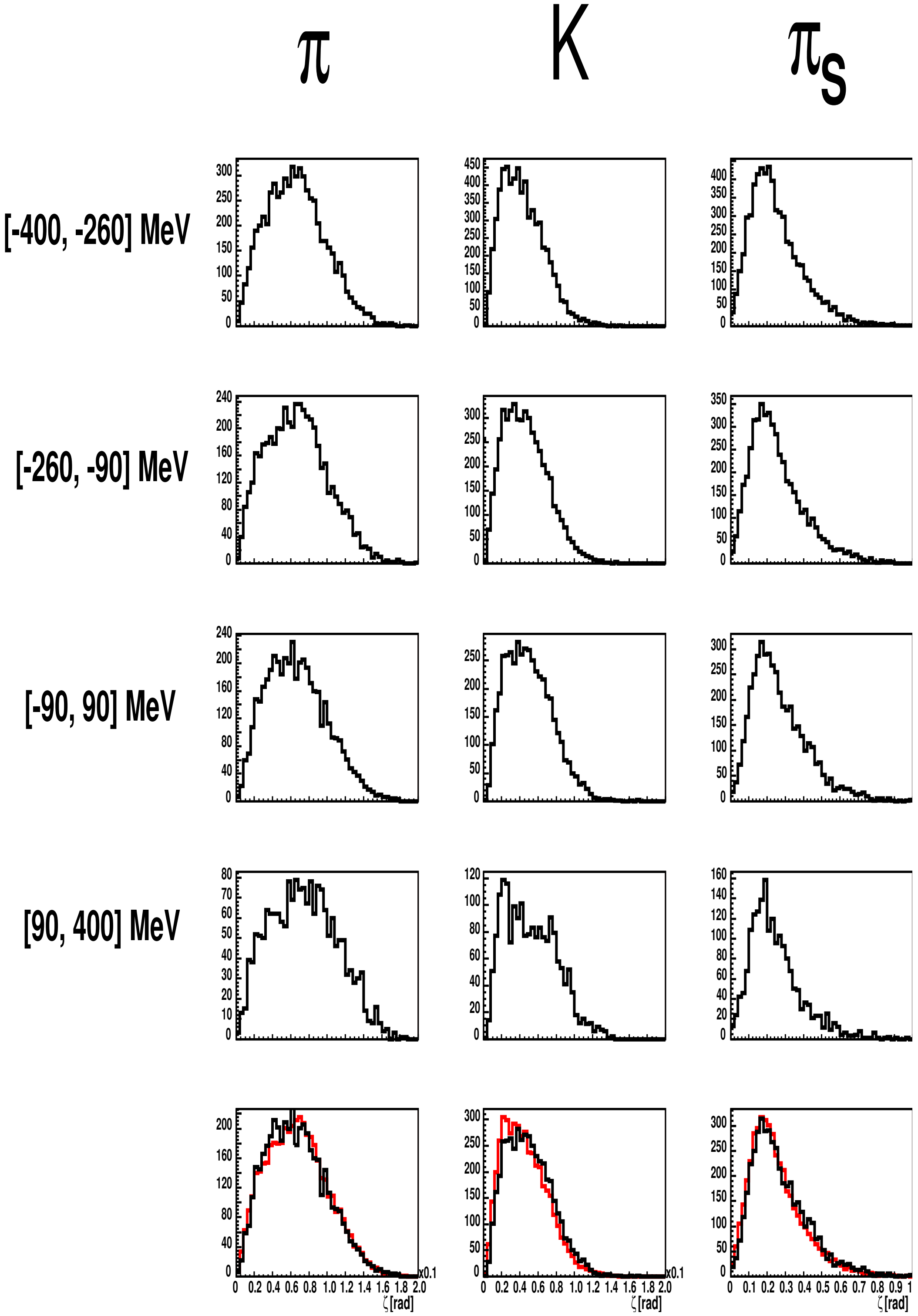

Figure 7.20: Same as in 7.17 but for the D^0–tagged sample and for ζ angle distribution.

7.6 Uncertainty of the Primary Vertices Reconstruction

Resolution of the primary vertex reconstruction along the Z direction (σ_{PV_Z}) depends on the Z coordinate of this vertex (PV_Z), Fig. 7.21. For vertices located in the downstream cell the resolution is significantly better than for vertices placed in the upstream one. The reason is that particles produced in a primary vertex which is more downstream, before being detected in the first tracking stations, SCIFI, MM or SDC, travel through thinner layers of the target material and thus are less affected by the multiple Coulomb scattering.

The uncertainty of the primary vertex reconstruction can influence the measured $\Delta G/G$ value in two ways. First, vertices from one cell may migrate to the other, and second, vertices originally located outside the polarised target material, after reconstruction are found within this material.

Event migration between cells is estimated using a Monte Carlo sample of 40 000 events containing D^0 mesons decaying into $K\pi$ pairs. The sample was generated with AROMA and reconstructed in COMGEANT–CORAL chain. COMGEANT simulates interactions inside the target halves only. Interactions with the vessel material and with the cooling system are not simulated.

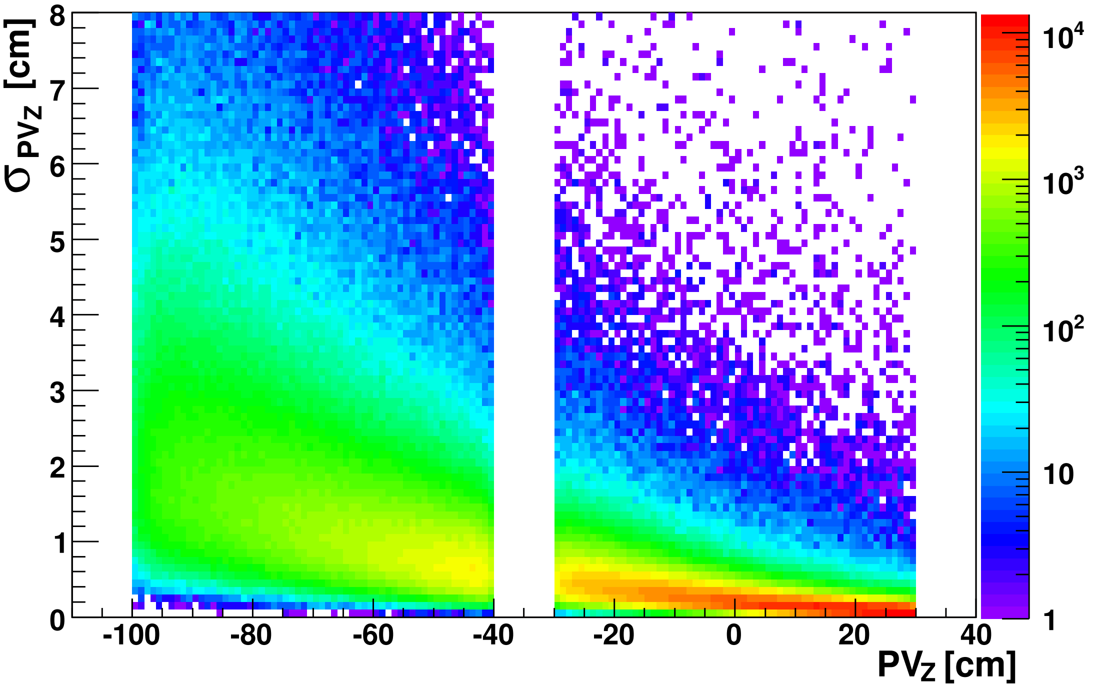

Figure 7.21: The resolution of the primary vertex reconstruction along the Z axis (σ_{PV_z}) versus Z coordinate of the primary vertex (PV_Z), plot obtained for the D^0–untagged sample.

Using the simulated events a number of vertices that were generated in one cell and reconstructed in the other is checked. No migration from the downstream cell to the upstream cell is found while after the reconstruction only two primary vertices located in the upstream cell migrated to the downstream one. The numbers coming from the data confirms this result. The average uncertainty of the Z position reconstruction for the whole D^0–untagged sample is 0.92 cm. For the subsample of events with primary vertex in the downstream cell at $Z < -25$ cm (5 cm from the upstream border of the downstream cell) the uncertainty is 0.65 cm while for the subsample with primary vertex in the upstream cell at $Z > -45$ cm (5 cm from the downstream border of the upstream cell) it is 1.1 cm. These numbers should be compared with a 10 cm wide gap separating both cells.

The influence of the primary vertices migration from one cell to another can also be checked by removing events that could be affected by the migration and keeping for $\Delta G/G$ calculation only those which really come from a given target cell. For this the sample of the open charm events was restricted to events satisfying the following condition:

- $PV_Z < (-40 \text{ cm} - 3\sigma_{PV_Z})$ or $PV_Z > (-30 \text{ cm} + 3\sigma_{PV_Z})$

Resulting $\Delta G/G$ values should be compared with those for the whole open charm sample. In Fig. 7.22 the difference of $\Delta G/G$ obtained for both samples is plotted. The error for each point is given by Eq. (7.11) as the samples are correlated. All the points in the figure are slightly positive. However their deviations from zero are at the level of 1 σ. It may be thus assumed that this effect is caused by statistical fluctuations.

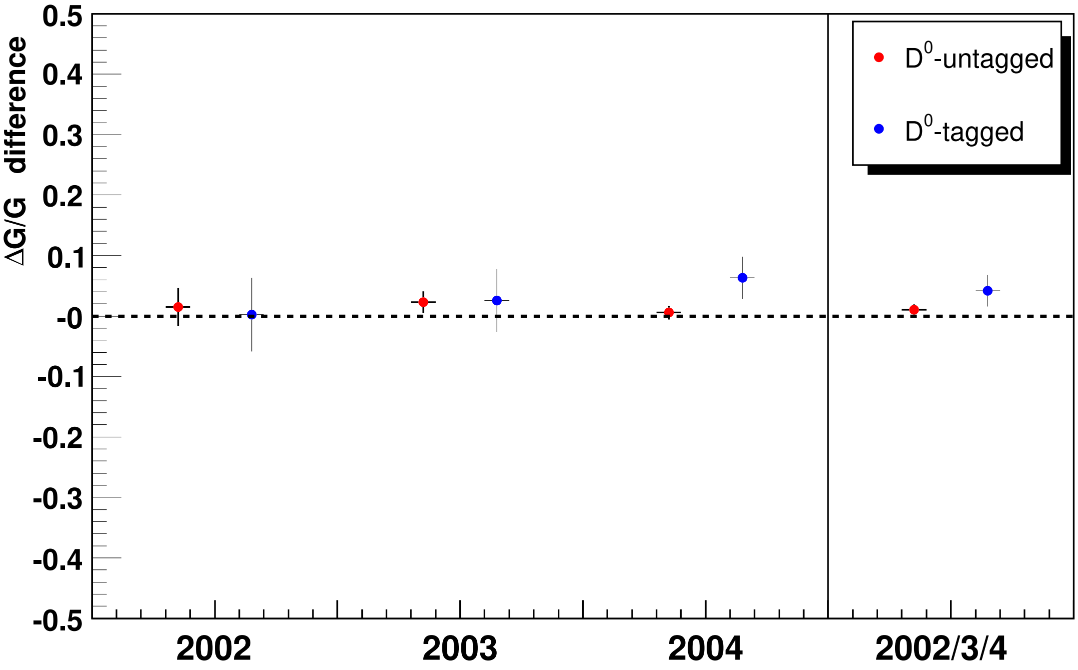

Figure 7.22: Difference between $\Delta G/G$ values obtained for the whole sample and the subsample with a stricter cut on the Z coordinate of the primary vertex (cf. text for details).

A number of muon interactions occur outside the target material, that is in the vessel enclosing the target and in the material of the cooling system. Some primary vertices corresponding to these interactions after the reconstruction are attributed to one of the target cells. Obviously they do not carry any information on the gluon polarisation and just dilute the measurement. The final value should thus be corrected for this effect. The correction will result in an increase of the absolute value of the measured $\Delta G/G$. The estimation of the size of the effect is done as follows. The largest event migration from the outside to the inside of the target cells is due to the poor vertex reconstruction in the Z direction. It is assumed that the density of the primary vertices outside the target, in the region adjacent to a given target border, is equal to 1/3 of the density of events inside the target next to that border. The σ_{PV_Z} for the events from outside the target is estimated separately for the events next to the downstream border of the downstream cell, upstream border of the downstream cell, downstream border of the upstream cell and upstream border of the upstream cell. In each case the σ_{PV_Z} is estimated as an average of the σ_{PV_Z} for events inside the target at most 5 cm from a given border. Then a simplified Monte Carlo simulation is prepared which takes into account the estimated number of events outside the target and σ_{PV_Z} values, and gives the fraction of events that after reconstruction are ascribed to the target material. The result of this procedure is presented in Tab. 7.3. It is found that about 0.1% and 1% of events with primary vertices reconstructed in the downstream and the upstream cells respectively come from the interactions with the material enclosing the targets. These fractions can be translated into an error on $\Delta G/G$. The upper limit for that error is thus 1% of the measured $\Delta G/G$ value, that is ~0.006. In comparison with other contributions to the systematic error the above uncertainty can be safely neglected.

Target border	σ_{PV_Z} [cm]	No. of events wrongly ascribed to the total no. of events in a given cell
downstream of downstream cell	0.10	0.0002
upstream of downstream cell	0.65	0.001
downstream of upstream cell	1.0	0.005
upstream of upstream cell	3.1	0.006

Table 7.3: Fractions of primary vertices reconstructed inside a target that come from the interactions with the material surrounding the target.

7.7 The $\hat{a}_{LL}$ Estimation

In the analysis leading to the $\Delta G/G$ measurement with the open charm method the Monte Carlo is used only for the preparation of the $\hat{a}_{LL}$ parameterisation. In this section a few tests concerning the $\Delta G/G$ result stability with respect to different changes in the parameters of the Monte Carlo used for the preparation of the parameterisation are outlined.

7.7.1 Mass of the Charm Quark

In AROMA, which is used to generate the Monte Carlo sample for the $\hat{a}_{LL}$ parameterisation, the charm quark mass was assumed to be equal to 1.5 GeV. Other values from the range 1.3–1.6 GeV are also considered as possible. The parameterisation of $\hat{a}_{LL}$ depends on the assumed mass of the charm quark. To estimate the size of this dependence three additional Neural Networks were created. Each of them was prepared using different

AROMA samples generated with charm quark masses 1.3, 1.4 and 1.6 GeV, respectively. For each parameterisation the $\Delta G/G$ was calculated using the standard Second Order Weighted Method. The results are collected in Tab. 7.4. Their standard deviation is 0.05.

Mass of the charm quark [GeV]	1.3	1.4	1.5	1.6
$\Delta G/G$	-0.53	-0.58	-0.57	-0.66

Table 7.4: The $\Delta G/G$ calculated using different Neural Networks taught on AROMA samples with various charm quark masses.

7.7.2 Other Tests Concerning $\hat{a}_{LL}$

AROMA generates parameters of the partons taking part in the interaction according to the Parton Distribution Functions. For the presented analysis the GRV98 set of functions was chosen. To test the influence of that choice on the $\hat{a}_{LL}$ parameterisation, a second Neural Network was prepared. It was taught on a Monte Carlo sample with another set of distribution functions – CTEQ5 at LO [143]. The resulting value for $\Delta G/G$ obtained with that parameterisation is -0.53 ± 0.41.

For preparation of the Neural Network an AROMA sample consisting of events with $D^* \rightarrow D^0\pi_S \rightarrow K\pi\pi_S$ decays was used. Obtained $\hat{a}_{LL}$ parameterisation was then employed for both channels: D^0–tagged and D^0–untagged. The question is, if the usage of the parameterisation prepared with D^* events is justified for the channel not tagged with D^* mesons. To answer this question yet another Neural Network was prepared. It was taught on the Monte Carlo sample containing D^0–untagged events. Then two parameterisations were used, one for each channel, to calculate $\Delta G/G$. The obtained value is $\Delta G/G = -0.58 \pm 0.41$.

Both values presented in this section are in a good agreement with the final value of the analysis, $\Delta G/G = -0.57 \pm 0.41$. Variations of the $\Delta G/G$ with the mass of the charm quark and with the change of the PDF, lead to the value of ± 0.05 as the estimate of systematic uncertainty introduced by the Monte Carlo.

7.8 Summary of the Systematic Uncertainties

Sources of the systematic uncertainties discussed along this chapter and the estimation of their contributions to the total systematic error are collected in Tab. 7.5.

Source of an error	Estimated size of an error on $\Delta G/G$
Background asymmetry	0.07
Binning procedure	0.04
False asymmetries	0.12
Primary vertex reconstruction	0.006
Parameters of AROMA	0.05

Table 7.5: Sources of the systematic uncertainties in the open charm analysis.

Apart of these contributions, there are three other quantities that introduce the systematic uncertainties to the final result. These are: the dilution factor f, the beam polarisation and the target polarisation (cf. Sections 5.1.1, 5.1.2 and 5.1.3 respectively). It is assumed that the relative errors of these quantities are about 5% each, which are the fractions used in previous COMPASS analyses, cf. Tab. 7.6. In the presented studies the radiative corrections are important only for the dilution factor f calculation, where they were taken into account in ρ (Sec. 5.1.1).

Source of an error	Estimated size of an error on $\Delta G/G$
Target polarisation	0.03
Beam polarisation	0.03
Dilution factor	0.03

Table 7.6: Additional sources of the systematic uncertainties in the open charm analysis.

To obtain the estimate of the total systematic error on $\Delta G/G$, all the contributions are added quadratically:

$$\delta(\Delta G/G)_{\text{syst}} = \sqrt{\sum_i \delta(\Delta G/G)_i^2} \tag{7.18}$$

This requires an assumption that the contributions are independent. For most of them it is well justified; exceptions are the contributions from false and background asymmetries that to some extend overlap and are correlated. Eq. (7.18) gives an upper limit for the systematic uncertainty.

The result for the $\Delta G/G$ including the systematic error is:

$$\mathbf{\Delta G/G = -0.57 \pm 041}(\text{stat.}) \pm \mathbf{0.17}(\text{syst.})$$

Combining the statistical and systematic uncertainties in quadratures:

$$\mathbf{\Delta G/G = -0.57 \pm 044}(\text{total})$$

Chapter 8

Summary and Outlook

The concept of spin is extremely important for different areas of science, from nuclear physics to stellar evolution. There are numerous applications that involve spin, just to mention the Nuclear Magnetic Resonance used in spectroscopy, chemistry and medicine; Electron Paramagnetic Resonance in chemistry and biology; spin transistors currently researched and to be used in new generations of computer storage devices. The influence of the idea of spin is even found in some economic models [150]! Although the physical phenomena related to spin being explored in so many fields of pure and applied science, still many fundamental questions remain. One of them is the relation of the nucleon spin to the spins of its constituents. In particular the contribution of spins of gluons to the total spin of the nucleon is an issue that recently receives tremendous attention from high energy physics.

In this thesis the analysis leading to the direct measurement of the contribution of the gluon polarisation to the nucleon spin was described. The studies rely on data coming from the COMPASS experiment. The experiment uses a polarised ^{6}LiD target and a 160 GeV polarised muon beam. The presented analysis encompasses the filtered and reconstructed data from COMPASS which were available at the beginning of 2007, *i.e.* collected in 2002–2004. The data from 2006 are still in the production phase and will be ready for analysing in the middle of 2007. The studies rely on the Photon-Gluon Fusion (PGF) process, that directly probe the gluon structure of nucleon. The PGF is tagged with open charm mesons. This analysis is the first implementation of that method of PGF tagging in the polarised scattering experiments.

The relative polarisation of gluons in the deuteron resulting from the analysis is:

$$\begin{aligned} \mathit{\Delta} G/G(x_g = \mathbf{0.15}, \mu^{\mathbf{2}} = \mathbf{13}\ \mathrm{GeV}^{\mathbf{2}}) &= -\mathbf{1.17} \pm \mathbf{0.54}(\mathrm{stat.}) \pm \mathbf{0.17}(\mathrm{syst.}) \\ \mathit{\Delta} G/G(x_g = \mathbf{0.15}, \mu^{\mathbf{2}} = \mathbf{13}\ \mathrm{GeV}^{\mathbf{2}}) &= \quad \mathbf{0.22} \pm \mathbf{0.62}(\mathrm{stat.}) \pm \mathbf{0.17}(\mathrm{syst.}) \end{aligned}$$

for the D^0-tagged and the D^0-untagged channels, respectively. The two results agree within statistical errors. As there is neither theoretical nor experimental indication that these two channels should be treated differently, the results are averaged which gives:

$$\begin{aligned} \mathit{\Delta} G/G(x_g = \mathbf{0.15}, \mu^{\mathbf{2}} = \mathbf{13}\ \mathrm{GeV}^{\mathbf{2}}) &= -\mathbf{0.57} \pm \mathbf{0.41}(\mathrm{stat.}) \pm \mathbf{0.17}(\mathrm{syst.}) \\ &= -\mathbf{0.57} \pm \mathbf{0.44}(\mathrm{total}) \end{aligned}$$

Taking into account D-state admixture in deuteron, as described in Sec. 2.2, the relative gluon polarisation inside the nucleon is:

$$\begin{aligned} \mathit{\Delta} G/G(x_g = \mathbf{0.15}, \mu^{\mathbf{2}} = \mathbf{13}\ \mathrm{GeV}^{\mathbf{2}}) &= -\mathbf{0.62} \pm \mathbf{0.44}(\mathrm{stat.}) \pm \mathbf{0.18}(\mathrm{syst.}) \\ &= -\mathbf{0.62} \pm \mathbf{0.48}(\mathrm{total}) \end{aligned}$$

The QCD scale for the PGF with charmed quark pair creation is 13 GeV^2. The average fraction of the nucleon momentum carried by the gluon in the PGF resulting in D^0 production in the final state is $x_g = 0.15$ with RMS of 0.08.

Proceeding in the same way as in Sec. 6.3, that is multiplying the value -0.62 ± 0.48 by G_{cor} factor calculated with GRV98 gluon distribution, one gets:

$$\begin{aligned} \varDelta G(x_g = \mathbf{0.15}, \mu^\mathbf{2} = \mathbf{13}\ \mathrm{GeV}^\mathbf{2}) &= -\mathbf{8.0} \pm \mathbf{6.2} \pm \mathbf{1.0}(G\ \text{distribution}) \\ &= -\mathbf{8.0} \pm \mathbf{6.3}(\text{total}) \end{aligned}$$

The uncertainty of the result is dominated by the statistical error. The main factor that limits the number of registered D^0 events and the purity of the sample is lack of a vertex detector. This drawback is unavoidable as in the experiment a massive target enclosed in the cooling system has to be used. On the other hand the systematic uncertainty is well controlled and the analysis only weakly depends on the assumptions introduced by a Monte Carlo. Therefore despite the large statistical uncertainty the result presented here is of a great importance, as it is almost completely independent of the models, contrary to the high–p$_\mathrm{T}$ analyses. The obtained value is in agreement with the results from the scaling violation of the g_1 structure function and from the high–p$_\mathrm{T}$ hadron method.

In Tab. 8.1 the $\Delta G/G$ values from lepton-nucleon scattering experiments are collected. They are also presented in Fig. 8.1 and compared with the curves from the NLO fit to the global g_1 data plotted for the scale 3 GeV^2 [46]. Two solutions for $\Delta G/G(x_g)$ were found with the QCD fit, one with positive and one with negative value of ΔG. For both $|\Delta G|$ is small, of the order of 0.2–0.3. The direct measurements also indicate that the gluon polarisation in the nucleon is small. However with the present precision they do not distinguish between a negative and positive solution obtained with the QCD fit. The scenarios with large $|\Delta G|$, greater than 1.0, seem to be ruled out.

Experiment	Process studied	$\langle x_g \rangle$	Scale [GeV^2]	$\Delta G/G(x_g)$
HERMES	high–p$_\mathrm{T}$ (small Q^2)	0.17	2.1	0.41 ± 0.18 ± 0.03
HERMES	high–p$_\mathrm{T}$ - inclusive hadron	0.22	1.35	0.071 ± 0.034 $^{+127}_{-105}$
SMC	high–p$_\mathrm{T}$ ($Q^2 > 1\mathrm{GeV}^2$)	0.07	3	-0.20 ± 0.28 ± 0.10
COMPASS	high–p$_\mathrm{T}$ ($Q^2 > 1\mathrm{GeV}^2$)	0.13	3	0.06 ± 0.31 ± 0.06
COMPASS	high–p$_\mathrm{T}$ ($Q^2 < 1\mathrm{GeV}^2$)	0.095	3	0.016 ± 0.058 ± 0.055
COMPASS	**open charm**	**0.15**	**13**	**-0.57 ± 0.41 ± 0.18**

Table 8.1: The comparison of the results for $\Delta G/G$ from different lepton-nucleon scattering experiments.

Presently also the preliminary data from polarised proton-proton collisions studied by STAR and PHENIX experiments at RHIC are available. Until now PHENIX has performed the asymmetry measurement for the neutral pions in the final state. Preliminary results of the charged pions and the asymmetries for the jets, the J/ψ and η particles production were released as well [151]. Chosen results are presented in Fig. 8.2. They are compared with predictions of NLO QCD fits with different constraints for the polarised gluons densities. STAR has presented the asymmetries for the inclusive jets, charged pions and neutral pions production [153], Fig. 8.3. All the results from the proton-proton interactions point towards a small or moderate gluon polarisation in the nucleon.

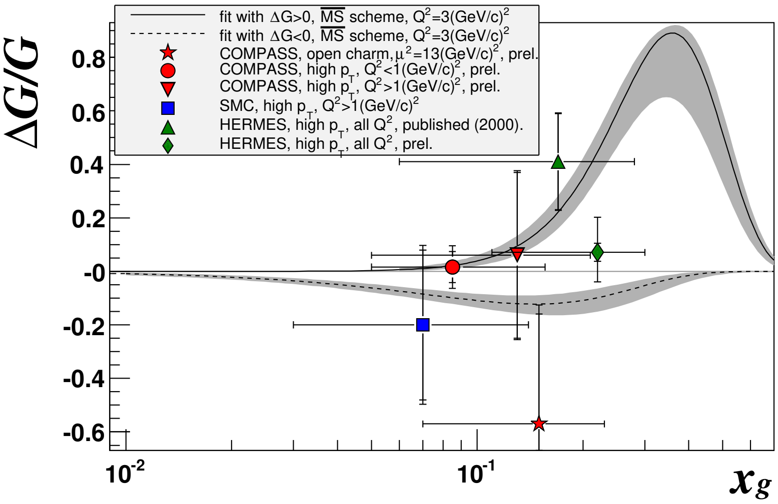

Figure 8.1: Gluon polarisation $\Delta G/G(x_g)$ at 3 GeV^2 scale, obtained from the COMPASS NLO QCD analysis (curves) and from direct measurements (points).

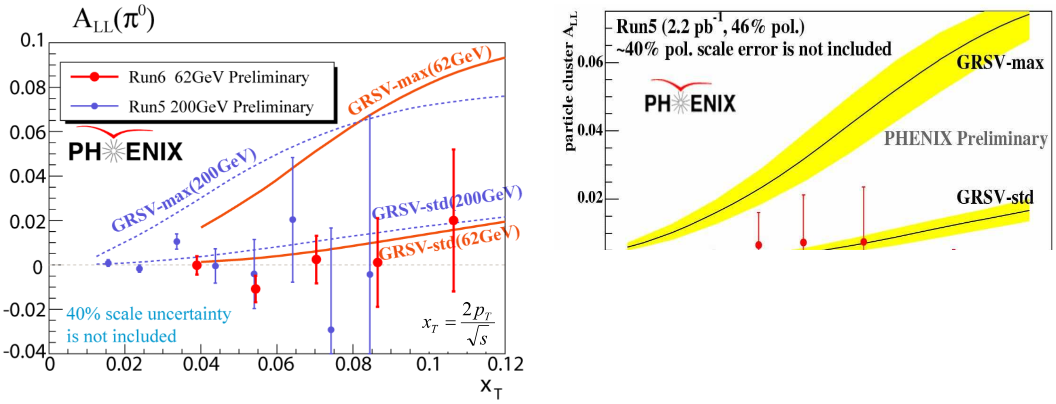

Figure 8.2: Chosen PHENIX results for the double spin cross-section asymmetries as functions of transverse momenta with respect to the beam. Left: neutral pions production; right: jets production. Errors are statistical. Predictions on asymmetries (curves) use GRSV NLO [152] parton distributions. The GRSV-std refers to the best global fit to the polarised data ($\Delta G = 0.4$), while GRSV-max to the case of maximally positive gluon polarisation. On the right plot also the scenario with vanishing gluon polarisation is presented. The plots were taken from [151] where more details can be found.

In the last few years a great progress in the measurements of the gluon polarisation was achieved. Not more than four years ago, before the COMPASS and RHIC results were released, the experimental data had allowed for ΔG as large as 2–3. Now such scenarios are excluded. However the data on ΔG are still not very precise and for instance two following scenarios can be considered:

$$\begin{array}{ccccccc} 1/2 & = & 1/2\ \ \Delta\Sigma & + & \Delta\mathrm{G} & + & \mathrm{J} \\ 1/2 & = & 1/2\ \ 0.3 & + & 0.35 & + & 0.0 \\ 1/2 & = & 1/2\ \ 0.3 & + & 0.0 & + & 0.35 \end{array}$$

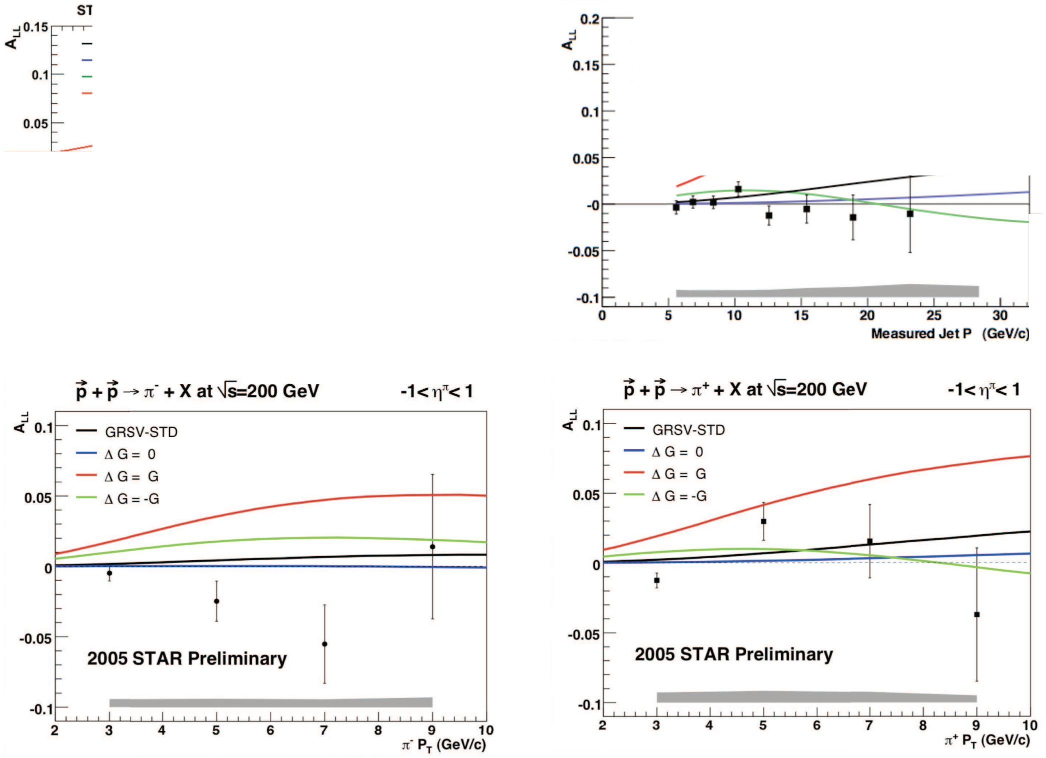

Figure 8.3: STAR results for the double spin cross-section asymmetries as functions of transverse momenta with respect to the beam or as functions of the momenta of jets. Top-left: neutral pions, top-right: jets, bottom-left: negative pions, bottom-right: positive pions. Error bars correspond to statistical errors while the bands at the bottom of each picture mark systematic uncertainties. Predictions on asymmetries (curves) use GRSV NLO [152] parton distributions. The GRSV-std refers to the best global fit to the polarised data. The cases for maximal positive, negative and vanishing gluon polarisation are also considered. For details see [153].

What are the improvements in the accuracy of the ΔG measurement expected in the near future?

Until now only a part of the collected data was analysed by COMPASS. The high–p_T ($Q^2 > 1$ GeV^2) channel was studied with the 2002–2003 data set only. The 2004 will double the statistics. Therefore the expected statistical uncertainty for this method for the whole 2002–2004 period is of the order of 0.22. The events recorded in 2006 are still in the production phase and their quality is not known yet. The expected reduction in the statistical error is 1.2–1.4 for all the channels.

Experiments at RHIC plan to take data with polarised beams for the next few years. PHENIX and STAR will greatly improve the measurements in all the channels. The improvement will be accompanied by measurements with direct photons. In 2009 PHENIX will be supplemented with a silicon vertex detector. With this detector the open charm mesons reconstruction will become feasible [154]. The spin programme at RHIC facility is expected to highly enhance the present knowledge of the gluon polarisation.

The nucleon spin decomposition will not be fully understood until the partons orbital angular momentum contribution is determined. The exclusive measurements of **D**eeply

Virtual **C**ompton **S**cattering (DVSC) will lead to determination of this quantity [155]. The COMPASS experiment is planning to perform these studies in the future.

The concept of spin was introduced to physics in the twenties of the last century. Since then it was intensively studied both: experimentally and theoretically. Now it seems that we are approaching to the understanding of the nucleon spin decomposition. However as history of spin research shows, the more answers found, the more questions risen. The significance of the spin studies and its impact on physics was summarised by J. D. Bjorken: *"Polarisation data has often been the graveyard of fashionable theories. If theorists had their way, they might just ban such measurements altogether out of self-protection."*.

Acknowledgement

I would like to express my deep gratitude to following persons:

- My supervisor, Professor Barbara Badełek, for her care, everlasting support, enthusiasm and her sagacity which she decided to share with me during my studies at Warsaw University. I am grateful to her for giving me the possibility to work for the COMPASS experiment.

- The Open Charm Group, especially: Susanne Koblitz, Florent Robinet, Joerg Pretz, Jean-Marc Le Goff and Oleg Kouznetsov. I am deeply indebted to Krzysztof Kurek, who is not only a member of the Open Charm Group, but also who showed me the depth and the beauty of the Spin Physics.

- My colleagues from Warsaw University whom I was sharing my office and my work with: Beata Pawlukiewicz-Kamińska and Marcin Stolarski. I am thankful to them for their help, advice and friendly atmosphere at work.

- The Warsaw COMPASS Group and the entire COMPASS Collaboration. Constructing and operating such a complicated machine as the COMPASS spectrometer is an enormous challenge. These great people were able to succeed with this endeavour. I am very happy that I had an opportunity to meet them and to work with them.

- All my friends at Warsaw University.

This work was partially supported by MNII research funds No. 1 P03B 043 28 and No. N202 027 32/0706.

I wish to thank my wife, Gabriela Głębocka, whose patience during many, long evenings and weekends when I was preparing my thesis has been extraordinary. Thank you for your unfailing love, endless support and encouragement. Last but certainly not least, many thanks to my Mother and Grandparents for teaching me how to live my life with a useful purpose.

Thank you!

List of Figures

List of Tables

Bibliography

[1] F. E. Close and R. G. Roberts, Phys. Lett. **B316** (1993) 165.

[2] E80, M. J. Alguard *et al.*, Phys. Rev. Lett. **41** (1978) 70.

[3] EMC, J. Ashman *et al.*, Phys. Lett. **B206** (1988) 364; J. Ashman *et al.*, Nucl. Phys. **B328** (1989) 1.

[4] SMC, B. Adeva *et al.*, Phys. Rev. **D58** (1998) 112001.

[5] HERMES, A. Airapetian *et al.*, Phys. Rev. **D** *(in press)* hep-ex/0609039.

[6] E142, P. L. Anthony *et al.*, Phys. Rev. **D54** (1996) 6620.

[7] E143, K. Abe *et al.*, Phys. Rev. Lett. **74** (1995) 346.

[8] E155, P. Anthony *et al.*, Phys. Lett. **B463** (1999) 339.

[9] COMPASS, G. Baum *et al.*, COMPASS proposal, CERN-SPSLC 96-14.

[10] G. Brona (for COMPASS Collaboration), Acta Phys. Polon. **B36** (2005) 2233.

[11] G. Brona (for COMPASS Collaboration), Czech. J. Phys **56** (2006) Suppl. F, 53.

[12] G. Brona (for COMPASS Collaboration), to appear in the proceedings of 42nd Recontre de Moriond: QCD and Hadronic Interactions, La Thuile, Italy, 2007.

[13] COMPASS, E. S. Ageev *et al.*, Eur. Phys. J. **C41** (2005) 469.

[14] J. D. Bjorken, Phys. Rev. **179** (1969) 1547; R. P. Feynman, Phys. Rev. Lett. **23** (1969) 1415.

[15] F. Halzen and A. Martin, Quarks and Leptons, John Wiley & Sons, 1984.

[16] L. G. Greeniaus, Deep Inelastic Scattering with Spin, Lectures presented for the Troisième Cycle de la Physique en Suisse Romande, Geneva, 2000.

[17] A. V. Manohar: Proceedings of Lake Louise Winter Institute, Lake Louise, Canada 1992, World Scientific, 1992.

[18] C. G. Callan and D. J. Gross, Phys. Rev. Lett. **22** (1969) 156.

[19] ZEUS, S. Chekanov *et al.*, Eur. Phys. J. **C21** (2001) 443.

[20] H1, C. Adloff *et al.*, Eur. Phys. J. **C21** (2001) 33.

[21] BCDMS, A. C. Benvenuti *et al.*, Phys. Lett. **B223** (1989) 485.

[22] E665, M. R. Adams *et al.*, Phys. Rev. **D54** (1996) 3006.

[23] NMC, M. Arneodo *et al.*, Nucl. Phys. **B483** (1997) 3.

[24] L. W. Whitlow *et al.*, Phys. Lett. **B282** (1992) 475.

[25] W.-M. Yao *et al.*, J. Phys. **G33** (2006) 1.

[26] G. S. Mitchel on behalf of the E155 Collaboration, presented at American Physical Society (APS) Meeting of the Division of Particles and Fields (DPF 99), Los Angeles, CA, 5-9 Jan 1999, hep-ex/9903055.

[27] P. Hoodbhoy, R. L. Jaffe and A. V. Manohar, Nucl. Phys. **B312** (1989) 571.

[28] H. Khan and P. Hoodbhoy, Phys. Lett. **B298** (1993) 181.

[29] HERMES, A. Airapetian *et al.*, Phys. Rev. Lett. **95** (2005) 242001.

[30] V. N. Gribov and L. N. Lipatov, Sov. J. Nucl. Phys. **15** (1972) 438.

[31] G. Altarelli and G. Parisi, Nucl. Phys. **B126** (1977) 298.

[32] Y. L. Dokshitzer, Sov. Phys. JETP **46** (1977) 641.

[33] G. Altarelli, R. D. Ball, S. Forte and G. Ridolfi, Acta Phys. Polon. **B29** (1998) 1145.

[34] W. Vogelsang, Phys. Rev. **D54** (1996) 2023.

[35] R. Mertig and W. L. van Neerven, Z. Phys. **C70** (1996) 637.

[36] S. Moch, J. A. M. Vermaseren and A. Vogt, Nucl. Phys. **B724** (2005) 3.

[37] M. Anselmino, A. Efremov and E. Leader, Phys. Rep. **261** (1995) 1.

[38] J. D. Bjorken, Phys. Rev. **148** (1966) 1467.

[39] W. A. Bardeen *et al.*, Phys. Rev. **D18** (1978) 3998.

[40] S. L. Adler and W. A. Bardeen, Phys. Rev. **182** (1969) 1517.

[41] S. L. Adler, Phys. Rev. **177** (1969) 2426.

[42] J. S. Bell and R. Jackiw, Nuovo Cim. **A60** (1969) 47.

[43] COMPASS, V. Yu. Alexakhin *et al.*, Phys. Lett. **B647** (2007) 330.

[44] E155, P. Anthony *et al.*, Phys. Lett. **B553** (2003) 18.

[45] E130, G. Baum *et al.*, Phys. Rev. Lett. **51** (1983) 1135.

[46] COMPASS, V. Yu. Alexakhin *et al.*, Phys. Lett. **B647** (2007) 8.

[47] HERMES, K. Ackerstaff *et al.*, Phys. Lett. **B404** (1997) 383.

[48] HERMES, A. Airapetian *et al.*, Phys. Rev **D71** (2005) 012003.

[49] SMC, B. Adeva *et al.*, Phys. Lett. **B420** (1998) 180.

[50] M. Hirai *et al.*, Phys. Rev. **D69** (2004) 054021.

[51] J. Blümlein and B. Böttcher, Nucl. Phys. **B636** (2002) 225.

[52] eRHIC project homepage, www.bnl.gov/eic/ .

[53] M. Klein, Int. J. Mod. Phys. **A15S1** (2000) 467.

[54] H1, C. Adloff *et al.*, Nucl. Phys. **B545** (1999) 21.

[55] A. Bravar, D. von Harrach and A. Kotzinian, Phys. Lett. **B421** (1998) 349.

[56] H. Jung, RAPGAP manual: http://www.desy.de/∼jung/rapgap/ .

[57] K. Kurek, (COMPASS), private communication, May, 2007.

[58] L. N. Hand, Phys. Rev. **129** (1963) 1834.

[59] S. Hedicke (COMPASS), PhD thesis, Albert Ludwigs Universität, 2005, Freiburg, Germany, wwwcompass.cern.ch/compass/publications .

[60] M. Glück, E. Reya and C. Sieg, Eur. Phys. J. **C20** (2001) 271.

[61] A. A. Sokolov and I. M. Ternov, Sov. Phys. Dokl. **8** (1964) 1203.

[62] HERMES, K. Ackerstaff *et al.*, Nucl. Instr. Meth. **A417** (1998) 230.

[63] HERMES, A. Airapetian *et al.*, Phys. Rev. Lett. **84** (2000) 2584.

[64] P. Liebing on behalf of the HERMES Collaboration, presentation during SPIN2006 conference, Kyoto, Japan, October 2, 2006,
www-nh.scphys/kyoto-u.ac.jp/SPIN2006 .

[65] SMC D. Adams *et al.*, Phys. Rev. **D56** (1997) 5330.

[66] SMC, B. Adeva *et al.*, Phys. Rev. **D70** (2004) 012002.

[67] G. Ingelman, A. Edin and J. Ratsman, Comput. Phys. Commun. **101** (1997) 108;
G. Ingelman, A. Edin and J. Ratsman, LEPTO 6.5, program manual, DESY 96-057
www.isv.uu.se/thep/MC/lepto .

[68] T. Sjöstrand *et al.*, Comput. Phys. Commun. **135** (2001) 238;
T. Sjöstrand, PYTHIA 5.7 and JETSET 7.4, CERN-TH.7112/93
www.thep.lu.se/∼tobjorn/Pythia.html .

[69] COMPASS, E. S. Ageev *et al.*, Phys. Lett. **B633** (2006) 25.

[70] STAR, K. H. Ackermann *et al.*, Nucl. Instr. Meth. **A499** (2003) 624.

[71] PHENIX, K. Adcox *et al.*, Nucl. Instr. Meth. **A499** (2003) 469.

[72] STAR, B. I. Abelev *et al.*, Phys. Rev. Lett. **97** (2006) 252001.

[73] COMPASS, P. Abbon *et al.*, Nucl. Instr. Meth. (2007) *(in press).*

[74] M. von Hodenberg (COMPASS), Diploma thesis, Albert Ludwigs Universität, 2002, Freiburg, Germany, wwwcompass.cern.ch/compass/publications .

[75] J-M Le Goff, COMPASS Internal Note 2002-2.

[76] See *e.g.*: http://sl.web.cern.ch/SL/eagroup/NewM2/main.html .

[77] SMC, D. Adams *et al.* Nucl. Instr. Meth. **A437** (1999) 23.

[78] A. Abragam and M. Goldman, Nuclear Magnetism: Order and Disorder, Clarendon Press, Oxford, 1982.

[79] S. L. Bültmann *et al.*, Nucl. Instr. Meth. **A425** (1999) 23; K. Kondo *et al.*, Nucl. Instr. Meth. **A526** (2004) 70.

[80] O. A. Rondon, Phys. Rev. **C60** (1999) 035201.

[81] J. Bisplinghoff *et al.*, Nucl. Instr. Meth. **A490** (2002) 101.

[82] H. Angerer *et al.*, Nucl. Instr. Meth. **512** (2003) 229.

[83] D. Thers *et al.*, Nucl. Instr. Meth. **A469** (2001) 133.

[84] M. C. Altunbas *et al.*, Nucl. Instr. Meth. **A490** (2002) 177.

[85] P. Barbaries *et al.*, COMPASS Internal Note 1998-9.

[86] V. N. Bychkov *et al.*, Part. Nucl. Lett. **111** (2002) 63.

[87] F. W. Brasse *et al.*, DESY F21-76/02.

[88] E. Albrecht *et al.*, Nucl. Instr. Meth. **A518** (2004) 586.

[89] COMPASS RICH web page,
http://wwwcompass.cern.ch/compass/detector/rich/welcome.html .

[90] G. Baum *et al.*, Nucl. Instr. Meth. **A502** (2003) 246.

[91] N. Akopov *et al.*, Nucl. Instr. Meth. **A479** (2002) 511.

[92] M. Aizawa *et al.*, Nucl. Instr. Meth. **A499** (2003) 508.

[93] S. Panebianco (COMPASS), PhD thesis, Univiversité de Paris-Sud, 2005, Orsay, France (in French), wwwcompass.cern.ch/compass/publications .

[94] E. Albrecht *et al.*, Nucl. Instr. Meth. **A502** (2003) 266.

[95] COMPASS muon trigger page,
wwwcompass.cern.ch/compass/detector/trigger/muon-trigger/triggerdoc.ps.gz .

[96] See: http://castor.web.cern.ch/castor .

[97] See: wwwcompass.cern.ch/compass/detector/daq/

[98] R. E. Kalman, Transactions of the ASME **D82** (1960) 35.

[99] V. Alexakhin *et al.*, COMPASS Internal Note 2001-17.

[100] See: http://ges.home.cern.ch/ges/phast .

[101] See: http://root.cern.ch .

[102] R. Hermann, COMPASS analysis meeting, January 27-28, 2005.

[103] Y. Bedfer (COMPASS), private communication, December, 2004.

[104] M. Ziembicki, COMPASS Collaboration meeting, Freiburg, March 23, 2007.

[105] G. Brona (COMPASS), Diploma thesis, University of Warsaw, 2004, Warsaw, Poland, wwwcompass.cern.ch/compass/publications .

[106] N. Dedek (COMPASS), PhD thesis, Ludwig Maximilians Universität, 2005, Munich, Germany (in German), wwwcompass.cern.ch/compass/publications .

[107] S. Godfrey and J. Napolitano, Rev. Mod. Phys. **71** (1999) 1411.

[108] ZEUS, S. Chekanov *et al.*, Phys. Lett. **B578** (2004) 33.

[109] L3, S. Braccini, Talk given at 37th Recontres de Moriond on Electroweak Interactions and Unified Theories, Les Arcs, France, 2002, hep-ex/0205035

[110] Cascade Physics: A New Window on Baryon Spectroscopy, conference web page, http://conferences.jlab.org/cascade .

[111] D. Strottman, Phys. Rev. **D20** (1979) 748.

[112] M. Praszałowicz, Skyrmions and Anomalies, Proceedings of the Cracow Workshop on Skyrmions and Anomalies, Mogilany, Poland, World Scientific (1987), p. 112.

[113] D. Diakonov, V. Petrov and M. V. Polyakov, Z. Phys. **A359** (1997) 305.

[114] V. D. Burkert, Int. J. Mod. Phys. **A21** (2006) 1764.

[115] NA49, C. Alt *et al.*, Phys. Rev. Lett. **92** (2004) 042003.

[116] H. G. Fisher and S. Wenig, Eur. Phys. J. **C37** (2004) 133.

[117] ALEPH, S. Schael *et al.*, Phys. Lett. **B599** (2004) 1.

[118] BABAR, B. Aubert *et al.*, Phys. Rev. Lett. **95** (2005) 042002.

[119] CDF, O. Litvintsev *et al.*, Nucl. Phys. Proc. Suppl. **142** (2005) 374.

[120] E690, D. Christian *et al.*, Phys. Rev. Lett. **95** (2005) 152001.

[121] FOCUS, K. Stenson, Int. J. Mod. Phys. **A20** (2005) 3745.

[122] HERA-B, I. Abt *et al.*, Phys. Rev. Lett. **93** (2004) 212003.

[123] HERMES, A. Airepetian *et al.*, Phys. Rev. **D71** (2005) 032004.

[124] WA89, M. Adamovich *et al.*, Phys. Rev. **C70** (2004) 022201.

[125] ZEUS, S. Chekanov *et al.*, Phys. Lett. **B610** (2005) 212.

[126] J. Pochodzalla (COMPASS), private communication, February, 2005.

[127] J. Zhao, COMPASS analysis meeting, March 21, 2005.

[128] M. Stolarski (COMPASS), Diploma thesis, University of Warsaw, 2002, Warsaw, Poland (in Polish), wwwcompass.cern.ch/compass/publications .

[129] O. Kouznetzov, COMPASS analysis meeting and private communication, September, 2006.

[130] A. Korzenev and S. Koblitz, COMPASS stability web page, http://wwwcompass.cern.ch/compass/software/offline/input/stab/index.html .

[131] M. von Hodenberg (COMPASS), PhD thesis, Albert Ludwigs Universität, 2005, Freiburg, Germany, wwwcompass.cern.ch/compass/publications .

[132] J. Pretz (SMC), PhD thesis, Johannes Gutenberg Universität, 1997, Mainz, Germany (in German).

[133] J. Pretz, COMPASS Internal Note 2004-11.

[134] J. Pretz (COMPASS), Habilitation thesis, Universität Bonn, 2007, Bonn, Germany.

[135] J. M. Le Goff, COMPASS Internal Note 2004-3.

[136] N. W. Schellingerhout *et al.*, Phys. Rev. **C48** (1993), 2714.

[137] K. Gustafsson, COMPASS Internal Note 2003-3.

[138] A. A. Akhundov, D. Y. Bardin, L. Kalinovskaya and T. Riemann, Fortsch. Phys. **44** (1996) 373.

[139] A. Bravar, K. Kurek and R. Windmolders, Comput. Phys. Commun. **105** (1997) 42.

[140] R. D. Peccei and R. Rückl, Nucl. Phys. **B162** (1980) 125.

[141] J. M. Le Goff and J. Pretz, COMPASS Internal Note 2004-4.

[142] G. Ingelman, J. Ratsman and G.A. Shule, Comput. Phys. Commun. **101** (1997) 135; AROMA manual, http://www.isv.uu.se/thep/aroma/ .

[143] H. L. Lai *et al.*, Eur. Phys. J. **C12** (2000) 375; S. Kretzer *et al.*, Phys. Rev. **D69** (2004) 114005.

[144] M. Glück, E. Reya and A. Vogt, Eur. Phys. J. **C5** (1998) 461.

[145] A. D. Martin *et al.*, Eur. Phys. J. **C39** (2005) 155.

[146] R. Sulej, www.ire.pw.edu.pl/∼rsulej .

[147] J. Pretz, COMPASS Internal Note 2005-12.

[148] J. Pretz, COMPASS analysis meeting, December 14, 2006.

[149] S. Koblitz and A. Korzenev, data grouping web page, http://wwwcompass.cern.ch/compass/software/offline/input/stab/grouping.html .

[150] B. Rosenow, cond-mat/0107018.

[151] K. Barish on behalf of the PHENIX Collaboration, presentation during SPIN2006 conference, Kyoto, Japan, October 2, 2006, www-nh.scphys/kyoto-u.ac.jp/SPIN2006 .

[152] M. Glück, *et al.*, Phys. Rev. **D63** (2001) 094005.

[153] B. Surrow on behalf of the STAR Collaboration, presentation during SPIN2006 conference, Kyoto, Japan, October 2, 2006, www-nh.scphys/kyoto-u.ac.jp/SPIN2006 .

[154] J. Lajoie on behalf of the PHENIX Collaboration, presentation during DIS2007 conference, Munich, Germany, April 19, 2007, http://www.mppmu.mpg.de/dis2007/ .

[155] M. Diehl, Phys. Rept. **388** (2003) 41.